Durham University

Durham E-Theses

The Generation Potential of Diffuser Augmented Tidal Stream Turbines

CRESSWELL, NICHOLAS,WILLIAM

How to cite:

CRESSWELL, NICHOLAS,WILLIAM (2015) *The Generation Potential of Diffuser Augmented Tidal Stream Turbines*, Durham theses, Durham University. Available at Durham E-Theses Online: http://etheses.dur.ac.uk/10980/

Use policy



This work is licensed under a Creative Commons Attribution 2.0 UK: England & Wales (CC BY)

Academic Support Office, The Palatine Centre, Durham University, Stockton Road, Durham, DH1 3LE
e-mail: e-theses.admin@durham.ac.uk Tel: +44 0191 334 6107
http://etheses.dur.ac.uk



The Generation Potential of Diffuser Augmented Tidal Stream Turbines

Nicholas William Cresswell

Submitted to Durham University for the degree of

Doctor of Philosophy

School of Engineering and Computing Sciences

2014

Abstract

This thesis investigates the power generation potential of diffuser augmented horizontal axis tidal stream turbines. The use of diffuser augmentation for such devices is not a new concept, though many questions remained unanswered regarding the device performance and economics. This work highlighted a number of limitations within the literature on such devices and aimed to clarify the main factors which affect their performance and economics in tidal stream flows.

Extant numerical modelling methods for diffuser augmented turbines were shown to produce inaccurate power prediction results due to modelling simplifications. The accurate numerical modelling of diffuser augmented turbines was made possible by the derivation of an extended blade element momentum turbine model within computational fluid dynamics. This model was verified experimentally and found to reproduce the experimental data accurately, matching both power outputs and diffuser surface pressures.

The investigation was undertaken using a combination of numerical modelling and wind tunnel experimentation. It was found that effective diffuser augmentation requires a rotor with a thrust of approximately 1/2 that of a bare rotor. The rotor geometry was found to have a significant impact upon the boundary layer flows and therefore the diffusion and power output. The impact of the hub and the component geometry interactions were also highlighted. It was also found that diffuser augmentation allows sustained performance under yawed flows and potential for improvement in highly turbulent flow. It was shown that diffuser augmented devices with lower area ratios are more efficient at power capture.

An economic analysis was performed, combining a derived cost model and an annual energy production analysis using real tidal stream data, incorporating flow yaw and turbulence effects. It was shown that using current technology, bare rotor type devices are the more economically viable means of power generation.

Declaration

This thesis is based on the work carried out by Nicholas William Cresswell, under the supervision of Dr. Grant Ingram and Dr. Robert Dominy as a part of the Energy Group, School of Engineering and Computing Sciences, Durham University. No part of this thesis has been submitted elsewhere for any other degree or qualification and all research included in this thesis is the author's own work unless referenced otherwise.

Copyright © 2014 by Nicholas William Cresswell

"The copyright of this thesis rests with the author. No quotations from it should be published without the author's prior written consent and information derived from it should be acknowledged."

Acknowledgements

I would like to thank my supervisors Dr. Grant Ingram and Dr. Robert Dominy for all of their efforts, time and patience during the course of this thesis. Their input has been invaluable throughout the course of the work.

I'm very grateful to the technical staff of the School for their assistance with the experimental studies. In particular I would like to thank Colin Wintrip, Paul Jarvis and Phillip Duffy from the mechanical workshop for their construction of the test rig and their support during testing. Thanks also to Ian Hutchinson, Ian Garrett and Martin Feeney from the electronics workshop for their support in the design and testing of the electrical aspects of the project.

Many students and staff members within the School of Engineering also deserve thanks for their efforts and discussions over the years. I would particularly like to thank Dr. David Sims-Williams, Dr. Richard Williams and Dr. Supakit Worasinchai for all that they have done.

I'd like to acknowledge the Bedford Institute of Oceanography of the Canadian Government, for providing the highly detailed tidal channel data which enabled the economic analysis to be completed.

This project would not have been possible without the financial support of the Engineering and Physical Sciences Research Council, who funded this work and also the Centre for Doctoral Training in Energy within Durham University. I am immensely grateful for this support.

On a personal note I would like to say thanks to all of those who have made my time during this thesis an immense amount of fun, especially the members of Ustinov College and the Ustinov College GCR. Without them the PhD experience would have been very different, though probably less stressful. To Rosi Jelfs, for putting up with me for so long and to Neal Brodsky who sadly never made it to this point himself and is missed by many, rest in peace.

Thanks finally to my family for their continuing support over many years. I would certainly not be here today were it not for them.

Table of Contents

List of Figures ..... **x**

List of Tables ..... **xx**

Nomenclature ..... **xxii**

1. Introduction **1**

1.1. Background 1

1.2. Tidal Generation 3

1.2.1. Extraction Methods 3

1.2.2. Terminology 4

1.2.3. Existing Tidal Stream Generation 4

1.3. Thesis Scope 6

1.4. Thesis Structure 7

2. Literature Review **9**

2.1. Tidal Stream Generation Environment 9

2.1.1. Freestream Energy 9

2.1.2. Tidal Stream Currents 9

2.1.3. Vertical Velocity Profile 10

2.1.4. Environmental Turbulence 10

2.2. Horizontal Axis Turbine Physics 11

2.2.1. Theoretical Limits to Power Extraction 11

2.2.2. Blade Forces and Power Output 11

2.2.3. Wake of a Horizontal Axis Turbine 12

2.3. Diffuser Flows 13

2.3.1. Purpose and Mechanism of a Diffuser 13

2.3.2. Effect of Reynolds Number on Diffusion 15

2.3.3. Effect of Swirl on Diffusion 16

2.3.4. Effects of Turbulence, Transience and Boundary Layers 19

2.3.5. Effect of Axial Velocity Profile and Diffuser Wall Jets 24
2.4. Diffuser Augmented Turbines 26
2.4.1. Physics of Power Augmentation 26
2.4.2. Quantifying Device Efficiency 27
2.4.3. Theoretical and Numerical Modelling of Augmented Turbines 28
2.4.4. Augmentation of Wind Turbines 31
2.4.5. Diffuser Augmentation of Tidal Turbines 39
2.4.6. Additional Benefits of Diffuser Augmentation 41
2.4.7. Demerits of Diffuser Augmentation 42
2.5. Concluding Remarks 42
3. Numerical Methods 45
3.1. Blade Element Momentum Model 45
3.1.1. Momentum Theory 45
3.1.2. Tip Loss Correction 48
3.1.3. Blade Element Theory 50
3.1.4. Blade Element Momentum Model 51
3.1.5. Ideal Bare Turbine Blade Shape 58
3.2. Computational Fluid Dynamics 59
3.2.1. Turbulence Modelling 59
3.2.2. Common Boundary Conditions 59
3.2.3. Material Properties 60
3.2.4. Actuator Disc Modelling 61
3.2.5. Meshing Parameters 63
3.2.6. Validation of CFD Methodology 66
3.3. Geometry Optimisation 70
3.3.1. Overall Procedure 70
3.3.2. Input Parameters 70
3.3.3. Design of Experiments 72

3.3.4. Coordinate Transformation 74
3.3.5. Geometry Creation 75
3.3.6. CFD Setup 76
3.3.7. Objective Function 77
3.3.8. Metamodelling 77
3.3.9. Genetic Algorithm 78
3.3.10. Convergence Assessment 79
3.3.11. Optimisation Summary 79
3.4. Concluding Remarks 80
4. Numerical Results 81
4.1. Experimental Turbine Blade Design 81
4.1.1. Cavitation 81
4.1.2. Blade Section Characteristics 82
4.1.3. Ideal Blade Shape 86
4.1.4. Designed Blade Shape 87
4.1.5. Power Output of the Bare Rotors 88
4.2. Experimental Diffuser Geometry Design 89
4.2.1. Effect of the Tip Gap Jet 89
4.2.2. Convergence of the Optimisation Routine 91
4.2.3. Diffuser Geometry Definition 94
4.3. Effect of the Reynolds Number 96
4.4. Effect of the Hub Geometry 103
4.4.1. Effect of the Hub Shape 103
4.4.2. Effect of the Hub Size 107
4.4.3. Experimental Hub Geometry 109
4.5. Further Diffuser Flow Modelling 111
4.5.1. Diffuser Leading Edge Modification 111
4.5.2. Effect of the Turbine Thrust 114

4.5.3. Effect of Freestream Turbulence on Power Output....118
4.6. Concluding Remarks....135
4.6.1. Turbine Modelling and Geometry....135
4.6.2. Hub Modelling and Geometry....136
4.6.3. Device Optimisation....136
4.6.4. Turbulence Modelling....137
5. Experimental Methods....138
5.1. Apparatus....138
5.1.1. Wind Tunnel....138
5.1.2. Diffuser & Turbine Experimental Rig Construction....139
5.2. Experimental Configurations....148
5.3. Data Collection and Measurement Techniques....153
5.3.1. Torque Sensor Measurements....153
5.3.2. Reflective Phototransistor....155
5.3.3. Pressure Transducers....156
5.3.4. Static Pressure Tappings....156
5.3.5. Five-Hole Pressure Probe....157
5.3.6. Force Balance....159
5.3.7. Three Phase Power Measurements....159
5.3.8. Logging Methodology....159
5.3.9. Filtering Methodology....160
5.3.10. Overall Estimate of the Uncertainty....161
5.4. Concluding Remarks....162
6. Experimental Results....163
6.1. Diffuser Characterisation....163
6.1.1. Effect of Reynolds Number....163
6.1.2. Effect of the Yaw Angle....164
6.1.3. Effect of the Nacelle Geometry....166

6.2. Rotor Characterisation....168
6.2.1. Effect of Reynolds Number....168
6.2.2. Verification of the Rotor Only Blade Element CFD....169
6.2.3. Effect of the Rotor Yaw Angle....170
6.2.4. Rotor Wake Flow Structure....175
6.3. Combined Diffuser and Rotor Characterisation....181
6.3.1. Effect of Reynolds Number....181
6.3.2. Verification of the Combined Blade Element CFD....185
6.3.3. Effect of the Device Yaw Angle....188
6.3.4. Diffuser and Rotor Wake Flow Structure....191
6.4. Concluding Remarks....199
6.4.1. Verification of Blade Element Momentum Turbine Model....199
6.4.2. Wake Recovery....200
6.4.3. Effect of Yaw....200
7. Diffuser Augmented Device Costs.... 201
7.1. Tidal Stream Turbine Cost Model....201
7.1.1. Assumptions of the Tidal Stream Turbine Cost Model....201
7.1.2. Capital Cost & Mass Model....203
7.1.3. Operation and Maintenance Cost Model....213
7.1.4. Model Verification....214
7.1.5. Tidal Stream Turbine Test Cases....215
7.1.6. Cost Model Results....216
7.2. Annual Energy Production Analyses....218
7.2.1. Annual Energy Production Methodology....219
7.2.2. Tidal Channel Data....222
7.2.3. AEP Model Input Data....226
7.3. Tidal Stream Turbine Cost of Energy....227
7.3.1. Effect of Flow Yaw....227

7.3.2. Case Study Location AEPs 230
7.4. Summary of the Factors Affecting Device Cost 232
8. Conclusions 234
8.1. Fluid Dynamics of Diffuser Augmented Turbines 234
8.2. Generation Potential of Diffuser Augmented Turbines 236
9. Further Work 238
9.1. Component Interaction Effects 238
9.2. Effects of Turbulence 238
9.3. Cavitation Inception 239
9.4. Effect of Shear Profiles and Wave Effects 239
10. References 240

List of Figures

Figure 1: Total annual CO_2 emissions 1850-2010 [3] 1
Figure 2: CO_2 emissions by source 2010 [4] 1
Figure 3: 2010 world electricity generation by source [5] 2
Figure 4: Example pre-commercial tidal stream generators [23] 5
Figure 5: Schematic diagram of a generalised duct arrangement 6
Figure 6: Forces on an aerofoil/hydrofoil section 12
Figure 7: Flow regime boundaries for conical diffusers [55] 14
Figure 8: Axisymmetric diffuser geometry terminology 15
Figure 9: Diffuser power coefficient against back pressure for diffuser augmented wind turbines surveyed by van Bussel [24] 37
Figure 10: Exit plane flange arrangement and flow schematic [84] 38
Figure 11: Momentum theory reference stations for a bare rotor 46
Figure 12: Definition of analysis annular streamtubes 47
Figure 13: Diagram of the vortex sheet shedding and flow around the vortex sheets for Prandtl's tip loss correction method 49
Figure 14: Flow angles and forces on a blade element 50
Figure 15: Diagrammatic representation of wind turbine wake states 52
Figure 16: Momentum theory reference stations for a diffuser augmented rotor 54
Figure 17: Example unstructured mesh for optimisation runs 64
Figure 18: Magnified views of the example unstructured mesh 64
Figure 19: Blocking strategy for structured meshing 65
Figure 20: Low mesh density view of a structured mesh 66
Figure 21: Detailed views of a full density mesh with porous cell zone 66
Figure 22: Reference dimensions for ESDU CFD verification cases 67
Figure 23: ESDU performance chart for conical diffusers with tail pipes [54] 67
Figure 24: CFD domain to mimic McDonald & Fox experimental setup 69
Figure 25: Comparison of McDonald & Fox data with CFD results 70
Figure 26: Geometry optimisation procedure 71
Figure 27: Tidal channel geometry and optimisation constraints 71
Figure 28: Example two dimensional face centred central composite and latin hypercube experimental designs 72
Figure 29: Degrees of freedom for control points 73
Figure 30: Optimisation domain and sub-domains 73

Figure 31: Transformation map from 2D Cartesian coordinates to shape functions.74
Figure 32: Computation domain schematic with boundary types 76
Figure 33: NACA63818 lift and drag coefficients against the angle of attack from XFoil at a Reynolds number of $2.5x10^5$.....82
Figure 34: NACA63818 and rounded NACA63818 aerofoil cross sections.....83
Figure 35: NACA63818 and rounded NACA63818 lift and drag coefficients against the angle of attack at a Reynolds number of $2.45x10^5$ 83
Figure 36: Pressure coefficients around the blade section at Re=$2.5x10^5$ for angles of attack of (a) 10° and (b) 22.5° for NACA63818 and rounded sections....84
Figure 37: Lift and drag coefficients of the rounded NACA63818 section over the operating range of Reynolds numbers and angles of attack.....84
Figure 38: Pressure coefficients around the blade section for a range of Reynolds numbers for angles of attack of (a) 10° and (b) 27.5° for the rounded section 85
Figure 39: Ideal distributions of the relative flow angle, angle of attack and normalised chord length for a rotor designed for a tip speed ratio of 4 ..86
Figure 40: Power coefficient against tip speed ratio for ideal rotor with NACA63818 blades at a Reynolds number of $5.3x10^5$ based on the rotor diameter 87
Figure 41: Relative flow angle, angle of attack and normalised chord length for the final blade design with a NACA63818 section at a tip speed ratio of 4 ..87
Figure 42: Power coefficient against tip speed ratio for design rotor with NACA63818 blades at a Reynolds number of $5.3x10^5$ based on the rotor diameter 88
Figure 43: Power coefficient against tip speed ratio for the rounded NACA63818 rotor blades at the two tested pitch angles 89
Figure 44: Simulation domain and setup for tip gap jet study.....89
Figure 45: Pressure recovery against area power coefficient for tip gap jet study....90
Figure 46: Area power coefficient against pressure recovery coefficient for the optimisation simulations with the diffuser inlet at the duct minimum diameter 92
Figure 47: Diffuser efficiency against the area power coefficient for the optimisation simulations with the diffuser inlet at the duct minimum internal diameter 93
Figure 48: Final NURBS output geometry from the optimisation routine.....93

Figure 49: Velocity contours and streamtraces for final NURBS output geometry from the optimisation routine at Re = 3.41×10^7 94
Figure 50: Cross-section of the final experimental diffuser shape 94
Figure 51: Velocity contours and streamtraces for tested diffuser at Re = 3.63×10^7 95
Figure 52: Pressure coefficients around the diffuser for the NURBS geometry and the experimental diffuser geometry 96
Figure 53: Diffuser and hub geometry in the Reynolds number sensitivity studies ..97
Figure 54: Power coefficient against Reynolds number for both the UAD and BEMAD turbine models 97
Figure 55: Velocity contours and streamtraces for UAD model at Re = 1.34×10^7 ...98
Figure 56: Velocity contours and streamtraces for BEMAD model at Re = 1.14×10^7 99
Figure 57: Comparison of diffuser exit swirl profile from CFD models at a Reynolds number of 1.14×10^6 with the equivalent Lamb-Oseen vortex 100
Figure 58: Velocity contours and streamtraces for UAD model at Re = 1.01×10^4 .100
Figure 59: Velocity contours and streamtraces for BEMAD model at Re = 1.28×10^4 101
Figure 60: Boundary layer thickness in the tip gap for the BEMAD cases 102
Figure 61: Hub shape geometries examined 103
Figure 62: Contours of velocity with streamtraces for hub shape 1 with a uniform actuator disc model at a Reynolds number of 4.07×10^5 and thrust coefficient of 0.646 104
Figure 63: Coefficients for hub geometry cases using the UAD model for thrust coefficient values approximating those of the standard pitch blading at TSR=4 104
Figure 64: Performance coefficients for hub geometry cases using the BEMAD turbine model and the standard pitch blading at TSR=4 105
Figure 65: Contours of velocity with streamtraces for hub 1 with a BEMAD model, standard pitch blading at TSR=4, Reynolds number of 2.84×10^5 and C_T=0.639 105
Figure 66: Power coefficient against tip speed ratio for diffuser with 8% and 20% hub sizes and the standard pitch experimental blading 108
Figure 67: Contours of velocity with streamtraces for 8% hub with a blade element actuator disc turbine model, the standard pitch blading at TSR=4, a Reynolds number of 3.38×10^5 and a thrust coefficient of 0.594 109

Figure 68: Experimental hub geometry definition.....110
Figure 69: Power coefficient against tip speed ratio for diffuser with 8%, 20% and experimental hubs and the standard pitch experimental blading 110
Figure 70: Contours of velocity with streamtraces for experimental hub shape with a blade element actuator disc turbine model, the standard pitch blading at TSR=4 and a Reynolds number of $2.86x10^5$ 111
Figure 71: Modified diffuser leading edge geometry.....112
Figure 72: Power coefficient against tip speed ratio for diffuser with 8% and 20% hubs, standard pitch blading and the original and modified diffuser leading edges.....112
Figure 73: Contours of velocity with streamtraces for 8% hub with a blade element actuator disc turbine model, standard pitch blading at TSR=4, a Reynolds number of $3.38x10^5$ and a thrust coefficient of 0.595.....113
Figure 74: Contours of velocity with streamtraces for 20% hub with a blade element actuator disc turbine model, standard pitch blading at TSR=4, a Reynolds number of $3.48x10^5$ and a thrust coefficient of 0.522.....114
Figure 75: Power coefficient based on the device outer area aginst the rotor thrust coefficient for a range of cases examined at a tip speed ratio of 4.....115
Figure 76: In situ C_T against the bare rotor C_T for a bare rotor and the leading edge modified diffuser with experimental blades & 20% hub at TSR = 4 117
Figure 77: Geometry used for bare rotor turbulence impact study.....120
Figure 78: Normalised power coefficient, thrust coefficient and cube of velocity against the freestream turbulence intensity for the bare rotor.....120
Figure 79: Wake recovery on the device centreline behind the hub for different freestream turbulence intensities in BEM CFD.....121
Figure 80: Geometry used for the analysis of the impact of turbulence on the diffuser derived from this thesis.....122
Figure 81: Normalised power coefficient against turbulence intensity for diffuser..122
Figure 82: Normalised swirl velocity at the exit plane of the diffuser for CFD simulations over a range of turbulence intensities for the derived diffuser geometry.....123
Figure 83: Pressure recovery and total pressure loss coefficients aginst turbulence intensity for the derived diffuser geometry.....123
Figure 84: Rotor plane normalised axial velocity profiles over a range of turbulence intensities for the derived diffuser geometry.....124

Figure 85: Geometry used for the analysis of the impact of turbulence on the diffuser used by Sun and Kyozuka [122] 125
Figure 86: Normalised C_P & U_x against I for Sun and Kyozuka diffuser 125
Figure 87: Contours of velocity with streamtraces for Sun & Kyozuka diffuser at (a) a Reynolds number of $2.23x10^5$ and turbulence intensity of 0.99% (b) a Reynolds number of $2.43x10^5$ and turbulence intensity of 25.05% 127
Figure 88: Experimental design for the parameterised diffuser geometries 128
Figure 89: Parametric diffuser and hub geometry for case 4 129
Figure 90: Power coefficient based on rotor area against area ratio & length to diameter ratio at I = 8.91%, with case locations and hub length line ..129
Figure 91: Pressure recovery coefficient against the area ratio and length to diameter ratio at I = 8.91%, with case locations and hub length line ..130
Figure 92: Power coefficient based on the diffuser outer area against the area ratio and length to diameter ratio at a turbulence intensity of 8.91%, with case locations 131
Figure 93: Power coefficient based on the device outer area against the diffuser area ratio at a freestream turbulence intensity of 12.71% 132
Figure 94: Contour plot of change in the rotor area power coefficient from 0.99% to 12.71% turbulence intensity, with lines of effective half angle and case locations 133
Figure 95: Contour plot of change in in the rotor area power coefficient from 0.99% to 22.42% turbulence intensity, with lines of effective half angle and case locations 133
Figure 96: Power coefficient based on the diffuser outer area against the area ratio and length to diameter ratio at a turbulence intensity of 22.62%, with case locations 134
Figure 97: Isometric wind tunnel view detailing the salient features 138
Figure 98: Traverse limits in the wind tunnel as a function of the blade radius 139
Figure 99: Diffuser and turbine rig salient features 140
Figure 100: Diffuser body cross section showing key dimenions 140
Figure 101: Diffuser assembly details 141
Figure 102: Diffuser static pressure tapping insert details 141
Figure 103: Mounting assemblies shown in rotor only configuartion view 142
Figure 104: Diffuser mounting assembly details and dimensions 143
Figure 105: Turbine blade details for non-pitched blade design 143

Figure 106: NACA63818 and rounded NACA63818 aerofoil cross sections.....144
Figure 107: Definition of the blade pitch angle.....145
Figure 108: Exploded view of the turbine drivetrain assembly.....145
Figure 109: Drivetrain and nacelle details and salient features.....146
Figure 110: Schematic of the electrical power, logging and speed control circuits..147
Figure 111: Resistance bank general arrangement.....148
Figure 112: Position of the experimental rig within the wind tunnel.....149
Figure 113: Diffuser only configuration within the wind tunnel looking upstream towards the working section inlet.....149
Figure 114: Rotor only configuration within the wind tunnel looking downstream towards the working section outflow.....150
Figure 115: Combined diffuser and rotor configuration within the wind tunnel looking downstream towards the working section outflow.....152
Figure 116: (a) Horizontal and (b) vertical planes and sampling points with coordinates normalised by the blade radius.....153
Figure 117: Logging layout for experimental runs.....154
Figure 118: Nacelle layout with location of the OPB704 reflective phototransistor155
Figure 119: Static pressure tapping locations on the diffuser surface.....157
Figure 120: Details of the Durham University five hole probe with hole numbering 157
Figure 121: Numerically filtered for example signal using a 5 Hz low pass filter....160
Figure 122: Experimental static pressure coefficient around the diffuser for empty diffuser with variation of the Reynolds number, showing the diffuser geometry.....163
Figure 123: Experimental and CFD static pressure coefficients around empty diffuser with variation of the Reynolds number, showing the diffuser geometry.....164
Figure 124: Definition of yaw angle for diffuser only cases.....165
Figure 125: Experimental static pressure coefficient around empty diffuser with variation of yaw angle on downstream section, showing the diffuser geometry.....165
Figure 126: Experimental static pressure coefficient around empty diffuser with variation of the yaw angle on upstream section, showing the diffuser geometry.....166

Figure 127: Static pressure coefficient around diffuser for diffuser and nacelle case with variation of the Reynolds number, showing the diffuser and nacelle geometries.....167
Figure 128: Contours of normalised velocity and streamtraces from CFD for experimental hub and diffuser with no turbine at Re = $5.9x10^5$.....167
Figure 129: Power coefficient against rotor tip speed ratio for bare rotors with variation of the Reynolds number (a) 0° pitch (b) -5° pitch.....168
Figure 130: Comparison of blade element momentum, blade element mometum CFD and experimental results at Re = $5.5x10^5$ for (a) 0° pitch (b) -5° pitch blades.....169
Figure 131: Definition of yaw angle and turbine rotation for rotor only case.....171
Figure 132: Effect of yaw angle and tip speed ratio variation on the power coefficient for bare rotors at Re=$5.1x10^5$ (a) 0° blade pitch (b) -5° blade pitch.....171
Figure 133: Rotor yaw coordinate system.....172
Figure 134: Local relative flow angle against the azimuth angle and yaw angle at mid-span for a planar rotor at a tip speed ratio of 4.....172
Figure 135: Diagrammatic representation of the effect of the hub support fairing on the flow direction at the rotor plane.....173
Figure 136: Normalised peak power coefficient against yaw angle for both blades.174
Figure 137: Angle of attack against the azimuth angle and yaw angle at mid-span for a planar rotor at a tip speed ratio of 4.....174
Figure 138: Location of the downstream offset plane relative to the bare rotor.....175
Figure 139: (a) Total and (b) static pressure coefficients for -5° blade pitch rotor at TSR=5.3 and Re=$4.9x10^5$, on Y-Z plane at 1.6 blade radii downstream of the rotor.....176
Figure 140: (a) Normalised velocity (b) turbulence intensity with -5° blade pitch at TSR=5.3 and Re=$4.9x10^5$, on Y-Z plane at 1.6 blade radii downstream of the rotor.....176
Figure 141: Normalised (a) radial and (b) tangential velocity with -5° blade pitch at TSR=5.3 and Re=$4.9x10^5$, on Y-Z plane at 1.6 blade radii downstream of the rotor.....177
Figure 142: Comparison of computed normalised axial velocity distribution at traverse plane with experimental data for the bare rotor with -5° blade pitch.....178

Figure 143: Spanwise distribution of the blade elements' contribution to the rotor power coefficient and the axial induction factor for the -5° blade pitch rotor at TSR=5.5 and Re=5.0x10^5, calculated using the blade element momentum model 178

Figure 144: (a) Yaw and (b) pitch angles in degrees in the rotor wake for -5° blade pitch rotor at TSR=5.3 and Re=4.9x10^5, on X-Y plane at turbine axis height 179

Figure 145: (a) Total and (b) static pressure coefficients in the rotor wake for -5° blade pitch rotor at TSR=5.3 and Re=4.9x10^5, on X-Y plane at turbine axis height 179

Figure 146: (a) Normalised velocity and (b) turbulence intensity in the wake for -5° blade pitch rotor at TSR=5.3 and Re=4.9x10^5, on X-Y plane at turbine axis height 180

Figure 147: Comparison of experimental and BEM CFD predicted wake recovery for -5° blade pitch rotor at Re=5.5x10^5, with a turbulence intensity of 4.71% 180

Figure 148: Effect of Reynolds number and tip speed ratio on the power coefficient of (a) 0° blade pitch (b) -5° blade pitch diffuser and rotor combinations 181

Figure 149: Pressure coefficient around diffuser for diffuser and rotor case with 0° blade with variation of Reynolds number at TSR = 5 182

Figure 150: Pressure coefficient around diffuser for diffuser and rotor case with -5° blade with variation of Reynolds number at TSR = 5 183

Figure 151: Pressure coefficient around diffuser for diffuser and rotor case with 0° blade with variation of the tip speed ratio at Re=6.3x10^5 184

Figure 152: Comparison of blade element mometum CFD and experimental results at a Reynolds number of 5.8x10^5 for (a) 0° pitch (b) -5° pitch blades .185

Figure 153: Pressure coefficient around diffuser for diffuser and rotor case with -5° pitch blade, TSR=5, Re=5.8x10^5, showing the diffuser, rotor and nacelle geometries 186

Figure 154: Static pressure coefficient around diffuser for diffuser and rotor with -5° pitch blade, TSR=1, Re=5.8x10^5, showing diffuser, rotor and nacelle geometries 187

Figure 155: Definition of yaw angle and turbine rotation for diffuser and rotor 188

Figure 156: Effect of the yaw angle and tip speed ratio on the power coefficient with (a) 0° blade pitch (b) -5° blade pitch rotors 188
Figure 157: Pressure coefficient around diffuser for diffuser and rotor case over yaw angle range, with -5° pitch blade, TSR=5, Re=5.5x10^5 189
Figure 158: Normalised peak power coefficient against the device yaw angle for both rotors with and without diffuser augmentation 190
Figure 159: Location of the downstream offset transect plane relative to the diffuser 191
Figure 160: (a) Total and (b) static pressure coefficients with -5° blade pitch at TSR=5.5 and Re=5.3x10^5, on Y-Z plane at 1.6 blade radii downstream of the rotor 192
Figure 161: (a) Normalised velocity and (b) Turbulence intensity with -5° blade at TSR=5.5 and Re=5.3x10^5, on Y-Z plane 1.6 blade radii downstream of rotor 192
Figure 162: Normalised (a) radial and (b) tangential velocity with -5° blade pitch at TSR=5.5 and Re=5.3x10^5, on Y-Z plane at 1.6 blade radii downstream of the rotor 193
Figure 163: Comparison of CFD normalised axial velocity distribution at traverse plane with experimental data for diffuser augmented rotor with -5° blade pitch 195
Figure 164: (a) Yaw and (b) pitch angles in degrees in the diffuser wake for -5° blade pitch rotor at TSR=5.5 and Re=5.3x10^5, on X-Y plane at turbine axis height 196
Figure 165: (a) Normalised velocity and (b) turbulence intensity in the wake for -5° blade pitch rotor at TSR=5.3 and Re=4.9x10^5, on X-Y plane at turbine axis height 196
Figure 166: (a) Total and (b) static pressure coefficients in the diffuser wake for -5° blade pitch rotor at TSR=5.5 and Re=5.3x10^5, on X-Y plane at turbine axis height 197
Figure 167: Experimental and BEM CFD wake recovery for -5° blade pitch rotor and diffuser augmented rotor at Re=5.5x10^5, with a turbulence intensity of 4.7% 198
Figure 168: Assumed configuration for the present study cost model 202
Figure 169: Cost breakdown for dual 16 m outer diameter devices on monopile foundation at a rated speed of 2.5 m/s 216

Figure 170: Levelised cost of energy components for a dual 16m outer diameter devices on a monopile foundation with a rated speed of 2.5 m/s.....217
Figure 171: Indicative levelised cost of energy components for early commercial wave and tidal energy arrays [195].....217
Figure 172: The effect of device radius on capital cost.....218
Figure 173: Diagrammatic representation of power capture against current velocity 219
Figure 174: Unaffected yaw angle against the diffuser length to diameter ratio.....221
Figure 175: Power reponses to the flow yaw angle for the devices examined.....221
Figure 176: Turbulence performance data for the devices examined.....222
Figure 177: Map showing the the Minas Passage, Map data ©2014 Google.....223
Figure 178: Aerial Image showing the six site locations within the Minas Passage, Map data ©2014 Google, Google Imagery ©2014 TerraMetrics.....223
Figure 179: Hodograph of the sample tidal velocities for Location 1.....224
Figure 180: Hodograph of the sample tidal velocities for Location 2.....224
Figure 181: Hodograph of the sample tidal velocities for Location 3.....224
Figure 182: Hodograph of the sample tidal velocities for Location 4.....225
Figure 183: Hodograph of the sample tidal velocities for Location 5.....225
Figure 184: Hodograph of the sample tidal velocities for Location 6.....225
Figure 185: Annual energy production for the trialled devices with a randomly yawed siusoidal input flow.....228
Figure 186: Cost per kWh for the devices with a yawed siusoidal input flow.....229
Figure 187: Yaw angle characteristics for the six case study sites.....230
Figure 188: Levelised cost of energy for the devices at the six case study sites.....231

List of Tables

Table 1: Summary of papers pertaining to Reynolds dependence of diffusion.....16
Table 2: Summary of papers relevant to the swirl dependence of diffusion.....19
Table 3: Summary of papers relevant to the dependence of diffusion on turbulence, transience and boundary layer development 23
Table 4: Literature summary on the effects of axial velocity profile on the diffusion 25
Table 5: Summary of papers on numerical modelling of diffuser augmented turbines 33
Table 6: Assumptions made here in momentum and blade element theories 46
Table 7: Assumptions of BEM theory as implemented within this thesis 57
Table 8: Assumptions of BEM CFD as implemented within this thesis.....57
Table 9: Computational time for the various turbine models per tip speed ratio.....58
Table 10: Common CFD solver parameters.....60
Table 11: Material properties of sea water 60
Table 12: Coefficients of air for use with Sutherland's law 61
Table 13: Dimensions for ESDU CFD verification cases.....68
Table 14: Comparison of CFD results with ESDU performance data 68
Table 15: Blade geometry details for the experimental blade sets 144
Table 16: Experimental tests conducted for the diffuser only configuration.....150
Table 17: Experimental tests for the rotor only configuration with each blade set 151
Table 18: Experimental tests conducted for the combined diffuer and rotor configuration with each blade set.....152
Table 19: Wake traverse details and flow conditions.....153
Table 20: Errors in the experimental and derived quantities.....161
Table 21: Circumferential RMS variations in the traverse plane flow properties ...193
Table 22: Masses of the rotor components in the two mass models.....203
Table 23: Capital costs of the rotor components in the two cost models 205
Table 24: Masses of the drivetrain components in the two mass models 205
Table 25: Capital costs of the drivetrain components in the two cost models.....206
Table 26: Masses of the generator and electrical components in the two mass models 207
Table 27: Costs of the generator and electrical components in the two cost models 207

Table 28: Masses of the electronics & control components in the two mass models 208
Table 29: Costs of the electronic & control components in the cost models 208
Table 30: Masses of the structural components in the two mass models 209
Table 31: Capital costs of the structural components in the two cost models 209
Table 32: Mass and capital cost of the diffuser in the present study 211
Table 33: Capital costs of civil engineering works in the two cost models 211
Table 34: Other capital costs in the two cost models 212
Table 35: Insurance and fiancial costs in the two cost models 213
Table 36: Operation and maintenance costs in the two cost models 213
Table 37: Estimates for the cost of array installation for MCT SeaGen devices 214
Table 38: Device sizes and power coefficients of the tidal stream turbine test cases 215
Table 39: Device velocity parameters for the AEP model 226

Nomenclature

English Symbols

Symbol	Definition	Unit
a	Axial induction factor	-
$\acute{a}$	Angular induction factor	-
A	Area	m^2
B	Number of blades	-
c	Blade chord	m
C	Coefficient, refer to subscript for meaning	m^2
d	Depth of point within channel	m
D	Total channel depth	m
E	Energy generated	kWh
f	Loss correction factor	-
F	Force	N
G	Augmentation ratio	-
k	Turbulent kinetic energy	J/kg
K	Pressure loss factor	m
L	Length	m
I	Turbulence intensity	-
m	Mass	kg
M	Bending moment	kNm
n	Number of sample points	-
N	Shape function	-
r	Radius from axis	m
R	Maximum radius	m
Re	Reynolds number	-
RMS	Root mean squared variation of variable	Refer to variable
p	Pressure (static pressure unless otherwise stated)	Pa
P	Power generated	W
q	Temperature	K
s	Sutherland temperature	K
S	Fluent source term	kg/s^2
t	Time	s

Symbol	Definition	Unit
T	Thrust force	N
u	Variable to estimate using Kriging model	Refer to variable
U	Velocity	m/s
V	Volume	m^3
w	Uniformly distributed load	N/m
W	Departure from Kriging model	Refer to variable
x	Distance in the x-axis direction from origin	m
y	Distance in the y-axis direction from origin	m
Y	Kriging model estimate	-
z	Distance in the z-axis direction from origin	m
Z	Kriging general model	Refer to variable

Greek Symbols

Symbol	Definition	Unit
α	Angle of attack	rad
β	Permeability of porous jump/media	m^2
γ	Blade pitch angle	rad
δ	Boundary layer thickness	m
ε	Diffuser efficiency	-
ϵ	Cavitation number	-
ζ	Coordinate axis 1 for transformation shape functions	-
η	Coordinate axis 2 for transformation shape functions	-
θ	Azimuthal angle	rad
κ	Process/component efficiency	-
λ	Tip speed ratio	rad
Λ	Correction factor	-
μ	Dynamic Viscosity	Pas
ϖ	Lamb-Oseen vortex model constant	-
ρ	Density	kg/m^3
σ	Rotor solidity	-
ς	Basin efficiency	-
τ	Shear stress	N/m^2

Symbol	Definition	Unit
φ	Local relative flow angle	rad
ω	Wake angular velocity	
ψ	Device yaw angle	rad
Δ	Difference between values	-
Ω	Turbine angular velocity	rad/s
∇	Gradient of field	-

Other Symbols

Symbol	Definition
£	Cost in Great British pound sterling
$	Cost in United States Dollars
€	Cost in Euros

Acronyms

Acronym	Definition
AC	Alternating Current
AEP	Annual Energy Production
BEMAD	Blade Element Actuator Disc
BL	Boundary Layer
CFD	Computational Fluid Dynamics
CNC	Computer Numerical Control
DC	Direct Current
DSW	Durham Software for Windtunnels
GBP	Great British Pounds
EUR	Euros
NREL	National Renewable Energy Laboratory
NURBS	Non-Uniform Rational Basis Spline
PC	Personal Computer
PWM	Pulse-Width Modulation
RMS	Root Mean Squared
RANS	Reynolds-Averaged Navier–Stokes

Acronym	Definition
TGS	Turbulence Generation System
TSR	Tip Speed Ratio
UAD	Uniform Actuator Disc
USB	Universal Serial Bus
USD	United States Dollars

Subscripts

Subscript	Meaning
$0,1,\ldots,j,..,n$	Referring to value at a point/station number
$Access$	Refers to equipment required for access
AEP	Refers to a value from an annual energy production analysis
$Avail$	Refers to the device availability
AVG	Mean value
$Bearing$	Refers to turbine mounting bearing
$Blade$	Refers to turbine blade
$Brakes$	Refers to turbine brakes
c	Value at edge of vortex core
$Capital$	Refers to the initial capital cost
COE	Refers to the cost of energy
$Cont$	Refers to turbine control system
$CutIn$	Refers to turbine cut in velocity
$CutOut$	Refers to turbine cut out velocity
D	Relating to drag
Di	Relating to the diffuser
$DSurf$	Relating to surface area of the diffuser
Dyn	Relating to the dynamic pressure
e	Value at exit
$EInt$	Relating to the device electrical interface
$ECon$	Relating to the device electrical connections
FCR	Refers to the fixed charge rate
$Found$	Relating to device seabed foundations
$Frame$	Relating to nacelle supporting structural frame

Subscript	Meaning
$Gear$	Relating to the turbine gearbox
Gen	Relating to the generator
Hub	Relating to a property of the hub
HUB	Relating to the value at the hub
Hyd	Relating to device hydraulics and cooling system
i	Value at inlet
ICC	Refers to the initial capital cost including bonds and premiums
IS	In-situ value
$INFLOW$	Total at domain inlet
$Inst$	Relates to the installation process
L	Relating to lift
$Lease$	Relating to the cost of seabed lease
LRC	Relating to the levelised replacement cost of device
LSS	Relating to the low speed shaft
max	Maximum value
M	Relating to the porous media/jump
$Maint$	Refers to the cost of maintenance
$Marine$	Refers to the cost of component marinisation
N	Normal to turbine/porous media/jump plane
$\acute{N}$	Parallel to turbine/porous media/jump plane
$Nacelle$	Refers to nacelle cover
$Nose$	Refers to the turbine nose cone
$O\&M$	Operations and maintenance costs
$OUTFLOW$	Total at domain outlet
pj	Pressure jump
pr	Pressure recovery
P	Relating to power
$P\&S$	Refers to port and staging
PA	Relating to area power
$Permit$	Relates to the necessary permits for device installation
$Pitch$	Relating to a property of the turbine blade pitching gear
$PITCH$	Relating to pitch angle
Q	Relating to torque
r	Value at radius r

Subscript	Meaning
$RATED$	Value at the device power rating
REF	Reference value
Rel	Relative
Ro	Relating to rotor
$Scour$	Relates to device scour protection
$Skin$	Relates to diffuser body thickness
$Surety$	Refers to the surety bond
t	Relating to total pressure
T	Relating to thrust
$T\&T$	Refers to the turbine and tower totals
$Tail$	Relating to diffuser tailpipe
TIP	Relating to blade tip
$Total$	Refers to the total value within the mass model
$Tower$	Relating to tower support
$Trans$	Refers to transmission of power
$Transport$	Refers to transportation of components
$Turb$	Refers to turbulence
V	Value at liquid/vapour transition
VSE	Relating to the variable speed electrics
WP	Refers to a warranty premium
x	Axial component
$XBeam$	Refers to crossbeam support
Yaw	Relating to turbine yawing mechanism
YAW	Relating to yaw angle
∞	Freestream value
θ	Swirl component

Superscripts

Superscript	Meaning
$\bar{}$	Area weighted average
$\bar{\bar{}}$	Tensor of variable
$\vec{}$	Vector of directional components

Superscript	Meaning
$\dot{}$	Flow rate (s^{-1})

1. Introduction

1.1. Background

The requirement to produce energy with low carbon emissions has been deemed increasingly important recently due to the increasing awareness of climate change. The research is unequivocal in the demonstration of the presence of climate change and that this has been caused to a large extent by the emission of greenhouse gases [1, 2]. The massive increase in CO_2 emissions caused by human activity in the last 160 years can be seen in Figure 1, and the economy sectors to which they were attributable in 2010 are shown in Figure 2.

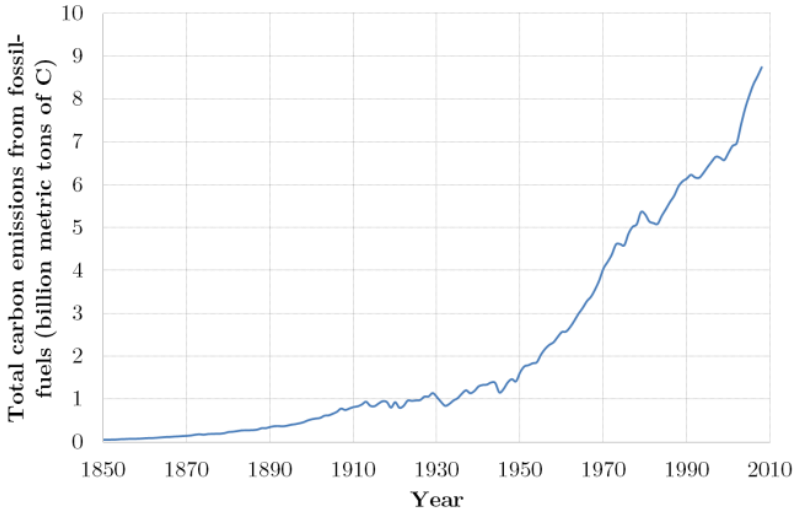


Figure 1: Total annual CO_2 emissions 1850-2010 [3]

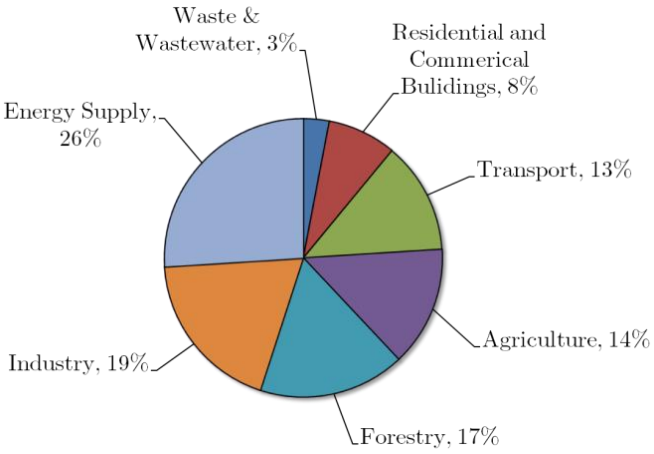


Figure 2: CO_2 emissions by source 2010 [4]

In order to avert potentially extensive ecological damage from climate change it has become to be seen as a necessity to combat greenhouse gas emissions. As can be seen in Figure 1, the largest single source of CO_2 emissions is the production of energy, which accounted for 26% of all CO_2 emissions in 2010. The fuel sources for the global electricity supply are shown in Figure 3. As can be seen, 66.5% of the world's electricity supply is generated from steam turbine power plants burning fossil fuels [5]. This type of generation is one of the prime drivers of greenhouse gas generation in the energy sector, which renewable energy aims to displace.

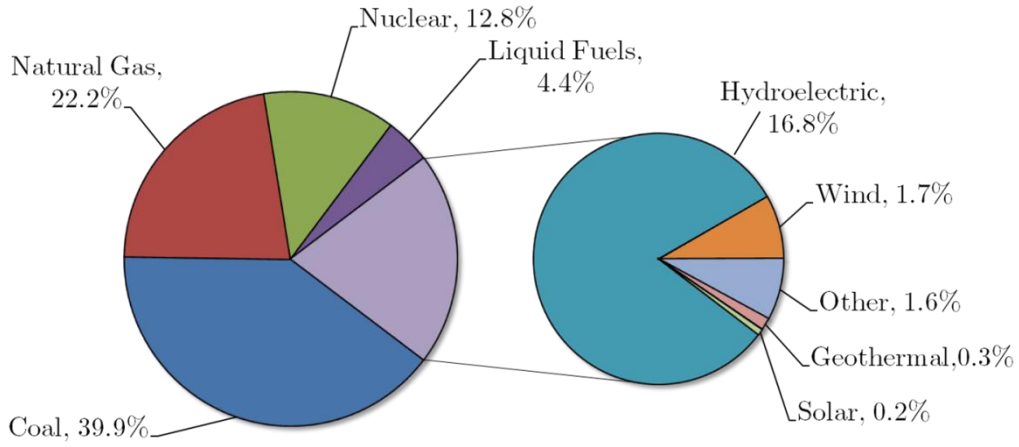


Figure 3: 2010 world electricity generation by source [5]

With the increased need for the generation of low emission energy, the study of renewable energy has been given a boost. The issue faced is the ability to economically capture sufficient quantities of energy to reduce or eliminate the need for nuclear or fossil fuel options. This has led to a significant investment in renewable energy, with a total market value of $247.6bn in 2013 [6]

Wind energy has thus far been the largest benefactor of the increased investment with 39% of the total renewable investment in 2007, a trend which is expected to continue with an estimated share of 32% in 2017 [7]. It is considered unlikely however that wind energy alone will ever be able to fulfil the energy needs of society due to the transient nature of the wind and relatively high unit power cost [8]. There are alternative energy sources that may aid in the transition, such as hydropower, ocean energy, solar energy, biomass and geothermal energy [9].

Hydropower is currently the world's largest source of renewable energy accounting for 83% of the global total, and forming 16.8% of the total world

electricity supply in 2010 [5]. The vast majority of this is the result of large scale "traditional" hydropower schemes such as those seen at Itaipu in Brazil or at the Three Gorges in China. Large scale hydropower, which is defined as having a capacity of greater than 10 MW, forms 94% of all hydropower generation, with the remainder from small hydropower [10]. The large scale schemes, whilst renewable in the sense that their fuel source is not depleted, have been questioned on their sustainability due to the environmental impact of the dams and associated hydrological issues [11, 12]. In addition to this, many of the developed world's large scale hydropower resources have already been tapped [13, 14].

The development of renewable energy and its commercial attraction requires sources of energy which are both relatively cheap and predictable. As a result of this there has been an interest in the exploitation of tidal power in its various forms due to the relatively high energy density for a renewable technology and the predictable, though periodic, nature of the power generation [15].

1.2. Tidal Generation

1.2.1. Extraction Methods

The power available in the tides can be exploited in one of two ways, either through more traditional approaches similar to those used for low head hydropower, or through the exploitation of tidal streams. The former option would encompass the construction of tidal barrages, such as that at La Rance [16], or tidal lagoons. These barrages or lagoons enclose a body of water which is either higher or lower than sea level, depending upon the tidal phase. Allowing the water to flow in or out of these water bodies through turbines will generate power. This method of extraction has the advantage that potentially large amounts of power can be generated, for example a conservative design for the proposed Severn Estuary barrage could provide up to 8.6 GW of power and supply 17 TWh of energy annually [17]. The costs associated with such projects are potentially large however and the potential environmental impacts could be significant [18].

Tidal stream generation operates in much the same way as wind energy. The kinetic energy of the free flowing fluid is converted into rotational energy of the turbine, spinning a generator from where the power is exported. This resource is available on a vast scale in the world's oceans, with an estimated 3TW of potential ocean current power available, although the amount considered feasible to extract is

only around 3% of this value [19]. This reduced figure of around 90GW is greater than the UK's peak power demand of 53.4GW in the winter of 2013/14 [20].

1.2.2. Terminology

For the purposes of this thesis, the term tidal stream generation is used for the conversion of freestream kinetic energy of a tidal flow into the kinetic energy of the turbine. There are many related terms which have been used to describe this, the more common being terms such as 'Marine Current Generation', 'Ocean Current Generation, 'Tidal In-Stream Energy Conversion' or 'Tidal Generation' [21].

Many aspects of the physics of tidal stream generation are applicable also to the capture of fluid kinetic energy from river flows. The term 'Hydrokinetic Energy Conversion' was proposed by Khan et al. [21] as terminology which reflects the interrelation between such devices.

1.2.3. Existing Tidal Stream Generation

In the recent past there has been a large amount of interest in the extraction of tidal stream power, with a range of extraction technologies suggested [21]. With the large body of technical expertise derived from the wind energy industry the horizontal axis turbine has received the most intense interest [15].

Horizontal axis machines dominate the existing examples of tidal stream generators, with 82% of the total commercial or pre-commercial projects in 2009 being of this type [21]. The prevalence of these units can largely be traced to the wind generation market, where the horizontal axis wind turbine (HAWT) has established superiority [22]. Due to the advanced nature of the research in the field it is easier to commercialise such technologies for tidal stream generation.

The predominance of horizontal axis turbines in the wind energy sphere has led to the development of very similar overall devices for tidal stream generation. There are many examples of companies with existing or planned test facilities for such devices, such as Alstom's Deepgen, MCT's SeaGen, Andritz Hydro's HS1000, Atlantis Resources AR1000 and Voith Hydro's HyTide 1000 [23]. Examples of some pre-commercial tidal stream generators which are under testing at the European Marine Energy Centre at the time of writing can be seen in Figure 4.

One proposed feature for the improvement of the generation performance of a horizontal axis turbine is the presence of a duct around the rotor to increase the

flow velocity at the rotor plane [24]. Ducting is the emplacement of profiled surfaces in the vicinity of the rotor to alter the flow characteristics at the rotor plane to maximise the generation potential. Figure 5 shows a schematic arrangement of a ducting system and its various components.

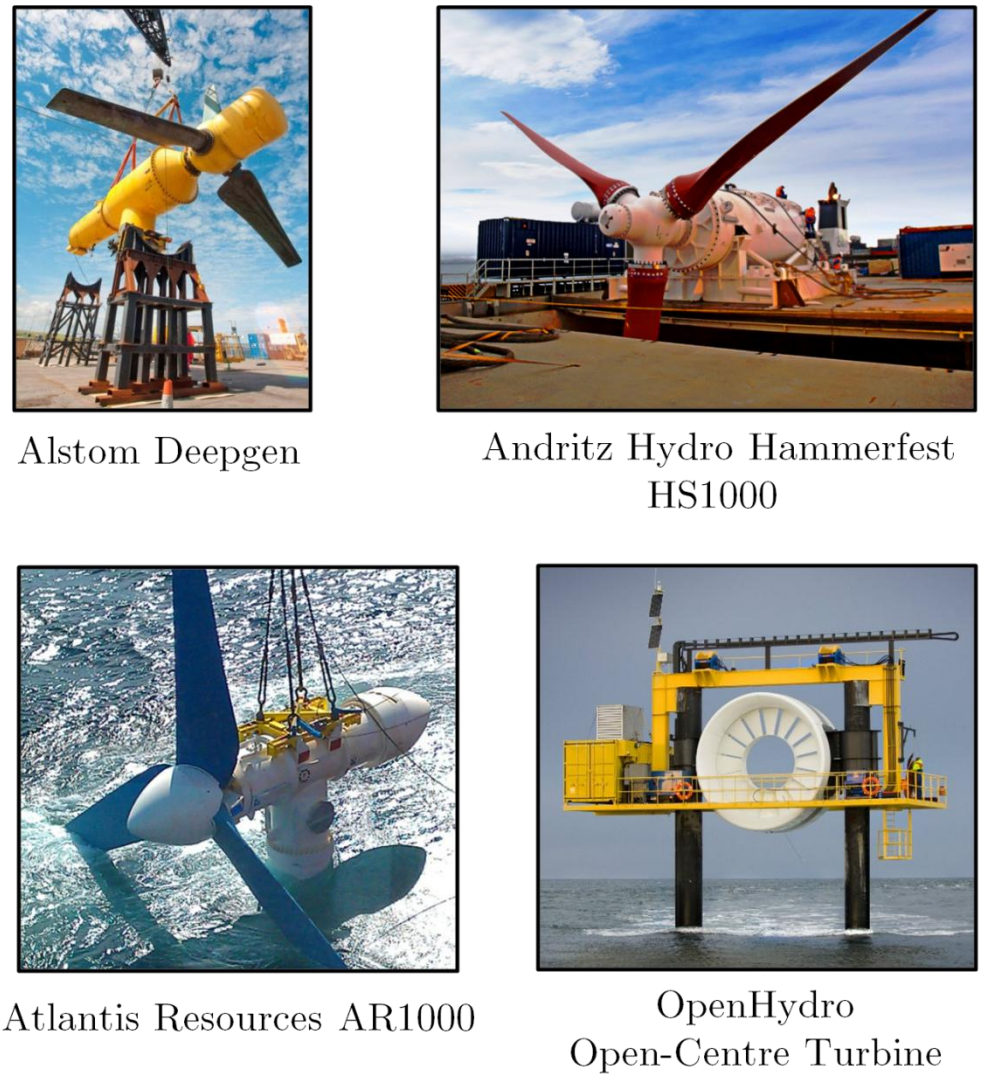


Figure 4: Example pre-commercial tidal stream generators [23]

Diffuser augmented turbines are not a new concept. The prospect of diffuser augmentation of wind turbines is something that has been considered for many years, with the history of development being summarised by Phillips [25]. The adoption of diffuser augmented wind devices has been questioned primarily on the basis of the generation potential, associated costs, performance at off angle flows and the necessity to design for storm loadings. The use of such devices for tidal stream generation is potentially more attractive as the loadings and directionality of the flow are much more predictable due to the nature of tidal flows [26].

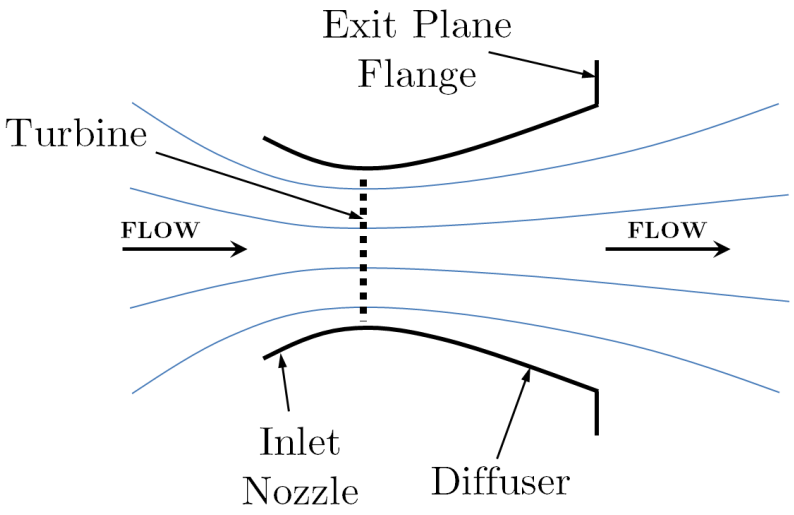


Figure 5: Schematic diagram of a generalised duct arrangement

The overall performance and cost effectiveness of diffuser augmented tidal stream generators are the factors on which the uptake of this technology will be decided. Though there has been renewed interest in the performance and modelling of such devices in the recent past, the situation remains far from clear.

1.3. Thesis Scope

This thesis examines the performance and merits of diffuser augmented tidal stream generators. Through a combination of computational fluid dynamics, numerical analysis and experimental work, the determinants of device performance are found and the efficacy of the device is assessed. This work has led to a number of original contributions to the study of diffuser augmented tidal stream generators.

Firstly, the modelling of diffuser augmented turbines has been addressed. Previously there was a considerable degree of uncertainty in the power prediction of diffuser augmented tidal stream generators, with a number of methodologies proposed. The implementation of blade element momentum theory within 2D computational fluid dynamics, coupled with tip loss correction and turbulence generation models has accurately replicated the turbine operation. This improved turbine model was verified experimentally, both with and without a diffuser, and was found to accurately predict the power output of the rotor.

A set of experimental results has been generated for representative diffuser geometry, along with a detailed procedure for their generation. This being the most

detailed set of experimental results for a diffuser augmented tidal stream turbine yet generated. The effects of yaw on diffuser augmented devices have been clarified.

The performance of a diffuser augmented tidal stream generator is assessed for the first time with a full assessment of hydrodynamic conditions. It is shown from a survey of historical diffuser augmented devices from both the wind and tidal sectors that no device has previously exceeded the peak power coefficient of a bare turbine. The device derived here also performs less efficiently than the bare rotor equivalent. It is shown however that the impact of turbulence and flow yaw on a ducted rotor is substantially different to that seen in a bare rotor. The diffuser augmented device is shown to exhibit limited performance degradation at yaw angles of up to $\pm 30°$, with performance improving in highly turbulent flow typical of a tidal channel.

Finally, the economics of diffuser augmented tidal stream generators are examined. Using a capital expenditure, operating and maintenance cost model built from previous studies and benchmarked against current commercial devices the cost of electricity is calculated and device configurations are contrasted.

1.4. Thesis Structure

The research presented in this thesis can be broken down into five sections:

1. The first two chapters, the introduction and literature review, provide an overview of the current state of tidal stream generation and how this fits into the broader need for renewable energy. The history, previous research and performance parameters defined in the literature are then summarised and presented. The necessity and basis for the work contained within this thesis are set out.
2. The next two chapters detail the numerical methodologies employed within this thesis and the results of the models. Methodologies are presented for geometry optimisation, computational fluid dynamics and the improved turbine modelling. The results of analyses of diffusers and diffuser augmented turbines are then presented.
3. The following two chapters provide information on the experimental methodology used within this thesis and the results of the testing. The design and construction of the test apparatus along with the measurement techniques and methods are provided. The results of the

tests are detailed and a comparison of the experimental results with those of the numerical models is presented.

4. Chapter 7 contains the assessment of the economics and power generation potential of a diffuser augmented tidal stream generator. The basis for the cost model is detailed along with the methodology and input data used for the assessment of the device performance. The output data from the assessment of a realistic tidal site using both bare and ducted rotors is presented.
5. The final part of this thesis draws together the information learned from the various investigations. The information is then used to produce conclusions on the performance of tidal stream generators, with a detailed comparison of bare and diffuser augmented units being drawn. Overall conclusions from the work presented are made and recommendations for future work are provided.

2. Literature Review

2.1. Tidal Stream Generation Environment

The tidal stream environment provides significant fluid dynamic complexity to the design and operation of generation devices. The flow velocity varies temporally, both over large timescales associated with the tides and short time scales associated with flow turbulence and free surface effects. The flow also varies spatially due to bathymetric effects and the effect of shear from the bed. This section provides a brief overview of these factors and the effects that they can have on a device.

2.1.1. Freestream Energy

The kinetic energy available in a freestream tidal flow is a function of the fluid density, the volumetric flow rate and the fluid velocity as seen in Equation 1.

$$P = {}^{1}/_{2}\, \dot{m}_{Ro} U_x{}^{2} = {}^{1}/_{2}\, \rho A_{Ro} U_x{}^{3} \qquad \text{Equation 1}$$

As can be seen from Equation 1, it is clearly beneficial to site generating units in areas with high flow velocities, as the available power is proportional to the cube of the velocity. The maximisation of velocity at the turbine plane is one of the key motivations for the augmentation of turbines through the use of ducting systems.

2.1.2. Tidal Stream Currents

The power available in a tidal stream is derived from the movement of large bodies of water between areas of differing elevation induced by lunar and solar movement relative to the earth [27]. Tides affect all seas and oceans, but the extent to which they generate the conditions for tidal energy extraction is highly dependent upon the tidal regime present at each individual site [28]. The tidal regime is informed by the bathymetry of the location and its surroundings and constraining of the flow by nearshore land masses [29]. The magnitude and direction of the flow velocity will change temporally and spatially due to the interaction of the tides with the complex nearshore and bathymetric situations [30-33]. These variations have an impact upon the generation potential of a tidal stream generator.

Since the tides are driven by the movement of the moon in the short term and the sun on a longer term basis, they are highly predictable. Most locations around the world experience semi-diurnal tides, with a period of approximately 12.5 hours. Other locations experience diurnal tides or mixed tides depending upon the local

geography [27]. Over a longer timescale of approximately 29.5 days the interaction of the sun with the moon creates the larger spring tides and the smaller neap tides.

2.1.3. Vertical Velocity Profile

The velocity throughout the depth of the water column in a tidal current flow changes greatly as it is subject to shear from the seabed. There are a variety of models which have been used to simplify this profile [31], the most commonly used being the $1/7^{th}$ power law [30] as seen in Equation 2.

$$U_x = U_{x_{max}} \left(\frac{z}{D}\right)^{1/7} \quad \text{Equation 2}$$

As a result of the velocity profile, the position of the rotor within the water column will have a significant impact upon the performance of a turbine. It is recommended that the turbine is kept away from the bed to maximise output and from the free surface to minimise wave effects and the impact on navigation [34].

The effect that the velocity profile has on the modelling of a tidal stream device was quantified by Mason-Jones et al. [35]. A combination of experimental and numerical data was used to verify non-dimensional relations of turbine performance for both uniform and profiled flow cases. It was concluded that in a uniform flow, so long as the volume averaged velocity across the turbine plane is used to calculate the coefficients relating to the performance of the device, the results were within 2% of those found with a vertical velocity profile.

2.1.4. Environmental Turbulence

The environment within which tidal stream generators operate is one with a significant degree of turbulence, with turbulent intensities at hub height typically being around 10% [36, 37]. The turbulence generation is primarily driven by the complex bathymetry in the vicinity of sites suitable for tidal stream generation.

The effect of turbulence on the performance of tidal stream generators is a source of ongoing research efforts. Maganga et al. [38] performed experimental tests on a horizontal axis turbine in a flume tank with a blockage ratio of 3.5%. The performance of their device was assessed at two turbulence intensities, 8% and 25%, over a range of tip speed ratios. It was found that the effect of the increased turbulence intensity was to reduce the peak power and thrust coefficients of the rotor by 14% and 13% respectively.

2.2. Horizontal Axis Turbine Physics

2.2.1. Theoretical Limits to Power Extraction

The extractable power available to the turbine is lower than that in the freestream flow due to the relationship between the change in momentum across the rotor plane and the mass flow rate. The available power is a function of the mass flow rate through the rotor and momentum change induced by it. If the velocity at turbine exit is zero, it therefore follows that the mass flow rate across the rotor is also zero, meaning zero power production. The Betz limit [39], or more precisely the Lanchester-Betz-Joukowsky limit [40] states that the maximum energy capture for an infinitely thin rotor is only 59.3% of the available energy. This limit is based on the application of momentum balance across the rotor with several assumptions. These assumptions are that the flow is axial, incompressible, has a constant upstream velocity and that the rotor does not possess a central hub or have any mass. It can be shown that maximum power extraction occurs when the downstream wake flow velocity is reduced to one third of that of the freestream velocity.

Limitations of the Betz model were noted and evaluated by Gorban et al. who derived a new model known as the GGS model for the evaluation of the maximum efficiency limit [41]. This model uses curvilinear flow and a velocity distribution across the blades to overcome some of the simplifying assumptions made in Betz's theory. Solution of the GGS model places the maximum efficiency of a plane rotor at 30.1%. This solution is overly conservative as devices with efficiencies greater than this have been tested in both wind and tidal environments [42].

2.2.2. Blade Forces and Power Output

A horizontal axis turbine generates power from the kinetic energy of a fluid through the use of profiled blades, which induce streamline curvature of the fluid and therefore generate a lift force. This force, which acts on the blade, is perpendicular to the local relative flow velocity and is what drives the turbine. As a direct consequence of the generation of lift, a force is generated which acts in the opposite direction to the lift and acts on the fluid. In addition to the lift force of the blade there is also a drag force generated as the blade passes through the fluid. The drag force also induces an opposing force in the fluid adding to the turbine thrust. These forces and the directions in which they act relative to the blade section can be seen diagrammatically in Figure 6.

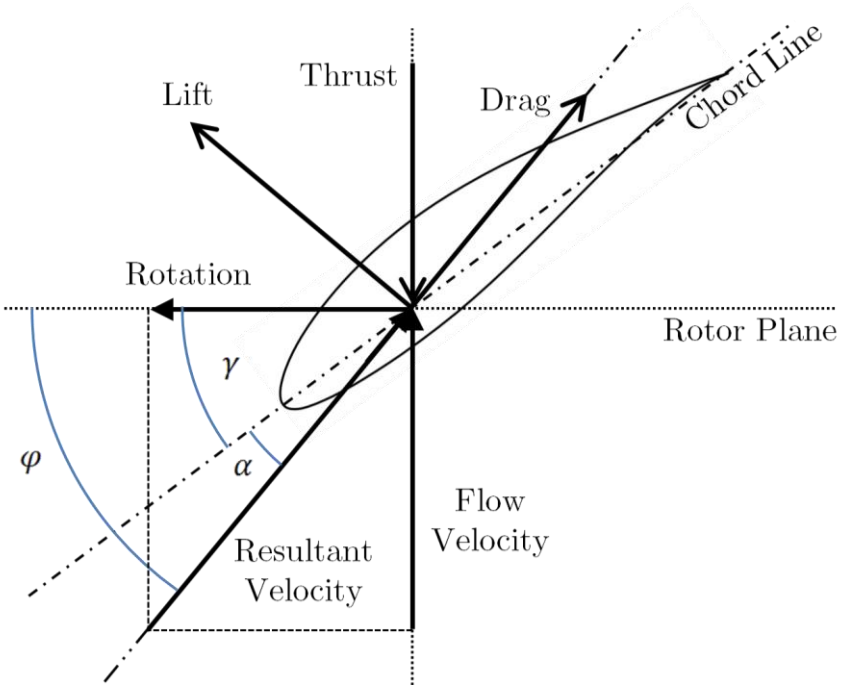


Figure 6: Forces on an aerofoil/hydrofoil section

It is the interaction of the various forces generated that drives the rotation of the turbine, generates power and causes the wake to possess the structure which it does. For a detailed treatment of the method of power production of a bare rotor the reader is referred to Manwell [43], Spera [22] or de Vries [44].

2.2.3. Wake of a Horizontal Axis Turbine

There are two main effects which the turbine blade forces cause on the wake of a horizontal axis turbine, a wake velocity deficit and a bulk swirling of the flow. The wake velocity deficit is caused by the thrust force which is exerted by the rotor on the fluid. This thrust force causes streamline expansion of the incoming flow around the rotor, which due to continuity means that the flow in the wake must move more slowly than the freestream flow. The wake swirl is induced by the rotor as a result of Newton's third law. Since the interaction of the fluid with the rotor forces rotation of the turbine, the turbine must force rotation of the flow.

The velocity deficit and turbulence characteristics of the far wake of a horizontal axis tidal stream generator are a source of interest as they determine the interaction of devices within an array [45]. The near wake structure will affect the power generation potential of the device [38]. There has been progress made in the study of the far wake with uniform actuator disc models [46-50], though these models cannot fully capture the device's impact upon the flow due to the omission

of effects such as swirl and turbulence generation. The effect of the omission of the interaction between the near and far wake is still unknown [47].

Experimental work to characterise the wake was conducted by Bahaj et al. [51] in a hydraulic flume with a cross section of 1.37 m width and a depth of 0.50 m. This work utilised a range of porous discs of 100 mm diameter and investigated the wake recovery. It was found that the far wake is similar across all thrusts after approximately 6 turbine diameters downstream. The structure of the near wake was not assessed and the study was limited by the approximation of the turbine as a disc, omitting swirl and tip vortices and assuming a uniform resistance profile.

Maganga et al. [38] performed experimental tests on a horizontal axis turbine in a flume tank with a blockage ratio of 3.5%. For the wake tests, the three blade rotor was operated at a tip speed ratio of 18 and a Reynolds number, based on the rotor diameter and freestream velocity, of $Re_{RoU_\infty} = 6.4 \times 10^5$. It was found that the wake structure and velocity deficits are highly dependent upon the overall level of turbulence in the wake. It was also found that the wake structures are similar to those exhibited in wind turbines, though as a result of the experimental parameters direct comparison with wind turbines was not possible.

The swirl level in the wake of a horizontal axis tidal stream generator was investigated by Morris et al. [52]. The level of swirl was investigated using computational fluid dynamics results from rotors with a range of blade numbers and tip speed ratios at a Reynolds number, based on the rotor diameter and freestream velocity, of $Re_{RoU_\infty} = 3.1 \times 10^7$. It was found that the near wake of the turbine forms a Rankine vortex but that the swirl was of insufficient strength to impact upon the axial velocity of the flow. For a three bladed rotor operating at a tip speed ratio of 2, the swirl in the wake was found to be weak, with a peak normalised swirl velocity of $U_\theta/U_\infty = 0.50$ at $x/R_{Ro} = 0.2$, degrading to $U_\theta/U_\infty = 0.198$ at $x/R_{Ro} = 2$. These values correspond to swirl angles of 26.5° and 11.2° respectively.

2.3. Diffuser Flows

2.3.1. Purpose and Mechanism of a Diffuser

Diffusers are used to slow the inlet fluid and recover the flow's kinetic energy in the form of pressure. This recovery of the turbine exhaust's kinetic energy allows for a significantly reduced pressure at the inlet [53]. Diffusion is the process whereby as the flow expands from the inlet it must lose velocity, but the energy (neglecting

loses) must remain constant and so the pressure must rise. As a result the diffuser performance is tied to the ratio of the inlet and outlet areas [54].

In reality the flow within a diffuser is more complex and is dominated by the boundary layer flow on the diffuser interior surface. The design of the diffuser and the flow conditions within the diffuser will determine the state of the boundary layer along the interior walls of the diffuser. If the flow is poorly conditioned, something that is dealt with later in this chapter, or the diffuser is poorly designed, flow separation will be induced. When flows separate from diffuser walls, losses are induced in addition to a reduction in the effective cross sectional area of the diffuser. This means that factors which cause adverse pressure gradients such as the divergence angle and curvature of the walls are of particular interest. The effect of the interaction between the area ratio and rate of expansion on the flow attachment can be seen in Figure 7, which shows the conical diffuser flow regimes with a uniform inlet flow profile, for a range of area ratio and wall angles [55].

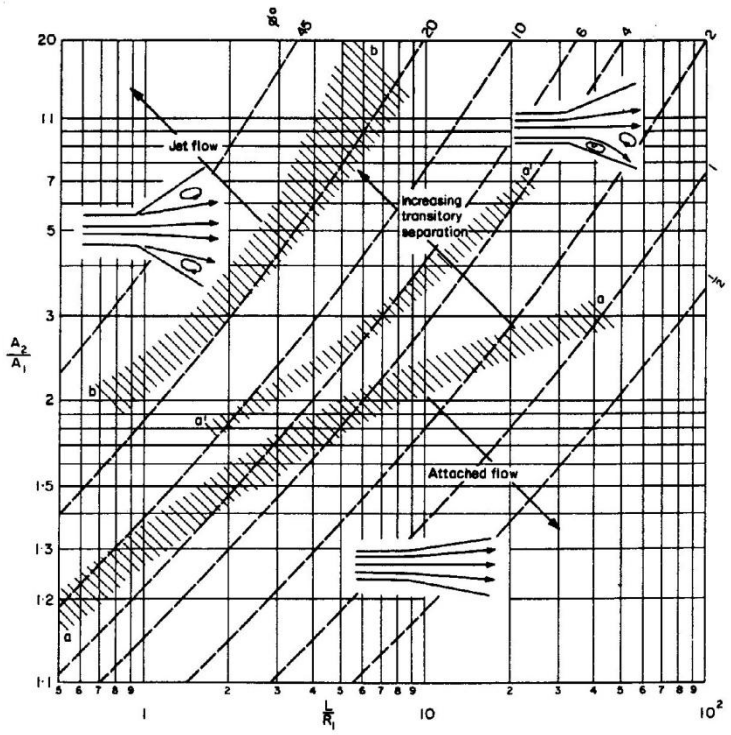


Figure 7: Flow regime boundaries for conical diffusers [55]

Typically, horizontal axis tidal turbine designs will employ a hub, situated on the diffuser axis, to house the generating and electrical gear for the device [56]. The inclusion of a hub within a diffuser design changes the type of diffuser and hence the flow dynamics. Figure 8 shows the diffuser types which are most pertinent to

diffuser augmentation of tidal stream turbines. As most turbine designs employ a hub which is of a limited radius, the geometry of the diffuser used for augmentation of tidal stream generators can best be thought of as a combination of a conical and an annular diffuser as seen in Figure 8. As a result of this combination there may be fluid dynamic effects from both types of diffuser present, depending upon the position within the diffuser and the relative component sizes.

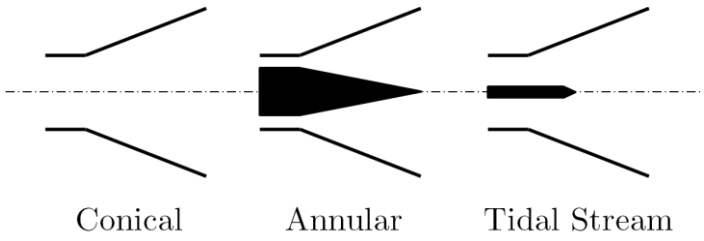


Figure 8: Axisymmetric diffuser geometry terminology

Commonly the performance of a diffuser is expressed by the static pressure recovery coefficient. This coefficient relates the pressure recovery from diffuser inlet to exit to the dynamic head at inlet as seen in Equation 3. Note that the values used in Equation 3 are area averaged values.

$$C_{pr} = \frac{\overline{p_e} - \overline{p_i}}{1/2\,\rho\overline{v_i}^2} \qquad \text{Equation 3}$$

The ideal pressure recovery is that which would occur in an idealised diffuser with no losses or flow separations. The ideal pressure recovery is a function of the area ratio between the diffuser inlet and outlet as expressed in Equation 4. The diffuser efficiency is an expression relating the actual and ideal pressure recovery coefficients as a measure of the diffuser efficiency. The diffuser efficiency ranges from no diffusion at 0, to unity with an ideal diffuser. The diffuser efficiency can be expressed as in Equation 5.

$$C_{pr_{Ideal}} = 1 - \left(\frac{A_i}{A_e}\right) \qquad \text{Equation 4}$$

$$\varepsilon = \frac{C_{pr}}{C_{pr_{Ideal}}} \qquad \text{Equation 5}$$

2.3.2. Effect of Reynolds Number on Diffusion

The Reynolds number will impact upon the flow in the diffuser as it will impact upon the boundary layer growth and separation along the interior surfaces.

McDonald et al. [57] investigated the effect of Reynolds number on a range of geometries of conical diffuser using water as the working fluid. Tests were conducted for Reynolds numbers, based on the diffuser throat diameter and flow velocity, in the range $Re_{DiU_{Di}} = 5.0 \times 10^3$ to $Re_{DiU_{Di}} = 1.0 \times 10^5$. It was found that there were significant Reynolds number effects below $Re_{DiU_{Di}} = 7.0 \times 10^4$, which were attributed to laminar separation downstream of the throat. When the Reynolds number is greater than $Re_{DiU_{Di}} = 7.5 \times 10^4$, the flow was turbulent at inlet and the Reynolds number influence ceased.

Gibson [58], Patterson [59] and Cockrell et al. [60] investigated the effects of a range of Reynolds number on conical diffusers with incompressible flow. The Reynolds numbers in these studies were calculated based on the diffuser throat diameter and flow velocity. Patterson and Cockrell et al. found that Reynolds number effects are negligible above a Reynolds number of $Re_{DiU_{Di}} = 3.5 \times 10^4$, with Gibson finding that dependency ceased at $Re_{DiU_{Di}} = 5.0 \times 10^4$.

The literature, which is summarised in Table 1, suggests that the main effect of the Reynolds number is to alter the inlet boundary layer profile and impact the diffusion through boundary layer development. The effect of the inlet boundary layer profile will be examined in more detail in Section 2.3.4. There is however broad agreement that at Reynolds numbers higher than $Re_{DiU_{Di}} = 7.5 \times 10^4$ there should not be any significant Reynolds dependency remaining.

Author	**Year**	**Diffuser Type**	**Reynolds Independence Above**
Gibson	1912	Conical	Re = 5.0x10^4
Patterson	1938	Conical	Re = 3.5x10^4
Cockrell et al.	1963	Conical	Re = 3.5x10^4
McDonald et al.	1966	Conical	Re = 7.5x10^4

Table 1: Summary of papers pertaining to Reynolds dependence of diffusion

2.3.3. Effect of Swirl on Diffusion

The effect of inlet flow swirl on the performance of diffusers is of importance as the wake of a turbine will generate a degree of flow swirl. Study of the impact of swirl on the performance of the diffuser has been approached by several authors.

Fox et al. [61] investigated 24 conical diffuser geometries at a Reynolds number, based on the diffuser throat and flow velocity, of $Re_{DiU_{Di}} = 1.5 \times 10^5$, with

inlet swirl angles of up to 22°. It was found that swirling inlet flow did not affect the performance of lightly separated or unseparated diffusers, however for those with larger separation, significant performance increases were obtained. It was shown that to achieve a prescribed pressure recovery, the diffuser can be made shorter for the same area ratio with the introduction of swirl.

Lohmann et al. [62] investigated the effect that inlet swirl had on annular diffusers formed of two cones, with a varying cant angle on the hub wall, which exhausted to the atmosphere. The Reynolds number was $Re_{DiU_{Di}} = 1.3 \times 10^5$, based upon the distance between the walls and mean flow velocity at inlet. It was found that when the cant angle of the hub was zero, when the hub walls were parallel to the axis, the diffuser effectiveness was increased by 9.7% by the addition of inlet swirl at an angle of 30°. In this case the area ratio was 1.5 and the ratio of the length to the inlet radius was 10. The presence of swirl was found to move the separation from the external wall to the hub wall of the diffuser, though in these experiments the hub radius was greater than the inlet height.

Elkersh et al. [63] examined the effect of inlet swirl and diffuser geometry on equiangular annular diffusers. Testing was undertaken on three geometries with different lengths, interior angles and area ratios at Reynolds numbers, based on the diffuser throat diameter and flow velocity, around $Re_{DiU_{Di}} = 3.0 \times 10^5$. It was found that for all geometries the inclusion of swirl of up to 30° increased the pressure recovery, but that beyond this angle the recovery dropped. This trend in the pressure recovery was due to the suppression of the wall separation at lower swirl angles and induced separation from the hub once beyond 30° of swirl.

Kumar et al. [64] found that for a range of straight-walled annular diffusers with Reynolds numbers, based on the diffuser throat diameter and flow velocity, in the range $Re_{DiU_{Di}} = 1.8 \times 10^5$ to $Re_{DiU_{Di}} = 2.9 \times 10^5$, the effect of swirl was to increase the pressure recovery up to a critical swirl angle, and to adversely affect it thereafter. Swirl was more beneficial in cases where there was appreciable flow separation for axial diffuser flow, with an optimum swirl angle of 25° being reported to increase pressure recovery by 18%. The mechanism for the improvement in pressure recovery was the suppression of separation on the diffuser wall, with the degradation at larger angles assigned to excessive rotational kinetic energy losses.

Clausen et al. [65] examined the influence of swirl on the boundary layer of a conical diffuser with an included angle of 20° at a Reynolds number, based on the diffuser throat diameter and flow velocity, of $Re_{DiU_{Di}} = 2.0 \times 10^5$. It was found that greater swirl tends to suppress flow separation from the diffuser at the expense of the generation of a region of flow circulation on the diffuser axis. The presence of swirl was found not to directly affect the boundary layer turbulence.

Cerantola and Birk [66] investigated the influence of swirl on a diffuser where the inlet flow was exhausted through a negative wall angled annular diffuser around an elongated centrebody into a conical diffuser section. Reynolds numbers, based on the diffuser throat and flow velocity, in the range $Re_{DiU_{Di}} = 0.9 \times 10^5$ to $Re_{DiU_{Di}} = 2.2 \times 10^5$ were examined with inlet swirl angles in the range 0° to 42°. An increase in the pressure recovery if the swirl angle was increased up to 11.5° was found, but that it dropped off rapidly thereafter. The reduction was caused by the formation of a large region of recirculation behind the rear of the centrebody. This suggests that the optimum swirl angle is lower than in previous studies, though this is due to the negative wall angles reducing separation on the diffuser wall. As the influence of swirl in previous studies was the suppression of diffuser wall separation it is therefore not surprising that limited gains were found when none is present.

There is broad agreement in the literature, which is summarised in Table 2, that moderate flow swirl can improve diffuser performance, particularly where separation occurs with no swirl present. The improvement is found to be most significant when the swirl angle is between 25° and 30°, and is generated through suppression of separation on the diffuser wall. At larger swirl angles the performance drops due to a combination of hub separations and rotational kinetic energy losses through skin friction on the diffuser wall. The swirl from a horizontal axis wind turbine, comparable to those examined in this thesis, was found by Medici et al. [67] to be 15° at one turbine diameter downstream, at tip speed ratios around the maximum efficiency point. It is therefore likely to be the case that diffuser inlet swirl at high turbine loadings typical of high power capture will be beneficial to the diffusing potential. At low rotor loadings the swirl is unlikely to be of a magnitude significant enough to effect the diffusion.

Author	Year	Diffuser	Re	Effect(s) of Swirl
Fox et al.	1971	Conical	$1.5x10^5$	Little impact where flow does not separate Acts to suppress separation and increases pressure recovery
Lohmann et al.	1979	Divergent Annular	$1.3x10^5$	Performance increased by suppression of diffuser wall separation Excessive swirl moves separation from diffuser to hub wall Optimum swirl is around 30°
Kumar et al.	1980	Divergent Annular	$1.8x10^5$ to $2.9x10^5$	Performance increased by suppression of diffuser wall separation Optimum swirl is around 25°
Elkersh et al.	1985	Equiangular Annular	$3.0x10^5$	Performance increased by suppression of diffuser wall separation Excessive swirl moves separation from diffuser to hub wall Optimum swirl is around 30°
Clausen et al.	1993	Conical	$2.0x10^5$	Swirl acts to suppress diffuser wall separation and generate hub recirculation
Cerantola & Birk	1993	Negative wall angle annular into conical	$0.9x10^5$ to $2.2x10^5$	Excess swirl acts to create a recirculating zone behind the centrebody Optimum swirl is around 11.5°

Table 2: Summary of papers relevant to the swirl dependence of diffusion

2.3.4. Effects of Turbulence, Transience and Boundary Layers

The effect of inlet turbulence on a plane walled diffuser was investigated by Hoffman [68]. Turbulence was generated using a set of rods which were orientated either between the two diverging walls or between the two end walls. The Reynolds number, based on the diffuser throat diameter and flow velocity, for all experiments was $Re_{DiU_{Di}} = 7.8 \times 10^4$. It was found that turbulence aided in the attachment of the flow to the diffuser walls and that the pressure recovery performance was increased for all conditions tested. An integral length scale of >7 times the inlet boundary layer displacement thickness and an intensity >3.5% provided the greatest benefit. An eddy orientation parallel to the wall and perpendicular to the flow was found to be the most beneficial. For an included angle of 20°, the peak pressure recovery coefficient was increased by 9.8%.

Further work by Hoffman [69] using the same diffusers and inlet conditions as previously [68] found that with high turbulent intensity (5%), small integral scale inlet turbulence, the pressure recovery coefficient for the 20° included angle diffuser could be increased by 22%. This improvement was assigned to the turbulence delaying separation and reducing flow distortions due to increased mixing.

Azad et al. [70, 71] investigated turbulent flow in a conical diffuser. It was found that the structure of the turbulence was more uniform close to the diffuser axis, but as the wall region was approached the magnitude of the turbulent orientations changed. The axial and circumferential components of the turbulence peaked at the wall and the radial component at the boundary layer interface.

Klein [72] reviewed the literature on the effects of inlet conditions on conical diffusers and found that an increased turbulent intensity increased the pressure recovery potential. The primary influence of the turbulence was stated to be the enhancement of turbulent mixing between the boundary layers and the remaining flow. It was noted that fully developed pipe flow at inlet produced a higher pressure recovery than uniform inlet flow. The influence of the Reynolds number was stated to be caused by its effect on the state of the boundary layer. The designs surveyed where the boundary layer had transitioned ahead of the diffuser were found to perform independently of the Reynolds number.

Fox et al. [73] investigated the flow regimes of curved diffusers with a range of flow turning angles at Reynolds numbers, based on the diffuser throat diameter and flow velocity, of up to $Re_{DiU_{Di}} = 3.9 \times 10^4$. The diffusers tested encountered the same flow regimes as straight walled diffusers, though at different area ratios depending upon the wall curvature. Stall inception was found to be a function of the included angle, turning angle and aspect ratio. It was found that for diffusers with turning angles of less than 30°, the conditions for the first appreciable stall were the same as for straight walled diffusers where the other parameters remained constant.

Dean [74] surveyed literature on the impact of the outflow from a compressor or centrifugal pump as the inlet flow to vaneless diffusers and attempted to model the flow theoretically. It was found that diffuser transience cannot be modelled with the use of axisymmetric inlet data and that total pressure loss in a diffuser may be reduced by the distortion of the flow accompanying turbomachine exit conditions.

Adenubi [75] assessed the impact of turbomachine exit flow conditions as the inlet conditions for an annular diffuser. A two stage compressor was used to generate a range of swirling turbulent inlet flows. It was found that the periodic unsteadiness in the wake was caused to dissipate rapidly by the diffuser, but that this generated high turbulence intensity flow. This increased intensity was found to improve diffuser performance over that for low turbulence, axial inflow conditions.

Zeier [76] investigated four annular diffuser geometries with a one stage compressor outflow as the inlet flow to the diffuser. It was found that the increased turbulence level in the flow leads to considerably higher pressure recoveries than for low turbulence, steady axial inflow due to the delay in flow separation.

Senoo et al. [77] examined the effect of aerofoil type vortex generators installed 0.4 throat diameters upstream of the inlet of conical diffusers with a range of divergence angles and area ratios of 4. The tests were conducted at Reynolds numbers, based on the diffuser throat diameter and flow velocity, of between $Re_{DiU_{Di}} = 3.0 \times 10^5$ and $Re_{DiU_{Di}} = 7.0 \times 10^5$. It was found that the presence of the vortices helped to suppress the separation of the flow from diffusers which would ordinarily separate. The number and angle of generators was found to be important, with a greater number of more heavily angled generators providing a better pressure recovery. The pressure recovery was found to be increased to the equal of the best conical diffuser for a prescribed area ratio through the use of the generators.

ESDU [55] summarised the research on vortex generators and provided a guide to their design for maximising pressure recovery. The vortex generators promote mixing between the boundary layer and bulk flow, increasing boundary layer momentum and preventing flow separation. It is suggested that the use of vortex generators alone is not an efficient means of control at half angles of over 15°.

Lengani et al. [78] investigated the use of low profile vortex generators within an asymmetric planar diffuser, with the generators mounted on the side parallel to the inflow. The generators were able to reduce losses within the diffuser by 50%, due to increased boundary layer mixing and suppression of flow separation.

Santner et al. [79] examined the influence of low profile vortex generators on the flow through an annular S-shaped inter-turbine diffuser and a 2D diffuser with the same radial curvature. It was found that for the 2D diffuser the vortex generators suppressed the flow separation. In the S-shaped inter-turbine diffuser total losses were increased by the presence of the vortex generators, despite the reduction in separation. This effect was said to be caused by the unsteady flow onto the generators preventing the formation of steady vortices. It could be inferred therefore that steady vortex structures, such as those emanating from a turbine blade tip at constant speed would improve the overall device performance.

Author	Year(s)	Study Type	Diffuser	Flow Conditions	Effect(s) Noted
Dean	1960	Literature Survey	Conical	Compressor or centrifugal pump outflow as inlet	Total pressure loss reduced by the flow distortions at inlet
Fox et al.	1962	Experimental	Conical Trumpet	Axial inlet flow with turbulent boundary layer	Flow regimes the same as conical diffusers Flow regime boundaries depend on the turning angle of wall, included angle and aspect ratio
Senoo	1974	Experimental	Conical	Vortex generators upstream of inlet	Separation suppressed by the generated vortices Vortices found to increase the pressure recovery to the equal of the best diffuser of a prescribed area ratio
Adenubi	1976	Experimental	Annular	Compressor outflow as inlet	Periodic unsteadiness in wake is broken down by diffuser, generating high intensity turbulence
Klein	1981	Literature Survey	Conical	Range of inlet conditions	Increased turbulence intensity increases pressure recovery potential Turbulence acts to increase mixing of the boundary later with the bulk flow Fully developed flow at the inlet tends to improve performance over uniform inflow Reynolds number effects caused by the state of boundary layer at inlet Turbulent boundary layer at inlet causes independence from Reynolds number

Author	Year(s)	Study Type	Diffuser	Flow Conditions	Effect(s) Noted
Hoffman	1981, 1984	Experimental	Plane Wall	Rod wakes generating aligned turbulence	Turbulence suppresses flow separation and improves performance Eddy orientation parallel to wall and perpendicular to flow most beneficial Turbulence intensities >3.5% and length scale of >7x inlet BL thickness produce best results
ESDU	1988	Literature Survey	Range	Vortex generators upstream of inlet	Vortex generators promote mixing of the bulk and BL flows and prevent flow separation Use of vortex generators alone is inefficient control above angle of 15°
Zeier	1995	Experimental	Annular	Compressor outflow as inlet	Increased turbulence intensity increases pressure recovery through separation suppression
Azad et al.	1989, 1996	Experimental	Conical	Fully developed pipe flow	Turbulence more uniform at diffuser axis Axial & circumferential turbulence peak at wall, radial component at the BL interface
Lengani et al.	2011	Experimental	Asymmetric Planar	Fully developed inflow with vortex generators at inlet	Losses reduced by 50% due to suppression of flow separation
Santner et al.	2012	Experimental	Annular S-shaped	Fully developed inflow with vortex generators after inlet	Steady vortices suppress flow separation and boost performance Losses increased for vortices formed in unsteady wakes
Zhang et al.	2012	Experimental	Conical	Fully developed with Karman vortex generators after inlet	Large potential increases of up to 97% in pressure recovery with Karman vortex generators

Table 3: Summary of papers relevant to the dependence of diffusion on turbulence, transience and boundary layer development

Zhang et al. [80] examined the effect of a Karman vortex generator on the diffusion within a conical diffuser. The Karman vortex generator is a ring torus of a diameter slightly smaller than the diffuser throat, mounted in the diffuser throat. The shape of the torus induced the formation of a von Karman vortex street which oscillates perpendicular to the diffuser wall direction. Through the suppression of separation it was found that the pressure recovery could be improved by 97% over the uncontrolled case, with a ring radius of $0.77R_i$ and a thickness of $0.077R_i$.

The literature, as summarised in Table 3, suggests that an increased turbulent intensity aids the diffusion potential of a diffuser through mixing and increased boundary layer momentum. The increase in momentum of the boundary layer flow prevents separation from the interior of the diffuser and increases the diffusion potential. It is suggested that the interaction of the transience from turbomachines with the diffuser breaks down periodic functions, generating high turbulence intensities and small length scales which further aid pressure recovery. The use of vortex generators has been shown in the literature to improve the pressure recovery performance of diffusers. It could be inferred from the literature that rotating vortices of constant strength, such as would be found in the wake of a horizontal axis tidal turbine would be likely to improve mixing of the boundary layer flow, postpone flow separation and improve performance.

2.3.5. Effect of Axial Velocity Profile and Diffuser Wall Jets

The effect of the axial velocity profile on the performance of a diffuser was noted by ESDU [54], who stated that the pressure recovery performance of a diffuser can be increased if the inlet flow profile is of a wake shape. The wake velocity profile being characterised by increased wall velocities with a reduced centreline axial velocity. The danger of reducing the centreline velocity too far and inducing a region of flow recirculation on the centreline was noted.

Nicoll et al. [81] tested the impact of annular injection immediately downstream of the diffuser inlet on the pressure recovery performance of three conical diffusers with included angles of 10°, 20° and 30° and a constant area ratio of 3. The tests were conducted with axial inlet flow at Reynolds numbers, based on the diffuser throat diameter and flow velocity, of between $Re_{DiU_{Di}} = 4.5 \times 10^5$ and $Re_{DiU_{Di}} = 9.1 \times 10^5$. It was found that an improvement in the pressure recovery of 130% over a design without injection was possible, with a mean injection velocity which was between 110% and 120% of the inlet mean velocity.

Kwong et al. [82] investigated active boundary layer control using blowing of wall jets for a conical diffuser with a range of included angles and Reynolds numbers. Methodologies used were steady annular blowing, steady blowing from discrete circumferential nozzles and actively controlled transient blowing from discrete circumferential nozzles. It was found that for a 16° included angle diffuser at a Reynolds number, based on the diffuser throat diameter and flow velocity, of $Re_{DiU_{Di}} = 3.0 \times 10^5$, that steady discrete circumferential blowing and steady annular blowing could increase the pressure recovery coefficient by 150% and 167% respectively, when the area normalised mass flow rate of the jet was 18% higher than the bulk flow. The pressure recovery from the transient blowing from discrete circumferential nozzles was stated to remain the same as for steady blowing, but was able to attenuate frequency effects as desired and reduce flow noise.

Lo et al. [83] investigated the transition of flow from an annular inlet to a conical diffuser section, as might be found in a diffuser augmented tidal stream generator. The inflow had a turbulent boundary layer on both the diffuser and centrebody walls and the option of Coanda blowing around the curved rear of the centrebody. It was found that the flow was prone to separating from the rear of the centrebody without blowing, but that blowing could suppress this. Blowing of too large a magnitude caused the flow to separate from the diffuser wall. A wake vortex formed at the rear of the centrebody during blowing, formed by the pressure distribution within the duct as the inflow had no swirl component. The diffuser performance was stated to be tied to the separation from the hub.

Author	Year	Diffuser	Inlet Profile	Effect(s) of Inlet Profile
Nicoll et al.	1970	Conical	Developed flow with annular injection jet	Improvement of pressure recovery in diffuser by 130% possible with jet Optimum jet velocity between 110-120% of the mean flow velocity
ESDU	1976	Range	Wake shape	Performance increase due to elevated wall velocity relative to centreline Reduction of centreline velocity too far leads to recirculating zone
Kwong et al.	1994	Conical	Range of wall blowing techniques	Pressure recovery increases of 150% and 167% for discrete and annular blowing respectively Transient discrete blowing enabled attenuation of specified frequencies
Lo et al.	2012	Conical	Centrebody wall blowing	Blowing allows suppression of centrebody wake separation through Coanda effect

Table 4: Literature summary on the effects of axial velocity profile on the diffusion

There is agreement within the literature, which is summarised in Table 4, that the pressure recovery performance of a diffuser can be increased through the application of wall jets. These jets act to delay separation from the diffuser interior surface and increase the volume in which diffusion can occur. The tip gap jet formed between a turbine and the casing is therefore likely to improve diffuser performance and hence increase the duct velocity. The jet thicknesses are small relative to the bulk flow. It could be expected that as the size of the gap and jet grow, there would be a loss of energy to the turbine as the flow is redirected. The hub wake is stated to have a more limited impact upon the performance of the diffuser.

2.4. Diffuser Augmented Turbines

The study of diffuser augmentation of horizontal axis turbines has been mooted for many years, with a large body of study within the wind energy industry [24, 25, 53, 84-98]. In recent years there has also been an interest in the potential for diffuser augmentation of tidal stream turbines [26, 99-110].

2.4.1. Physics of Power Augmentation

The augmentation available from ducting comes from an increased mass flow rate, which increases the flow velocity at the rotor plane [24, 26, 84, 92, 96, 108]. The main mechanism for increasing the mass flow rate is a reduction of the pressure, both at the rotor plane and the diffuser exit, to below that which would be possible to sustain for a bare turbine. This pressure reduction causes additional flow to be drawn into the duct. Since the cross sectional area of the duct is fixed at the rotor, continuity means that an increase in the mass flow rate causes an increase in the flow velocity. As can be seen from Equation 1, this increase in the velocity causes an appreciable increase in the power available for extraction by the rotor.

Ducts use a variety of methods, such as nozzles, diffusers and flanges to reduce the exit pressure, maximise the flow velocity and draw more fluid through the rotor plane. The degree of augmentation available will depend upon the duct design and the interaction of the duct with the turbine [26]. Various types of ducting have been proposed, ranging from simple geometries with only a diffuser, to more complex ones integrating the use of aerofoils with slotted diffusers. The main components that are used in ducting are inlet nozzles, diffusers and exit plane flanges.

2.4.2. Quantifying Device Efficiency

Whilst the theoretical limitations of Section 2.2.1 still apply to turbine units when ducted, the power output can be increased via an increase in the mass flow rate across the rotor [24, 84]. The augmentation quantifies the ability of the duct surrounding the rotor to increase the flow rate through the rotor rather than a change in the physics underlying the conversion of energy. In order to provide an accurate comparison of devices, a number of metrics have been proposed, the most simplistic of which is using the turbine power coefficient as defined in Equation 6. This metric is easy to understand and provides a useful comparator to the performance of other devices but does not reflect the need to make best use of the channel cross section. It can also give the impression of a performance which is superior to a bare rotor without properly quantifying the effect of the duct.

$$C_{P_{Ro}} = \frac{\mathrm{P}}{1/_2 \rho {U_\infty}^3 A_{Ro}} \qquad \text{Equation 6}$$

An augmentation factor is defined by Igra [94] as in Equation 7. The augmentation factor uses the pressure drop across the turbine and the volumetric flow rate through the turbine to express the power available to the ducted unit, which is then normalised by the comparable freestream energy, limited by the Betz limit. This equation compares the power output from a ducted turbine with that of an ideal bare turbine. This metric is not however very intuitive and provides a poor comparator of performance relative to a bare turbine.

$$G = \frac{\Delta p_{Ro} \dot{V}_{Ro}}{0.593/_2 \rho {U_\infty}^3 A_{Ro}} \qquad \text{Equation 7}$$

Belloni and Willden [99] proposed the use of the basin efficiency, defined as the output power from the turbine normalised by the overall power removed from the flow by the presence of the device, as shown in Equation 8. This metric is useful when considering the effect of a device upon the performance of an array of devices, but is again a less intuitive comparator of relative device performance. This metric is easily calculable from CFD data but would be problematic in the real world as the data far upstream and downstream of the device is most often unknown.

$$\varsigma = \frac{P}{(p_t U_x dA)_{INFLOW} - (p_t U_x dA)_{OUTFLOW}} \qquad \text{Equation 8}$$

In order to simplify the assessment of the relative power output and to reflect the need to make best use of the available channel cross section, it is proposed that the power coefficient based on the duct's outer area is used. This metric, as defined in Equation 9, enables a more direct comparison of the relative performance of devices and prevents the appearance of potentially misleading performance figures.

$$C_{P\,Di} = \frac{\mathrm{P}}{{}^{1}/_{2}\,\rho U_{\infty}{}^{3} A_{Di}} \qquad \text{Equation 9}$$

2.4.3. Theoretical and Numerical Modelling of Augmented Turbines

Fletcher [88] used blade element theory and assumptions of the diffuser performance to examine the theoretical performance of bare and diffuser augmented turbines. The model showed broad agreement with the experimental data which was used to verify it. It was noted that the use of screens for the modelling of diffuser augmented turbines may under predict their output power by up to 30%. The optimum solidity of a turbine was estimated to be between 0.10 and 0.15, depending upon the blade section used for the rotor construction.

Loeffler [111] applied the method of singularities to the calculation of the flow field within a slotted diffuser. It was found that this model provided agreement to the flow field found in this case, as the slots prevent flow separation meaning that an inviscid approximation holds to some extent. For diffusers with some degree of separation this method is likely to be ineffective in its prediction of the flow.

Dick [112] applied momentum theory to investigate the power capture limits of wind energy concentrator systems. It was found that the limit on the outer area power coefficient of the device may be increased by a factor of 1.3 above the Betz limit. The author qualifies that this prediction is based upon simplifications and that the experimental data used for verification was taken from small scale models.

Hansen et al. [92] used an actuator disc model implemented within CFD to analyse the performance of a diffuser augmented wind turbine. The model was verified for a bare turbine against one dimensional theory and the diffuser was placed around the rotor and again verified against one dimensional theory. The author states that the power augmentation cannot exceed the cube of the increase in the throat velocity and that an actuator disc model is sufficient to model the flow in the diffuser. The statement that diffuser augmented flow can be adequately modelled by an actuator disc rests on invalid assumptions however. The CFD model,

where no flow swirl or turbulence are present is validated against one dimensional theory, where again these effects are not present.

Lawn [113] used one dimensional theory to examine the power production possibilities of a diffuser augmented turbine. By modelling the duct using prescribed efficiencies for the inlet and diffuser geometries and using this to calculate the momentum balance, an analysis of different operating conditions was completed. It was found that if an efficient diffuser is coupled with a lightly loaded rotor then a power enhancement of 33% over a bare turbine of the same outer diameter can be achieved. If the relative areas were taken into account the power coefficient would most likely be lower than the equivalent bare rotor. This approach is based very heavily on correct estimation of the duct's swallowing capacity from the efficiencies and would therefore require validation of the results before use.

Werle et al. [114] utilised a one dimensional analysis of a diffuser augmented flow to express the likely effect of a diffuser on power production and found that it is dominated by the duct's non-dimensional force coefficient. This model is validated against the CFD data of Hansen [92]. The model matched the CFD data well at low turbine thrusts, but as a one dimensional model fails to predict the separation in the diffuser, at high turbine thrusts the model becomes invalid. It should also be noted that the data against which it is validated is itself limited as previously discussed.

A one dimensional modelling methodology based on momentum theory was presented by van Bussel [24]. It was found that the augmentation potential of a ducted unit was tied to the mass flux through the rotor plane and predicted that the rotor behaved exactly as it would for a bare turbine in a higher velocity flow with an optimum pressure drop of 8/9 of the local dynamic pressure over the rotor plane. It was found that the means to increase the mass flux was a reduced diffuser exit pressure. This model was again validated against Hansen's [92] CFD data.

Phillips [25] used a modified blade element momentum method to predict the performance of a diffuser augmented wind turbine. The effect of the diffuser was incorporated using an empirical equation for the throat velocity. The model showed good agreement with the experimental results when amended data for the lift and drag of the blade sections was used. The limitations of this model are that the empirical equation requires experimental data to be fitted and is only valid for that

specific diffuser and rotor geometry. The requirement to have experimental data before calculating the power means that this model is ineffective as a design tool.

Gaden and Bibeau [100] used a uniform actuator disc momentum source model implemented within CFD to evaluate the performance of diffuser augmented tidal stream turbines. The momentum source model was validated for a bare turbine by comparing the wake velocity deficit for a number of operating points to theoretical predictions. The validation is therefore only validating the fact that the momentum source is replicating an idealised uniform actuator disc and not the behaviour of a turbine. In addition the model omits the effects of swirl and turbulence on the flow.

Sun et al. [101] used the blade element momentum method to predict the performance of a diffuser augmented tidal turbine. The results of this model were verified against experimental results from a model device in a circulating water channel. Whilst this method produced a match with the experimental results, it separated the problem into three stages; determination of the throat velocity profile with a CFD analysis of an open diffuser, prediction of the output power of the turbine using the BEM method and application of a correction factor. The key disadvantages of this approach are that a correction factor has to be obtained in advance and the rotor flow profile is not updated for the interactions between the diffuser and rotor. The omission of the variation of rotor thrust, and therefore the change of the mass flow rate in the duct with the changing tip speed ratio is likely to have caused the difference between the calculated and experimental results.

Shives [115] further developed the theory of Lawn [113], by including the blade element momentum method and thereby including the effects of wake rotation and radial variation in the rotor plane velocity. An implementation of the blade element actuator disc model within CFD, which modelled the rotor's impact on the flow solely on the blade's lift and drag forces, was also developed. The ducted BEM approach is limited by the need to estimate the efficiency of diffusion of the geometry without the impact of the rotor wake being known. This limitation is overcome by the BEM CFD, where the rotor and diffuser interaction is explicitly modelled and the diffuser efficiency is calculated. Using this calculated efficiency the two models were compared and found to provide results which matched well. The limitations of this approach are that the implementation of the BEM CFD overlooks the impact of turbulence, tip losses and the turbine's wake state on the performance.

As a result, although the two models matched well, they do not provide an accurate assessment of the device's power output.

McIntosh et al. [116] implemented the blade element model momentum model within CFD for the assessment of flow within a duct. This model was again based upon blade lift and drag forces only, though tip loss corrections were implemented for bare rotors. The tip loss model was not implemented for diffuser augmented units as it was found by Fleming et al. [117] that the tip vortices which generate these losses do not form in a diffuser. Fleming et al. matched the diffuser throat diameter to the rotor diameter, omitting a tip gap, which explains the finding that the vortices do not form, as there is no gap through which the flow can pass.

Ohya et al. [118] implemented another version of BEM CFD initially based upon the blade lift and drag forces only. It was found that the results from this model did not match experimental results as the tip gap jet was not replicated. In response a tip loss model was developed, which was formed of a linearly increasing tip loss in the region $r/R_{Ro} > 0.93$. It was found that this tip loss model improved the accuracy of the predictions but did not fully replicate the jet profile. The model was not extended for the quantification of the power output of the device.

The literature on the modelling of diffuser flows, as summarised in Table 5 is limited in the extent to which flow effects such as swirl and turbulence have been considered. One dimensional approaches over simplify the analysis of diffuser augmented units, which are subject to complex flows. Agreement is reached between the one dimensional models, but these are validated against further numerical data, which has in itself incorrect underlying assumptions of the flow field. The blade element momentum approach provides a more complete and accurate assessment of the flow physics, but has not yet been implemented in a way which allows for direct analysis of the performance of the device or the full quantification of interactions.

2.4.4. Augmentation of Wind Turbines

The study of diffuser augmentation of turbines dates back a number of years, with the idea originally intended for use with wind turbines. With the physics of wind and tidal turbines being so similar, studies of the work on the augmentation of wind turbines are directly relevant to diffuser augmentation of tidal turbines.

Author	Year(s)	Model Basis	Methodology	Limitation(s)
Fletcher	1981	BEM Theory	Diffuser effect on momentum modelled via exit pressure and efficiency	Requires experimental or numerical results to calculate the diffuser coefficients
			Momentum used to infer uniform throat velocity for BEM power estimate	Idealised throat velocity distribution
				Effect of turbine on the diffuser coefficients ignored
Loeffler	1981	Method of Singularities	MoS uses potential flow with discrete vortices (singularities) to model turbine and diffuser	Flow is assumed to be inviscid i.e. no separation possible in diffuser
			10 vortices used for diffuser and 40 for turbine	Uniform resistance assumed for turbine
Dick	1986	Momentum Theory	Diffuser effect on momentum calculated from forces derived from literature and extrapolated	Modelled largely on experimental data using screens for the turbine model
			Power estimated from actuator disc theory	Effects of turbine influence largely neglected
Hansen et al.	2000	Uniform Actuator Disc CFD	Uniform momentum sink implemented in CFD to mimic turbine	Flow swirl, turbulence, tip loss, radial thrust distribution and wake state neglected
			Model verified against momentum theory and then extended to include diffuser	
Lawn	2003	Momentum Theory	Diffuser effect on momentum modelled via inlet and exit efficiencies	Flow swirl, turbulence, tip loss, radial thrust distribution and wake state neglected
			Power estimated from actuator disc theory	
Phillips	2003	BEM Theory	Empirically derived throat velocity distribution from gauze screen experimental data	Flow swirl, turbulence, tip loss and wake state neglected
			Power estimated from BEM theory	Requires experimental or numerical results to calculate the power output
van Bussel	2007	Momentum Theory	Momentum used to infer uniform throat velocity via area ratio and exit pressure	Flow swirl, turbulence, tip loss, radial thrust distribution and wake state neglected
			Power estimated from actuator disc theory	Model validated against the data of Hansen et al.

Author	Year(s)	Model Basis	Methodology	Limitation(s)
Werle et al.	2008	Momentum Theory	Diffuser effect on momentum calculated from force based on pressure jump across rotor Power estimated from BEM theory	Flow swirl, turbulence, radial thrust distribution and wake state neglected
Gaden & Bibeau	2010	Uniform Actuator Disc CFD	Uniform momentum sink implemented in CFD to mimic turbine Power estimated from actuator disc theory	Flow swirl, turbulence, tip loss, radial thrust distribution and wake state neglected
Shives	2011	BEM CFD	Blade element resolved momentum sink in CFD to mimic turbine thrust Blade element resolved momentum source in CFD to mimic turbine tangential forces Power output calculated using the axial force and velocity	Flow turbulence, tip loss and wake state neglected Power output does not account for the tangential component of the velocity
McIntosh et al.	2011	BEM CFD	Blade element resolved momentum sink in CFD to mimic turbine thrust Blade element resolved momentum source in CFD to mimic turbine tangential forces	Flow turbulence and wake state neglected Tip loss model implemented for a bare rotor but nor used with the ducted rotor Calculation of power output not stated
Sun et al.	2012	CFD & BEM	Flow field for an empty diffuser calculated using CFD Power output calculated using flow field, velocity reduction factor and BEM theory	All interaction effects between the rotor and diffuser neglected Velocity factor needs combined device experimental data and empty CFD to calculate
Ohya et al.	2012	BEM CFD	Blade element resolved momentum sink in CFD to mimic turbine thrust Blade element resolved momentum source in CFD to mimic turbine tangential forces Linear tip loss correction model implemented	Turbulence and wake state neglected Tip loss model assumes linear relation to radius for the tip section of the blade No power output results provided or method of calculation of power output given

Table 5: Summary of papers on numerical modelling of diffuser augmented turbines

2.4.4.1. Inlet Geometry

The inlet nozzle is a common feature of duct configurations and exists to guide the flow towards the rotor plane with the minimum of losses. Work by Ohya et al. [97], which looked at the concepts of diffuser augmentation from first principles, highlights the necessity of a suitably designed inlet section to prevent flow separation from the duct's surface prior to a rear diffusing section. In the case of Ohya's trials, improvements in the throat velocity of 17% were found when an inlet was incorporated with a conservative diffuser design with a half angle of 4°. The importance of the inlet would become more pronounced as the geometry becomes more severe and the adverse pressure gradient on the boundary layer increases.

2.4.4.2. Diffuser Augmentation

For a full treatment of the stages of diffuser augmented wind turbine (DAWT) history the reader is referred to Philips [87]. What follows is an overview of developments pertinent to the development of diffuser augmented tidal turbines.

Kogan and Seginer [119] examined a range of shroud configurations with a combination of inlet designs, conical diffuser designs and annular aerofoil exit rings. The investigation was conducted experimentally with the use of a range of screens of varying thrust and centrebodies of different thicknesses. Experiments were conducted between Reynolds numbers, based on the diffuser throat diameter and freestream flow velocity, of $Re_{DiU_\infty} = 3.5 \times 10^4$ and $Re_{DiU_\infty} = 6.0 \times 10^5$, with a trend for increasing performance with Reynolds number. This trend could be explained by the degradation of diffuser performance at low Reynolds number as detailed in Section 2.3.2. The performance was independent of the device yaw angle for ±20° of yaw and the performance increased in the configuration with the largest radial size at a yaw angle of 30°. Though it is not possible from the data presented to calculate the blockage effects at yaw, the author states that it was not possible to rotate the device in the wind tunnel beyond a certain point. This suggests that the device may be considerably oversized for the tunnel within which it was tested.

Kogan and Seginer found the optimum augmentation factor to be 4.46, with a ring shaped aerofoil at exit, a diffuser length to diameter ratio of 7, diffuser exit area ratio of 3.5 and a flap exit area ratio of 7. The power coefficient based upon the exit outer diameter is calculated as 0.38, as noted by Igra [93] however, the size of the duct makes this design impracticable.

Igra [93, 94], following from the work of Kogan and Seginer and recognising that diffusers form the most significant part of ducting systems, experimented with a variety of configurations of diffuser geometries in order to derive compact duct units. In these experiments, a progression was made from longer, diffuser only geometries, tested with screens, to shorter ducts incorporating turbine models. The key finding from Igra's work was that the augmentation can be improved via the use of boundary layer control methods. The control methods tested were bleeding holes and annular wings at diffuser exit, which formed an effective extension to the diffuser with external blowing. It was found that bleed holes were difficult to optimise, whilst annular rings could increase the augmentation factor, as defined by Equation 7, by 65%. The relationship between the thrust of the rotor and the diffuser augmentation was noted, with the peak performance being found at lower disc loadings, the value depending upon the duct geometry.

The peak power coefficient found by Igra, based upon the outer diameter from the trialled geometries, was around 0.25 for the case of an aerofoil cross section annular wing diffuser with bleeding. This geometry was tested with a screen across the throat area to mimic the turbine. This simplification could lead to poor prediction of the output due to the omission of flow swirl and the tip gap jet.

Igra also suggested that blade tip losses could be reduced in the case of ducted units as a result of the proximity of the rotor to the duct walls. The potential gains from this effect were not quantified but would depend upon the tip gap's size relative to the blade geometry. A smaller gap may well cause reduced blade tip losses, but would also interfere with the formation of the tip gap jet and act to suppress near wall turbulence in the diffuser. Both of these effects would act to reduce the possible diffusion as a result of mechanisms detailed in Sections 2.3.4 and 2.3.5, and therefore act to reduce power output for the device.

In addition to the above it was also found by Igra [94] that the diffuser continues to operate without a degradation of efficiency at yaw angles of up to $\pm 30°$, due to the flow being aligned with the rotor within the duct. It was noted by the author that blockage effects may be partially responsible for this effect.

Foreman [89] and Gilbert et al. [53] of the Grumman Aerospace Corporation investigated the use of diffuser designs based upon a conical geometry with the inclusion of boundary layer control methods. The turbine was modelled by a screen

and a centrebody was included to replicate hub effects. It was found that the turbine must be sited in an area of constant cross section to prevent separation prior to diffuser inflow. The use of slots within a wide angle diffuser was found to suppress separation and enhance diffuser performance, though flow swirl and tip jets were omitted. In this study the best geometry was an approximately conical diffuser with a curved inlet and an included angle of 60°, employing slots at two downstream locations. The optimum geometry was found to give an augmentation factor of 1.89, with an area ratio of 2.78, meaning that the power coefficient of the device based on the outer diameter was 0.40. This compares well with efficient bare turbines but is likely an inaccurate assessment of the output due to the turbine model. The omission of tip jets is less important due to the boundary layer slots in the diffuser.

Gilbert et al. [91] refined the modelling of the Grumman Aerospace diffuser augmented turbine through the use of a scale turbine to replace the screen. In the case of the small scale models a Reynolds dependency was found as the Reynolds number, based on the diffuser throat diameter and freestream flow velocity, was below the $Re_{DiU_\infty} = 7.5 \times 10^4$ limit suggested by the literature in Section 2.3.2. For larger scale models no relationship was noted. The turbine wake's swirl was noted to improve diffuser performance, with the throat flow velocity being found to be 35% higher than for a screen of the same thrust. The concept of a dump diffuser or exit plane flange, dealt with in more detail in Section 2.4.4.3, was formed by structural considerations. For the final design incorporating an exit plane flange an augmentation factor of around 3.2 was found, though the size of components is not stated and so it is not possible to translate this into a power coefficient value.

Flay et al. [87] and Phillips [25] report on the construction, monitoring and subsequent improvements to the Vortec 7, a full scale version of the diffuser developed at Grumman Aerospace. The original design had a power coefficient based on the diffuser exit area of around 0.18. The improved design, a multi-slotted diffuser with an area ratio of 2.22, was found to have a power coefficient based on the device outer diameter of 0.37. The design of Phillips had the ability to maintain performance in yawed flow of up to ±15°. The performance at yaw was assigned to the slots in the diffuser wall allowing the flow to remain attached to the interior wall around the circumference and therefore align the bulk flow with the rotor.

Bet et al. [85] examined the use of small annular aerofoil section diffusers, finding that a design with two annular sections with a gap between to form a slot

provided the best performance. It was found that an increase of the output power to twice that of a bare turbine could be generated by a diffuser with an area of approximately 2.4 times larger, meaning that the power output would only be 83% of an equivalently large rotor. It was found that the addition of freestream turbulence aided the performance of the diffuser.

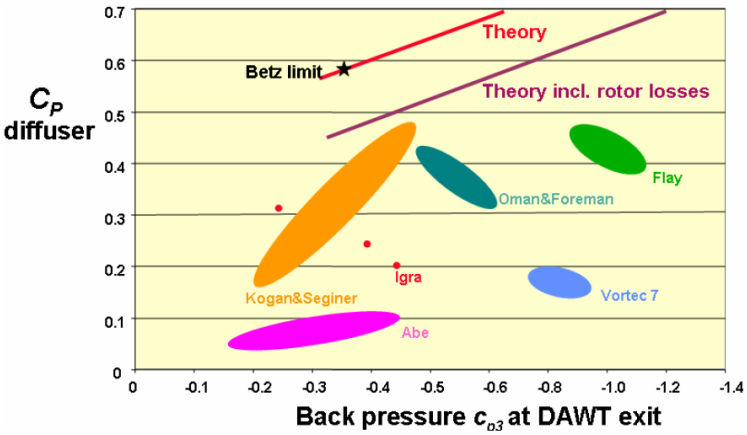


Figure 9: Diffuser power coefficient against back pressure for diffuser augmented wind turbines surveyed by van Bussel [24]

The power coefficients based on the diffuser exit area from a survey by van Bussel [24] of diffuser augmented wind turbines are presented against the diffuser back pressure in Figure 9. The power coefficients here may relate to variants of the authors designs which are not their final stated design, for example because the overall device length was considered too high. This diagram shows that although no diffusers augmented devices are close to the Betz limit, the performance is broadly comparable to a modern high efficiency wind turbine.

The literature on diffuser augmented wind turbines suggest that the development of such units has not led to a design which outperforms a bare turbine of an equivalent size to the outer diameter of the duct. The interest in diffuser augmentation of wind turbines can be seen to fade after 2003 as a result of their perceived shortcomings, though there has been subsequent interest in diffusers with exit plane flanges.

2.4.4.3. Exit Plane Flange

It has been found that an exit plane flange can reduce the diffuser exit pressure, boost the flow velocity through a duct and therefore increase the power available to the rotor. A body of work has been generated around flange

augmentation to which the reader is referred for more detail [84, 86, 96-98, 111]. The typical configuration of an exit plane flange can be seen in Figure 10.

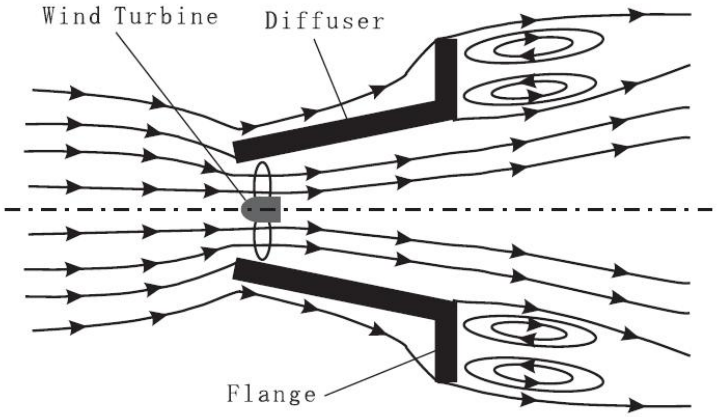


Figure 10: Exit plane flange arrangement and flow schematic [84]

Ohya [97] conducted wind tunnel tests on a diffuser with varying diffuser half angles and exit plane flange heights at a Reynolds number, based on the freestream velocity and throat diameter, of $Re_{DiU_\infty} = 2.4 \times 10^5$. The optimum size of the exit plane flange was found to be a function of the diffuser's length and diameter at exit. It was found that for a diffuser with a length to diameter ratio (L/D) of 1.5 and half angle of 12°, the optimum flange size, defined by the ratio of flange height to diffuser diameter (h/D), was 0.5 with a turbine model in the throat. If the flange size was increased beyond this point, an increase in the pressure upstream of the diffuser inlet was created, degrading the unit's efficiency. It was also found that the introduction of an exit plane flange provides passive yaw control, which allows for the simplification of the ducted unit. A power output of 4 to 5 times that of a bare turbine was generated through the use of this duct arrangement, though when normalised by the duct's outer area the power coefficient would be reduced to between 57% and 72% of that of the bare turbine.

Further work by Ohya [96] extended the use of exit plane flanges to "compact wind lenses". The longer straight walled conical diffuser was replaced with shorter, curved wall diffusers with the exit plane flanges still present. The radius of the diffuser was significantly reduced, with the ratio of the duct's external area to the throat area being only 1.87 for the case selected for field testing and the exit plane flange height being significantly reduced to only 10% of the throat diameter. A peak power coefficient based on the duct's outer area of 0.48 to 0.54 was found in field

tests, though it does not state the time period over which these values were achieved and whether or not they might be as a result of transient effects.

Chen et al. [86] investigated the use of a small flanged diffuser augmented wind turbine for power capture from moving vehicles. The investigations were conducted experimentally in a wind tunnel with low blockage. A range of rotor solidities were tested, with and without the duct, over a range of Reynolds numbers, based on the diffuser throat diameter and freestream flow velocity, from $Re_{DiU_\infty} = 2.3 \times 10^5$ to $Re_{DiU_\infty} = 4.6 \times 10^5$. The performance of the device relative to the bare turbine was dependent upon the rotor solidity, with the greatest relative performance improvement being 164% at a Reynolds number of $Re_{DiU_\infty} = 2.3 \times 10^5$ and a solidity of 30%. When this improvement is normalised, the performance is only 65% of that of a comparably sized bare rotor. It was noted that the turbine's solidity had an inverse relationship with the potential for power capture of the diffuser augmented unit, an effect which could be predicted by the increased thrust in the diffuser throat. It was also seen here that the Reynolds number has an inverse relationship with the diffuser performance, which runs contrary to the theory seen in Section 2.3.2. This effect is likely to be due to flow separation at inlet due to the omission of inlet geometry and the consequent jet flow in the diffuser.

The literature on exit plane flanges suggests that their inclusion may in fact reduce the power coefficient of a ducted device relative to the bare rotor of the same outer diameter. The use of smaller flanges has been found to increase the performance of the ducted unit but this was with a much reduced height and it is unclear to what extent this was attributable to the flange or whether it was in fact the result of an improved diffuser design.

2.4.5. Diffuser Augmentation of Tidal Turbines

The first attempt to the author's knowledge to use a duct for the augmentation of water current turbines was made by Kirke [26], who used a two dimensional slotted diffuser for the augmentation of a Savonius vertical axis turbine. It was found that an increase in the power output of 70% could be made. The throat and exit areas of the diffuser are not given; however an approximation measured from the sectional diagram indicates that the area ratio is around 3. This means that the power coefficient of the device based on the outer diameter would in fact be only 57% of that of the bare rotor.

Setoguchi et al. [108] examined the performance of two way diffuser augmented devices, aiming to remove the need to move the device in a reversing tidal current. Experimental work was performed in a wind tunnel on three geometries with retractable exit plane flanges at each end, which would be activated depending upon the flow orientation. No turbine model of any kind was used in the throat during these experiments, which were conducted at a Reynolds number of $Re_{DiU_\infty} = 6.0 \times 10^5$. The peak flow velocity through the duct was found to be 1.3 times larger than the freestream flow when the brim diameter was twice the throat diameter, meaning an increase in the available power of 220%. The area ratio of the device even without a brim would be 10.8, the diffuser power coefficient could therefore not possibly meet or exceed that possible for a bare turbine.

Munch et al. [105] and Luquet et al. [103] reported on the design and performance assessment of a dual ducted turbine unit developed under the MegaWattForce Project. Computational optimisation and experimentation were conducted on diffuser and rotor geometries for tidal turbines using an undisclosed optimisation methodology. A small included angle, high aspect ratio, curved wall diffuser coupled with a twin curved blade rotor was derived from the optimisation. Experiments were conducted in a towing tank at a Reynolds number, based on the diffuser throat diameter and freestream flow velocity, of $Re_{DiU_\infty} = 6.1 \times 10^5$. It was observed that a two bladed rotor outperformed a four bladed version, something that could be explained by the reduced thrust increasing the swallowing capacity of the duct. The peak power coefficient based on the diffuser outer diameter was found to be 0.335 for the runs conducted. The full scale device design uses a pump system within a small nacelle to provide high pressure fluid for land based turbines. As a result of pressure transmission losses the overall system efficiency is likely to be significantly lower than for a comparably sized bare turbine and generator unit.

Belloni et al. [99] studied the effect of geometry and thrust on open centred and bi-directionally ducted turbines. The study was conducted using 3D CFD with a porous media to simulate the turbine. The study was conducted at a Reynolds number, based on the diffuser throat diameter and freestream flow velocity, of $Re_{DiU_\infty} = 1.6 \times 10^7$, representative of full scale tidal flow. It was found that although there was a thrust dependency on the power output, the power was never ever able to reach that of a bare turbine of the same outer diameter.

Reinecke et al. [107] derived an inflected wall diffuser using axisymmetric two dimensional computational fluid dynamics with a uniform actuator disc turbine model and a support vector regression metamodel. The derived model was tested in a towing tank at a Reynolds number, based on the diffuser throat diameter and freestream flow velocity, of $Re_{DiU_\infty} = 3.7 \times 10^5$ with the rotor of Bahaj et al. [120, 121]. A peak power coefficient based on the turbine diameter of 1.74 was found, when calculated over the diffuser diameter a peak power coefficient of 0.528 was found. However the blockage ratio of 15.6% is large and no blockage correction was applied. To give an idea of the correction which may be necessary, Bahaj [120, 121] cites a correction of 18% to the power coefficient of a bare rotor with a blockage ratio of 17% and a thrust coefficient of 0.8. As the diffuser is a solid body, the thrust, and therefore the correction in this case may be still higher.

Sun et al. [122] utilised the duct geometry of Ohya et al. [96] with a rotor designed specifically for this purpose. The blades sections were a modified Gottingen 570 at the root and an M-F07x, developed by AIST (National Institute of Advanced Industrial Science and Technology in Japan) and Fuji Heavy Industries, elsewhere. The combined device was tested in a circulating water channel at a Reynolds number, based on the diffuser throat diameter and freestream flow velocity, of $Re_{DiU_\infty} = 1.9 \times 10^5$. It was found that a peak power coefficient based on the turbine area of 0.88 was attained at a blockage ratio of 7.4%. When the power coefficient is calculated over the duct's outer area the result is 0.47, a value which corresponds to that found by Ohya et al. [96].

The literature surveyed is of agreement that the use of bi-directional ducts causes the power coefficient of the overall device to drop relative to a bare rotor. There is a trend for the use of lower thrust rotors to maximise the power output of diffuser augmented devices.

2.4.6. Additional Benefits of Diffuser Augmentation

A number of additional merits of diffuser augmentation of tidal stream devices have been claimed in the past. Kirke [26] states that the use of a duct acts as a barrier between marine life and the turbine, though the inverse would seem to be true as there is a likelihood of objects passing in front of the duct being drawn through the duct and turbine. It is also stated that the duct blocks sunlight, which will interfere with the growth of marine life on the blade and duct surfaces, increasing the performance in the long term. The use of a duct may also act to

reduce the cost of the device powertrain as the size of the rotor can be reduced and the generator speed can be increased.

It has been claimed by several authors [26, 115, 116, 123] that the use of a duct has the potential to suppress the tip vortices and losses associated with bare turbines. This is disputed however by Ohya et al. [118], whose experimental results and numerical model appear to indicate the presence of such losses.

2.4.7. Demerits of Diffuser Augmentation

The main issue facing the use of diffuser augmentation of turbines is the cost of the diffuser structure itself. Phillips [25], de Vries [44] and Shives [115] all make reference to this, with Shives going so far as to say that it would seem unlikely that they can be made to operate economically as a result. As the device economics are ultimately the main factor in their acceptance this is therefore something which must be investigated further.

Shives [115] and Ohya et al. [118] note large scale unsteadiness and recirculation in the wake of the diffuser. It is suggested by Shives that this could lead to a fluctuating rotor plane velocity and therefore cyclical loading on the blading, leading to fatigue of the rotor blades and ultimately to blade failure.

2.5. Concluding Remarks

The literature suggests that many of the features which are exhibited in the wake of a turbine, such as increased turbulence, tip vortices, swirl etc, are those which also benefit the pressure recovery performance of a diffuser. Though to the author's knowledge there has been no study on the interaction of these effects on the performance. The presence of a jetting flow in the tip gap region between the rotor and casing is also something which has large potential gains for diffusion. It is suggested that the careful choice of the turbine parameters could greatly affect the performance of the combined device.

The modelling of diffuser augmented turbines has proven to be limited in its effectiveness due to the assumptions made about the flow. Many of the studies, both experimental and numerical, have noted that the omission of flow effects through the use of an actuator disc model or screen does not accurately reflect performance. In particular it is noted that the omission of swirl has a large impact upon the performance of a diffuser augmented device. This is something which is a reflection of the evidence that moderate flow swirl at diffuser inlet increases the diffuser's

pressure recovery ability. There currently exists no accurate analytical or numerical model for the prediction of performance of diffuser augmented turbines.

The performance of diffuser augmented turbines relative to that of a bare turbine of the same outer diameter has been a source of debate. Claims in the literature of diffuser augmented devices exceeding the Betz limit are made based on the use of the rotor area as a reference, which is misleading. The literature suggests that the Betz limit also holds for the rotor area if corrections are made for the increased mass flux across the rotor plane which the diffuser induces. A survey of the literature suggests that no extant diffuser augmented device has outperformed a modern, high efficiency, horizontal axis turbine of the same outer diameter.

The testing methodologies of diffuser augmented devices, the range of performance metrics used and the range of device designs has led to a lack of clarity on the subject of diffuser augmented turbines. There is little comparative study on standardised geometries and the basic fluid interaction is not well understood. The lack of inclusion of blockage correction for both experimental and numerical results is something which has caused over inflation of potential power outputs.

The effect of a realistic tidal flow on the performance of a diffuser augmented turbine is one which has not hitherto been answered. It has been reported that the performance of bare rotors is degraded by both flow which is yawed relative to the turbine and turbulent flow. The literature suggests that turbulent flow may in fact be beneficial to diffuser augmented devices and that yawed flow may not impact diffuser augmented devices until at a large yaw angle.

The main stated demerit and ultimately the main point which must be answered in order for diffuser augmentation to be used commercially is the cost element. The cost of a diffuser for an augmented tidal stream device has not previously been examined.

Findings from the literature provide scope for research into the following areas:

1. Generation of a methodology to accurately assess the performance of diffuser augmented devices.
2. Production of a generic diffuser geometry and analysis of the important aspects of turbine and diffuser interaction.

3. Assessment of the effects of a realistic tidal flow on the generation potential of a diffuser augmented device.
4. Quantification of the cost and generation potential of diffuser augmented tidal stream turbines.

3. Numerical Methods

This chapter presents the methods, models and parameters employed within the numerical models and simulations within this thesis. The use of the classical blade element momentum method is detailed along with the derivation of the blade element momentum method equations for use with computational fluid dynamics. The CFD setup, common parameters, techniques and solution methods are provided. The methodology for the derivation of the diffuser geometry is detailed, including details of the problem definition, objective function, numerical setup and resolution.

3.1. Blade Element Momentum Model

Blade element momentum theory is used in the classical form within this thesis to predict the performance of bare turbines, but has also been adapted to model both bare and diffuser augmented turbines when coupled with the CFD code. The classical blade element momentum method is introduced and derived and the extensions and changes made from this for the actuator disc CFD code are detailed.

As detailed in Chapter 2, the use of blade element momentum theory within CFD is not a new concept but has omitted key aspects of the rotor flow profile in the modelling versions attempted thus far. In the variations seen so far, at least one, though usually two or more of the parameters, including tip losses, turbulence generation functions or a defined power output calculation methodology are omitted. The implementation detailed here brings together all of these into an integrated model with low computational expense which is suitable for the power output and flow profile assessment of horizontal axis tidal turbines, be they bare or ducted.

The aspects of the derivation of blade element and momentum theory which are pertinent to the derivation of the implementation of the blade element momentum within computational fluid dynamics are detailed within this section. For further information on the derivation of the classical BEM method the reader is referred to Manwell et al. [43] or de Vries [44].

3.1.1. Momentum Theory

Momentum theory is based upon actuator disc modelling of the turbine, where a number of assumptions are made. The actuator disc is a simplified representation of the rotor, where the rotor is infinitely thin and circumferentially uniform. The assumptions made in momentum theory are detailed in Table 6.

Number	Assumption
1	Ambient pressure both far upstream and downstream
2	Homogenous, steady and incompressible flow
3	An infinite number of blades
4	No change in elevation
5	Uniform disc thrust
6	No frictional drag

Table 6: Assumptions made here in momentum and blade element theories

During the derivation of momentum and blade element theories reference locations relative to the turbine are used, these are indicated in Figure 11. Here, position 1 is far upstream of the turbine at ambient pressure and freestream velocity, with position 4 also at ambient pressure. Across the rotor from position 2 to position 3, there is a discontinuity in the pressure, but the velocity is continuous.

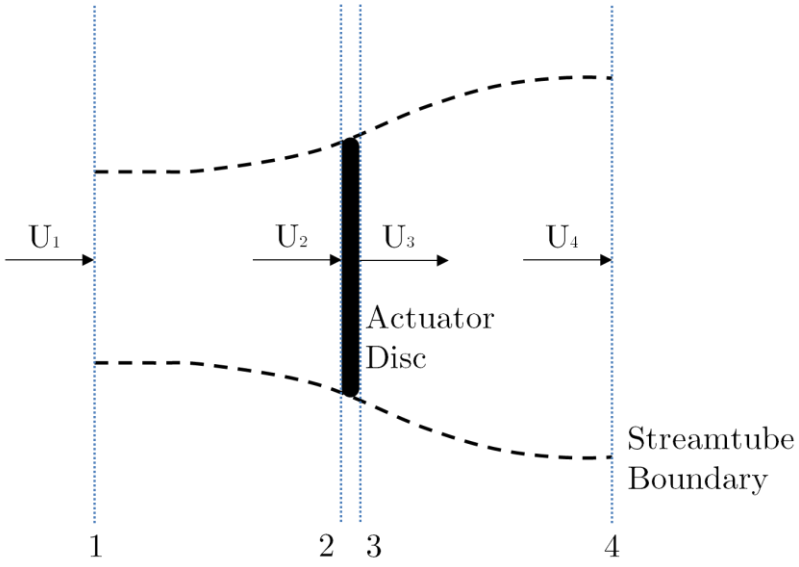


Figure 11: Momentum theory reference stations for a bare rotor

Due to the conservation of momentum, the thrust on the rotor is equal to the change in fluid momentum from the actuator disc as expressed in Equation 10.

$$T = U_1(\rho A_1 U)_1 - U_4(\rho A_4 U)_4 \qquad \text{Equation 10}$$

Using Bernoulli's principle, taking one control volume upstream of the rotor and one downstream, Equation 11 and Equation 12 can be written respectively.

$$p_1 + {}^1/_2\,\rho U_1{}^2 = p_2 + {}^1/_2\,\rho U_2{}^2 \qquad \text{Equation 11}$$

$$p_3 + {}^1/_2\,\rho U_3{}^2 = p_4 + {}^1/_2\,\rho U_4{}^2 \qquad \text{Equation 12}$$

Combining Equation 10 with Equation 11 and Equation 12, and noting that the velocities at stations 2 & 3 are identical, the thrust on the rotor can now be expressed as in Equation 13.

$$T = {}^1/_2\,\rho A_2\left(U_1{}^2 - U_4{}^2\right) \qquad \text{Equation 13}$$

The relationship between the velocities at the different stations is commonly expressed using the axial induction factor which is defined in Equation 14.

$$a = \frac{U_1 - U_2}{U_1} = \frac{1}{2}\left(1 - \frac{U_4}{U_1}\right) \qquad \text{Equation 14}$$

The theory up to this point neglects the radial distribution of thrust and the rotation of both the turbine and the wake. In order to include these effects it is necessary to adapt the treatment of the previous equations and to include additional rotational terms. The radial variation in the thrust distribution can be accounted for by breaking the rotor streamtube into a number of separate concentric annular streamtubes as shown diagrammatically in Figure 12.

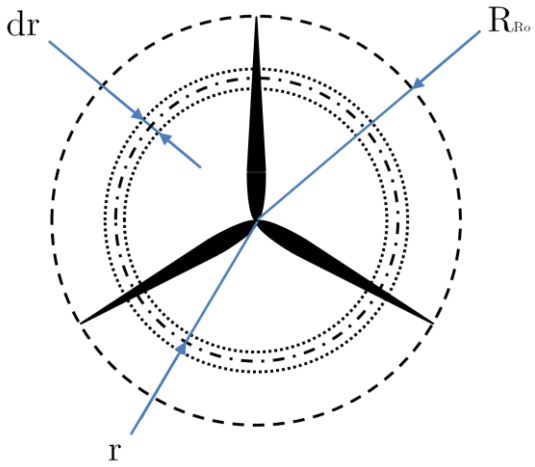


Figure 12: Definition of analysis annular streamtubes

Using Equation 13 and Equation 14, the thrust on an annular streamtube can be expressed as Equation 15.

$$dT = 4\rho U_1{}^2 a(1-a)\pi r dr \qquad \text{Equation 15}$$

The rotation can now be included within the method by the use of Equation 16, as derived by Glauert [124].

$$p_2 - p_3 = \rho\left(\Omega + {}^{1}/_{2}\,\omega\right)\omega r^2 \qquad \text{Equation 16}$$

Defining an angular induction factor as in Equation 17, the thrust on a streamtube can now be expressed as in Equation 18, with the torque on the rotor expressed as Equation 19.

$$a' = \frac{\omega}{2\Omega} \qquad \text{Equation 17}$$

$$dT = 4\rho U^2 a(1-a)\pi r dr \qquad \text{Equation 18}$$

$$dQ = 4\rho U\Omega a'(1-a)\pi r^3 dr \qquad \text{Equation 19}$$

The power output from an annular element of the rotor can now be found using the relation given by Equation 20.

$$dP = dQ\Omega \qquad \text{Equation 20}$$

3.1.2. Tip Loss Correction

In order to enhance the accuracy of the analytical predictions of momentum theory it is necessary to account for tip losses from the blade. The most common method for this is Prandtl's tip loss correction, calculated using Equation 21.

$$f_{TIP} = \left(\frac{2}{\pi}\right) cos^{-1}\left[exp\left(-\left\{\frac{({}^{B}/_{2})\left[1 - {}^{r}/_{R_{Ro}}\right]}{\left({}^{r}/_{R_{Ro}}\right) sin\varphi}\right\}\right)\right] \qquad \text{Equation 21}$$

The losses from the near hub region of the turbine blades can also be accounted for using the Prandtl model by amending Equation 21 as shown in Equation 22. The total loss function can then be defined as the product of the hub and tip loss functions as in Equation 23.

$$f_{HUB} = \left(\frac{2}{\pi}\right) cos^{-1}\left[exp\left(-\left\{\frac{({}^{B}/_{2})\left[{}^{r}/_{R_{Ro}} - {}^{r}/_{R_{HUB}}\right]}{\left({}^{r}/_{R_{HUB}}\right) sin\varphi}\right\}\right)\right] \qquad \text{Equation 22}$$

$$f = f_{TIP} f_{HUB} \qquad \text{Equation 23}$$

The Prandtl tip loss correction is based upon a simplification of the vortex sheets shed in the wake of the turbine, where it is assumed that the sheets are shed as planar sheets parallel to the rotor plane at periods tied to the blade passing frequency. The spacing of these sheets can then be calculated as a function of the turbine radius, tip speed ratio and the number of blades. This sheet shedding and the flow around the sheets are shown diagrammatically in Figure 13.

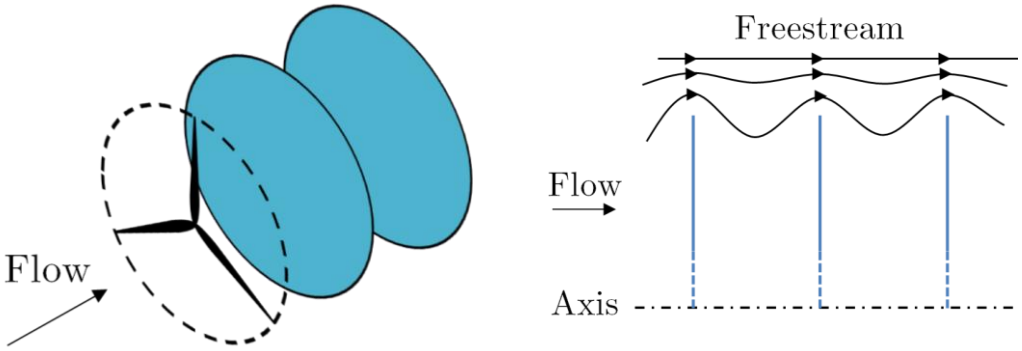


Figure 13: Diagram of the vortex sheet shedding and flow around the vortex sheets for Prandtl's tip loss correction method

The influence of the induced radial velocity on the axial velocity is calculated using potential flow theory, assuming that the blades are infinitely long. The reduction in axial velocity is used to assess the tip loss correction with Equation 21.

The limitations of the Prandtl model at higher tip speed ratios and with fewer blades were noted by Glauert [124], who compared it to the Goldstein solution [125]. The Goldstein solution assesses the problem in a more complete way, replicating the helical vortex structure in the wake using Bessel functions. As a result of the increased fidelity of the model it is accepted that the Goldstein solution is the more accurate tip loss correction model [126]. Due to the significantly higher computational expense, difficulty of application and relatively minor difference in results, the Goldstein solution is not commonly used within BEM, and it is the Prandtl model that is most commonly applied [44, 127].

The combined tip and hub loss correction factor provides a coefficient varying along the blade length, tending to zero at both blade extremes. When corrected, the expressions for the thrust and torque from Equation 18 and Equation 19 now become those in Equation 24 and Equation 25 respectively.

$$dT = 4f\rho\Omega^2 a'(1+a)\pi r^3 dr \qquad \text{Equation 24}$$

$$dQ = 4f\rho U\Omega a'(1-a)\pi r^3 dr \qquad \text{Equation 25}$$

3.1.3. Blade Element Theory

In blade element theory, the rotor is broken down into a number of non-interacting elements which are treated separately. It is assumed that since the elements are small, the forces on the rotor blades can be calculated from the sum of the lift and drag forces acting on the blade elements. Figure 14 shows the flow angles and forces acting on a blade element.

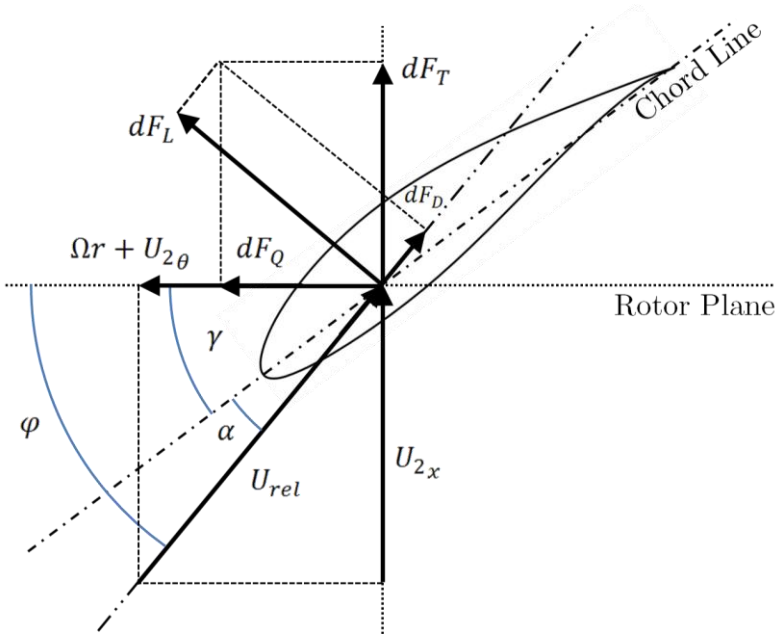


Figure 14: Flow angles and forces on a blade element

The rotational speed of the turbine is usually quantified within horizontal axis turbines by the tip speed ratio of the rotor, which is defined as in Equation 26. The local tip speed ratio for each blade element is then given by Equation 27.

$$\lambda_R = \frac{\Omega R}{U_1} \qquad \text{Equation 26}$$

$$\lambda_r = \frac{\Omega r}{U_1} = \frac{\lambda_R r}{R_{Ro}} \qquad \text{Equation 27}$$

The relative velocity of the flow onto the blade element can be calculated using Equation 28 and the angle of relative flow found using Equation 29.

$$U_{REL} = \sqrt{[U_1(1-a)]^2 + [\Omega r(1+a')]^2} \quad \text{Equation 28}$$

$$\tan\varphi = \frac{U_1(1-a)}{\Omega r(1+a')} \quad \text{Equation 29}$$

The angle of attack of the blade section can then be calculated using Equation 30. The angle of attack allows the blade section's lift and drag data to be queried and the lift and drag coefficients to be found.

$$\alpha = \varphi - \gamma \quad \text{Equation 30}$$

Using the blade section's lift and drag data, the lift and drag forces on the blade element can be expressed as in Equation 31 and Equation 32 respectively.

$$dF_L = {}^1\!/_2\, C_L \rho U_{REL}{}^2 c\,dr \quad \text{Equation 31}$$

$$dF_D = {}^1\!/_2\, C_D \rho U_{REL}{}^2 c\,dr \quad \text{Equation 32}$$

The thrust force and the torque on the annular section exerted by the blade element can then be calculated using Equation 33 and Equation 34 respectively.

$$dF_T = {}^1\!/_2\, B \rho U_{REL}{}^2 (C_L \cos\varphi + C_D \sin\varphi) c\,dr \quad \text{Equation 33}$$

$$dQ = {}^1\!/_2\, B \rho U_{REL}{}^2 (C_L \sin\varphi - C_D \cos\varphi) c r\,dr \quad \text{Equation 34}$$

3.1.4. Blade Element Momentum Model

By coupling momentum theory and blade element theory the flow at the rotor plane and the rotor's power output can be predicted. This section provides the details of two coupling methods, that for classical BEM and that for BEM CFD. The classical BEM, which can be used for direct calculation of the power coefficient of the rotor utilises the upstream flow data and relies on the assumptions of momentum theory to infer the rotor plane velocities. The BEM CFD uses the CFD solver to analyse the flow pattern and relies much more on blade element theory.

3.1.4.1. Coupling in Classical Blade Element Momentum Theory

Blade element theory has been used extensively in the past for the performance prediction of bare rotors. The BEM model is used within this thesis to assess the power output of bare rotors and is also the basis for the extended BEM CFD detailed in Section 3.1.4.2. To combine the blade element and momentum models, the thrusts from Equation 24 and Equation 33 are equated, including the

rotor solidity as defined by Equation 35. The drag coefficient term is ignored as is the common practise within the blade element method, as this has a limited impact upon the power output from a bare rotor model [44]. The resulting expression for the axial induction factor is as Equation 36.

$$\sigma = \frac{Bc}{2\pi r} \qquad \text{Equation 35}$$

$$a = \frac{1}{1 + \frac{4\mathrm{f}sin^2\varphi}{\sigma C_L cos\varphi}} \qquad \text{Equation 36}$$

The validity of Equation 36 depends upon the wind turbine's wake state. Eggleston and Stoddard [128] define two wake states pertinent to wind turbines, the windmill state and the turbulent state. These states are illustrated diagrammatically in Figure 15. The type of the wake state depends upon the thrust of the rotor and hence the axial induction factor. As the rotor thrust increases from the lightly loaded windmill state, the rotor streamtube expands on the downstream side due to the retarding effect of the turbine. Once the rotor thrust passes the critical value of $C_T = 0.96$ the rotor wake becomes highly turbulent with areas of flow recirculation and the one dimensional momentum theory is no longer valid.

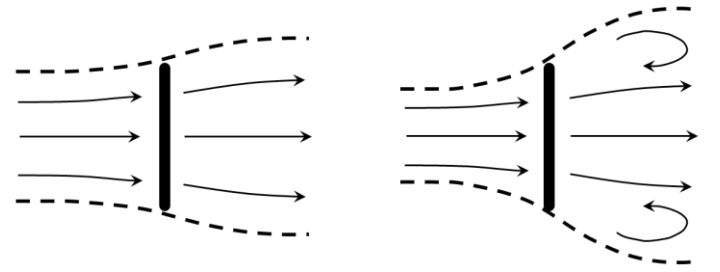


Figure 15: Diagrammatic representation of wind turbine wake states

The expression for the axial induction factor seen in Equation 36 holds when the rotor is operating in the windmill state. When the axial induction factor exceeds 0.4, which is at a thrust coefficient of approximately 0.96, the turbine begins to operate in the turbulent wake state and Equation 36 is no longer valid. To account for this effect, an empirical relationship for the axial induction factor was computed by Glauert [128], which uses the thrust coefficient from Equation 37 to calculate the axial induction. This expression is given by Equation 38.

$$C_T = \frac{dF_T}{\rho U_1{}^2 \pi r dr}$$ Equation 37

$$a = \left(1/f\right)\left[0.143 + \sqrt{0.0203 - 0.6427(0.889 - C_T)}\right]$$ Equation 38

To combine the blade element and momentum torque models it is necessary to equate Equation 25 and Equation 34, again ignoring the drag term, with the angular induction factor then being defined as Equation 39.

$$\acute{a} = \frac{1}{\frac{4f cos\varphi}{\sigma C_L} - 1}$$ Equation 39

In order to solve this set of equations for the axial and angular induction factors it is necessary to iteratively approach the solution. Using a suitably selected initial value (see Manwell et al. [43]) the procedure can be iterated until the difference between the estimates from one iteration to the next become negligible.

Once the axial and angular induction factors and the angle of the relative flow are known, the turbine power coefficient can be calculated using Equation 40.

$$C_P = \frac{8}{\lambda_R{}^2}\int_{\lambda_{HUB}}^{\lambda_R} f sin^2\varphi(cos\varphi - \lambda_r sin\varphi)(sin\varphi + \lambda_r cos\varphi)\left[1 - \left(C_D/C_L\right)cot\varphi\right]\lambda_r{}^2 d\lambda_r$$

Equation 40

3.1.4.2. Coupling for Blade Element Momentum CFD

The assumptions made in classical BEM theory that are used to infer the rotor plane velocity may not necessarily hold since they are defined for an idealised case where the only factor which affects the flow is the turbine. In reality the flow at the rotor will be influenced by a number of other factors, for example the turbine's hub, the support structure, the local bathymetry or bodies in the vicinity of the rotor such as a diffuser. To accurately predict the power coefficient in these conditions a flow solver must be coupled with BEM theory to assess the flow. This section deals with the coupling of equations with reference to a diffuser augmented turbine, though the methods are also applicable for use with bare rotors.

With a diffuser augmented device the relationship of the upstream and downstream velocities to the rotor plane velocity via the axial induction factor becomes invalid due to the effect of the duct on the flow around the rotor. In this

case, the streamtube that passes through the rotor contracts as it passes through the duct and then expands again within the diffuser and wake as seen in Figure 16. The axial induction factor retains a physical meaning, and can be used to predict the thrust force exerted by the rotor on the flow, but cannot be used to infer the rotor plane axial velocity from the upstream velocity, or to predict the far wake velocity.

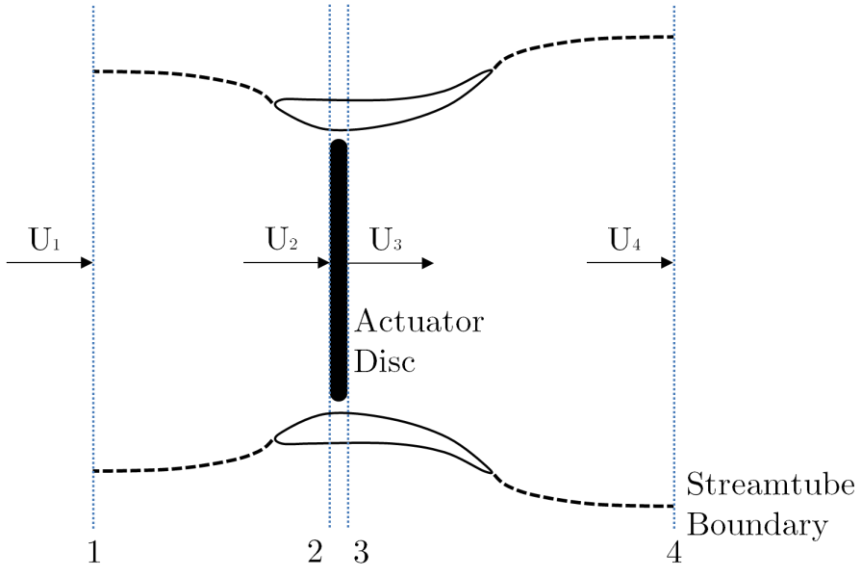


Figure 16: Momentum theory reference stations for a diffuser augmented rotor

This decoupling of the axial induction factor and the upstream velocity means that the approach used for a bare rotor will no longer be valid for a diffuser augmented device. As a result, the relations derived for the analysis of a bare rotor which refers to the upstream velocity need to be removed and the equations instead reframed to perform an analysis at station 2. The relative velocity and the angle of relative flow now become Equation 41 and Equation 42 respectively.

$$U_{REL} = \sqrt{{U_{2_x}}^2 + \left[\Omega r + U_{2_\theta}\right]^2} \qquad \text{Equation 41}$$

$$\tan\varphi = \frac{U_{2_x}}{\Omega r + U_{2_\theta}} \qquad \text{Equation 42}$$

In order to calculate the axial induction factor Equation 43 is used. This is an updated version of Equation 36, where the effect of the drag coefficient has been carried through. The motivation for this is the effect of the thrust of the rotor on the swallowing capacity of the duct and hence the rotor plane velocity. An accurate prediction of the rotor thrust is required for the flow solver to assess the flow field in and around the diffuser, due to diffusers' sensitivity to rotor thrust.

$$a = \frac{1}{1 + \frac{4fsin^2\varphi}{\sigma(C_L cos\varphi + C_D sin\varphi)}}$$ Equation 43

As with the bare rotor, the axial induction factor derived using Equation 43 is only valid in the windmill wake state, where the thrust coefficient is below 0.96. The axial induction factor must therefore be calculated using Equation 38. Due to the presence of the diffuser, the thrust coefficient must be calculated using the local flow conditions rather than those of the upstream flow. The thrust coefficient can now be derived from Equation 15 and Equation 33, and expressed as Equation 44.

$$C_T = \frac{\sigma(1-a)^2(C_L cos\varphi + C_D sin\varphi)}{sin^2\varphi}$$ Equation 44

The calculation of the angular induction factor is achieved through a derivation based upon Equation 25 and Equation 34. This was necessary as it was found that the equivalent function for the angular induction to Equation 43 caused numerical instabilities in the flow solver. Working through the derivation the angular induction can be expressed as Equation 45.

$$\acute{a} = \frac{\sigma U_{2_x}}{4fr\Omega sin^2\varphi}(C_L sin\varphi - C_D cos\varphi)$$ Equation 45

The expressions for the axial and angular induction factors are implemented within the CFD as momentum sinks and sources respectively using the methodology detailed in Section 3.2.4.2. Once implemented within the cell zone the CFD solver was iterated and the velocity field calculated. In order to calculate the power coefficient the axial and angular velocities at the rotor plane are exported from the flow solver. This velocity data allows the direct calculation of the relative flow angle onto the rotor at each radial station using Equation 42.

The power coefficient of the rotor can be calculated once the variables have been reframed for use at the rotor plane. In order to reframe Equation 40 for use at station 2, it is necessary to remove reference to the upstream velocity. Therefore, to calculate the local tip speed ratio Equation 26 and Equation 29 must be combined and rearranged to give the local tip speed ratio as Equation 46. This relationship breaks down when a>0.4, and the local tip speed ratio for that element must be calculated using interpolation or extrapolation from adjacent elements. The local tip speed will now be lower within the duct than if it were inferred from the relationship of the tip speed ratio and the local radius due to the increased axial

velocity at the rotor plane as a result of the presence of the duct. The equation for the power coefficient can now be rewritten as Equation 47.

$$\lambda_r = {}^{1}/_{tan\varphi}\frac{(1-a)}{(1+\acute{a})} \qquad \text{Equation 46}$$

$$C_P = \frac{8}{{\lambda_R}^2}\int_{\lambda_{HUB}}^{\lambda_R} f cos^3\varphi\left[sin\varphi + \frac{cos^2\varphi}{sin\varphi}\left(\frac{1-a}{1+\acute{a}}\right)\right]\left[\frac{(1-a)^2(a+\acute{a})}{(1+\acute{a})^3}\right]\left[1-\left({}^{C_D}/_{C_L}\right)cot\varphi\right]d\lambda_r$$

Equation 47

Evaluation of Equation 47 can also provide the power output of a turbine using the classical coupling of blade element theory. Equation 47 is in fact interchangeable with Equation 40, since at this stage the upstream flow references have been rephrased using geometric relations to remove the relevant upstream flow references. Evaluation of the $d\lambda_r$ term must now take account of the effect of the duct and the impact that this may have on the local tip speed ratio in addition to the need to account for the change in blade radius. The expression for the change in the local tip speed ratio can be evaluated using Equation 48. The power coefficient can be calculated by numerically integrating Equation 47 along the blade.

$$d\lambda_r = \frac{\Omega \mathrm{r_j}}{\mathrm{U_1}} - \frac{1}{tan\varphi_{j-1}}\frac{\left(1-a_{j-1}\right)}{\left(1+\acute{a}_{j-1}\right)} \qquad \text{Equation 48}$$

An approximate analytical approach to the solution of the above equations may be possible using the theory of Lawn [113]. This neglects a number of factors however, importantly the flow swirl and velocity profile across the rotor are neglected. Analysis would also require the efficiency of the diffuser to be known as a function of the rotor behaviour, which without prior work is not possible.

In order to solve the above system of equations it is necessary to implement the blade element momentum model within a flow solver, which will enable the interaction of the rotor and diffuser flows to be arrived at precisely. The flow velocities necessary for the computation of the power output can be output from the CFD model, the angles calculated, and using the methodology detailed above the power coefficient can be found for any operating condition.

This model provides the first complete methodology for the assessment of the performance of diffuser augmented tidal stream turbines. The model can be

implemented with a low computational expense relative to fully resolved CFD simulations, whilst retaining the ability to accurately predict the power output.

3.1.4.3. Modelling Limitations and Computational Expense

The computational expense and accuracy of the calculation of the power coefficient of a horizontal axis turbine will decide the method which is employed. The method chosen will usually be that which meets the modelling requirements of the problem at the least computational expense. The accuracy of the method will depend upon whether it accounts for the full range of flow phenomenon which are present in the modelled scenario. For example classical BEM would not be used where the rotor was ducted, nor would 2D BEM CFD be used where the flow was yawed. The assumptions of the implementation of blade element momentum theory contained within this thesis are detailed in Table 7.

Number	Assumption
1	Ambient pressure both far upstream and downstream
2	Homogenous, steady and incompressible flow
3	Flow is unconstrained by the surroundings
4	No change in elevation
5	Uniform disc thrust
6	No rotor coning, tilt or deflection
7	No rotor yaw

Table 7: Assumptions of BEM theory as implemented within this thesis

The 2D implementation of BEM CFD within this thesis reduces the number of assumptions made by the incorporation of the flow solver. The flow solver allows the impact of the rotor's surroundings to be modelled whilst maintaining a relatively low computational expense. The assumptions of BEM CFD are detailed in Table 8.

Number	Assumption
1	Steady flow
2	No change in elevation
3	No rotor coning, tilt or deflection
4	No rotor yaw

Table 8: Assumptions of BEM CFD as implemented within this thesis

Rotor coning, tilt, deflection and yaw can all be incorporated within both BEM and 2D BEM CFD via coordinate transformations based upon the rotor geometry. For more details on the use of such transformations see Mikkelsen [129].

The computational times for the blade element momentum model, blade element momentum computational fluid dynamics in both two and three dimensions, and fully resolved 3D CFD are presented in Table 9. The details of the 3D BEM CFD and the fully resolved 3D models are taken from McIntosh et al. [130].

Method	CPU Time (hrs)	No. Cells
Blade Element Momentum	1.37×10^{-5}	-
Blade Element Momentum CFD - 2D	2.53	2.55×10^{5}
Blade Element Momentum CFD - 3D	8	7.00×10^{5}
Fully Resolved	2000	4.40×10^{6}

Table 9: Computational time for the various turbine models per tip speed ratio

As can be seen from Table 9 the method of choice would be the BEM method where possible due to its high speed. As detailed above however there are a number of scenarios in which the modelling assumptions of BEM preclude its use and where another model must be applied. For the calculation of the power coefficient of a diffuser augmented turbine the 2D BEM CFD is by far the most efficient means.

3.1.5. Ideal Bare Turbine Blade Shape

The ideal shape of a turbine blade incorporating wake swirl can be calculated by following the methodology detailed in Manwell et al. [43]. This method neglects the tip losses and drag of a real rotor and is therefore not truly ideal, but provides a starting point for the assessment of a suitable blade shape. Partially differentiating Equation 40 by the angle of relative flow and rearranging gives Equation 49.

$$\lambda_r = \frac{sin\varphi(2cos\varphi - 1)}{(1 - cos\varphi)(2cos\varphi + 1)} \qquad \text{Equation 49}$$

Using Equation 49, the ideal angle of relative flow and ideal chord can be found using Equation 50 and Equation 51 respectively. The lift coefficient here should correspond to the angle of attack where the ratio F_Q/F_N is at a minimum.

$$\varphi = {}^{2}/_{3}\, tan^{-1}\left({}^{1}/_{\lambda_r}\right) \qquad \text{Equation 50}$$

$$c = \frac{8\pi r}{BC_L}(1 - cos\varphi) \qquad \text{Equation 51}$$

3.2. Computational Fluid Dynamics

The computational fluid dynamics undertaken within this thesis uses two commercial codes, one for meshing and another for the problem solution using the Reynolds-Averaged Navier–Stokes equations. Meshing was conducted using Ansys ICEM 14.0 and the calculations were performed using Ansys Fluent 14.0.

3.2.1. Turbulence Modelling

The turbulence model used for all simulations was the Transition SST implementation of the k-ω SST model. In a comparative study of turbulence models for flow within a planar asymmetric diffuser, El-Behery and Hamed [131] found that the k-ω SST and v^2-f models performed well. DalBello et al. [132] investigated the flow in a planar subsonic diffuser and also found that the k-ω SST model accurately predicted separation and velocity profiles. The k-ω SST model has been used for the study of draft tubes for hydropower turbines [133] and diffuser augmented stream tidal turbines [99, 104, 110, 122] and has been found to perform well.

The Transition SST implementation of the k-ω SST model within Ansys Fluent is as detailed by Menter et al. [134] and Langtry and Menter [135]. The Transition SST model differs from the k-ω SST model in that it includes two additional transport equations, one for the intermittency and one for transition onset utilising the momentum thickness Reynolds number. The advantages of this model are that it is largely grid independent and provides enhanced accuracy in the prediction of separation. The grid independence is as a result of the use of automatic wall treatment, where the solver uses a blending function to ensure a smooth transition between fully resolved modelling of the boundary layer and wall function modelling. The addition of the terms for intermittency and the momentum thickness Reynolds number are based upon empirical data.

3.2.2. Common Boundary Conditions

The velocity profile that would be present in a tidal channel was neglected in all cases to simplify the calculations. It has been shown by Mason-Jones et al. [35], that the key performance characteristics found in a uniform flow and those found in a flow with a vertical velocity profile are within 2% of one another when the area-averaged velocity across the rotor plane is used. The velocity profile was therefore

neglected, enabling axisymmetric two dimensional modelling in all cases. In all of the CFD calculations the solver settings used were as detailed in Table 10.

Parameter	Setting
Solver Type	Pressure-Based
Density Model	Incompressible
Turbulence Model	Transition SST
Pressure-Velocity Coupling	SIMPLE
Gradient Spatial Discretisation	Standard
Under Relaxation Factors	0.1 - 0.7
Spatial Discretisation	2nd Order Upwind

Table 10: Common CFD solver parameters

3.2.3. Material Properties

Within this thesis there are three basic simulation types when broken down by material properties, with the material used for the calculations depending upon the purpose of the simulation. The first of these is full scale simulations of tidal stream devices, for which the material used was sea water. Runs conducted to verify the accuracy of the CFD approach using the data of other authors were run using the material properties used by those authors in their experiments. Details of these verification runs can be found in Section 3.2.6. The final simulation type is that aimed to replicate experimental data from the wind tunnel, where the material properties of the air were calculated as detailed below. In all cases the fluid is treated as being incompressible, as a result either of being incompressible with water or being approximately incompressible at the tested flow speeds in air.

Where sea water is used as the fluid, the material properties were found using a data set provided by Sharqawy et al. [136], at a temperature of 5°C and a salinity of 35g/kg. The material properties can be seen in Table 11.

Parameter	Setting
Density	1028 kg/m^3
Dynamic Viscosity	1.6345x10^{-3} Pas

Table 11: Material properties of sea water

Where air was used as the fluid to match the wind tunnel results, the material properties were matched to each experimental case according to the ambient conditions at the time. The dynamic viscosity was calculated using Sutherland's law, as detailed in Equation 52, with the coefficients for air being as given in Table 12. The density was calculated using the ideal gas equation for dry air.

$$\mu = \mu_{REF}\left(\frac{q}{q_{REF}}\right)^{3/2}\frac{q_{REF}+s}{q+s} \qquad \text{Equation 52}$$

Variable	Value	Units
μ_{REF}	$1.1716\text{x}10^{-4}$	kg/ms
q_{REF}	273.15	K
s	110.4	K

Table 12: Coefficients of air for use with Sutherland's law

3.2.4. Actuator Disc Modelling

The modelling of a turbine within the CFD in this thesis is achieved through the use of an actuator disc model, be that a uniform actuator disc or one based on blade element momentum theory. Both of these models require user specified momentum sink profiles acting on either a face zone between cells or a group of cells known as a cell or porous zone. The key difference between the two implementations is the complexity of the user specified resistance profile.

3.2.4.1. Uniform Actuator Disc Model

The uniform actuator disc model can be implemented as either a porous jump or a porous media within the CFD. The porous jump is a simplified model which acts on a face zone between adjacent cells; the porous media has more modelling parameters available and acts on a cell zone. The porous jump acts in the direction perpendicular to the face, whereas the porous media can have separate momentum sink components in the x, y and z directions. In this thesis, the porous media is homogenous and is located such that the flow direction is perpendicular to the boundary and the models can therefore be viewed as being essentially identical.

The pressure drop for a porous jump and the momentum source term for a homogenous porous media can be seen in Equation 53 and Equation 54 respectively.

The difference between the two being that in the porous jump, a notional thickness is specified, whereas in the porous media the thickness is that of the cell zone.

$$\Delta p = -\left(\frac{\mu}{\beta} U_N + C_{pj} p_{Dyn}\right) \Delta x_M \qquad \text{Equation 53}$$

$$\mathrm{S} = -\left(\frac{\mu}{\beta} U_N + C_{pj} p_{Dyn}\right) \qquad \text{Equation 54}$$

In Equation 53 and Equation 54 there are viscous and inertial terms. Since the pressure loss in a turbine is proportional to the flow's dynamic head, the viscous term was neglected and the sources simplified as Equation 55 and Equation 56.

$$\Delta p = -\left(C_{pj} p_{Dyn}\right) \Delta x_M \qquad \text{Equation 55}$$

$$\mathrm{S} = -\left(C_{pj} p_{Dyn}\right) \qquad \text{Equation 56}$$

The source terms are implemented within the momentum conservation equation in the CFD code within the body force term $\vec{\mathrm{F}}$ in Equation 57, which also includes the other external body forces.

$$\frac{\delta}{\delta t}\left(\rho \vec{U}\right) + \nabla \rho \vec{U} \vec{U} = -\nabla p + \nabla . \left(\bar{\bar{\tau}}\right) + \rho \vec{\mathrm{g}} + \vec{\mathrm{F}} \qquad \text{Equation 57}$$

In order to make a representative turbine model implementation with porous models, the source must be related to the turbine thrust. The thrust coefficient of a turbine is as given by Equation 58. The definition of the static pressure drop across the porous model, assuming only inertial losses, is as seen in Equation 59.

$$C_T = \frac{T}{p_{Dyn_\infty} A_{Ro}} = \frac{\Delta p_{\mathrm{tRo}}}{p_{Dyn_\infty}} \qquad \text{Equation 58}$$

$$\Delta p_{\mathrm{tRo}} = K p_{Dyn_{Ro}} = \Delta x_M C_{pj} p_{Dyn_{Ro}} \qquad \text{Equation 59}$$

Since the velocity across the turbine plane is continuous in the case of a porous jump and essentially continuous for a thin porous media, the total pressure change across the rotor is then the static pressure change. Combining Equation 58 with Equation 59, the thrust coefficient can be expressed as in Equation 60.

$$C_T = \left(\frac{{U_N}^2}{{U_\infty}^2}\right) K_L = \left(\frac{{U_N}^2}{{U_\infty}^2}\right) \Delta x_M C_{pj} \qquad \text{Equation 60}$$

3.2.4.2. Blade Element Actuator Disc Model

The blade element actuator disc was implemented within a cell zone in the CFD using the blade element approach detailed in Section 3.1.4.2. The forces for the source terms were found using Equation 61 and Equation 62, which are derived from Equation 15 and Equation 19 respectively.

$$dT = \frac{\rho {U_2}^2 4a\pi r dr}{(1-a)} \quad \text{Equation 61}$$

$$dF_Q = 4\acute{a}\rho U_2 \pi r^2 \Omega dr \quad \text{Equation 62}$$

The turbulence generated by a turbine is included within the CFD through the use of an empirical relation derived by Crespo and Hernandez [137]. The turbulence intensity is related to the axial induction of the rotor by Equation 63. The turbulent kinetic energy can be found using Equation 64 to derive Equation 65.

$$I = 0.725a \quad \text{Equation 63}$$

$$k = {}^{3}/_{2}\,(U_2 I)^2 \quad \text{Equation 64}$$

$$k = {}^{2523}/_{1600}\,\pi r dr \rho {U_2}^3 a^2 \quad \text{Equation 65}$$

To arrive at the source terms, the forces and turbulent kinetic energy must be applied per unit cell volume and so the source terms are simply the forces calculated at the cell centroid divided by the cell volume. In cases where the cell zone is more than one cell thick, the term must be divided by both the cell volume and the thickness of the cell relative to the thickness of the cell zone.

3.2.5. Meshing Parameters

During the course of the numerical work, meshing was undertaken using both structured and unstructured meshes. The unstructured meshing was used for all simulations within the optimisation procedure detailed in Section 3.3, with structured meshing being used for simulations in all other cases.

3.2.5.1. Near Wall Mesh Parameters

The near wall region of the unstructured meshes was generated such that the y^+ value was below 5 except where there was significant flow acceleration, where it was below 10. For the structured cases, the y^+ was below 1 everywhere. This resolution is improved over that of Shives and Crawford [110] and Mehmood et al.

[104] for the modelling of diffuser augmented turbines. In these cases acceptable matching to the results against which the models were validated was found.

The low value of y^+, coupled with the numerical setup of the problems means that whilst the solver is not fully resolving the boundary layer flow within the diffuser, the boundary layer structure will be accurately replicated [132]. Boundary layer resolution being important to accurately asses the separation point within the diffuser and hence the diffuser performance.

3.2.5.2. Unstructured Meshing

An unstructured meshing approach was used for the optimisation routine within this thesis in order to ensure that the mesh quality within each grid would be of an equal quality. This was important given the necessity to give a fair comparison of the range of geometries. A fully unstructured mesh was used by Shojaeefard et al. [133] for the optimisation of draft tubes for micro hydro turbines, who validated their results against experimental data. The predictions of the pressure recovery coefficient for the draft tube from the CFD were found to correlate with the experimental results with a coefficient of 0.9993.

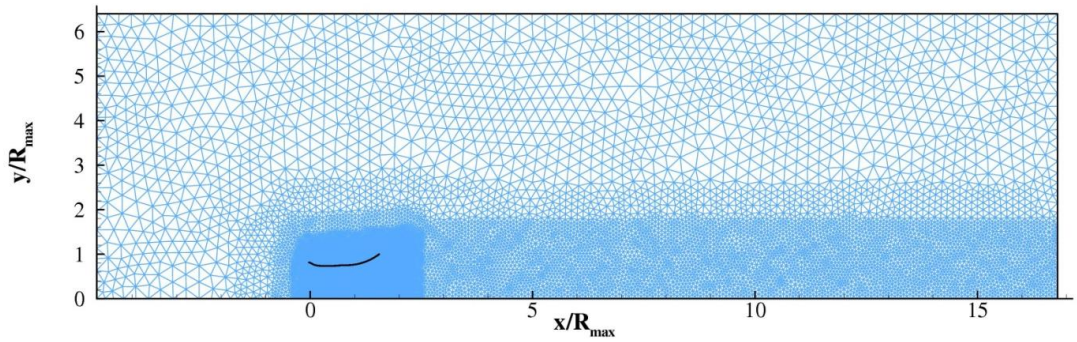


Figure 17: Example unstructured mesh for optimisation runs

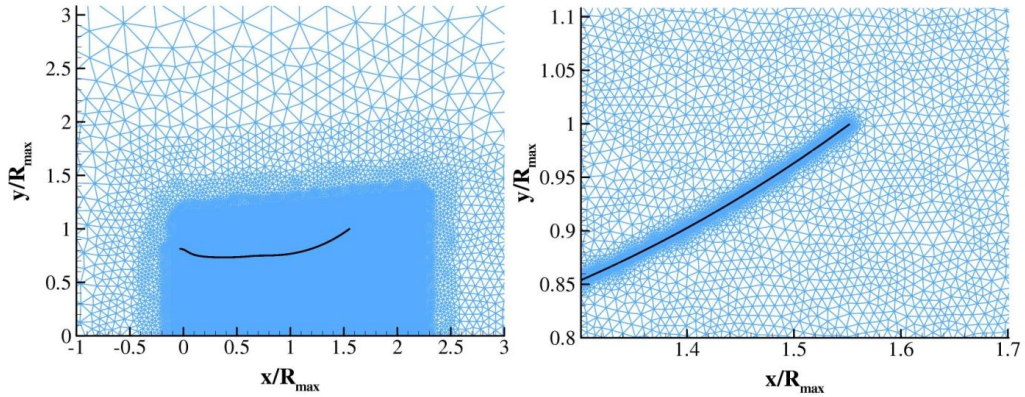


Figure 18: Magnified views of the example unstructured mesh

The mesh used for the optimisation was refined to produce a small y^+ value in the boundary layer. The entire mesh was refined in the wake of the device, with an increasing refinement closer to the device and a finer still refinement around the rotor model. An example of a full mesh can be seen in Figure 17, which shows the full extents of an example automatically generated mesh. Magnified views of the same mesh can be seen in Figure 18.

3.2.5.3. Structured Meshing

The approach used during structured meshing was to use a variable cell density, with higher cell concentrations in areas where the flow was influenced by the objects being modelled. The mesh was such that the boundary layer was again fully resolved within the CFD. The blocking strategy used for the structured meshes is shown in Figure 19. An example of a low density mesh can be seen in Figure 20.

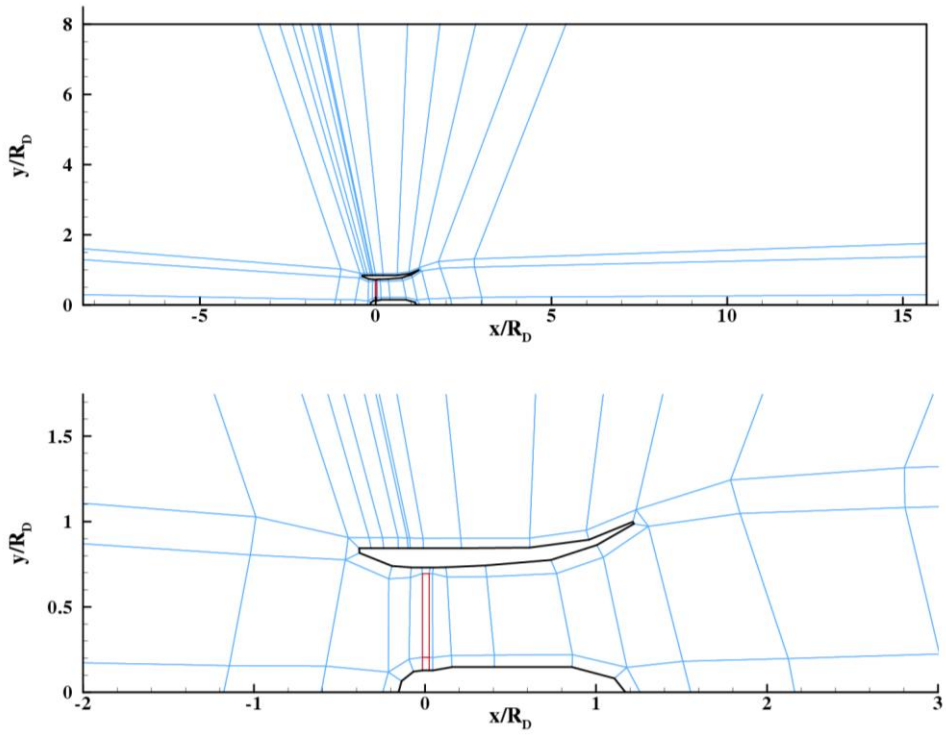


Figure 19: Blocking strategy for structured meshing

Magnified views of the mesh for a full density combined diffuser and porous cell zone mesh can be seen in Figure 21. The refinement of the grid around the diffuser structure and the high density mesh within the tip gap jet region can both be seen. The cell zone into which the turbine model was implemented is also clearly visible here as the region of red cells at the diffuser throat.

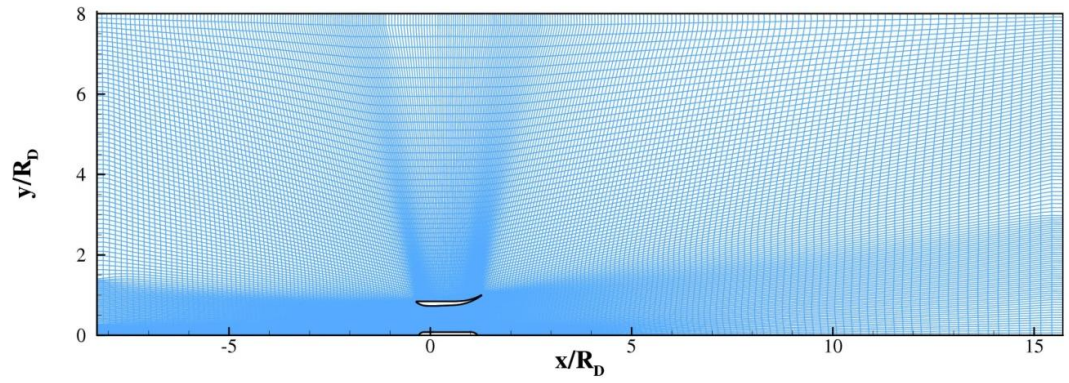


Figure 20: Low mesh density view of a structured mesh

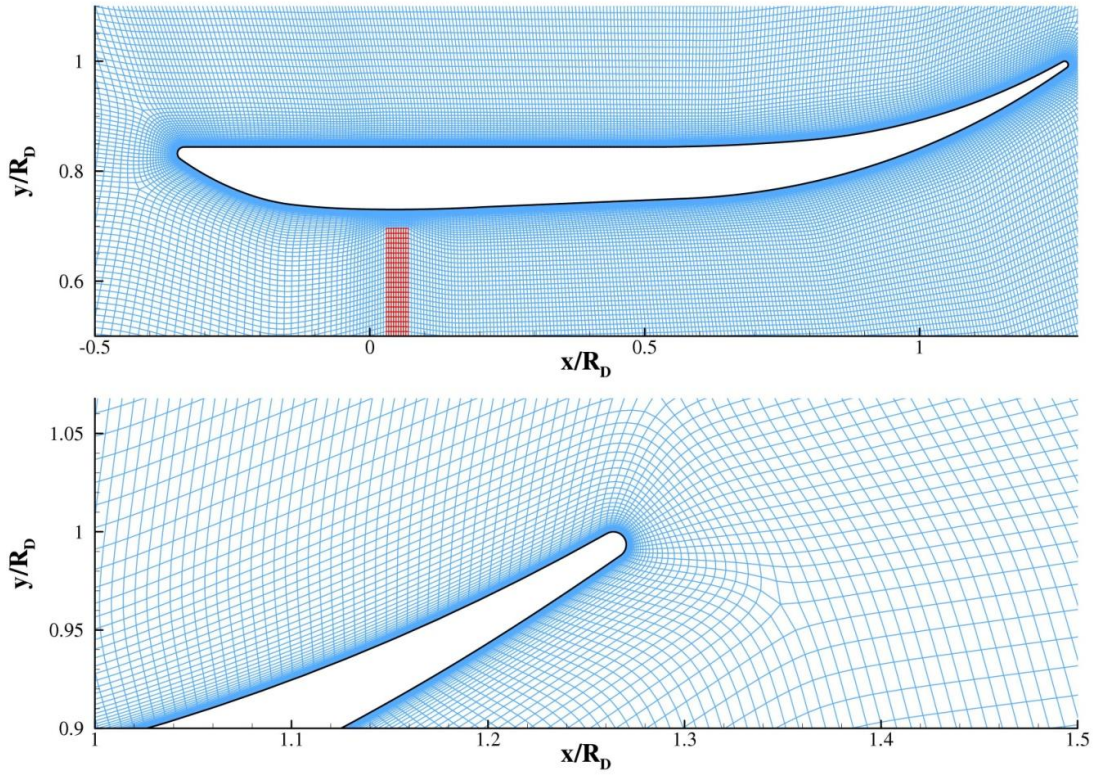


Figure 21: Detailed views of a full density mesh with porous cell zone

3.2.6. Validation of CFD Methodology

The CFD methodology employed within this thesis was validated using experimental data from two sources, firstly against diffuser data provided by ESDU [54] and then against data from McDonald and Fox [57].

3.2.6.1. CFD Validation against ESDU Data

ESDU characterises the flow in a diffuser according to a number of flow regimes, which are described by the degree of transience and attachment to the interior diffuser wall. In order to assess the ability of the CFD methodology used

here to replicate diffuser performance under a range of different flow conditions, a range of geometries were chosen to be simulated and the results verified.

The ESDU results were obtained for diffusers and tailpipe combinations with a range of lengths, area ratios and angles. The ESDU experiments were obtained with incompressible flow and a uniform inlet velocity, with an inlet pipe length of $\geq 2R_i$ and tailpipe length of $4R_e \leq L_{Tail} \leq 16R_e$. A schematic of the tested geometry, which was then used as the CFD input geometry can be seen in Figure 22. The results of the experiments summarised by ESDU are shown in Figure 23.

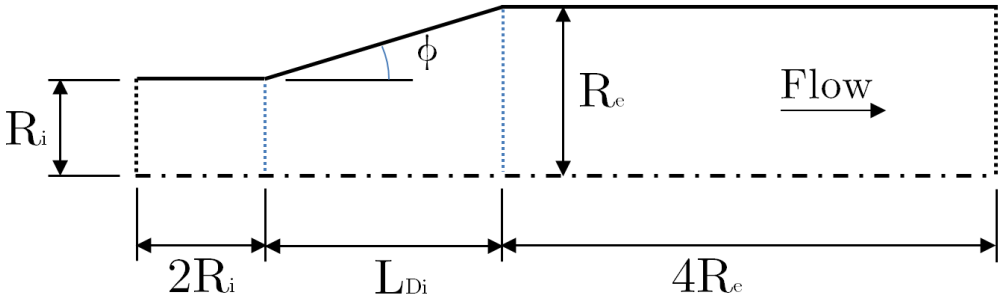


Figure 22: Reference dimensions for ESDU CFD verification cases

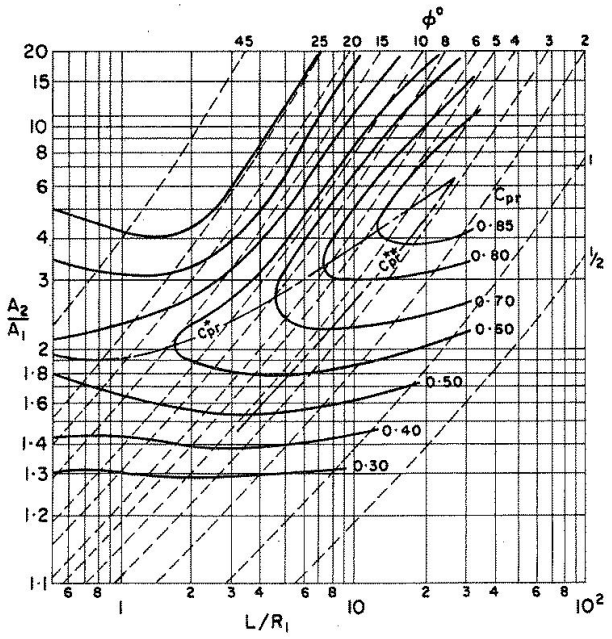


Figure 23: ESDU performance chart for conical diffusers with tail pipes [54]

The details of the geometries tested and the key dimensions for the CFD cases tested can be seen in Table 13. In all of the cases listed in Table 13, the material used was water, with a density of 1000 kg/m^3 and a viscosity of 0.001 Pas.

Variable	Units	Case 1	Case 2	Case 3	Case 4	Case 5	Case 6
Half angle	°	6	4	10	8	45	20
R_i	m	0.200	0.200	0.200	0.200	0.200	0.200
R_e	m	0.242	0.256	0.271	0.312	0.600	0.491
L_{Di}	m	0.400	0.800	0.400	0.800	0.400	0.800
L_{Di}/R_i	-	2	4	2	4	2	4
A_e/A_i	-	1.465	1.638	1.830	2.440	9.000	6.031
Re	-	8.00E+05	8.00E+05	8.00E+05	8.00E+05	8.00E+05	8.00E+05

Table 13: Dimensions for ESDU CFD verification cases

A wide range of possible geometries were tested, with cases from all of the flow regimes as presented by ESDU. The results of the CFD runs detailed in Table 13 are presented against the equivalent experimental cases in Table 14.

Variable	Units	Case 1	Case 2	Case 3	Case 4	Case 5	Case 6
C_{pr} CFD	-	0.495	0.587	0.607	0.698	0.193	0.366
C_{pr} ESDU	-	0.450	0.540	0.590	0.690	0.200	0.360
Difference	%	10.000	8.704	2.881	1.159	-3.500	1.667

Table 14: Comparison of CFD results with ESDU performance data

The results of this verification show that the CFD methodology is accurate in assessing the flow development within diffusing flows for a wide range of boundary conditions. The performance at lower diffuser angles is modelled with a lower degree of accuracy than for the higher angles, which is due to the under prediction of the total pressure losses resulting from wall turbulence at these low angles. The total pressure losses were under predicted by 9.69% and 5.89% for cases 1 and 2 respectively, a large part of the difference in the pressure recovery coefficients. Since diffusers used for the augmentation of tidal stream turbines are shorter, higher angle diffusers, this CFD methodology is well suited to the present application.

3.2.6.2. CFD Validation against McDonald & Fox Data

McDonald & Fox [57] conducted a large number of experimental runs on a range of diffuser geometries using water as a working fluid aiming to derive maps of diffuser performance. In addition, runs were conducted on a 15.6° half angle diffuser with $L_{Di}/R_i = 4$, to investigate the effect of the Reynolds number on the diffuser pressure recovery. It was found that at Reynolds numbers, based on the diffuser throat diameter and flow velocity, of below $Re_{DiU_{Di}} = 7.5 \times 10^4$ there is a sudden

loss of performance due to laminar separation upstream of the diffuser inlet. Above this value the flow behaves independently of the Reynolds number.

To validate the performance of the CFD for a range of Reynolds numbers, a set of simulations were run in order to replicate the experimental data. The geometry used by McDonald and Fox was two large water tanks with differing heads, connected by a conical diffuser. To replicate this, the CFD geometry was established as shown in Figure 24. The working fluid for the CFD simulation was water, with a density of 1000 kg/m^3 and a viscosity of 0.001 Pas.

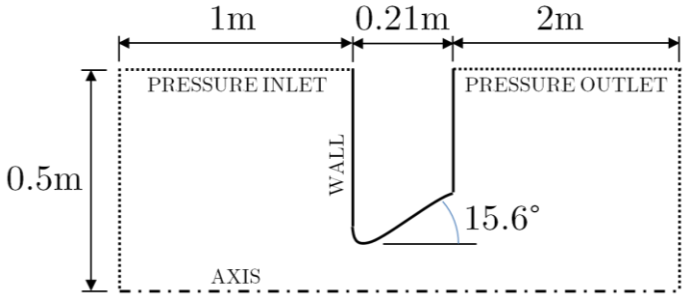


Figure 24: CFD domain to mimic McDonald & Fox experimental setup

The results of the CFD simulations are shown in Figure 25, along with the results of McDonald & Fox [57]. It can be seen that the CFD captures the effects of the laminar separation, replicating the maximum and minimum pressure recovery coefficients well. The prediction of the point at which the laminar separation starts to become suppressed within the diffuser is also well predicted. However, the stall recovery within the CFD occurs more gradually than in the experimental data. The accuracy of the separation prediction capabilities of CFD codes are a well documented issue and so this is not entirely surprising [138, 139].

The present CFD approach is sufficiently accurate to capture the flow effects present within the diffuser as a result of Reynolds number dependent separations. The resolution of the point at which the laminar separation reduces is accurate to within a Reynolds number difference of 2.0×10^3. The accuracy of the resolution of the elimination of the laminar separation with Reynolds number is less precise, though the CFD agrees with experimental data on the magnitude of the pressure recovery. As the work undertaken here has Reynolds numbers which will be of the order of $Re_{DiU_{Di}} > 3.0 \times 10^5$ this is thought to be minor as the magnitude of the pressure recovery response is predicted to within 1.49% at higher Reynolds numbers.

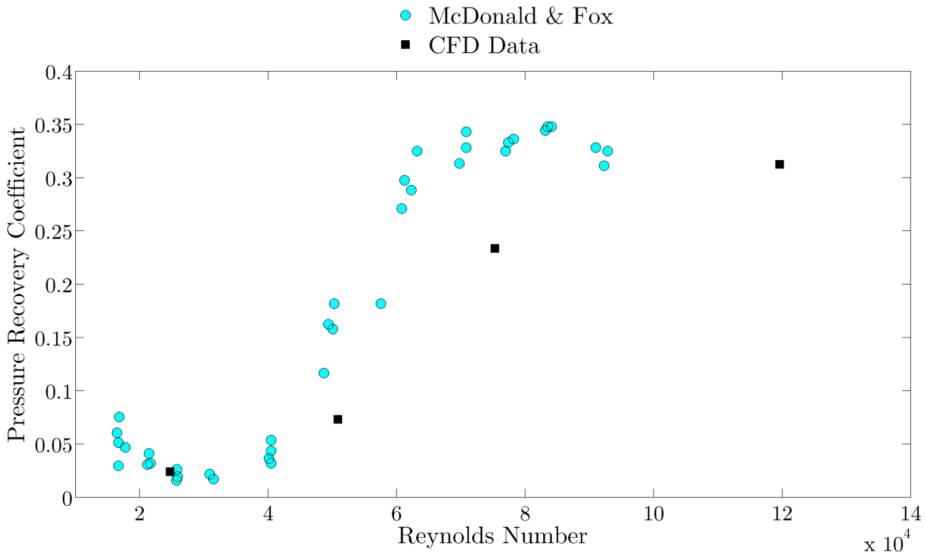


Figure 25: Comparison of McDonald & Fox data with CFD results

3.3. Geometry Optimisation

The methodology for the optimisation of the geometry uses CFD, a Kriging surrogate model and a genetic algorithm to produce a representative model for further numerical and experimental investigation.

3.3.1. Overall Procedure

The design methodology is broken into a number of stages: specification of the domain and design conditions, generation of the input geometries, testing of the input geometries, Kriging surrogate model generation, searching of the surrogate model and retrieval of the optimal solution. The final stages of this cycle are repeated until the results converge, at which point the optimum solution has been found. The optimisation procedure can be seen diagrammatically in Figure 26.

3.3.2. Input Parameters

The extents of the domain and the conditions under which the process was undertaken were informed by real world constraints and assumptions of them. Since the device was assumed to be unidirectional, the size of the optimisation domain was decided by the assumed channel depth of 30 m and the need for rotation of the device to face the reversed tidal current. The assumed channel depth was chosen as being towards the lower end of possible operational depths for tidal stream devices given the current state of the art [28]. A further constraint was that there should be a clearance of 2 m at all times between the device and the seabed or the free surface, meaning that the radius of rotation must be limited to 13 m.

Initial work indicated that $L_{Di}/R_e = 2$ provided an upper limit for the length of the device to balance best use of the channel cross section during operation with the need for rotation. It was therefore decided to use a maximum length of 16m and a maximum radius of 10 m. Figure 27 shows the domain and assumptions employed.

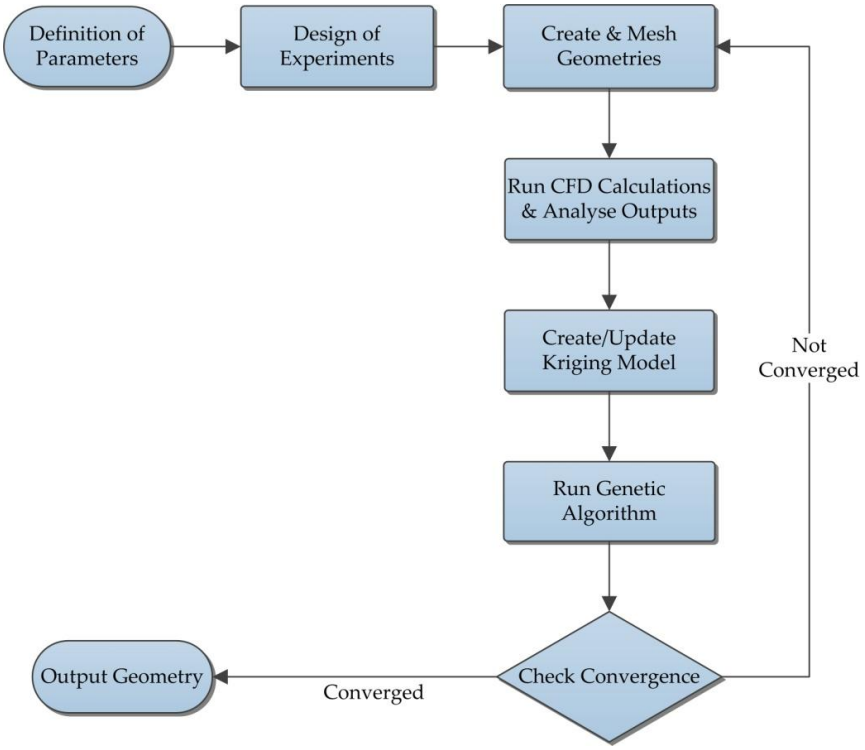


Figure 26: Geometry optimisation procedure

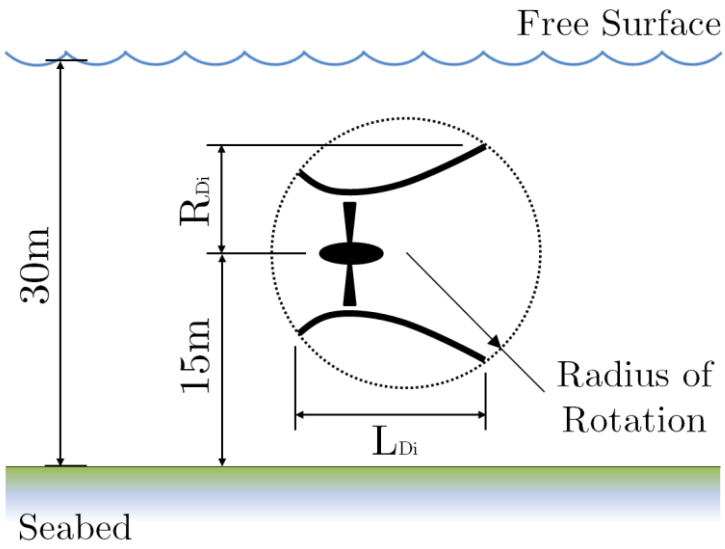


Figure 27: Tidal channel geometry and optimisation constraints

3.3.3. Design of Experiments

The experimental design is of importance to the overall model accuracy that can be achieved from the initial generation of CFD runs. There are a variety of experimental design methods which could be employed, with the choice depending upon the nature of the problem which is being evaluated. A comprehensive survey conducted by Simpson et al. [140] states that there is a general consensus amongst researchers that the best methods for use with deterministic experiments are space filling designs. Space filling designs are created to cover the computational domain with a distribution of experiments that is as close as possible to a constant density.

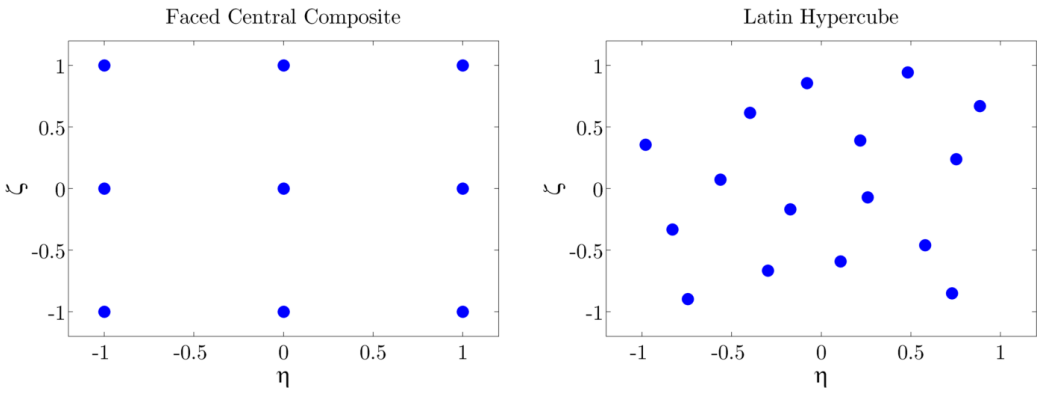


Figure 28: Example two dimensional face centred central composite and latin hypercube experimental designs

There are a variety of space filling designs available, but the most common is the use of a Latin Hypercube design as proposed by McKay et al. [141]. The Latin Hypercube design used was that implemented within MATLAB. This function allows for progressive iterations of the design to be made to allow for optimisation according to a variety of criteria. The design used in this optimisation was iterated to maximise the minimum distance between adjacent design points and therefore to ensure, as far as possible, a uniform distribution across the design space. Example two dimensional face centred central composite and Latin hypercube experimental designs of the same sample size can be seen in Figure 28. Note that the face centred central composite design has a number of central points.

In the optimisation there were six points which formed the control points for the Non-Uniform Rational Basis Spline diffuser geometry. These points were free to move with the degrees of freedom shown in Figure 29, giving a total number of variables for the experimental design of 11.

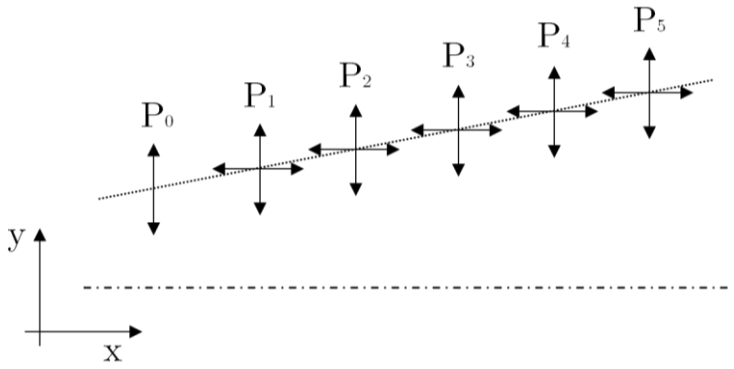


Figure 29: Degrees of freedom for control points

Initial simulations suggested that a conical diffuser with an included angle of 8° and an inlet radius of 8.5 m provided the best pressure recovery in the diffuser. This information was used to generate the centreline of the optimisation domain. The extents of the domain were set such that the limits were everywhere within 2 m of the centreline, unless this violated the original maximum size constraints, in which case they were then curtailed. The domain was split up into five sub-domains of equal size, and the movement of the associated control point was limited by the extents of the sub-domain. The sub-domains were employed to ensure that the geometries do not depart too markedly from montonicity, so that the NURBS curve does not self-intersect and so that the size of the surrogate model can be minimised. Figure 30 shows the optimisation domain with the point sub-domains.

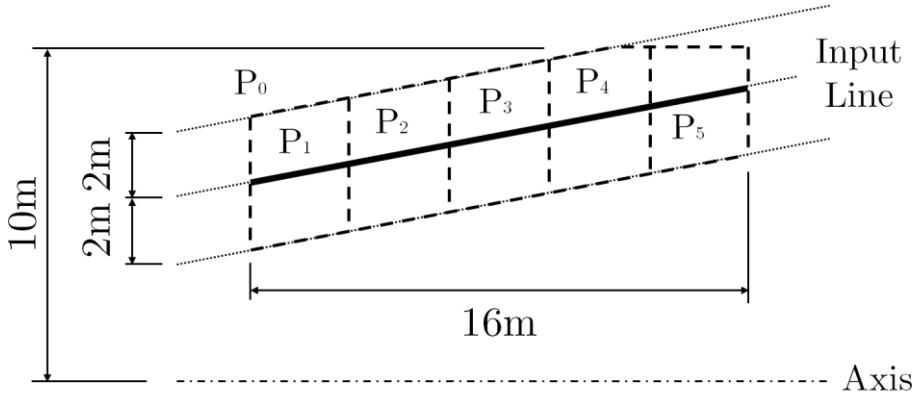


Figure 30: Optimisation domain and sub-domains

The design of experiments methodology generates a series of values, $-1 < \eta, \zeta < 1$, for each of the design variables. These values are then translated into the Cartesian coordinate system using shape functions.

3.3.4. Coordinate Transformation

In order to translate the coordinates from the experimental design into Cartesian coordinates, shape functions were used similar to those used in finite element analysis. There were two types of shape function used, depending upon whether the point was free to vary in one or two dimensions. The one dimensional shape functions were used to determine the coordinate for the inlet radius since the axial coordinate was fixed at the origin. For all of the other points, a two dimensional transformation was used. The transformation of the two dimensional coordinates is mapped as indicated in Figure 31.

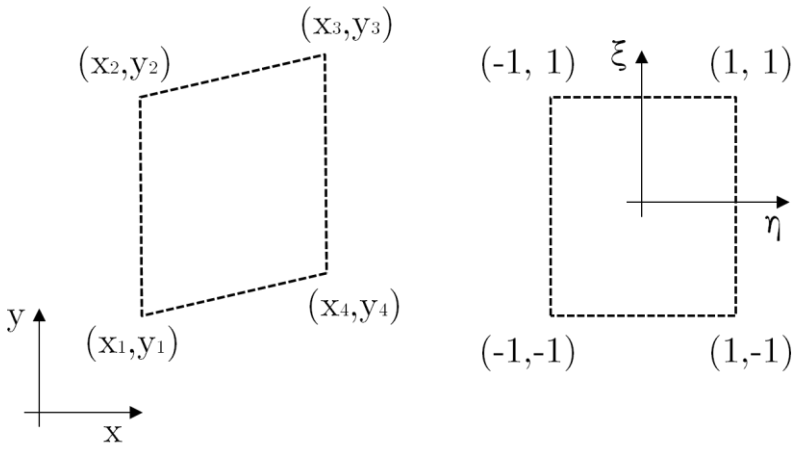


Figure 31: Transformation map from 2D Cartesian coordinates to shape functions

The Cartesian coordinates were calculated with Equation 66, Equation 67 or both, depending upon whether the transformation was one or two dimensional.

$$x = \sum_{i=1}^{n} N_i x_i \qquad \text{Equation 66}$$

$$y = \sum_{i=1}^{n} N_i y_i \qquad \text{Equation 67}$$

The one dimensional shape functions use only the one variable to transform the coordinates, since there are two points then there are two shape functions, given by Equation 68 and Equation 69.

$$N_1 = {}^1/_2\,(1 - \xi) \qquad \text{Equation 68}$$

$$N_2 = {}^1/_2\,(1 + \xi) \qquad \text{Equation 69}$$

For the two dimensional shape functions, there are four points and so there are four shape functions for the coordinates, given by Equation 70 to Equation 73.

$$N_1 = {}^1/_4 (1-\eta)(1-\xi) \quad \text{Equation 70}$$

$$N_2 = {}^1/_4 (1+\eta)(1-\xi) \quad \text{Equation 71}$$

$$N_3 = {}^1/_4 (1+\eta)(1+\xi) \quad \text{Equation 72}$$

$$N_4 = {}^1/_4 (1-\eta)(1+\xi) \quad \text{Equation 73}$$

3.3.5. Geometry Creation

3.3.5.1. Diffuser Geometry

The geometry for the diffuser was created using NURBS curves as these allow for the creation of complex, curved geometry, with only a limited number of control points. This is useful for the optimisation as it allows the representation of complex diffuser geometries with a minimal number of variables from the experimental design. For a full treatment of NURBS and their mathematical background the reader is referred to Piegl & Tiller [142]. For the purposes of the optimisation contained within this thesis cubic basis functions were utilised.

3.3.5.2. Hub Geometry

The geometry of the hub was excluded from the optimisation as it was assumed that the effect would be limited. Research conducted by Phillips [25] suggested that the effect of a small hub or centrebody within the diffuser did not produce a large wake and so would consequently have a limited impact upon the flow. As a result of this and the desire to simplify the optimisation procedure as far as possible, the hub was omitted.

3.3.5.3. Extents of Computational Domain

The NURBS diffuser geometries were imported into the meshing software and the computational domain was constructed around them. The extents of the domain can be seen schematically in Figure 32 along with the boundary types.

The diffuser was inserted at x=0 m with a porous jump to represent the turbine extending from the axis to 95% of the throat radius. The tip gap of 5% of the throat radius gap was included as it was found during preliminary calculations that this enhanced the diffuser pressure recovery. The problem was formulated with

a velocity inlet upstream, an outflow downstream, a zero-shear wall along the exterior of the domain and an axis passing along the turbine and diffuser axis.

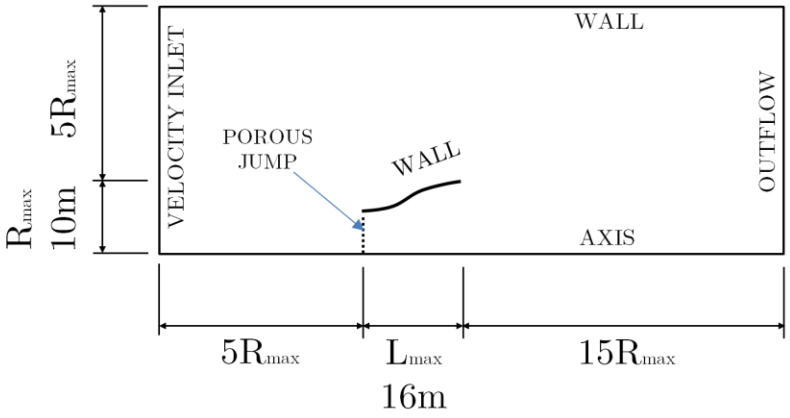


Figure 32: Computation domain schematic with boundary types

3.3.6. CFD Setup

3.3.6.1. Boundary Conditions

A freestream velocity of 2.75 m/s was used for the inlet flow velocity as this is a representative value for the rated velocity of existing tidal devices [56]. Inlet turbulence was set at a low level, with a turbulence intensity of 2% and a length scale of 10 mm. The porous jump was specified in order to be representative of a high performance rotor and diffuser coupling. Given the input parameters, an examination of a summary of diffuser augmented wind turbines from Phillips [25] suggested that for a high augmentation, a thrust coefficient of approximately 0.45 would be an appropriate value for the rotor. As can be seen in Equation 60, the thrust coefficient is tied to the ratio of the square of the freestream and turbine plane velocities. Since the form of the duct geometry is unknown beforehand, and therefore so is the flow velocity at the rotor plane, it was assumed that the effect of the duct would be to accelerate the flow to the freestream velocity in the throat, meaning that the velocity ratio term can be neglected. As a result, in order to achieve a thrust coefficient of 0.45, the porous jump was specified with a thickness of 0.1 m and a pressure jump coefficient of 4.5 m^{-1}.

3.3.6.2. Convergence

The CFD was run for 4000 iterations, with the convergence criterion for the CFD being the weighted residuals dropping to $1x10^{-4}$. The transcript files and outputs files were then collated by the optimisation code. If the solution failed to

converge, the result was given an objective function value of zero as it was assumed that this was a poorly conditioned diffuser causing convergence difficulties.

3.3.7. Objective Function

To compare the performance of a duct to that of a bare rotor, the metric must reflect the power capture abilities of the duct relative to its outer dimensions. Since the power in the fluid which is available to the rotor is proportional to the cube of the throat velocity, an area power coefficient was defined as in Equation 74.

$$C_{PA} = \frac{{}^{1}/_{2\rho A_{Ro} U_{Ro}{}^{3}}}{{}^{1}/_{2\rho A_{Di} U_{\infty}{}^{3}}} = \frac{R_{Ro}{}^{2} U_{Ro}{}^{3}}{R_{Di}{}^{2} U_{\infty}{}^{3}} \qquad \text{Equation 74}$$

The area power coefficient is analogous to the power coefficient based on the diffuser's outer area for an actuator disc of a prescribed thrust. The thrust of the actuator disc model will depend upon the velocity ratio as seen in Equation 60. The relative device performance was found to be the same whether the area power coefficient or the power coefficient based on the diffuser's outer area was used.

3.3.8. Metamodelling

The use of metamodelling for optimisation problems within engineering has been the subject of much research, with notable reviews being published by Simpson et al. [140] and Wang and Shan [143]. Since the CFD modelling results are deterministic and the underlying physical phenomena highly non-linear, a Kriging approach to metamodelling is appropriate.

Kriging is a mathematical method, originally created for geostatistics, that estimates a variable at an unobserved location given a set of input sample values for the variable. A review of Kriging methodology is outlined by Kleijnen [144]. Kriging has previously been used successfully for engineering optimisations in a range of environments and conditions [145-148]. The Matlab implementation of Kriging was achieved using the Design and Analysis of Computer Experiments (DACE) toolbox of Lophaven et al [149]. The DACE toolbox is a Matlab toolbox for the implementation and analysis of Kriging models in computational experiments.

The Kriging model specifies a general model and a set of departures from that model and can be expressed as in Equation 75.

$$Y(u) = Z(u) + W(u) \qquad \text{Equation 75}$$

The objective function results from the CFD were used to construct a Kriging model within DACE using the standard regpoly0 regression function and exponential correlation. The regression function was chosen as due to the relatively sparse nature of the sample points, higher order functions cannot be used. The correlation function was chosen to be non-differentiable as the highly non-linear nature of the flow separation effects in the diffuser meant that a continuously differentiable function would not adequately represent the flow conditions. As a result the exponential correlation was chosen as the most commonly used of the non-differentiable functions [150].

3.3.9. Genetic Algorithm

Due to the size of the design space and the number of variables present, it was not feasible to interrogate the Kriging model for every possible design, meaning that a search algorithm was necessary. There are a wide variety of search methods which exist for the location of an optimum, a genetic algorithm was chosen as it provides one of the most commonly used and promising search algorithms [147]. The use of a surrogate model and genetic algorithm allows for a significantly reduced amount of computation over the use of a genetic algorithm alone [147, 151].

A genetic algorithm is designed to mimic the evolutionary behaviour which is seen in nature and as such each successive generation should be an improvement on the last. The genetic algorithm which was used here was formed from several steps. The first step was to produce the initial population, which was generated using a Latin Hypercube experimental design, with 1000 points from the entire design space. Once the initial generation had been decided, a fitness level was associated to each member of the population. The fitness in this case was the Kriging predictor of the objective function added to the departure term. This addition was required as the Kriging predictor alone otherwise peaks at, or close to, the sample points.

The next stage of the process was to randomly split the population into two sections, the males and the females. It should be noted that all ‘random’ processes within this algorithm are controlled by Matlab’s random number generator. Once the split is complete the mating of the two halves is allowed to take place such that a proportion of the populace, controlled by the crossover rate, are allowed to mate. In this case a crossover rate of 0.7 was used. If a male and a female mate, the

offspring contains a random number of chromosomes (design variable values) from one partner and the remainder from the other. The remaining 30% of the original population who do not mate survive until the next generation.

Once mating has been completed a mutation phase commenced. In this phase, 1% of the population was randomly selected and a random number of its chromosomes were changed. The change in chromosome values was controlled by a random generation of a value subject to the design space limits. After this phase has been completed, a fitness level was calculated for the new generation by interrogating the Kriging model. The fittest member of that generation was noted and the next generation was allowed to evolve. In this optimisation, 100 generations of the genetic algorithm were completed for each iteration loop seen in Figure 26.

Once the last generation was created, the overall optimum value was found by evaluating the best individual from all of the fittest individuals for each generation. The optimum was used to determine the input for the next step of the optimisation.

3.3.10. Convergence Assessment

Since the fitness level for each predicted value was defined as the sum of the prediction and the associated error, this allowed for a measure of the model convergence to be evaluated. The optimisation procedure was iterated until the prediction of the objective function by the optimisation routine was within 1% of the associated prediction from the CFD simulation. Once this criterion had been reached the solution was said to have converged and the global optimum found.

3.3.11. Optimisation Summary

The optimisation routine detailed above allows the derivation of high efficiency diffuser geometry for use with a horizontal axis turbine. The motivation for running through the above procedure, which involves a significant quantity of computation, is to arrive at a diffuser geometry which is devised to directly address the challenges of the tidal stream environment. In particular the procedure is a direct means of addressing the need to make best use of the channel cross section by maximising the power per unit of device frontal area.

The alternatives to the use of this methodology for the selection of diffuser geometry are to employ an alternate optimisation routine or to manually select one. The use of alternative algorithms would likely require still greater computational expense due to the inefficiencies of those methodologies as opposed to that detailed

here [147, 151]. Manual selection of diffuser geometry, based for instance on existing hydrofoil sections, would require a considerable time investment and would most likely result in a sub-optimal design.

3.4. Concluding Remarks

This chapter details the numerical methodologies and their setups used within this thesis, the motivation for their use and where relevant their derivation. This chapter contains the derivation and implementation details of the extended blade element momentum model for use within computational fluid dynamics which was generated as a part of this thesis. This chapter also provides the optimisation routine by which the diffuser geometry used within this thesis was derived.

The models derived here are used for detailed assessments of bare and diffuser augmented turbine flows in Chapter 4. The output results from these models are then compared with experimental results in Chapter 6.

4. Numerical Results

This chapter presents the results obtained from the numerical analyses performed as a part of this thesis. Results from both the blade element momentum model and the computational fluid dynamics runs are detailed.

4.1. Experimental Turbine Blade Design

The blade element momentum model was implemented as a stand alone program for the assessment of the performance of bare rotors. The BEM code was used as a tool to assist in the design of the turbine for use within this thesis.

4.1.1. Cavitation

In the development of the blade design the effect of cavitation on the rotor must be considered. Cavitation occurs when the pressure in water drops to a value below the vapour pressure and the water vaporises. Cavitation can adversely affect the efficiency of a rotor both in the short term due to reduced lift and increased drag, and in the long term by damage to the rotor [152]. The cavitation performance can be evaluated using the cavitation number, which is seen in Equation 76.

$$\epsilon = \frac{p - p_V}{{}^1/_2 \rho U_\infty{}^2} = \frac{p_{AT} + \rho g d - p_V}{{}^1/_2 \rho U_\infty{}^2} \qquad \text{Equation 76}$$

The extent of cavitation will depend upon the value of the cavitation number. The higher the cavitation number the less likely cavitation is to occur and vice-versa. Cavitation is more likely near to the free surface due to the decreased pressure and would be more likely within a diffuser due to the reduced sub-ambient pressures.

In order to control cavitation at a given depth, either the static or dynamic pressure at the object of interest must be controlled. In the case of a turbine, the former can be achieved through careful hydrofoil section and size selection [153]. The latter can be controlled by minimising the dynamic pressure that the blade experiences. This means that a rotor with a high efficiency at a low tip speed ratio is desirable. The rotor in this case was designed to operate at a tip speed ratio of 4.

The use of a rotor within a duct is likely to increase the inception of cavitation due to the reduced pressure at the rotor plane. This is an effect which has been noted in hydropower turbine draft tubes, particularly with wake swirl and the

associated low pressure vortex core [152]. To account for the increased risk of cavitation it is desirable to increase the resistance of the bare rotor to cavitation.

4.1.2. Blade Section Characteristics

The aerofoil section that was chosen for the design of the turbine was from the NACA638xx family of sections. This aerofoil family has been used previously by Molland et al. [153], Batten et al. [154] and Bahaj et al. [120], the work of whom is widely referred to in the literature. In order to simplify the rotor design a NACA63818 section was used at all radii on the blades. The lift and drag coefficients as calculated by XFoil [155] at a Reynolds number, based on the blade chord and freestream flow velocity, of $Re_{cU_\infty} = 2.5 \times 10^5$, can be seen plotted against the angle of attack in Figure 33.

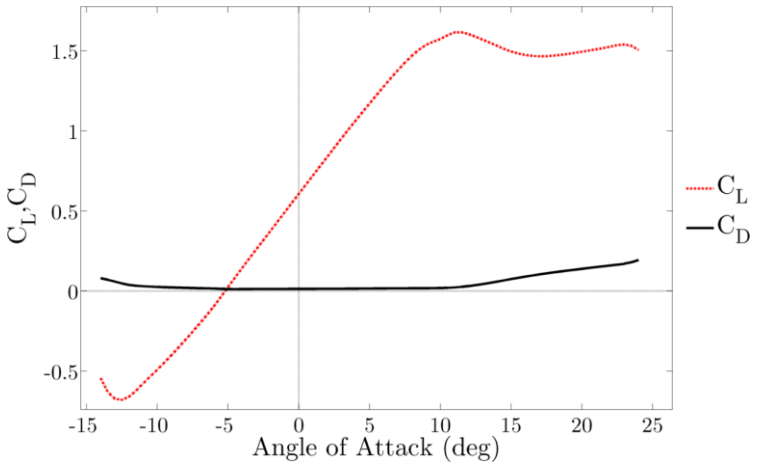


Figure 33: NACA63818 lift and drag coefficients against the angle of attack from XFoil at $Re_{cU_\infty} = 2.5 \times 10^5$

As a result of manufacturing limitations for the experimental rig, which are detailed in Section 5.1.2.3, the blade section used for the experimentation was an adaption of the NACA63818 geometry. The trailing edge of the NACA63818 section was rounded to allow for precise manufacture at the scales at which the experimental rig was constructed. The trimming of the rear part of the section had the effect of increasing the angle of the section relative to the original chord line. The curtailing also increases the degree of symmetry across the chord line. The two blade sections can be seen in Figure 34.

The performance of the rounded NACA63818 section was assessed using CFD, as due to the trailing edge modifications, XFoil is no longer suitable to model the flow at the rear of the section. The behaviour of the rounded section is different to

that of the NACA63818 section as can be seen in Figure 35, which shows the lift and drag coefficients for the two blade sections against the angle of attack.

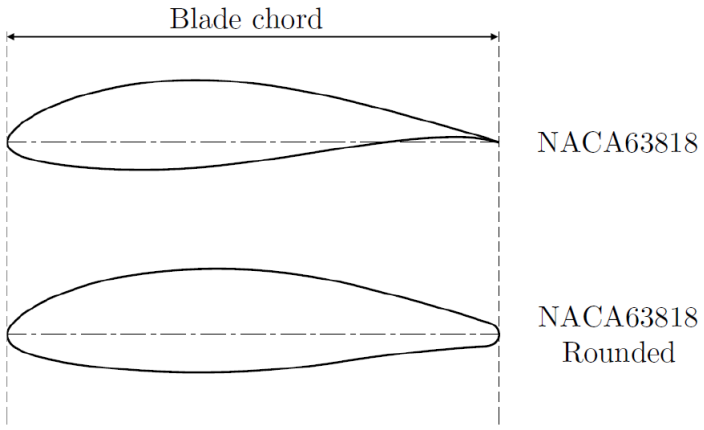


Figure 34: NACA63818 and rounded NACA63818 aerofoil cross sections

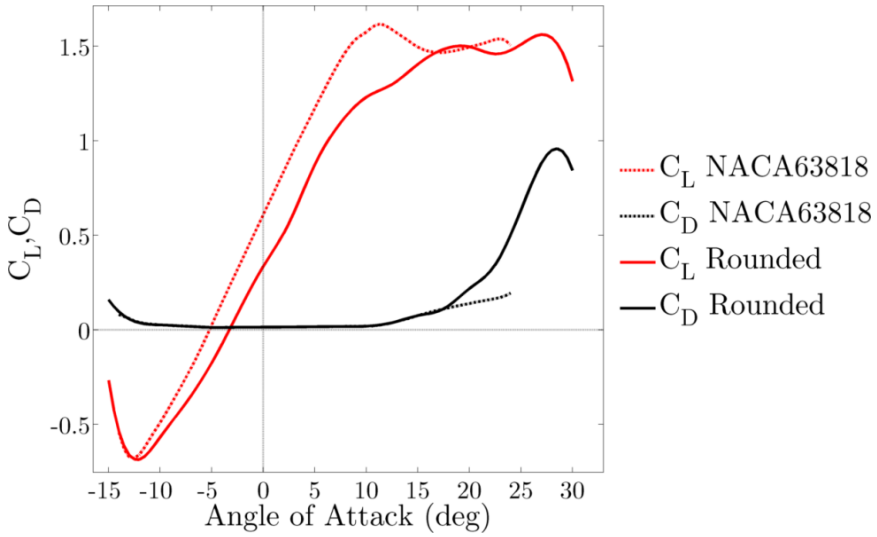


Figure 35: NACA63818 and rounded NACA63818 lift and drag coefficients against the angle of attack at $Re_{cU_\infty} = 2.5 \times 10^5$

The behaviour at low and negative angles of attack is similar in both cases, albeit with a higher lift coefficient in the case of the NACA63818 section. This could be expected as there should be a greater degree of streamline curvature induced by the sharp trailing edge on the NACA63818 section and therefore greater lift. This can be seen in Figure 36(a), where there is a reduced pressure at the trailing edge in the rounded case which, when coupled with the higher leading edge pressure on the suction side, serves to reduce the lift coefficient.

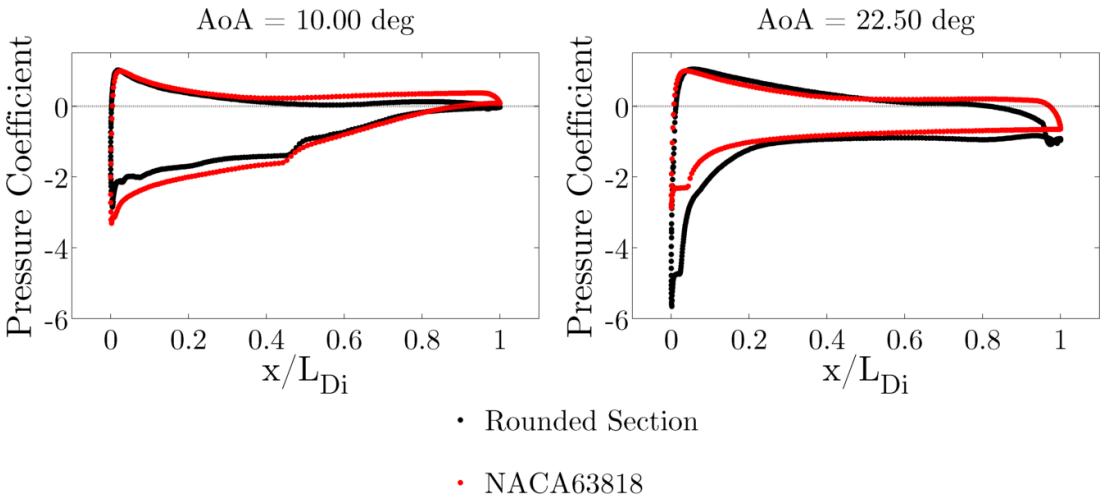


Figure 36: Pressure coefficients around the blade section at $Re_{cU_\infty} = 2.5 \times 10^5$ for angles of attack of (a) 10° and (b) 22.5° for NACA63818 and rounded sections

At high angles of attack, the variation of the trailing edge means that the drag is significantly increased due to the low pressure separated region behind the section. This can clearly be seen in Figure 36(b), where there is low pressure on both blade faces at the rear of the section in the rounded case.

The CFD simulations were conducted at three Reynolds numbers to capture the effects due to the change of relative velocity experienced by the blade during rotation. The results of these analyses can be seen in Figure 37.

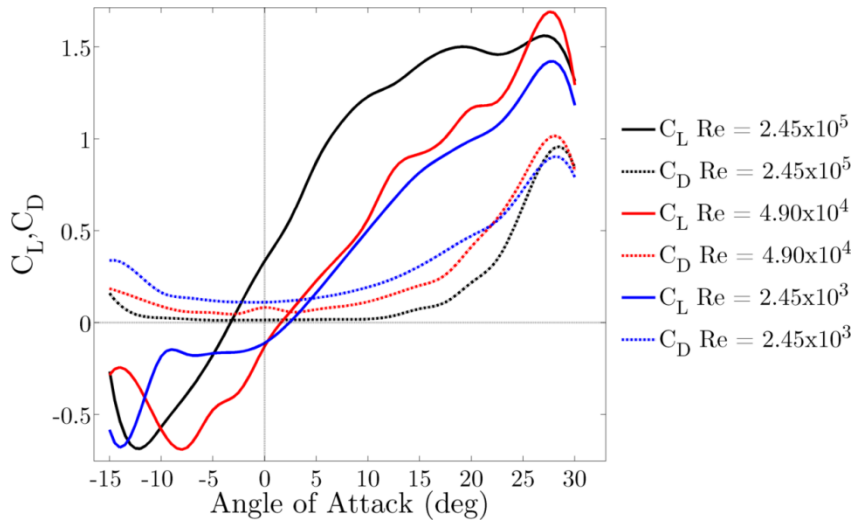


Figure 37: Lift and drag coefficients of the rounded NACA63818 section over the operating range of Reynolds numbers and angles of attack

It is clear from Figure 37 that the NACA6318 profile with the rounded trailing edge has a considerable Reynolds number dependency. This dependency being due

to the pattern of laminar separation on the suction side of the blade and whether there is sufficient energy in the flow to re-attach and form a separation bubble. The pressure coefficient distribution around the section at angles of attack of 10° and 27.5° can be seen in Figure 38.

It can be seen in Figure 38(a) that at the higher Reynolds number and low angles of attack there is a laminar separation bubble which forms at $x/L_{Di} \approx 0.3$ and re-attaches around $x/L_{Di} \approx 0.45$. In the lower Reynolds number cases there is laminar separation and complete detachment from the section and generation of vortex shedding from the rear. This complete detachment and vortex generation leads to a substantially reduced lift and an increased drag. This pattern mirrors one which has been previously detailed by Yarusevych et al. [156] for low Reynolds numbers aerofoil flows such as those for small wind turbines.

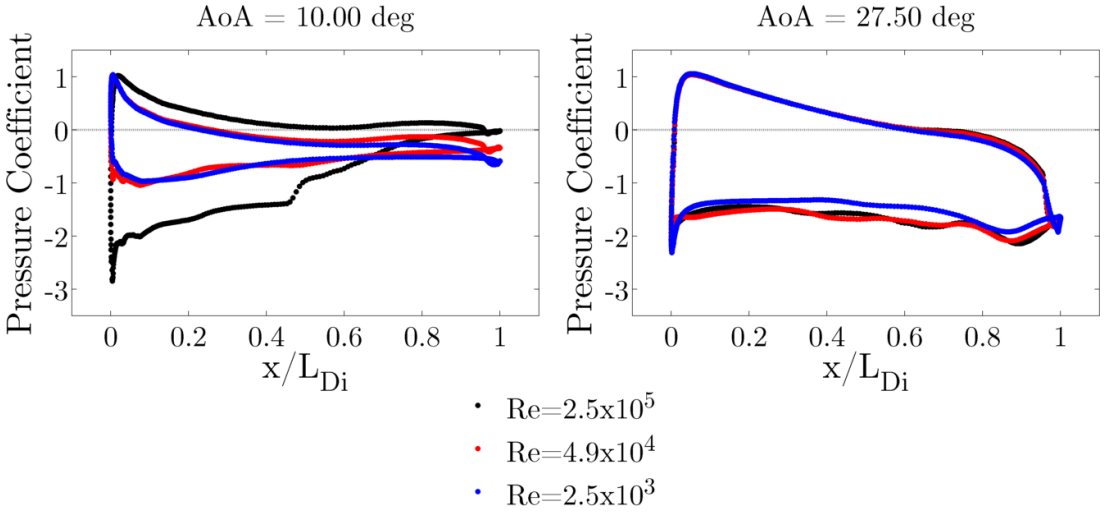


Figure 38: Pressure coefficients around the blade section for a range of Reynolds numbers for angles of attack of (a) 10° and (b) 27.5° for the rounded section

At higher angles of attack the behaviour of the sections becomes much more alike, with separation from close to the leading edge on the suction side as seen in Figure 38(b). This similarity of flow regimes as the angle of attack increases is the reason why at a high angle of attack the lift and drag properties of the section converge. The convergence is as a result of the increasingly complete separation from the section as the angle of attack increases, which by 27.5° is fully developed. The large drag forces are generated by the large low pressure region of recirculating flow to the rear of the blade section.

4.1.3. Ideal Blade Shape

The blade design for the turbine was initiated from an assessment of the ideal blade shape as given by Manwell et al. [43]. For an ideal bare rotor with wake swirl, the optimum angle of relative flow and the optimum chord distribution are given by Equation 11 and Equation 12 respectively. The value of C_L used here is that which corresponds to the angle of attack at which the ratio F_Q/F_N is the highest.

$$\varphi = \left(\frac{2}{3}\right)\tan^{-1}\left(\frac{1}{\lambda_r}\right) \qquad \text{Equation 77}$$

$$c = \frac{8\pi r}{BC_L}(1-\cos\varphi) \qquad \text{Equation 78}$$

Using Equation 11 and Equation 12, the design tip speed ratio of 4, a three bladed geometry and the lift and drag data for the NACA63818 airfoil, the ideal distributions of the local relative flow angle, angle of attack and the chord length can be found, which are displayed in Figure 39.

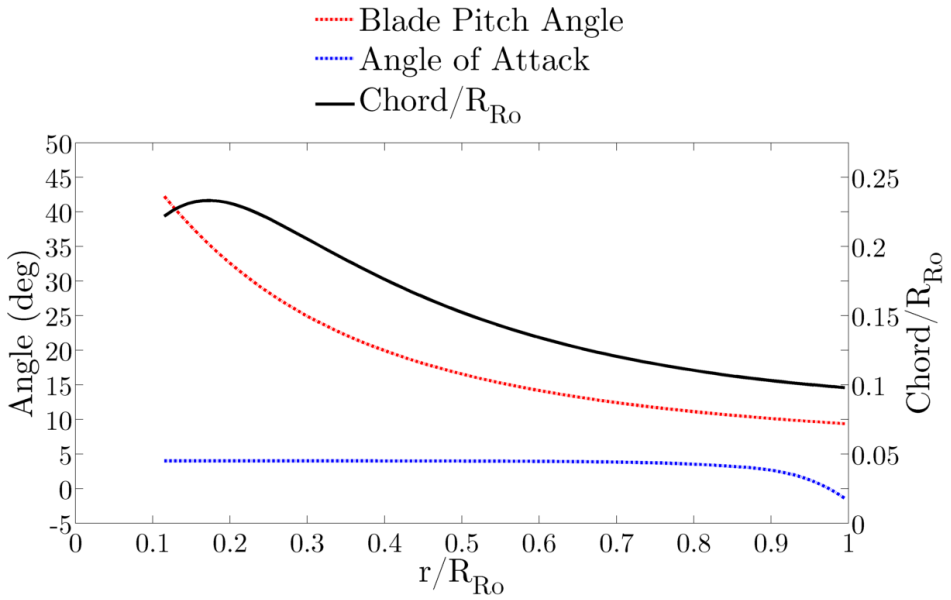


Figure 39: Ideal distributions of the relative flow angle, angle of attack and normalised chord length for a rotor designed for a tip speed ratio of 4

The distributions show the variations in the ideal shape are non-linear along the blade length and that both geometrical properties decrease asymptotically towards the blade tip. These results would be expected, with a longer chord and higher blade pitch in the root section to exploit the lower relative flow velocities and higher relative flow angles at the blade root. The angle of attack is held constant at the optimum for the section, except where the tip losses dominate.

The performance for the ideal rotor at $Re_{RoU_\infty} = 5.3 \times 10^5$ based on the rotor diameter and freestream velocity can be seen in Figure 40. The ideal blade shape has a peak power coefficient of 0.443 at the design tip speed ratio of 4.

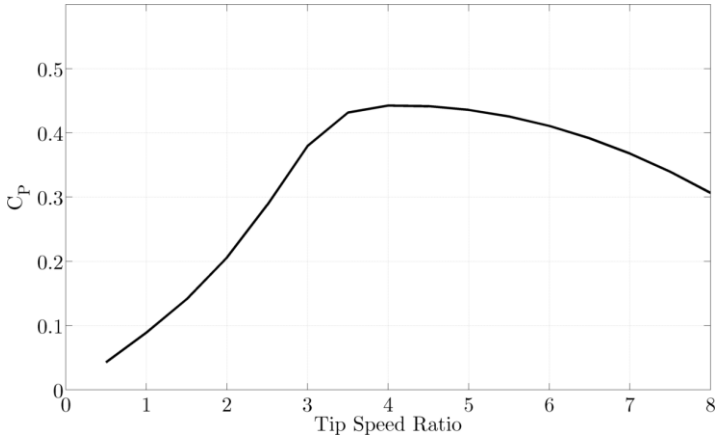


Figure 40: Power coefficient against tip speed ratio for ideal rotor with NACA63818 blades at a Reynolds number of $Re_{RoU_\infty} = 5.3 \times 10^5$ based on the rotor diameter

4.1.4. Designed Blade Shape

In order to simplify the manufacture and subsequent analyses it was decided that the use of a blade with a linear distribution of both blade pitch and chord was preferable. Using the ideal blade shape as a guide, a blade geometry was derived with the blade pitch and chord distributions as seen in Figure 41.

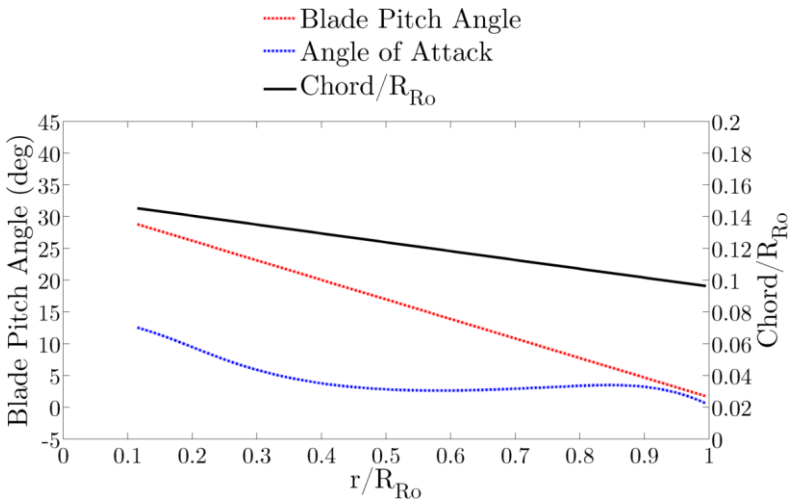


Figure 41: Relative flow angle, angle of attack and normalised chord length for the final blade design with a NACA63818 section at a tip speed ratio of 4

The differences between the blade shapes in the ideal and design cases are evident upon examination of Figure 39 and Figure 41. In the design case, because of

the enforced linearity in the blade pitch distribution, the angle of attack varies along the blade, whereas in the ideal case the angle of attack is held constant at the optimum condition. This variation in the angle of attack away from the optimum means that the performance of the rotor will be inhibited. The performance curve of the ideal blade rotor and the design case rotor can be seen in Figure 40 and Figure 42 respectively. The ideal blade shape has a power coefficient of 0.443 at the design tip speed ratio of 4. The design case has a power coefficient of 0.394. The effect of the reduced lift at low angles of attack relative to the NACA63818 section, as seen in Figure 35, causes a reduction in the peak power coefficient by 11.1%. The increase in drag can be seen to significantly degrade the performance of the rotor at high tip speed ratios, where the relative velocity and therefore drag force is highest.

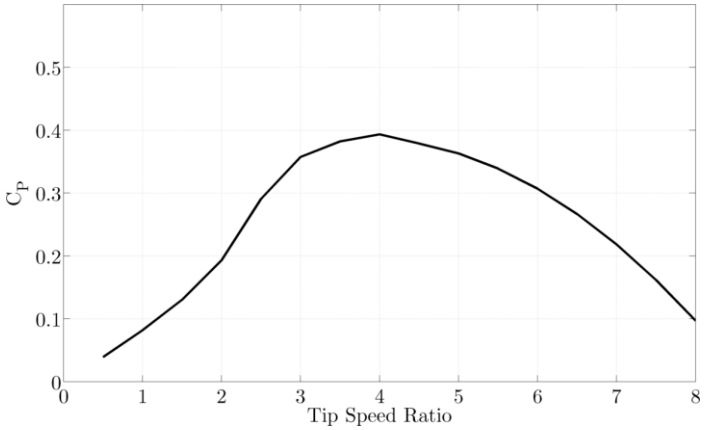


Figure 42: Power coefficient against tip speed ratio for design rotor with NACA63818 blades at $Re_{RoU_\infty} = 5.3 \times 10^5$

4.1.5. Power Output of the Bare Rotors

When the shape of the rounded NACA63818 blade sections used on the experimental rig and detailed in Section 4.1.2 is taken into account, the performance of the rotor is altered. The performance curves for the rotor at zero pitch and with the pitch angle reduced by 5° can be seen in Figure 43. The increases in the drag coefficient have reduced the performance of the rotor over the range of tip speed ratios. The range of tip speed ratios over which the rotor can generate power has been reduced and the power output at all operating points has also been reduced. These rotors perform well given the limitations of the blade section used for their construction and are representative of horizontal axis turbine physics. The use of these rotors to investigate the properties of diffuser augmented turbines and the interaction of the diffuser and the rotor will produce representative results.

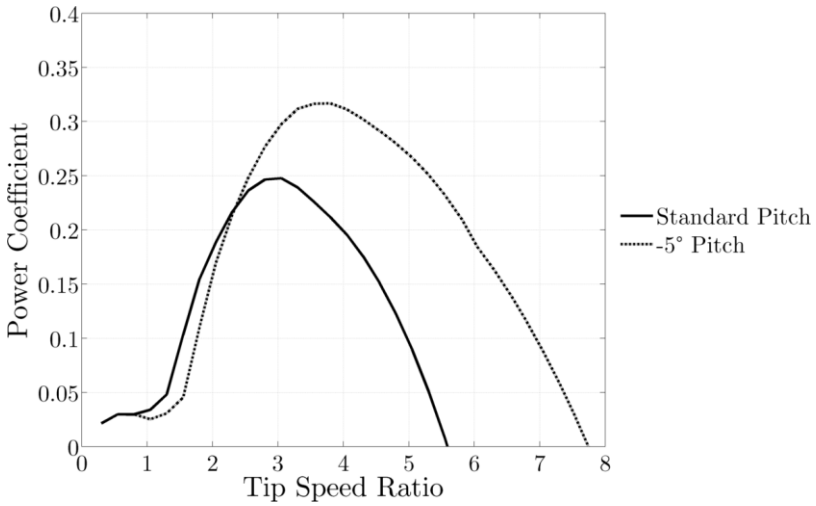


Figure 43: Power coefficient against tip speed ratio for the rounded NACA63818 rotor blades at the two tested pitch angles

4.2. Experimental Diffuser Geometry Design

The geometry optimisation routine detailed in Section 3.3 was iterated to generate the diffuser geometry used within this thesis. In this section the model's assumptions are justified, the convergence and accuracy of results are analysed and the final output geometry used for further investigation is detailed.

4.2.1. Effect of the Tip Gap Jet

The effect of the tip gap jet on the performance of a diffuser augmented turbine was examined through simulation of conical diffusers with uniform actuator disc turbine models at inlet. The cases examined had the same geometries as the ESDU cases used to verify the CFD, the exception being that here the diffusers had no inlet nozzle or tailpipe and were also subject to external flow. The simulation domain can be seen in Figure 44. The geometries are detailed in Section 3.2.6.1.

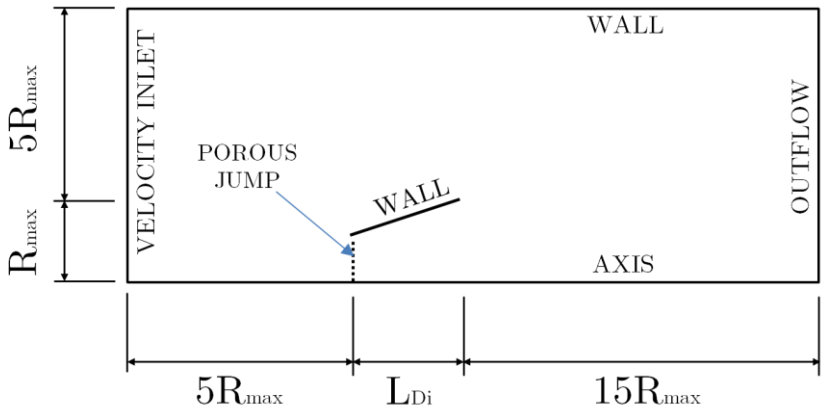


Figure 44: Simulation domain and setup for tip gap jet study

The tip gap was varied by altering the proportion of the diffuser throat which was covered by the porous jump, i.e. a 5% tip gap has 95% of the radial throat distance covered by the porous jump. The porous jump used for the uniform actuator disc was specified as being the same as for the optimisation, as detailed in Section 3.3. Three tip gap sizes were used for this study, no tip gap, 5% and 10% tip gap. The results of these simulations can be seen in Figure 45.

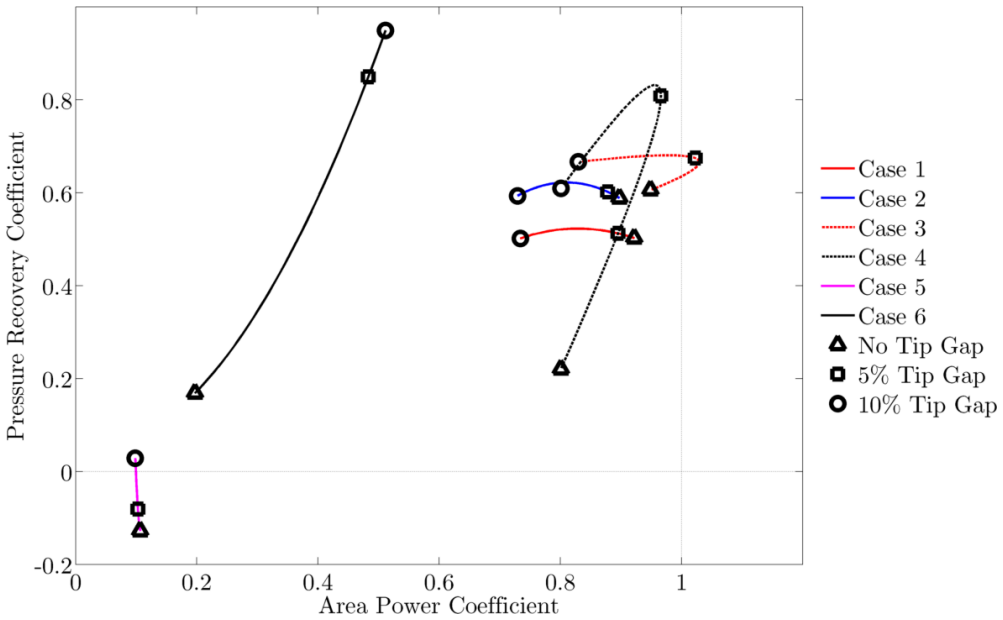


Figure 45: Pressure recovery against area power coefficient for tip gap jet study

The results shown in Figure 45 reveal a great deal about the performance characteristics of diffuser augmented turbines. There are three types of diffuser which can be seen here, low, medium and high angle diffusers. For the low angle diffusers, which are exemplified by Case 1 and Case 2, the inclusion of a tip gap jet flow inhibits augmentation performance. There is no appreciable increase in the pressure recovery caused by the jet as the flow is able to remain attached to the diffuser's inner surface without the additional boundary layer momentum of the tip gap jet. As there is no gain in pressure recovery, there is therefore no potential gain in the power output. In fact, the power output drops as the area of the turbine model is decreased as the mass flow rate through the rotor drops.

For the medium angle diffusers, such as Cases 3 & 4, the tip gap jet effect is significant. The flow is unable to remain attached to the diffuser interior wall without the addition of energy to the boundary layer through the tip gap jet. This means that the pressure recovery and power augmentation performance both increase with a jet of moderate size. In Case 3, as the jet size increases beyond the

critical point the performance is once again inhibited by both the reduction of the rotor area and the fact that the separation from the diffuser wall has already been fully suppressed. In Case 4, the pressure recovery performance is also inhibited by the enlargement of the tip gap jet beyond the critical point as the velocity of the jet relative to the bulk flow is reduced. This reduction in the jet's relative energy causes the flow to begin to separate again towards the rear of the diffuser.

With the high angle diffusers, there are two flow regimes. In the less extreme Case 6, the tip gap jet is demonstrably very effective at increasing both the pressure recovery and the power augmentation. This is due to the momentum increase in the boundary layer which is increasingly effective as the size of the tip gap jet grows up to 10% and is able to move the separation point further along the diffuser interior wall in the streamwise direction. In Case 5, the tip gap jet is ineffective due to the jet separating from the wall very early and blowing into the diffuser's interior. This combination of the minor pressure recovery improvement and the reduction in rotor area means that the power output is reduced by the presence of the jet.

It can be seen from Figure 45 that there is only limited correlation between the pressure recovery performance of the device and the area power coefficient, with the best diffusing device not necessarily being the best at power augmentation. It can be concluded however that a for a conical diffuser with no inlet swirl and a constant pressure loss across the throat the performance is best with a moderate wall angle and a tip gap jet of around 5% of the throat radius.

4.2.2. Convergence of the Optimisation Routine

The optimisation routine started with 250 geometries defined by the Latin Hypercube experimental design. The routine converged within a further 23 CFD simulations. The results for the area power coefficients can be seen against the pressure recovery coefficients for those devices in Figure 46. The strength of the optimisation methodology in preventing further poor quality simulations after the initial generation is visible in these results. The optimisation is therefore able to accurately predict the locations within the design space at which there are high quality geometries. The ability to rule out large parts of the design space allows improved rates of convergence over routines which do not employ a metamodel.

The speed of convergence of the optimisation routine could be due to a number of factors. It has been noted that the spacing and locations of the initial

generation of points affects the error of a sample point [151]. The genetic algorithm's efficiency will also affect the performance of the algorithm. There is also however an element of chance within the speed of convergence due to the random nature of both the initial geometry sampling methodology and the progression of the genetic algorithm. Since the error in a Kriging model is heavily tied to the distance of an unknown point from the nearest known points, the predictions will be better if the initial sample point falls closer to the optimum. This improved prediction means that fewer points will have to be evaluated before the routine converges.

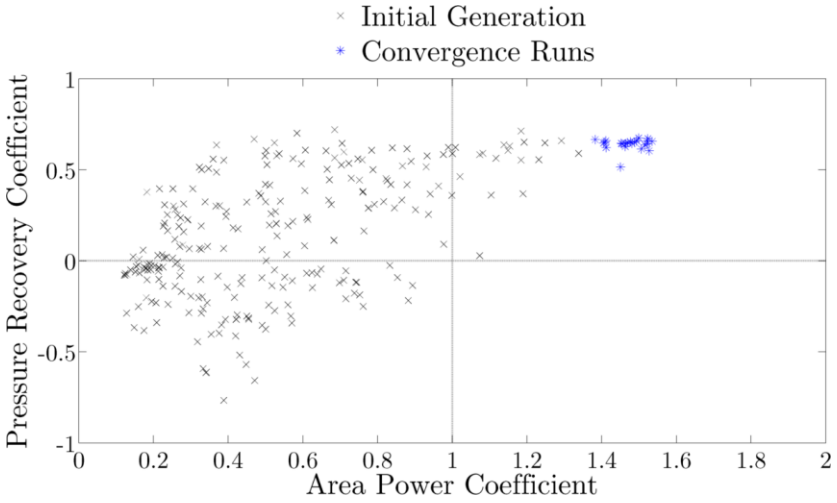


Figure 46: Area power coefficient against pressure recovery coefficient for the optimisation simulations with the diffuser inlet at the duct minimum diameter

The pressure recovery in some cases is below zero due to the shape of the diffuser. Where there is limited or negative expansion in the streamwise direction, a low or negative pressure recovery coefficient can exist due to the lack of diffusion. It is evident that there is a relationship between the area power coefficient and the pressure recovery coefficient. The best performing devices tend to have a high pressure recovery coefficient and a low total pressure loss. Figure 47 shows the diffuser efficiency against the area power coefficient. The trend for higher performance at higher diffuser efficiency, i.e. at a high pressure recovery coefficient and a low total pressure loss coefficient, leads to the conclusion that the performance of a diffuser augmented device is correlated to the efficiency of diffusion.

The final geometry output from the optimisation routine can be seen in Figure 48. As can be seen, the optimisation routine has produced a diffusing duct shape which also has an inlet nozzle. The is due to the optimisation routine compensating for the lack of a specified inlet geometry, minimising the losses which would

otherwise occur due to separation from the leading edge of the duct. It can also be seen that the optimisation has maximised the size of the duct within the computational domain, with both the maximum possible axial and radial sizes which were specified as boundary conditions for the optimisation routine.

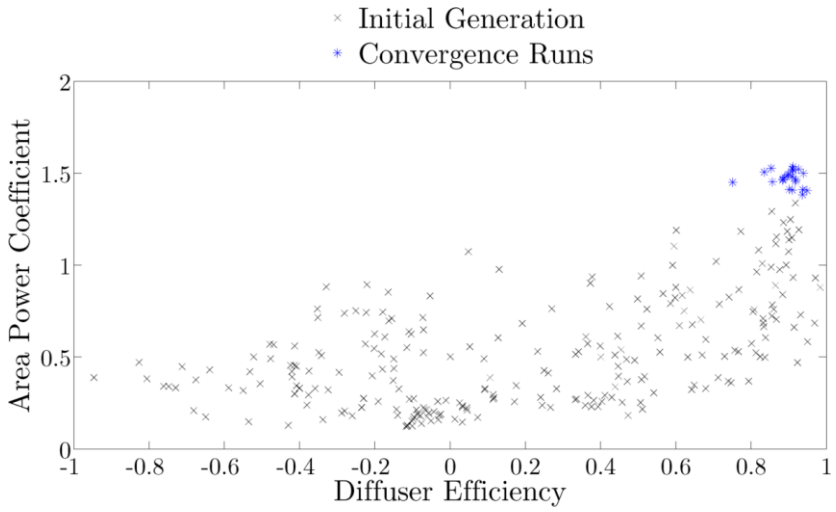


Figure 47: Diffuser efficiency against the area power coefficient for the optimisation simulations with the diffuser inlet at the duct minimum internal diameter

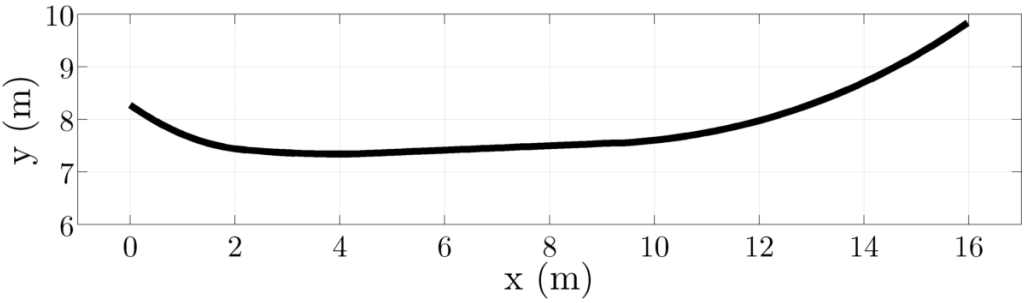


Figure 48: Final NURBS output geometry from the optimisation routine

The final output diffuser geometry from the optimisation, as seen in Figure 48, when combined with a uniform actuator disc turbine model with a tip gap of 5% of the diffuser throat radius, has an area power coefficient of 1.535 and a pressure recovery coefficient of 0.511 (0.744 when defined from the point of maximum contraction) under the optimisation flow conditions. The power coefficient based on the duct outer area is 0.691 at a thrust coefficient of 0.986. As can be seen from Figure 49, the high performance is as a result of the duct shape coupled with the tip gap jet suppressing almost all separation from the diffuser wall. This, in addition to the inlet contraction acting to suppress any separation from the diffuser inlet mean that the device is highly efficient and is able to recover more pressure and increase

the flow velocity at the rotor plane. This design is however idealised due to the zero thickness geometry and the use of a uniform actuator disc turbine model.

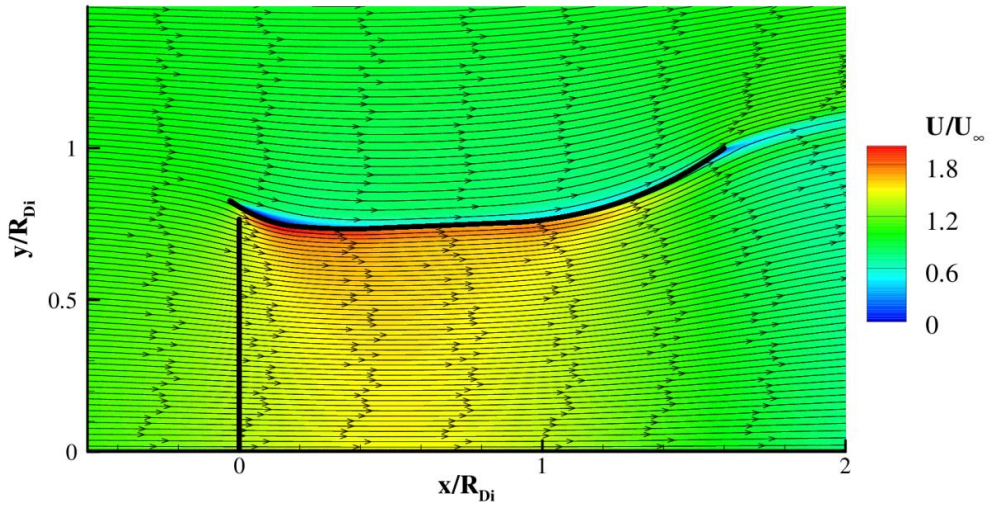


Figure 49: Velocity contours and streamtraces for final NURBS output geometry from the optimisation routine at $Re_{DiU_\infty} = 3.4 \times 10^7$

4.2.3. Diffuser Geometry Definition

Once the geometry from the optimisation run had been finalised it was necessary to make amendments in order to make the device three dimensional, easily manufactured and to remove some of the simplifications made in the optimisation routine. In order to achieve this, the duct was moved axially forward such that the turbine was situated at the throat of the duct. The exterior surface of the duct was generated by taking a line axially in the streamwise direction from the NURBS duct's leading edge, rounding the leading edge and blending this with a curve at the rear. The curvature of the rear section was specified to maintain a smooth thickness distribution along the rear part of the duct. The leading and trailing edges of the duct were then rounded. A cross-section of the geometry which was used for experimental testing can be seen in Figure 50.

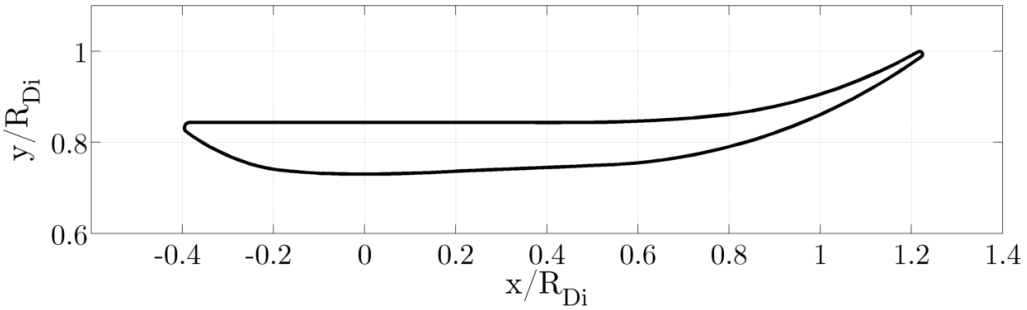


Figure 50: Cross-section of the final experimental diffuser shape

When combined with a uniform actuator disc turbine model with a tip gap of 5% of the diffuser throat radius, this geometry has a power coefficient based on the duct outer area of 0.612 and a pressure recovery coefficient of 0.659 at a Reynolds number, based on the diffuser throat diameter and freestream flow velocity, of $Re_{DiU_\infty} = 3.6 \times 10^7$ and a thrust coefficient of 0.890. The diffuser flow under these conditions can be seen in Figure 51 along with velocity contours and streamlines.

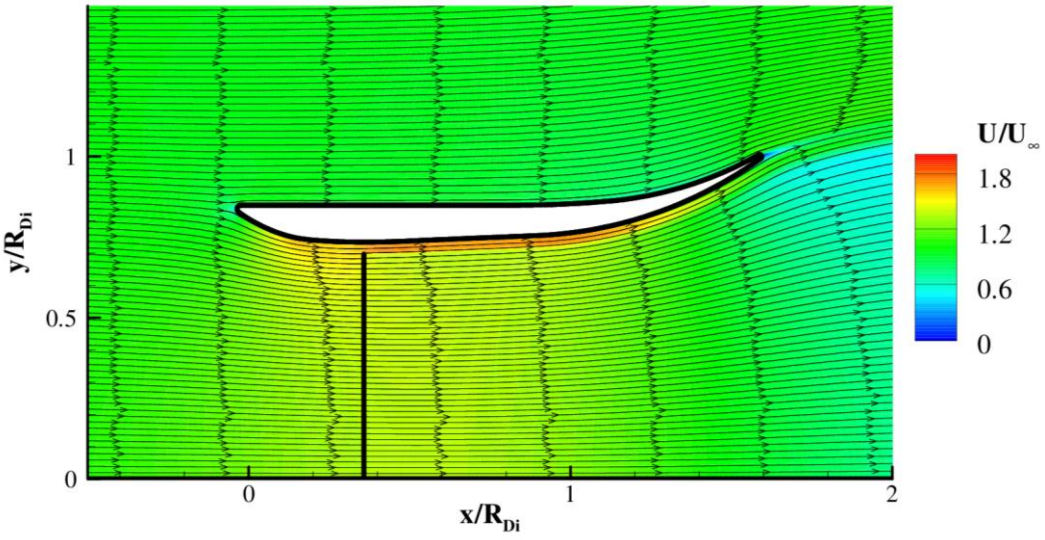


Figure 51: Velocity contours and streamtraces for experimentally tested diffuser at $Re_{DiU_\infty} = 3.6 \times 10^7$

It can be seen that there is a change in the flow structure between the optimisation output device as seen in Figure 49, and the tested diffuser shape as seen in Figure 51. The main cause of this variation is the reduction of the "lift" force generated by the geometry. The loss of lift means that the swallowing capacity, the ability of the duct to draw flow in towards the turbine, is reduced, which in turn reduces the mass flow rate through the rotor plane and the available power.

The loss of lift is caused by the reduction of the streamline curvature caused by the duct and the associated increase in the interior pressure and drop in the exterior pressure as can be seen in Figure 38. This drop in pressure on the exterior of the duct reduces the pressure differential across the duct wall and means that less flow is drawn through the duct. This change in pressure distribution can be seen in Figure 52. The reduction in the pressure recovery of the device with the experimental geometry is due to the loss of lift associated with the change of geometry. The pressures in the diffuser throat are lower in the NURBS geometry

however as the pressures at the exit are almost the same in both cases, the pressure recovery is higher in the NURBS case despite the dynamic pressure being higher.

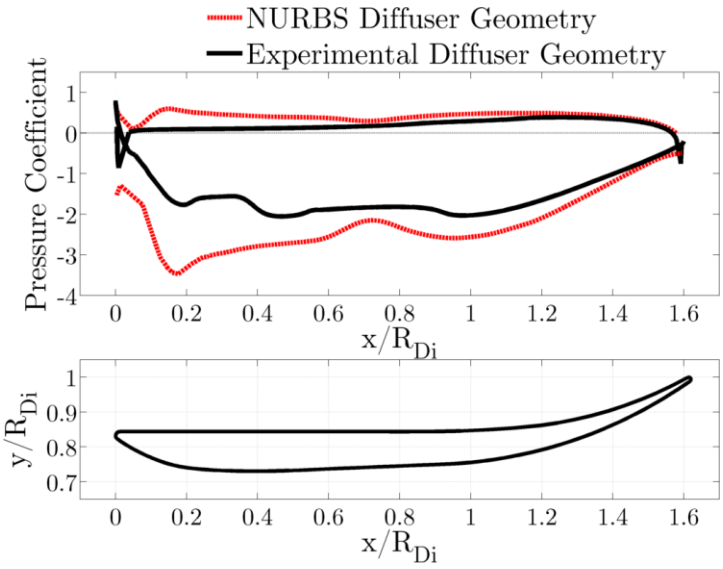


Figure 52: Pressure coefficients around the diffuser for the NURBS geometry and the experimental diffuser geometry

The necessity to make a workable 3D design for the diffuser means that there will be some degree of loss of lift in order to facilitate this. The design here is provides a high efficiency diffuser which is suitable for the experimental work.

4.3. Effect of the Reynolds Number

The impact of the Reynolds number on the power output of a diffuser augmented turbine was examined using both the uniform actuator disc turbine model and the blade element actuator disc model. This enabled the quantification of the Reynolds number effects on a device and allows for the comparison of responses between the two turbine models. In order to increase the applicability of the results to a real device, the geometry of the hub is now included within the computations. The hub used has a radius of y/R=0.20 and a length of x/R=1.5. The geometry used for the assessment of the Reynolds number effects can be seen in Figure 53.

The analyses were conducted in the range $2.0 \times 10^3 < Re_{DiU_\infty} < 1.0 \times 10^7$, which covers the Reynolds numbers for both full scale tidal device operation and also model scale. The Reynolds number was calculated based upon the diffuser throat diameter and the diffuser throat area averaged velocity. The power coefficients resulting from both turbine models can be seen plotted against the Reynolds number in Figure 54.

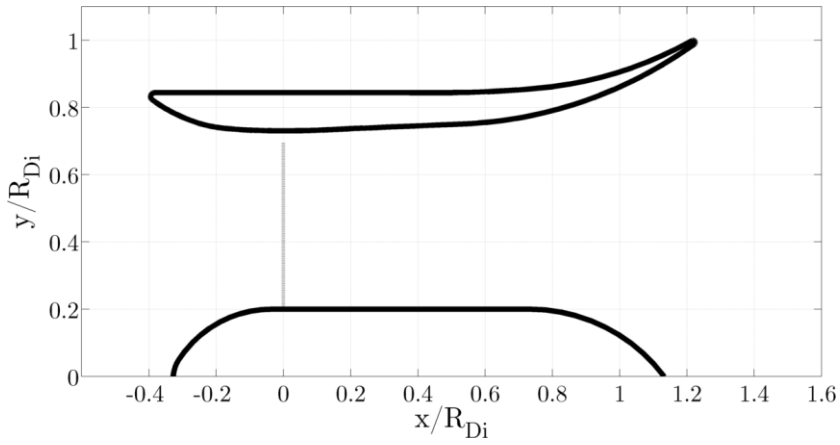


Figure 53: Diffuser and hub geometry in the Reynolds number sensitivity studies

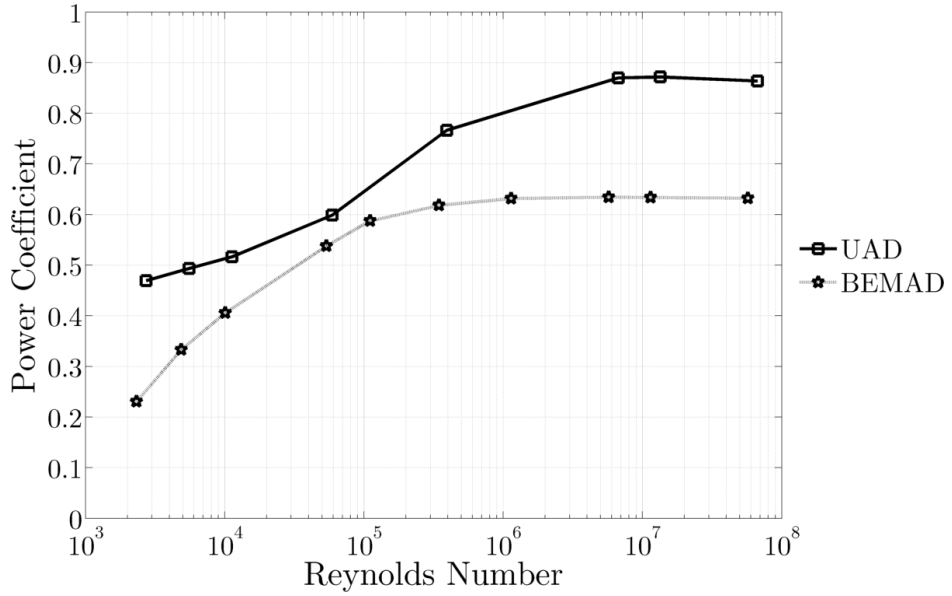


Figure 54: Power coefficient against Reynolds number for both the UAD and BEMAD turbine models

It is evident from Figure 54 that each turbine model responds differently to the Reynolds number. The blade element actuator disc model, the more complete of the two, predicts a response where there is low performance at low Reynolds numbers, which increases with Reynolds number and is more or less constant by $Re_{DiU_\infty} \approx 3.0 \times 10^5$ and has a static value by $Re_{DiU_\infty} \approx 1.0 \times 10^6$. The uniform actuator disc model predicts a more complex response which is highly dependent upon the Reynolds number.

It is clear from Figure 54 that the absolute value of the power output and the trends in the power output predicted by the uniform actuator disc and the blade element actuator disc models differ greatly. The absolute value of the power

coefficient is consistently lower in the blade element actuator disc cases than the uniform actuator disc cases due to simplifying assumptions made in the calculation of the power coefficient for the UAD cases. The power coefficient is calculated for the blade element actuator disc as detailed in Section 3.1.4.2 and for the uniform actuator disc as in Section 3.2.4.1. It is clear that assuming that the entirety of the total pressure drop across the rotor plane is converted to a work output in the uniform actuator disc model is highly idealised. The accurate assessment of the likely loses in the flow and the efficiency of energy conversion are problematic and would be difficult to predict from the flow field calculated by the CFD as it is markedly different from that which would be obtained from a real turbine as can be seen from Figure 55 and Figure 56.

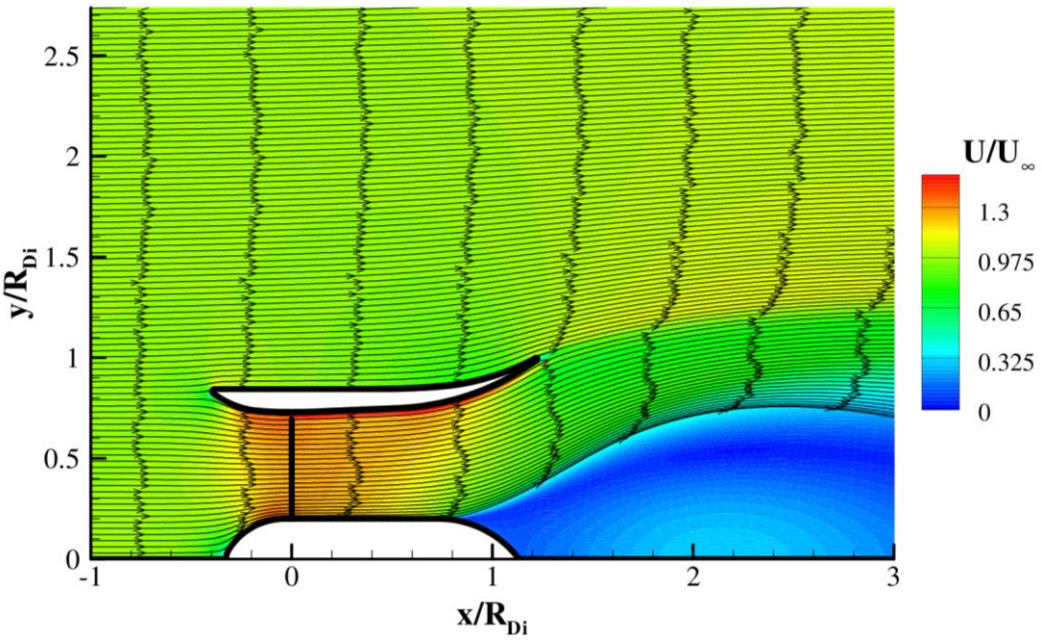


Figure 55: Velocity contours and streamtraces for UAD model at $Re_{DiU_\infty} = 1.3 \times 10^7$

It is evident from Figure 55 and Figure 56 that the flow structure differs greatly between the uniform actuator disc and blade element actuator disc cases. The primary difference is caused by the inclusion of flow swirl in the blade element model, which induces a vortex in the rear of the diffuser.

A vortex can be defined by one of a number of vortex models, with the Rankine and Lamb-Oseen vortex models being amongst the most common [157]. The Rankine vortex model assumes an instantaneous break between the rotational core part of the vortex and the irrotational outer part of the vortex. The more complete Lamb-Oseen vortex model, described by Equation 79, removes this

singularity and more accurately predicts the interface between the two regions. The value used here for ϖ is 1.25643, as suggested by Devenport et al. [158].

$$U_\theta(r) = U_{\theta_c}\frac{r_c}{r}\left(1+\frac{1}{2\varpi}\right)\left[1-\exp\left(-\varpi\frac{r^2}{{r_c}^2}\right)\right] \qquad \text{Equation 79}$$

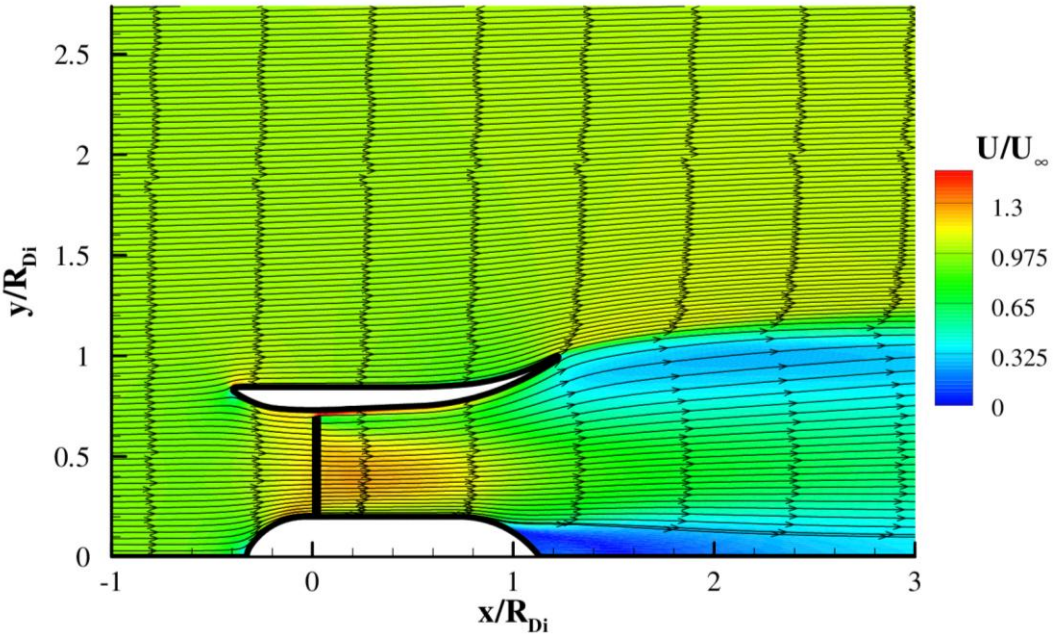


Figure 56: Velocity contours and streamtraces for BEMAD model at a Reynolds number of $Re_{DiU_\infty} = 1.1 \times 10^7$

When the outflow swirl profile from the blade element actuator disc model diffuser is plotted against the equivalent Lamb-Oseen vortex, as seen in Figure 57, it is evident that there is a close match in the core region which breaks down as the radial distance is increased. This breakdown in the matching is due to two factors, the constrained radial distance due to the diffuser interior wall and the forcing influence of the rotor on the flow. In the idealised model, the flow outside of the diffuser would also be free to rotate with the vortex, however in the diffuser case the rotational energy is localised to the flow within the diffuser. The more significant effect however is due to rotational forcing by the rotor, where swirl is induced along the length of the blade as opposed to emanating from a central point as is assumed in the Lamb-Oseen model. This forcing means that the outer part of the vortex can no longer be considered to be purely irrotational and so will have a higher swirl velocity than the Lamb-Oseen model predicts. The effect of the rotor (radius of $r/r_c \approx 8$) can be seen clearly in Figure 57, where the swirl drops off rapidly beyond this critical radius.

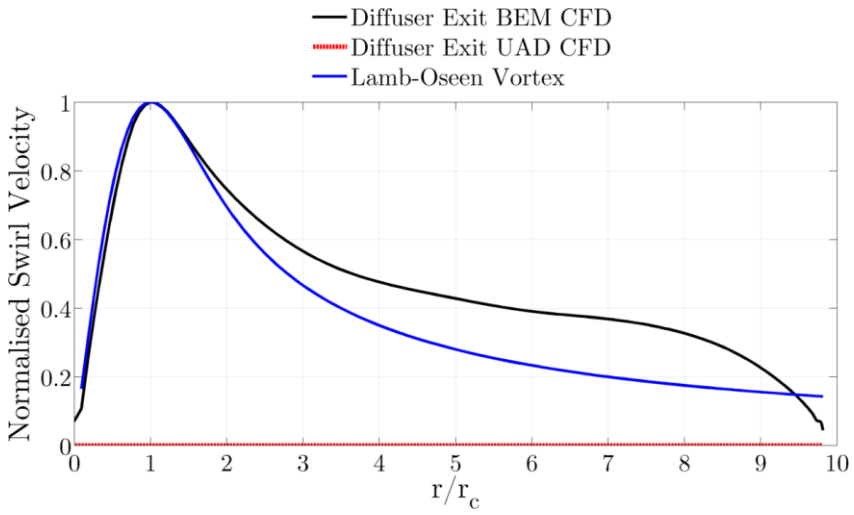


Figure 57: Comparison of diffuser exit swirl profile from CFD models at a Reynolds number of $Re_{DiU_\infty} = 1.1 \times 10^6$ with the equivalent Lamb-Oseen vortex

The response of the uniform actuator disc model to the Reynolds number is caused by two main factors which vary with the Reynolds number, the strength of the tip gap jet and the extent of the flow attachment to the hub. The blade element actuator disc model's response to the Reynolds number is driven by the tip gap jet flow and the blade section lift and drag data.

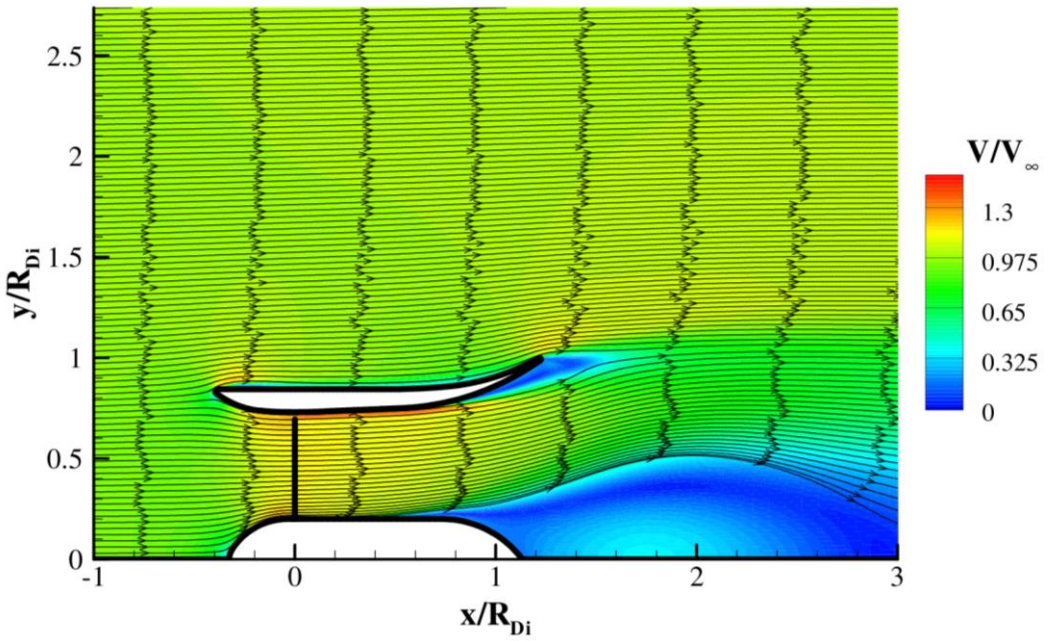


Figure 58: Velocity contours and streamtraces for UAD model at $Re_{DiU_\infty} = 1.0 \times 10^4$

The strength of the tip gap jet varies with the Reynolds number as it is influenced by the boundary layer thickness in the gap between the turbine tip radius

and the diffuser wall. With a higher blockage of the gap, the energy in the jet is reduced, meaning that the flow separates from the interior of the diffuser due to insufficient momentum transfer to the boundary layer in the rear of the diffuser, as can be seen in Figure 58 and Figure 59 for the UAD and BEMAD cases respectively.

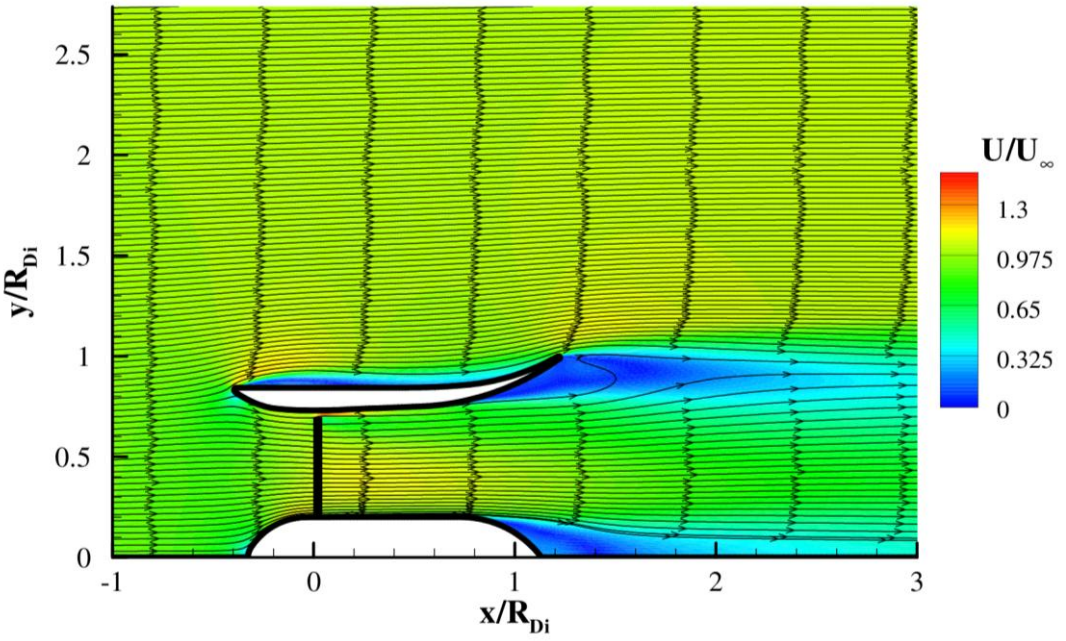


Figure 59: Velocity contours and streamtraces for BEMAD model at a Reynolds number of $Re_{DiU_\infty} = 1.3 \times 10^4$

The thickness of the boundary layer, and therefore the blockage of the gap, is dependent upon the state of the boundary layer at the turbine plane. The thickness of the boundary layer at the turbine plane for the uniform actuator disc cases can be seen in Figure 60. At lower Reynolds numbers the boundary layer is laminar at the turbine plane and blocks up to 25% of the tip gap. As the Reynolds number increases the laminar boundary layer reduces in thickness and the blockage effect is reduced, diffusion increases and therefore the power output increases. Once transition to a turbulent boundary layer occurs at Reynolds numbers of around $Re_{DiU_\infty} = 1.5 \times 10^6$ the boundary layer remains thin at the turbine plane.

The levelling of the power output from the BEMAD cases is largely dependent upon the blade section characteristics and the Reynolds numbers at which these are provided. The data provided to the model here is such that by a Reynolds number of $Re_{DiU_\infty} = 1.0 \times 10^6$ all sections will be utilising the same lift and drag curves.

The uniform actuator disc response follows a different trend to the blade element actuator disc as the flow also has a tendency to separate from the hub as a result of the more adverse pressure gradient along the hub surface due to the lack of a trailing vortex. At low Reynolds numbers the device suffers from separation from the hub surface, which causes a significant reduction of the volume available for diffusion and hence the power output. As the Reynolds number increases this separation reduces as the separation point moves further towards the rear of the hub. By $Re_{DiU_\infty} = 5.7 \times 10^6$ the flow is able to remain attached to the full length of the hub and the power coefficient is unchanged beyond his point.

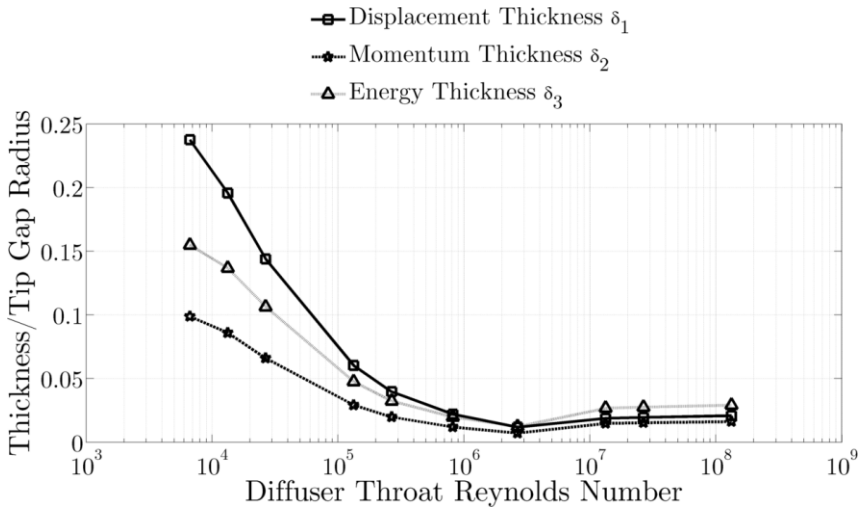


Figure 60: Boundary layer thickness in the tip gap for the BEMAD cases

Given the propensity of the uniform actuator model to predict a flow structure which is so different from that of a real turbine, the accurate prediction of the power output using the uniform actuator model cannot be achieved. It is therefore recommended that the assessment of the diffuser performance is only undertaken with the use of representative rotor modelling, whether that is a blade element actuator disc or a fully resolved 3D model.

The reaction of the blade element actuator disc to the Reynolds number indicates that the flow structure remains very similar at Reynolds numbers above $Re_{DiU_\infty} = 3.4 \times 10^5$ and is almost unchanged above $Re_{DiU_\infty} = 1.1 \times 10^6$. In reality there may be changes at higher Reynolds numbers since the BEM CFD input data stops for a Reynolds number based on the blade chord of $Re_{cU_\infty} = 2.5 \times 10^5$. Any changes above this Reynolds number would be likely to happen more gradually however as the majority of transition effects have occurred by this Reynolds number.

The importance of these findings are that it is therefore acceptable to test a device at the model scale and still be able to accurately replicate the flow dynamics which are found in a full scale device. This is particularly important for tidal stream devices, where full scale Reynolds numbers can be of the order of 10^7 or 10^8.

4.4. Effect of the Hub Geometry

In order to adapt the geometry derived from the optimisation routine to one which was more representative of a real device and therefore suitable for further development it was necessary to include the hub geometry.

4.4.1. Effect of the Hub Shape

In order to understand both the effect of modelling methods and the effect of the hub geometry, a range of hub geometries were examined using the experimental diffuser geometry and both the uniform actuator disc and blade element actuator disc turbine models. The hub shapes tested in this study can be seen in Figure 61. The hub geometries, all of which have a hub radius of y/R = 0.2, were derived to attempt to suppress hub separation. Preliminary investigations of the flow field using the UAD model and hub 1 indicated that there was separation from the hub surface at x/r ≈ 0.6 as can be seen in Figure 62. As a result of this perceived separation issue, hub geometries which expanded in the streamwise direction with a variety of end shapes were investigated. In addition a hub with a flat end was trialled to investigate the effect of a dump hub on the power output, similar in conception to the dump/exit flanges detailed in Section 2.4.4.3.

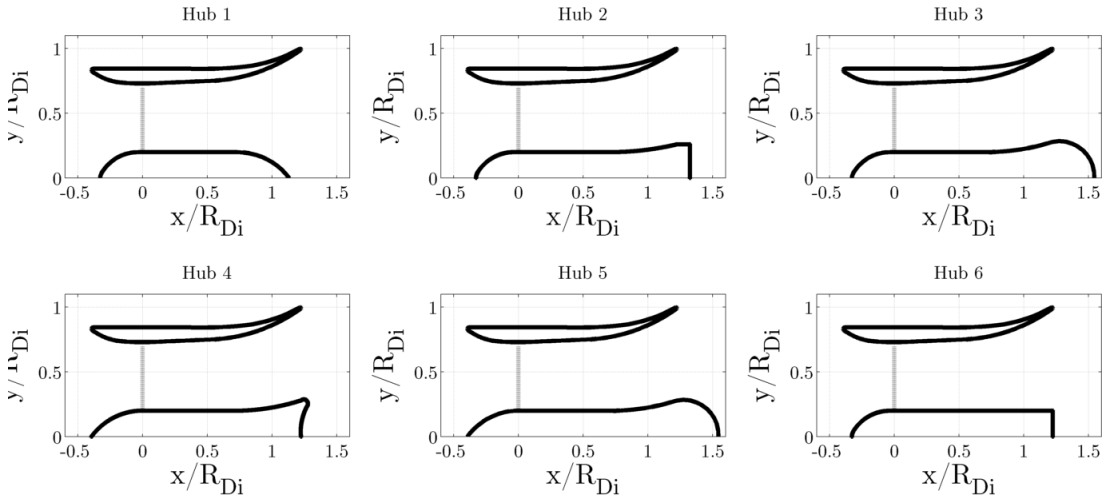


Figure 61: Hub shape geometries examined

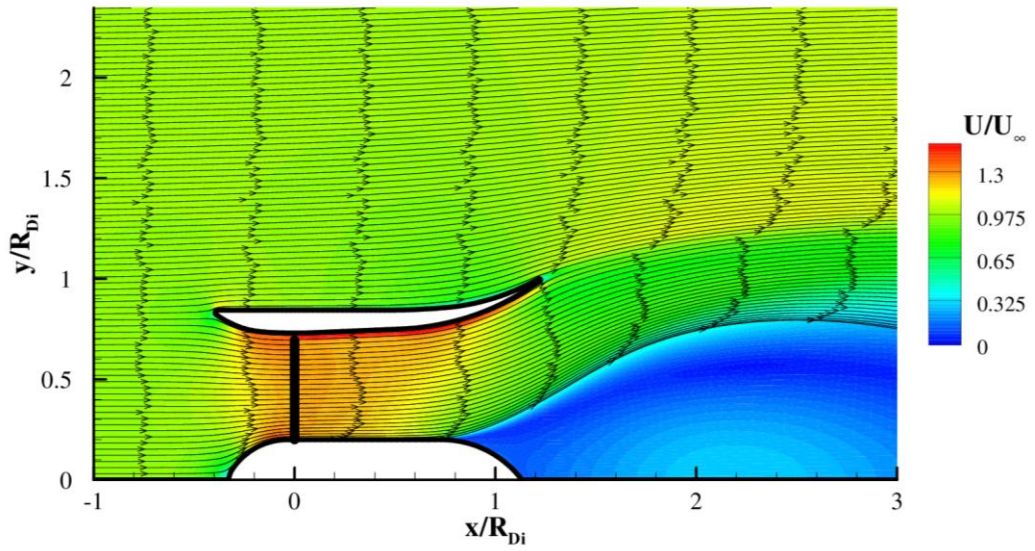


Figure 62: Contours of velocity with streamtraces for hub shape 1 with a uniform actuator disc model at $Re_{DiU_\infty} = 4.1 \times 10^5$ and thrust coefficient of 0.646

The performance of the devices seen in Figure 61 was assessed using both the blade element actuator disc and uniform actuator disc models in order to assess the impact that the modelling assumptions would have on the predictions of the device's power output. The results from the uniform actuator disc and blade element actuator disc models can be seen in Figure 63 and Figure 64 respectively, which show the power, pressure recovery and thrust coefficients for each case.

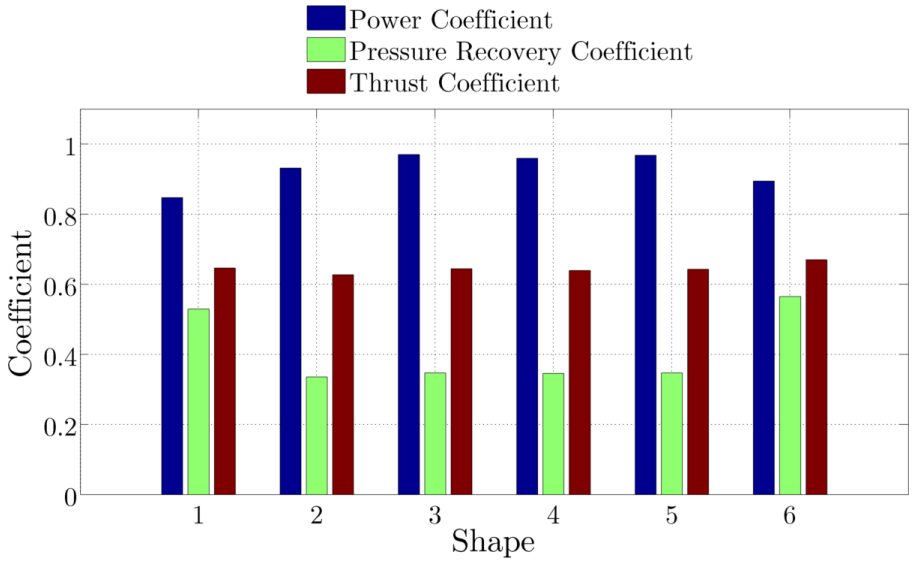


Figure 63: Coefficients for hub geometry cases using the UAD model for thrust coefficient values approximating those of the standard pitch blading at TSR=4

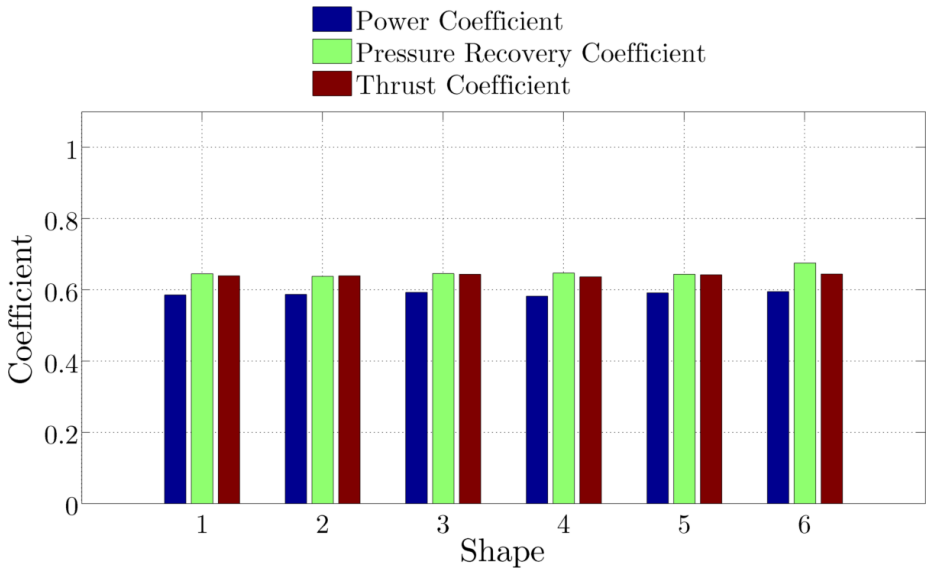


Figure 64: Performance coefficients for hub geometry cases using the BEMAD turbine model and the standard pitch blading at TSR=4

It is evident from Figure 63 and Figure 64 that there are significant differences in the performance of the diffuser augmented devices when using the different turbine models, with large differences in the prediction of the device's pressure recovery and power generation characteristics. These differences are due to the markedly different flow regimes induced in the diffuser by the different turbine models. Normalised velocity contours and streamlines for the blade element actuator disc model for hub shape 1 can be seen in Figure 65.

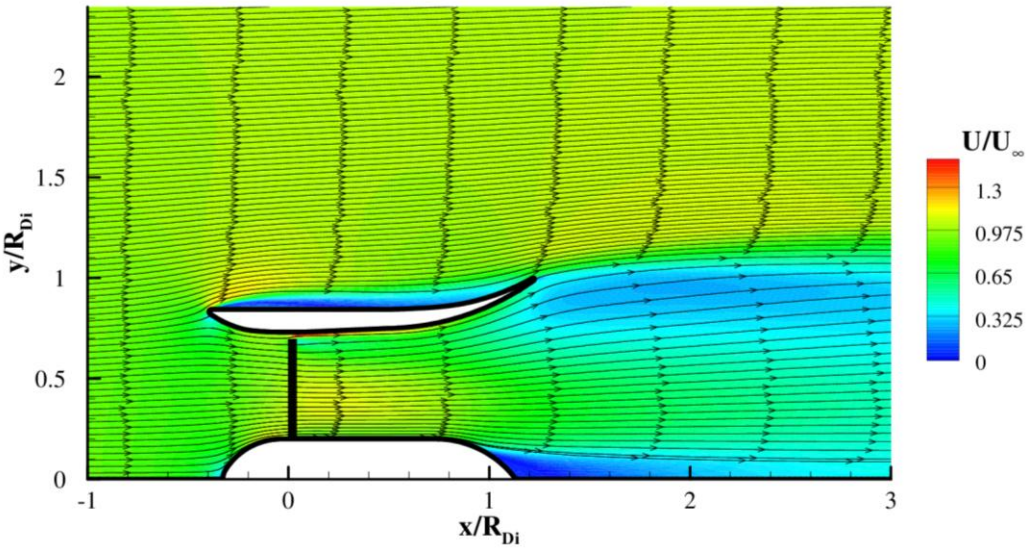


Figure 65: Contours of velocity with streamtraces for hub 1 with a BEMAD model, standard pitch blading at TSR=4, $Re_{DiU_\infty} = 2.8 \times 10^5$ and C_T=0.639

When the blade element flow profile seen in Figure 65 is contrasted with the comparable uniform actuator disc results as seen in Figure 62, it is evident that the swirl is having a significant impact upon the flow within the diffuser. The flow profile has changed due to the rotor inducing flow swirl in the rear of the diffuser, with a low pressure region behind the rear of the hub, which causes the flow to be drawn into a vortex around the diffuser axis. The absolute velocity in the diffuser throat is also reduced as a result of the inclusion of the blade element actuator disc model, despite both models having almost the same thrust coefficient.

The change in the axial velocity distribution within the diffuser throat as a result of the inclusion of the blade element actuator disc model is due to the thrust distribution in the rotor. In the uniform actuator disc model, where the value $\Delta x_m C_{pj}$ is constant across the blade area, the thrust is related only to the dynamic head of the flow. As a result of the uniform boundary condition there is a tendency towards a more uniform throat velocity. In the blade element actuator disc model, where the thrust is tied to the blade geometry and the section lift and drag properties, the thrust and velocity distribution are non-linear along the blade.

The reduction in the throat velocity with the inclusion of the blade element actuator disc for an identical thrust is due to the inclusion of swirl into the flow. The change of a portion of the flow momentum from purely axial flow to a combined axial and rotational wake means that the axial velocity in the throat must be reduced. This change results in a 36.3% reduction in the average throat velocity when the blade element model replaces the uniform actuator disc model.

This change of the flow profile causes the difference in the pressure recovery performances seen between Figure 63 and Figure 64. The significantly increased pressure recovery seen in the BEMAD cases is due to the flow's ability to remain attached to both the hub and wall geometries and so to expand. This is further aided by the lower throat velocity and the resulting lower dynamic pressure by which the static pressure rise is normalised. There is a marked difference in the pressure recovery performance of the devices relative to one another. In the BEMAD cases, the hub shape is seen to have relatively little impact upon the pressure recovery performances of the devices, with a maximum difference of 5.8% in the pressure recovery coefficient, as opposed to 62.9% in the UAD cases. In the UAD cases, the geometries with the streamwise hub expansion fair poorly compared to those without, due to a tendency for the flow to follow the hub geometry and

separate from the diffuser wall. This preference for diffuser wall separation means that the effective area ratio is smaller and there is a reduced potential for diffusion.

The trend seen in the pressure recovery coefficient is also seen in the power coefficient, with the blade element actuator disc model cases being within a much narrower envelope, with a maximum difference of 1.6% in the power coefficient as opposed to 14.5% in the uniform actuator disc model. It can therefore be inferred that the effect of the hub shape upon the power output of the device is limited in the case of the more realistic blade element actuator disc model. This therefore means that the hub shape is not likely to be a significant factor in the performance of a diffuser augmented turbine so long as it does not interfere with the generation of the vortex trailing from the rear of the hub or induce separation from the hub.

The most significant implication of the results is that the uniform actuator disc model greatly over predicts the power output of the diffuser augmented device, with the average difference between the two model cases being a 36.4% reduction in the power coefficient when the BEMAD model replaces the UAD model. This difference in the calculation of the generated power is due to simplifications made in the calculation of the uniform actuator disc power as stated in Section 4.3.

It is evident that if a uniform actuator disc model is used for the design of hub geometry then an incorrect design choice could be made. The overestimation of the power coefficient, omission of the flow swirl and inability to accurately model the pressure recovery coefficient mean that a uniform actuator disc model is insufficient for the modelling of diffuser augmented flows.

4.4.2. Effect of the Hub Size

The second part of the analysis of the hub geometry was to analyse the effect of the hub radius on the power output of the diffuser augmented device. In order to examine these effects two hub sizes were analysed, one with a radius of 8% of the diffuser outer radius, and another of 20%. These sizes were chosen to be representative of existing hub sizes for extant horizontal axis tidal stream devices and to examine the effects of hub blockage respectively. The hub geometry used in the 20% case is that detailed in Section 4.4.1 as hub shape 1. The 8% hub geometry is the same shape with the geometry scaled by a factor of 0.4 in the radial direction.

The analyses were conducted using the standard pitch blading, scaled in the radial direction such that the blade root extends to the hub. The computations were

performed with the blade element actuator disc model over a range of tip speed ratios. The results of the analyses can be seen in Figure 66.

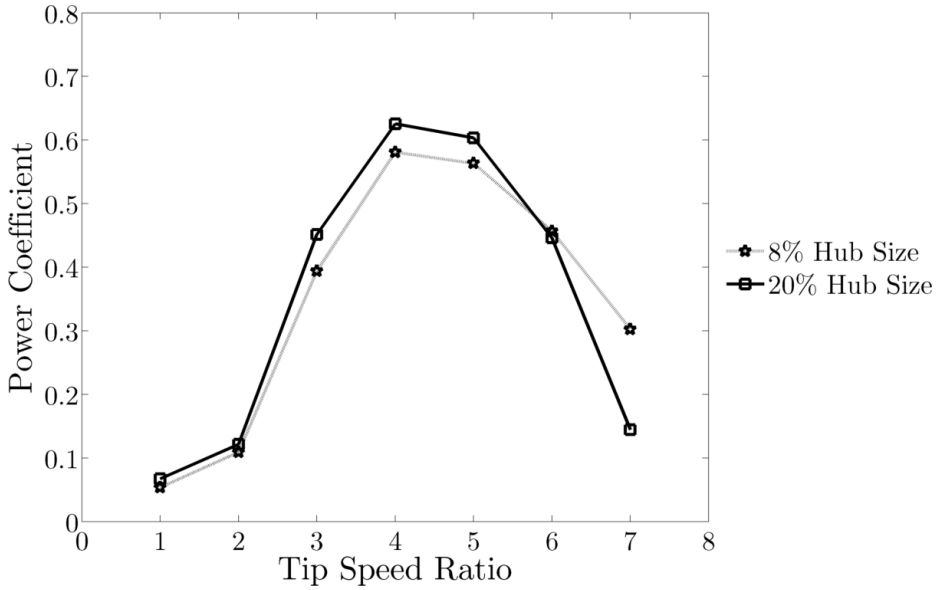


Figure 66: Power coefficient against tip speed ratio for diffuser with 8% and 20% hub sizes and the standard pitch experimental blading

It is evident from Figure 66 that the hub radius has a significant effect upon the power output of a diffuser augmented turbine. Interestingly the larger hub size increases the peak power output of the diffuser augmented device despite the higher throat blockage. The flow through a diffuser with a hub radius of 8% can be seen in Figure 67, which is equivalent to the 20% hub data presented in Figure 65.

It can be seen from Figure 65 and Figure 67 that the presence of the larger hub acts to shift the streamlines radially from the diffuser centreline and increases the throat velocity. The hub size has not increased the thrust within the diffuser throat in a way such that the flow is significantly retarded from the turbine. Although there will be a point at which this retarding would occur, a comparatively large hub, such as the 20% hub seen here, in fact increases the power output of a diffuser augmented device.

This increase in peak power at larger hub radii is due to the hub causing the flow drawn through the diffuser to be shifted radially from the turbine centreline towards the centre of the blades. Due to the higher relative velocities of the flow at greater radii from the centreline, larger forces and therefore torques are generated and a larger amount of power is able to be extracted.

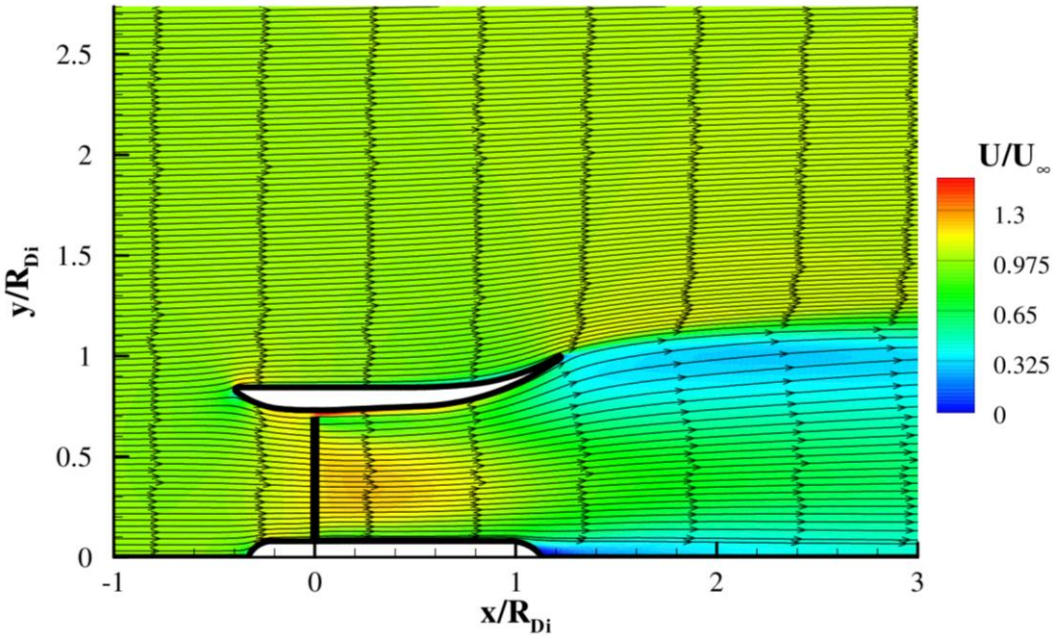


Figure 67: Contours of velocity with streamtraces for 8% hub with a blade element actuator disc turbine model, the standard pitch blading at TSR=4, a Reynolds number of $Re_{DiU_\infty} = 3.4 \times 10^5$ and a thrust coefficient of 0.594

At higher tip speed ratios the performance of the larger 20% hub drops rapidly and falls below that of the 8% hub, due to the increased thrust force which is present. Although at a given tip speed ratio the rotor has nominally the same thrust coefficient for both hub sizes, the hub itself also induces a thrust force on the fluid due to the throat blockage. The larger of the two hubs is therefore more sensitive to increases in the rotor thrust as the throat is blocked to a greater extent than with the smaller hub and the combined thrust of the rotor and hub is greater.

4.4.3. Experimental Hub Geometry

The hub geometry used for the experimental runs was the result of number of design considerations, the most important being the choice of drivetrain and the need for cooling of the generator. As a result of these, which are covered in more detail in Chapter 5, the geometry size and shape was constrained. The experimental hub geometry is shown in Figure 68 along with the relevant parts of the turbine and drivetrain. Initial studies indicated that the cooling slot flow and rotation of the drivetrain had only minor impacts upon the flow over the diffuser. For the sake of simplicity the geometry was modelled such that all components were stationary and the cooling slot was covered by an expansion as can be seen in Figure 70.

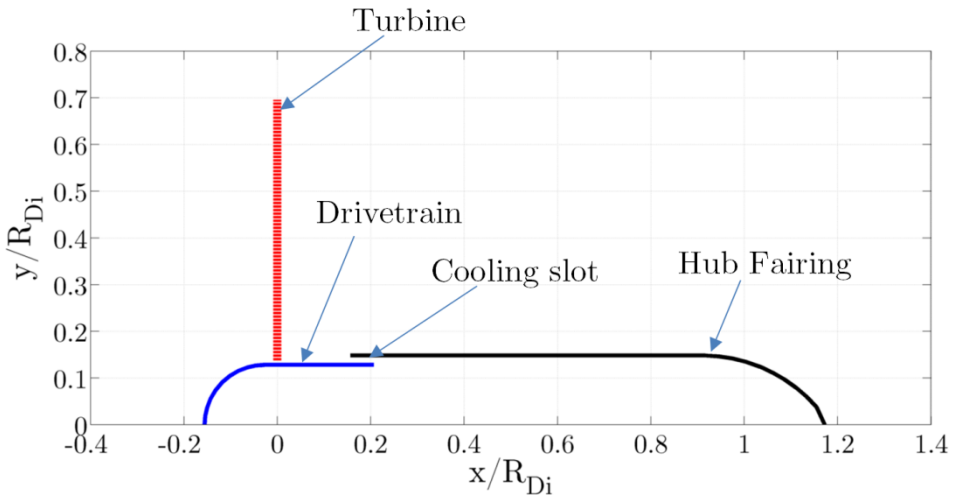


Figure 68: Experimental hub geometry definition

The experimental hub has a radius of 12.8% of the diffuser outer radius at the rotor plane and a maximum radius of 14.8% to the rear. The expansion in the geometry was included to allow for the creation of a cooling flow to be bled behind the rotor, past the drivetrain and out of the tunnel. The performance of the device can be seen relative to the 8% and 20% hubs in Figure 69.

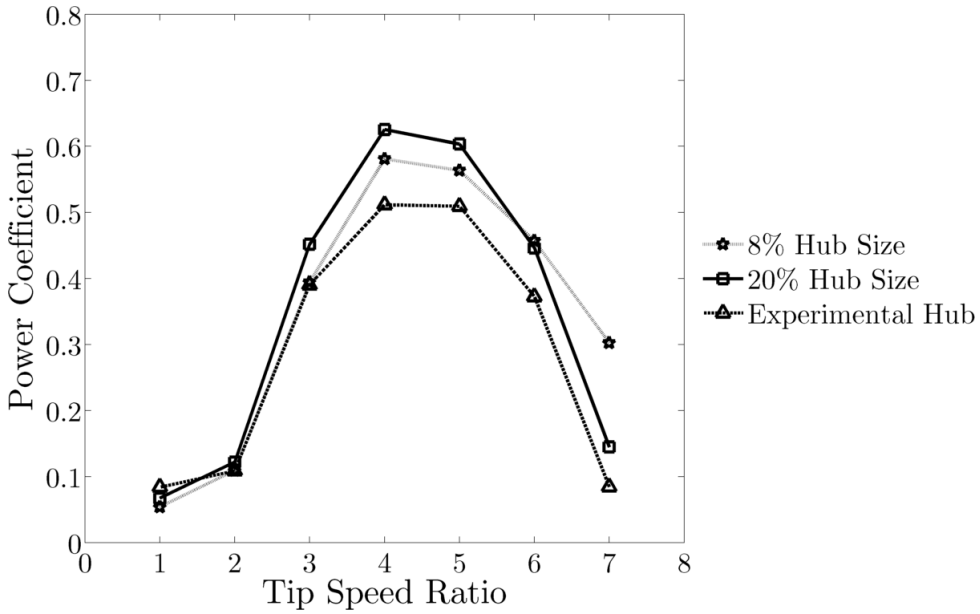


Figure 69: Power coefficient against tip speed ratio for diffuser with 8%, 20% and experimental hubs and the standard pitch experimental blading

Figure 69 shows clearly that the experimental hub design performs appreciably worse than both previously trialled hubs, even the smaller of the two, over almost the full range of tip speed ratios examined. This finding runs counter to the findings

in Section 4.4.2, where it is shown that larger hubs tend to perform better. The reason that the performance of the experimental hub is degraded is that the cooling slot and expansion, which are present in the experimental hub at x/R ≈ 0.1, cause flow separation from the hub. This separation means that a large volume of recirculating flow blocks the diffuser exit and reduces the effective area ratio in which diffusion can occur. This reduction in the diffusion potential means that the diffuser's swallowing capacity is reduced, reducing the rotor plane velocity and the available power. The flow around the device at a tip speed ratio of 4 and a Reynolds number of $Re_{DiU_\infty} = 2.9 \times 10^5$ can be seen in Figure 70.

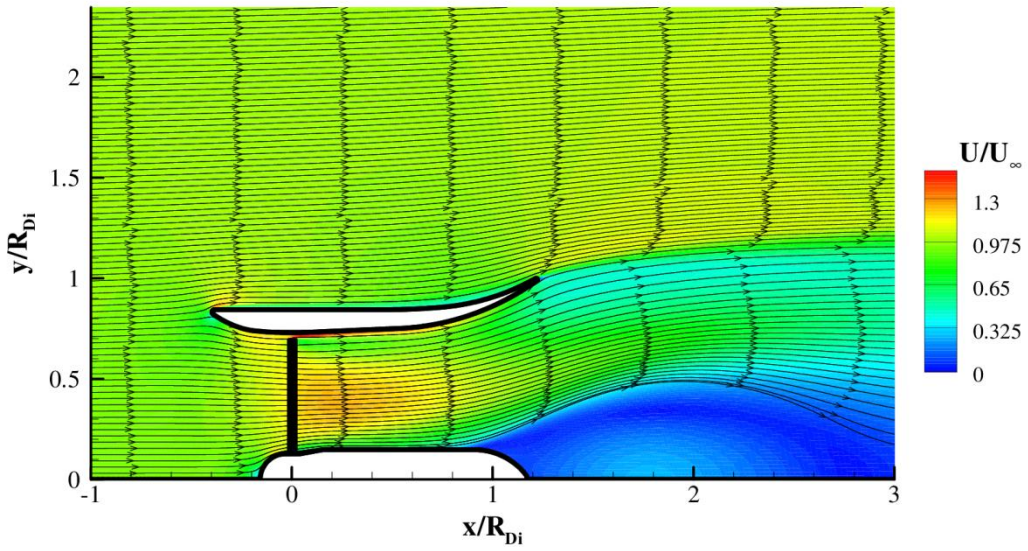


Figure 70: Contours of velocity with streamtraces for experimental hub shape with a blade element actuator disc turbine model, the standard pitch blading at TSR=4 and $Re_{DiU_\infty} = 2.9 \times 10^5$

4.5. Further Diffuser Flow Modelling

4.5.1. Diffuser Leading Edge Modification

During the analysis of the diffuser augmented device it was noted that at high rotor thrusts, which are particularly prevalent at higher tip speed ratios, there was a tendency for the flow to separate from the nose on the exterior of the diffuser. This separation effect can be seen clearly in Figure 65. In order to further improve the performance of the device a profiled leading edge for the exterior of the diffuser was trialled. This geometry modification, which can be seen in Figure 71, involved the radial expansion of the diffuser leading edge such that flow which approaches the leading edge with a radial velocity is gradually redirected rather than separating.

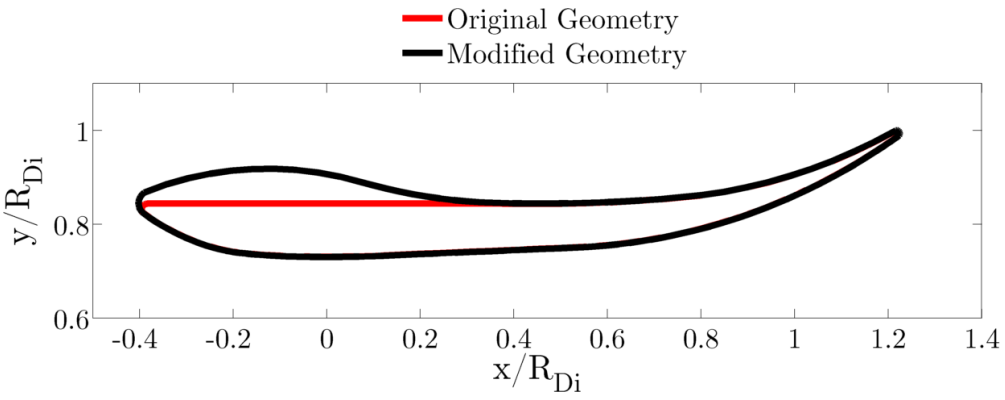


Figure 71: Modified diffuser leading edge geometry

The modified geometry was trialled with the standard pitch blading and both the 8% and 20% hubs. The results can be seen in Figure 72. It can be seen that the modification to the leading edge is able to improve the performance of the device under certain conditions. In the case of the 8% hub, the thrust of the combined rotor and hub is low, but grows as the tip speed ratio is increased. This increase in the thrust causes minor flow separation from the diffuser leading edge on the exterior surface in the original geometry, with re-attachment further downstream. When the new geometry is trialled instead the separation is suppressed, as seen in Figure 73 and the performance at higher tip speed ratios is improved.

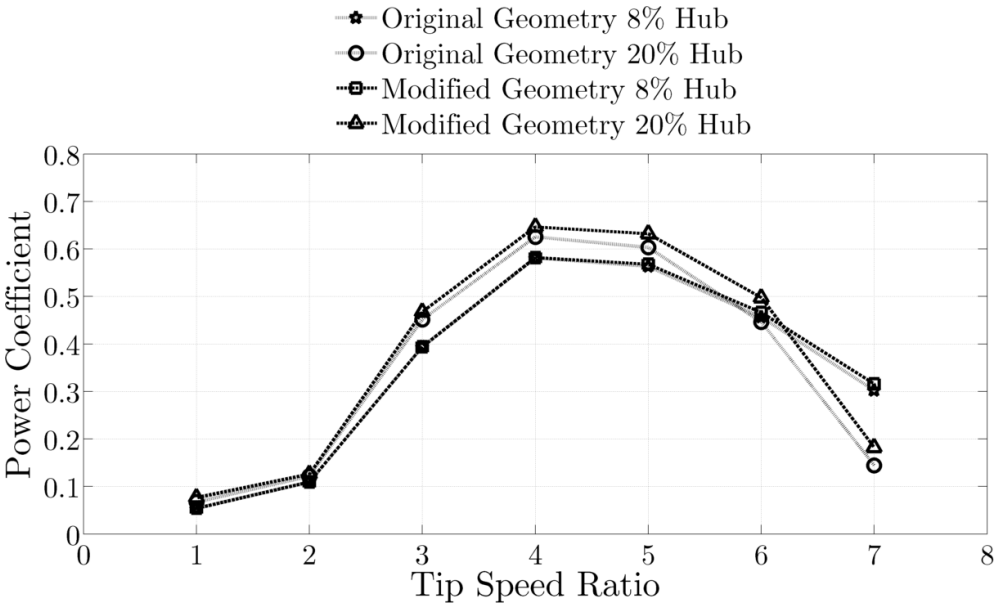


Figure 72: Power coefficient against tip speed ratio for diffuser with 8% and 20% hubs, standard pitch blading and the original and modified diffuser leading edges

In the case of the 20% hub, the overall thrust within the diffuser throat is increased for any given tip speed ratio relative to the 8% hub. This increased thrust

leads to almost complete flow detachment from the exterior of the diffuser at the leading edge with high rotor thrust as seen in Figure 65. This detachment causes a loss in the "lift" force that the diffuser structure can generate and therefore reduces the velocity at the rotor plane. When the leading edge modification is included, the separation from the leading edge is completely suppressed as seen in Figure 74. This suppression means that the power output of the device is increased by 3.4% at the design tip speed ratio of 4 and by up to 26.0% at a tip speed ratio of 7.

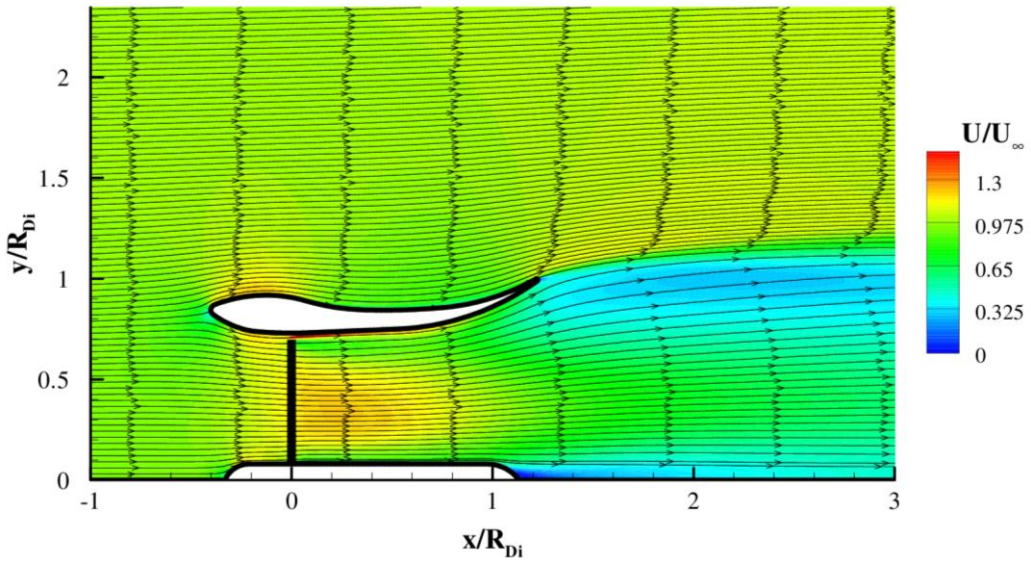


Figure 73: Contours of velocity with streamtraces for 8% hub with a blade element actuator disc turbine model, standard pitch blading at TSR=4, a Reynolds number of $Re_{DiU_\infty} = 3.4 \times 10^5$ and a thrust coefficient of 0.595

The radial magnitude of the hub wake is seen to increase with the inclusion of the leading edge modification, as seen from Figure 65 and Figure 74. This change of the wake shape does not however adversely affect the power output of the device as the increased hub losses are mitigated by the increased diffusion in the portion of the diffuser where x/R>1 and 0.75<y/R<1. In this region the increased streamline curvature induced by the improved diffuser leading edge section means that the region of slower moving fluid to the rear of the diffuser is reduced. The pressure recovery performance of the device at the operating tip speed ratio of 4 is also improved by 3.4% as a result of the change of geometry.

The geometry seen in Figure 74 has a peak power coefficient of 0.654 based on the rotor area and a peak power coefficient of 0.317 based upon the device outer area. It is this device which is used within Chapter 7 for the comparison of device

economics. The significance of this power coefficient is that the equivalent bare rotor geometry with the standard pitched blading has a peak power coefficient of 0.233. This means that for a low thrust rotor with a simplified rotor geometry the diffuser is able to augment the power output of the device by 36.05%. When the blades are pitched by 5°, the peak power coefficient based on the device outer area is increased from 0.294 in the bare case to 0.305 in the diffuser augmented case, representing a power augmentation of 3.7% over the bare rotor. The power output is however 3.8% lower than for the standard pitched, more lightly loaded rotor. These results suggest that augmentation is improved for more lightly loaded rotors and that high thrust designs of the type typically employed for commercial scale bare rotors may suffer from degraded performance from diffuser augmentation.

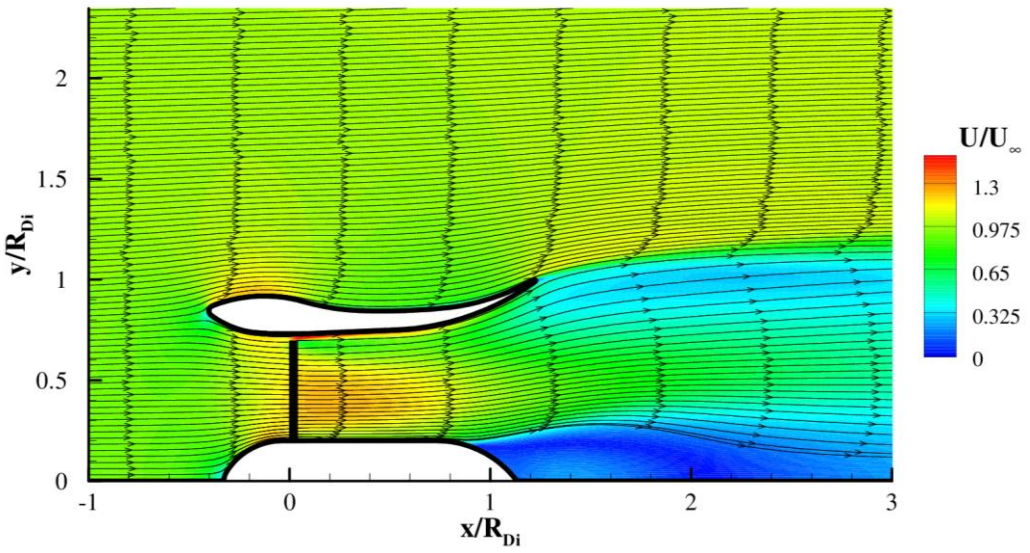


Figure 74: Contours of velocity with streamtraces for 20% hub with a blade element actuator disc turbine model, standard pitch blading at TSR=4, a Reynolds number of $Re_{DiU_\infty} = 3.5 \times 10^5$ and a thrust coefficient of 0.522

4.5.2. Effect of the Turbine Thrust

The effect of the turbine thrust on the performance of the device was examined using the blade element momentum CFD model. There are two diffuser cases, the standard diffuser as defined in Section 4.2.3 and the diffuser with the leading edge modification as defined in Section 4.5.1. There are also two rotor cases, the blades used during experimentation as defined in Section 4.1.4 and the ideal blade geometry as defined in Section 4.1.3. The ideal blades were used for a comparison as they give an approximately uniform thrust distribution across the rotor. The turbine tip speed ratio was held constant at 4 and the thrust coefficient

of the rotor was varied by pitching of the blades. The effect of the turbine thrust on the diffuser's power output can clearly be seen in Figure 75, which shows the power coefficient based on the device outer area against the thrust coefficient for the rotor when bare for the range of cases examined.

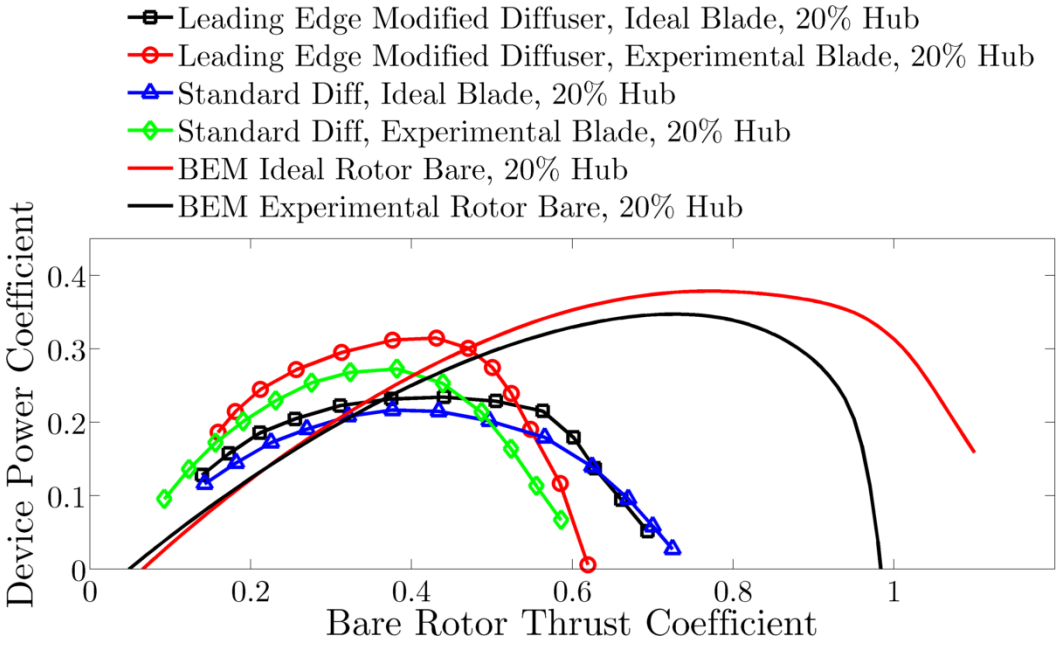


Figure 75: Power coefficient based on the device outer area aginst the rotor thrust coefficient for a range of cases examined at a tip speed ratio of 4

It is immediately evident from Figure 75 that the ideal bare rotor thrust coefficient for a diffuser augmented rotor is approximately half that for when it is operated in isolation. This is due to the interaction of the rotor with the diffuser swallowing capacity. As the rotor thrust increases, the mass flux through the rotor plane drops sharply and the power available to the rotor also falls rapidly. This drop is particularly steep in the case of the experimental blading due to the rapid stall of the blade tip region where the majority of the power is generated.

Another important finding that the results shown in Figure 75 highlight is the fact that the rotor which performs less well when bare, is the rotor which performs better when it is placed within a diffuser. The ideal rotor, which has an almost uniform thrust distribution across the rotor plane, is well suited to bare rotor operation since it optimises the axial induction of the rotor and maximises the power extraction for the given blade section. For diffuser augmented operation the power output is a function not only of the rotor's characteristics, but also the effect that the rotor wake has on the performance of the diffuser. In this case the

experimental rotor outperforms the ideal rotor as the thrust distribution across the rotor causes a stronger tip gap jet, whilst having a reduced thrust at the hub. This flow profile supports attachment to both the diffuser and hub and therefore increases the diffusion and swallowing capacity.

The improved performance with what at first appears to be an inferior rotor design emphasises the importance of combined design for diffuser augmented devices. In order to fully realise the potential of diffuser augmented devices it would be necessary to consider the design of the diffuser, hub and rotor geometries simultaneously since they are highly interrelated.

Given the arbitrary rotor design used within this thesis it is thought that further gains could be made to the power coefficient of the device if all are optimised simultaneously. McIntosh et al. [116] report a 17% increase in the power coefficient when a bare rotor design is modified for the velocity profile that it induces within the diffuser. This large improvement was found with only one step of what is essentially an iterative procedure and so further gains may well be possible.

A 17% gain such as this would have the potential to increase the power coefficient of the device derived here to 0.371, which is comparable with a typical horizontal axis tidal stream turbine [159]. The use of combined optimisation, where all components are considered together, has the potential to increase the power coefficient above this. The simplified modelling methods derived within this thesis would be ideally placed for such an analysis given the low computational expense.

The effect that the leading edge modification of the diffuser has on the power coefficient is also clearly visible. In addition to the increased peak power coefficient, there is also a shift of the rotor thrust at which this occurs to a higher value. Since the rotor thrust is a by-product of the power capture process, it is therefore not surprising that allowing a higher rotor thrust also allows greater power capture. This highlights the extent to which the device design relies not only on the internal diffusing flow, but also on the exterior flow of the device, in order to generate the lift force which causes the flow acceleration and hence the power augmentation.

The effect that the lower ideal thrust coefficient has on the rotor design requires a more detailed examination of the forces during operation, since the forces will be amplified relative to a bare rotor due to the increased mass flux across the rotor plane. In order to examine this, the in situ thrust coefficient is used, which is

defined as in Equation 80. This is defined as the thrust force of the component in its operating environment normalised by the fluid force in a streamtube the size of the device outer area at the freestream velocity. For a bare rotor this is identical to the thrust coefficient, for a diffuser augmented device this reflects the changes of the forces due to the flow conditions induced by the rotor. The in situ thrust coefficient is plotted against the bare rotor thrust coefficient for a bare rotor and the leading edge modified diffuser with the experimental blades and 20% hub case at a tip speed ratio of 4 in Figure 76.

$$C_{T_{IS}} = \frac{T}{1/2\,\rho A_{Di} U_1^{\,2}} \qquad \text{Equation 80}$$

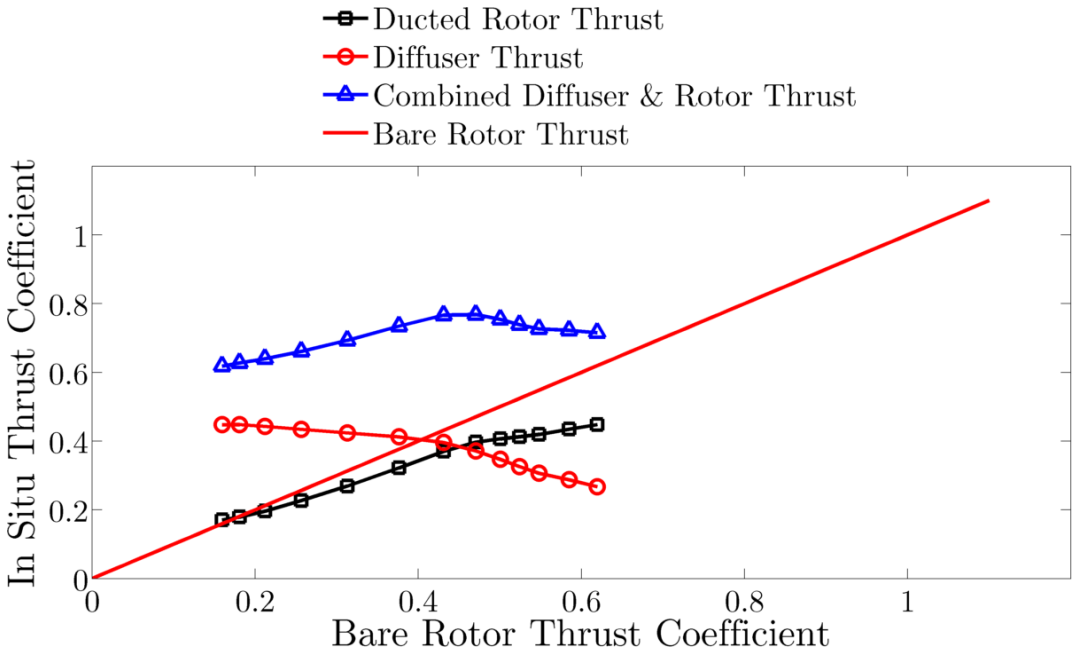


Figure 76: In situ C_T against the bare rotor C_T for a bare rotor and the leading edge modified diffuser with experimental blades & 20% hub at TSR = 4

The results seen in Figure 76 show that the relation of the thrust force to the rotor thrust coefficient for a diffuser augmented device are non-linear. It also shows that at any given bare rotor thrust coefficient, the forces on the diffuser augmented blade are less than for the comparable bare rotor case. The non-linearity of the relationship between the two thrust coefficients is due to the effect that the rotor thrust has on the swallowing capacity of the diffuser. At the higher bare rotor thrust coefficients, the velocity in the throat falls and so the forces on the blades level off, whilst the diffuser thrust falls due to the reduced axial velocity.

The fact that at any given bare rotor thrust coefficient the forces on the diffuser augmented blade are lower than for the comparable bare rotor case would be expected since the rotor area and therefore the forces are smaller, despite the increase in the rotor plane mass flux. For the diffuser augmented cases, at the peak power coefficients the rotor thrust forces are lower than for the comparable bare rotor cases, whilst the combined thrust is similar, with $C_{T_{IS}} = 0.77$ at the peak output as opposed to $C_T = 0.72$ for the equivalent bare rotor. It can also be seen that the thrust coefficient peaks at the same point as the power output for the diffuser augmented case, with the combined thrust dropping away at higher bare rotor thrusts due to a reduced velocity.

The reduced blade force coupled with the reduced blade radius will mean a lower bending moment on the blade during operation. The reduced stresses on the blade mean that there is a potential here for cost savings to be made in the blade design. Since the overall device thrusts are comparable at the optimum operating points, there will be little effect of the device type on the structural considerations of the tower and foundations if this diffuser type were used.

4.5.3. Effect of Freestream Turbulence on Power Output

The majority of tidal power sites evaluated at the time of writing have turbulence intensities in the range 10-14%, but with higher values at some sites [160] and when there are lower mean velocities [36, 37, 161, 162]. Turbulence intensities vary between sites, with some sites' turbulence intensity also exhibiting little correlation to the mean velocity. The level of turbulence at a tidal power site will be tied to the channel geography and bathymetry in the local area [163].

In order to assess the impact that the freestream turbulence has on tidal stream devices, analyses were conducted on a range of device geometries using the blade element momentum model CFD. The turbulence was specified as an inlet boundary condition with a length scale of $0.86R_{Ro}$ and a turbulence intensity which was varied between simulations. This value of the length scale was chosen as it is approximately that which would be found in a typical potential tidal stream power site [162]. The blade element actuator disc turbine model with the standard pitch blading at a tip speed ratio of 4 was used for all of the cases detailed in this section.

The methodology used here represents a significant simplification of the turbulence field that a tidal stream device will encounter as it omits the transient

nature of the turbulence, the spectrum across which it occurs and the anisotropy which is present [162]. A further limitation of this approach is that there is a noted drop in the level of turbulence in the flow from the inlet to the device itself [47]. In order to correct for this loss of turbulence within the flow, the reference turbulence was taken at a plane which was situated 1/2 blade radius ahead of the device.

Despite the limitations of the modelling approach it is thought that the simulations detailed within this section provide a useful approximation and a good first estimate of the effects of turbulence on the power output of devices.

4.5.3.1. Bare Rotor

The effect of turbulence on the power output of a bare rotor is something that has been examined previously by a number of authors [38, 164-166], and is covered in more detail in Chapter 2. Research conducted using scale models in water flumes suggests that the power output of a turbine is adversely affected by the presence of higher turbulence intensities, though the extent to which this occurs is contended [38, 166]. No cause has been given for this reduction in either of these studies.

It was found by Watkins et al. [167], that on blades operating at low Reynolds numbers, based on the blade chord and freestream velocity, of $Re_{cU_\infty} = 7.5 \times 10^4$, an increase in the turbulence intensity from 1.2% to 12.6% reduces the lift force at low angles of attack, particularly between 5° and 10°, whilst improving performance at high angles by preventing stall. This behaviour was also noted by Devinant et al. [168], who performed experiments at Reynolds numbers, based on the blade chord and freestream velocity, of between $Re_{cU_\infty} = 1.0 \times 10^5$ and $Re_{cU_\infty} = 7.0 \times 10^5$, and turbulence intensities from 0.5% to 16.0%. This reduction in performance at low angles of attack, where turbines at higher tip speed ratios operate, was assigned to fluctuations in the boundary layer created by small, high energy, turbulent eddies.

Research conducted experimentally in a flume using porous disks and measuring the drag force on the disks, suggested that the power output may increase with an increase in the turbulence up to turbulence intensities of around 13% for small length scales [165]. It has been suggested that changes in the power coefficient of up to 20% could result from variations of the upstream turbulence level. It was found that increases in the turbulence intensity always acted to increase the drag coefficient, which is identical to increasing the thrust. The turbulent length scale interaction was more complicated, with higher drag

coefficients generally found at length scales around 1/2 of a rotor radius. At length scales approximately equal to the blade radius, the minimum drag was found, with continual increase of drag with turbulent intensity.

The results of the present analysis, which was conducted on the geometry as seen in Figure 77, can be seen in Figure 78. It can be seen that in this analysis the increased turbulence intensity acts to increase the power output and thrust of the rotor as has been previously predicted by porous disk experimentation [165].

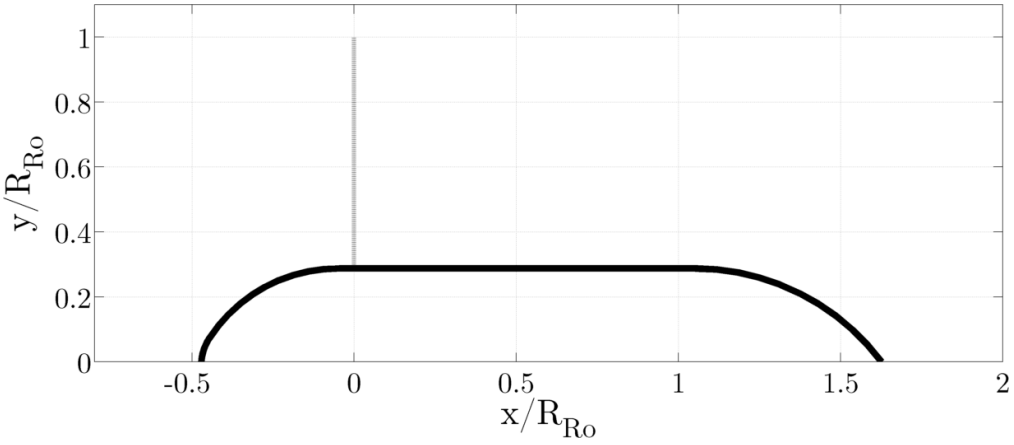


Figure 77: Geometry used for bare rotor turbulence impact study

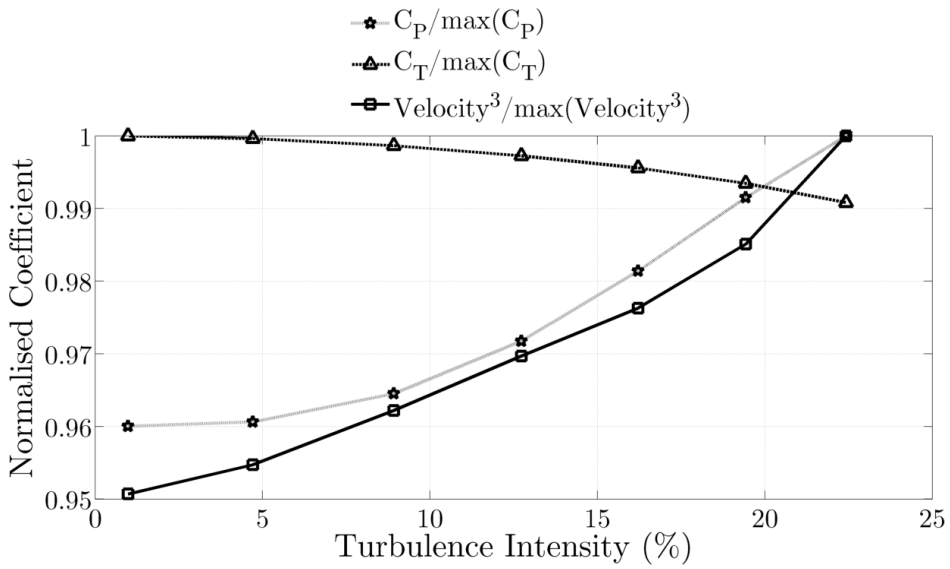


Figure 78: Normalised power coefficient, thrust coefficient and cube of velocity against the freestream turbulence intensity for the bare rotor

In the case of the blade element actuator disk used within this analysis, it is evident that it is the increase of velocity through the rotor plane and the associated increase in the available power that causes this. The increase in velocity, despite the

increase in the thrust, is due to increased levels of wake mixing as seen in Figure 79. This mixing energises the wake and increases the bulk velocity downstream, allowing an increase in the velocity at the rotor plane. The minor differences in the trends of the velocity and power coefficient seen in Figure 78 are as a result of the change of the angle of attack and hence the forces on the blades as the velocity of the fluid through the rotor plane changes.

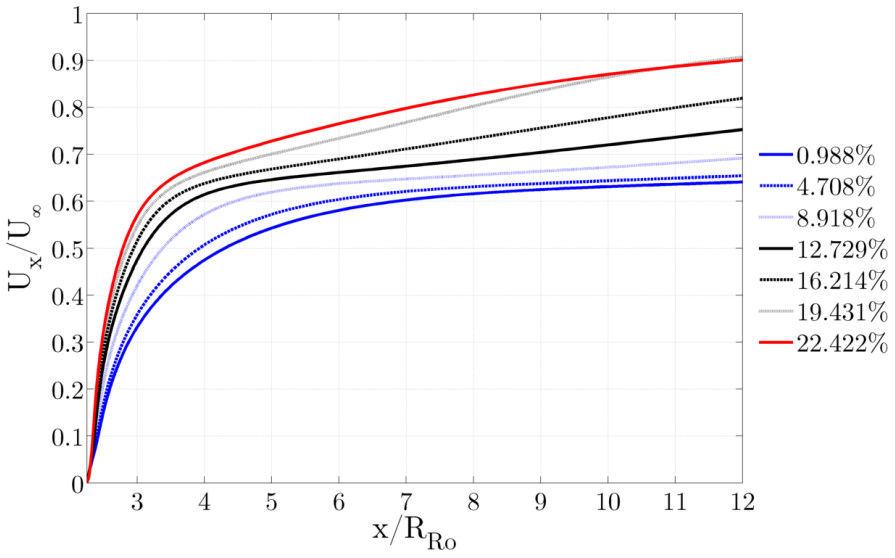


Figure 79: Wake recovery on the device centreline behind the hub for different freestream turbulence intensities in BEM CFD

It can be said that due to differences noted between the performance trends of actuator disks, whether blade element or uniform, and those of fully resolved turbines, that modelling of turbines in turbulence using actuator disks should be approached cautiously. Since the degradation in performance is suspected to be due to changes in the lift and drag of the blade section, there is no reason in principle why the blade element actuator disk model cannot be used for such modelling provided that it is provided with lift and drag data across the turbulence spectrum.

4.5.3.2. Derived Diffuser Geometry

The study of the turbulence response of the diffuser derived from this thesis was undertaken using the geometry with a hub of 20% of the diffuser outer radius and the diffuser casing leading edge geometry modification as seen in Figure 80. The results from these runs can be seen in Figure 81, which shows the normalised power coefficient against turbulence intensity. The trend seen here is the result of the vortex generated in the diffuser due to the swirl pattern which is set up by the rotor wake, and the enhanced uniformity caused by the flow turbulence.

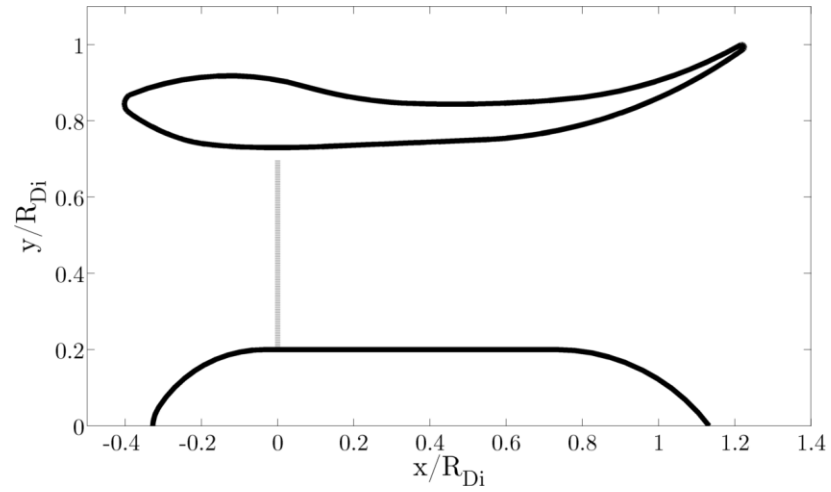


Figure 80: Geometry used for the analysis of the impact of turbulence on the diffuser derived from this thesis

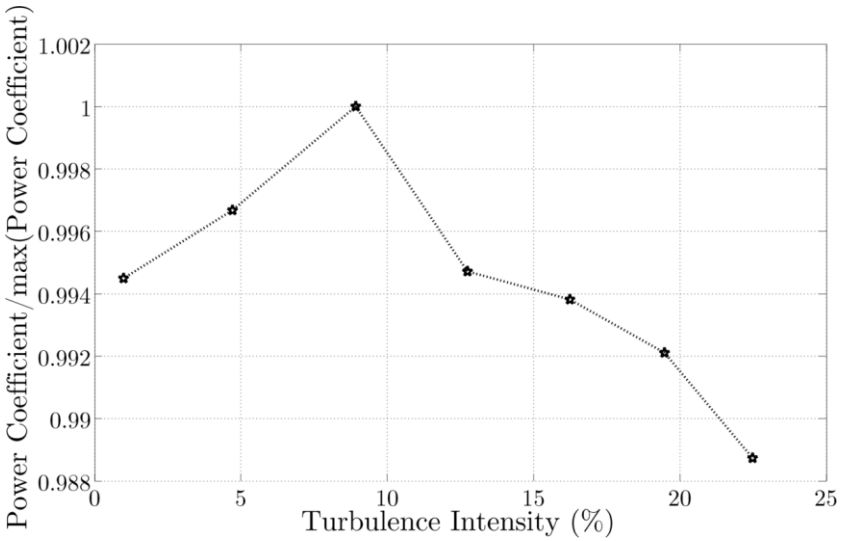


Figure 81: Normalised power coefficient against turbulence intensity for diffuser

The normalised swirl velocity at the exit plane of the diffuser is shown in Figure 82. At lower levels of turbulence intensity, between 0% and 9%, the swirl has not been able to fully suppress the separation at the rear of the hub. The increase in performance with increased turbulence intensity over this range is due to the strength of the vortex growing and reducing the core radius, allowing a greater volume for diffusion of the bulk flow in the region to the rear of the hub. This therefore leads to an increased throat velocity and an increased power output. At turbulence intensities above 9%, the hub separation is suppressed and the vortex structure begins to weaken due to mixing caused by the strength of the surrounding turbulence field [169].

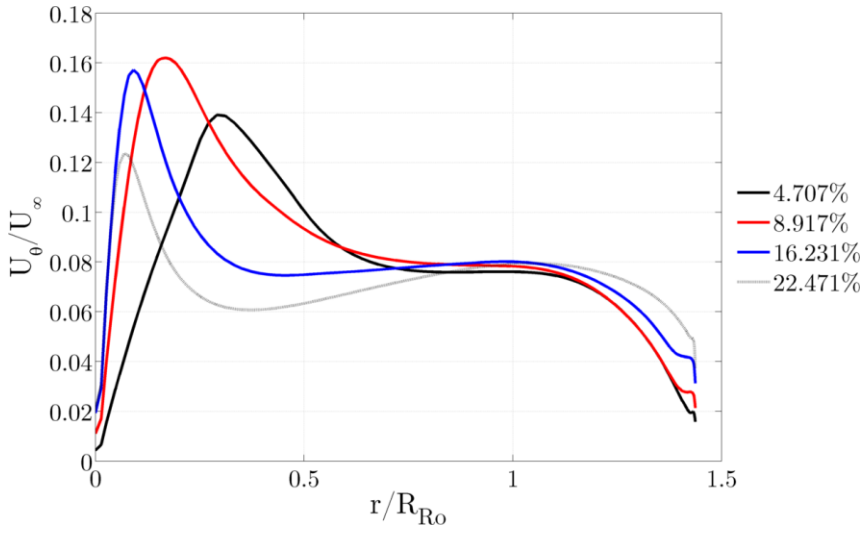


Figure 82: Normalised swirl velocity at the exit plane of the diffuser for CFD simulations over a range of turbulence intensities for the derived diffuser geometry

Increased mixing behind the rotor as a result of the higher turbulence intensities leads to a weakening of the vortex at the rear of the diffuser and increased total pressure losses due to energetic mixing of the flow [54, 170]. These increased losses also lead to a reduced pressure recovery. The pressure recovery coefficient and total pressure loss coefficients can be seen against the turbulence intensity in Figure 83.

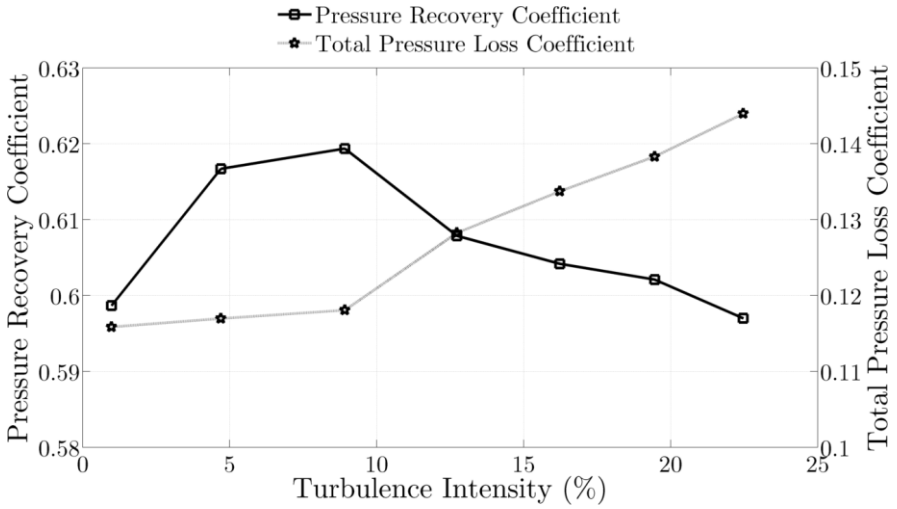


Figure 83: Pressure recovery and total pressure loss coefficients aginst turbulence intensity for the derived diffuser geometry

The increased mixing also serves to alter the velocity profile at the rotor plane as can be seen in Figure 84. At low intensities, the velocity tends to peak more in the centre of the blade, where the majority of the power is generated. As the

turbulence intensity increases, the throat velocity becomes more uniform along the length of the blade, with the most significant change being the reduction of the peak velocity at the blade centre. It is this redistribution which causes the loss of power output at higher turbulence intensities.

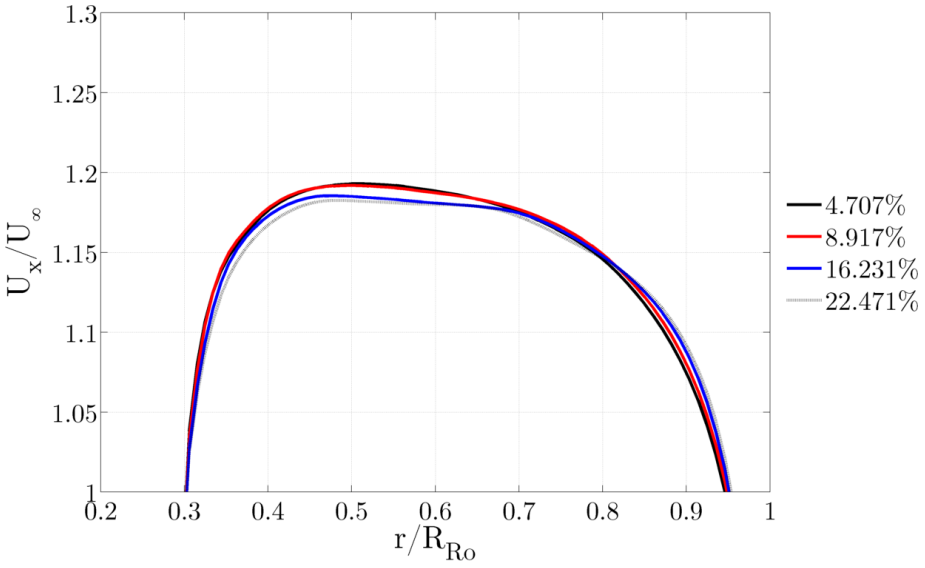


Figure 84: Rotor plane normalised axial velocity profiles over a range of turbulence intensities for the derived diffuser geometry

These findings suggest that for diffusers which are optimised for low turbulence environments there is little to be gained in performance with changes in the turbulence intensity. Although minor gains in performance are noted with an increase in the turbulence intensity from 0% to 9%, these are eliminated by around 13%. The maximum change in the power coefficient from the low turbulence environment, in which most devices are initially tested, to the high turbulence environment is only 0.6% of the maximum power. This limited reaction to the turbulence intensity means that this particular diffuser geometry can be considered to perform almost independently of the turbulence intensity.

The limitations of this analysis are however similar to those noted in Section 4.5.3.1, where the higher turbulence may increase the thrust of the rotor. As has previously been noted in Section 4.5.2, an increased rotor thrust has the potential to degrade the relative performance of the device due to a reduced swallowing capacity. It is suggested therefore that although this analysis provides a starting point for the assessment of turbulence on the performance of a diffuser augmented turbine, more work still needs to be done to examine the effects of the full device interaction.

4.5.3.3. Sun and Kyozuka Diffuser

The turbulence response of the Sun and Kyozuka diffuser [122] was modelled using the geometry which can be seen in Figure 85. The hub shape here was defined to match the radial size of the Sun and Kyozuka hub, though the geometry is not exactly the same as it has a rounded trailing edge.

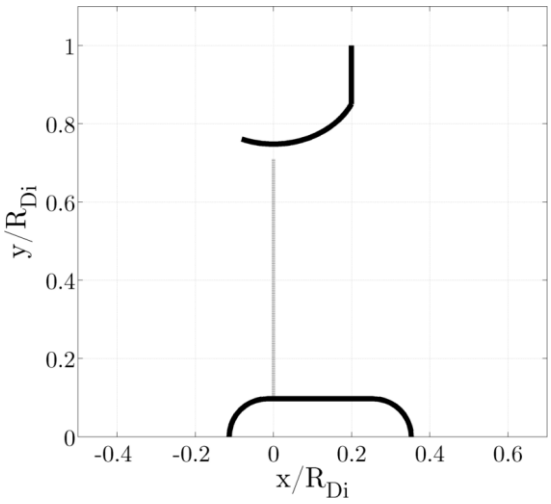


Figure 85: Geometry used for the analysis of the impact of turbulence on the diffuser used by Sun and Kyozuka [122]

The results of this analysis can be seen in Figure 86, which shows the normalised power coefficient and the normalised cube of the axial velocity against the turbulence intensity. This diffuser geometry has potentially significant power coefficient gains possible as a result of the turbulence and that these gains are attributable to the significant possible gains in the swallowing capacity of the duct.

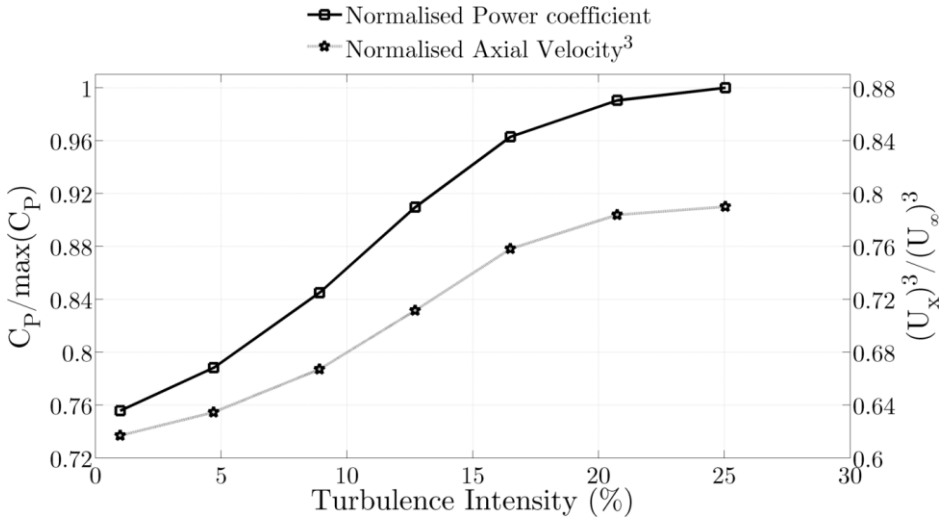


Figure 86: Normalised C_P & U_x against I for Sun and Kyozuka diffuser

The flow field around the diffuser at turbulence intensities of 0.99% and 25.05% can be seen in Figure 87(a) and Figure 87(b) respectively. It is immediately evident that the area of flow recirculation behind the exit plane flange is suppressed to a great extent by the increased level of turbulence. It can also be seen that the path and nature of the tip gap jet differs greatly between the two cases. At low levels of turbulence there is a splitting of the tip gap jet from the bulk flow and it is then directed around the rear of the exit plane flange by the recirculation. At high turbulence intensities the gap between the two flow structures reduces and the jet is directed towards the former centre of the region of recirculating flow. This redirection of the jet removes the majority of this area of recirculating flow allowing enhanced diffusion and an enhanced swallowing capacity. By a turbulence intensity of 22% this process has been largely completed and the power output levels.

Examining Figure 86 it can be seen that the normalised rotor plane axial velocity is below unity at all locations and is closer to what may be expected from a bare rotor. The rotor used here has a peak power coefficient of 0.233 and thrust coefficient of 0.504 when operating as a bare rotor. The power coefficient based on the diffuser outer area of the combined device is found to be 0.173 at a turbulence intensity of 0.99%, which is below that of the bare rotor. At a typical tidal stream turbulence intensity of 12.71% the power coefficient improves to 0.209, but is still below that which would be expected of a bare rotor.

It was found by both Sun and Kyozuka [122] for a tidal device and by Ohya and Karasundi [96] for a wind turbine that this diffuser geometry enables power coefficients based upon the diffuser outer area of around 0.475. The rotor geometry used by Sun and Kyozuka combined the use of two basic hydrofoil geometries, a T41 (a modified Gottingen 570) at the root and M-F07x sections for the remainder. The rotor geometry of Ohya and Karasundi is not given. This suggests that the rotors of both Sun & Kyozuka and Ohya & Karasundi perform considerably better than the one used here. When the rotor of Sun and Kyozuka was modelled within the diffuser augmented BEM CFD at turbulence intensity of 2%, the power coefficient based on the device outer area was found to improve to 0.190.

The response of the Sun and Kyozuka device to the freestream turbulence shows that for devices which operate in regimes with high degrees of flow separation and recirculation at low turbulence levels, there are potentially large gains in the power output with increased turbulence intensities. The extent to which these gains

are possible would depend upon the extent of the separation and the scale of the turbulence. There is a noted trade off between the improvement potential at high turbulence intensities and maximising the diffuser outer area power coefficient.

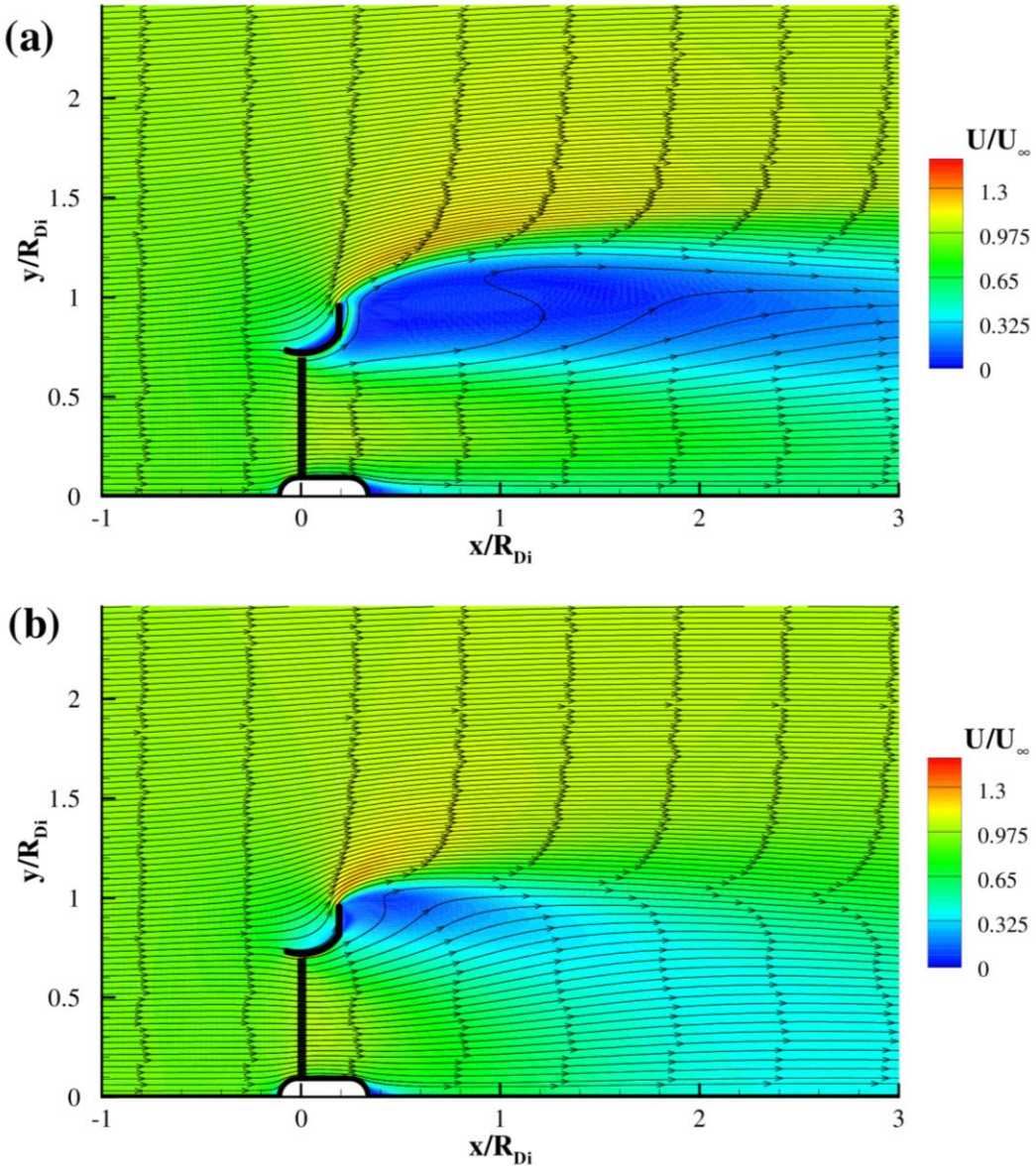


Figure 87: Contours of velocity with streamtraces for Sun & Kyozuka diffuser at (a) $Re_{DiU_\infty} = 2.5 \times 10^5$ and I=0.99% (b) $Re_{DiU_\infty} = 2.5 \times 10^5$ and I=25.05%

4.5.3.4. Diffuser Parametric Study

The effect of freestream turbulence on the power output of a diffuser was investigated through the generation of a range of diffuser geometries based upon parameterised designs. The data used to create these designs was generated using a two variable inscribed central composite experimental design, with the area ratio and length to diameter ratio of the diffuser used as the variables. The area ratio

between the diffuser throat and the diffuser exit plane was allowed to vary in the range $1.50<A_e/A_i<4.00$ and the length to exit diameter ratio in the range $0.25<L_{Di}/2R_e<1.00$. These ranges were chosen as they encompass the majority of diffuser augmented device designs which have been trialled as detailed in Chapter 2. The trial points can be seen in Figure 88, which shows the experimental design.

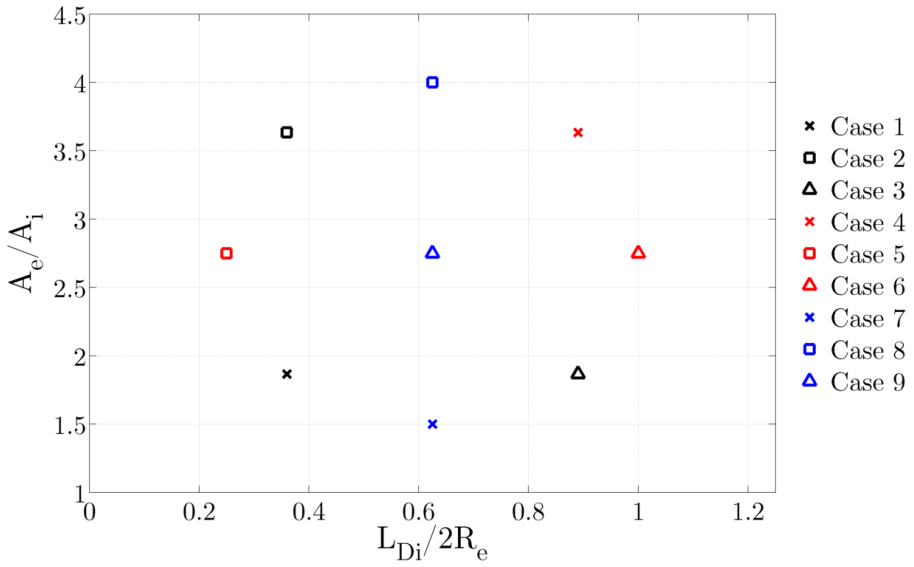


Figure 88: Experimental design for the parameterised diffuser geometries

The geometries themselves were created as trumpet shaped diffusers formed of cycloid curves, an example of which can be seen in Figure 89. The cycloid curves were specified based upon the geometric information from the experimental design and were formed adjoining a fixed geometry inlet section. The inlet section was created to be of a minimal size and can be seen in Figure 89 from $x<0$. The purpose of the inlet design was to suppress any separation from the leading edge of the geometry and therefore give a fair comparison between the cases. The turbine was situated at $x=0$, with a 5% tip gap between the turbine and the diffuser interior wall. A hub of a thickness of 28.7% of the rotor diameter, with an overall length of $x/R_{Ro}\approx2.1$ was used for all of the diffuser models.

The power coefficient based upon the rotor cross sectional area can be seen in Figure 90, where it is plotted against the diffuser area ratio and length to outer diameter ratio. The additional dotted line within Figure 90 represents the length of the hub within the diffuser. This shows that there is a tendency for higher area ratio, longer length diffusers to outperform smaller ones in terms of absolute power generated due to their improved ability to diffuse the flow and increase the swallowing capacity. This trend is due to the reduced wall angles present if a

diffuser maintains the same area ratio when elongated. This reduced wall angle leads to lower pressure gradients through the diffuser in the streamwise direction which reduces separation of the flow from either the hub or casing surfaces.

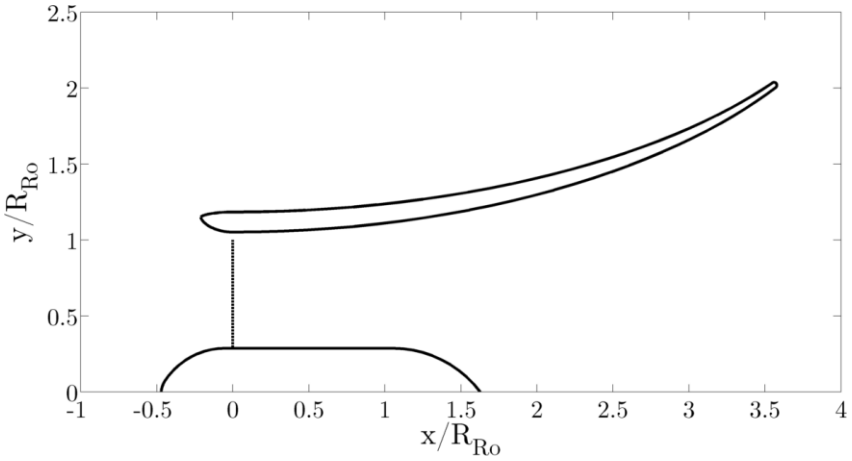


Figure 89: Parametric diffuser and hub geometry for case 4

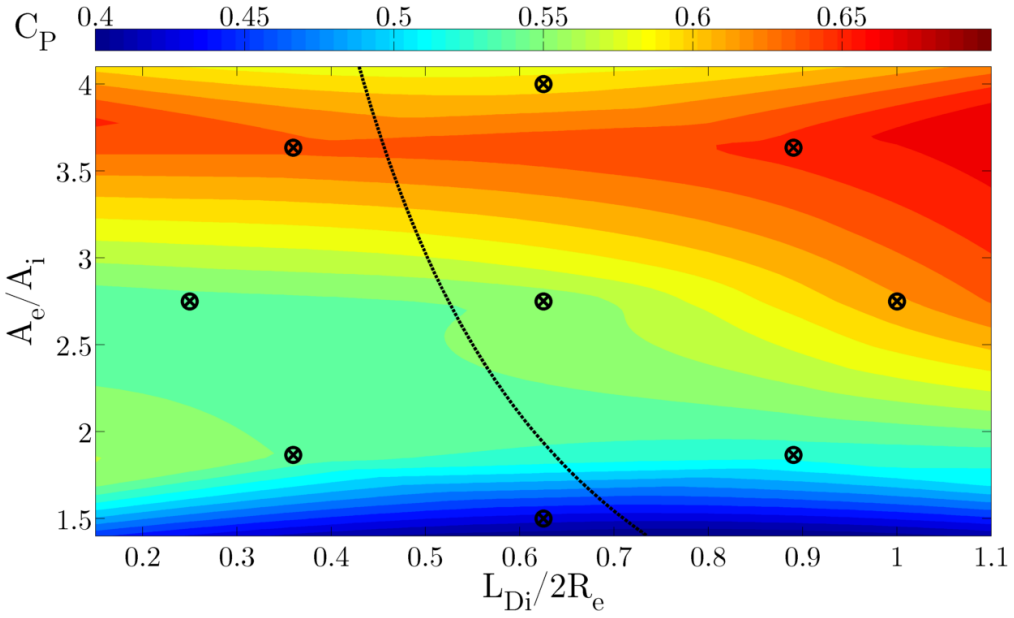


Figure 90: Power coefficient based on rotor area against area ratio & length to diameter ratio at I = 8.91%, with case locations and hub length line

The pattern holds well for diffuser lengths above the hub length, but for shorter diffusers this pattern is decreased and the area ratio is the primary driver. This is due to the fact that for the longer diffusers there is the additional region behind the hub into which the flow can diffuse. This means that the real area ratio of the devices to the right of the dividing line is in fact higher. As the short diffusers, particularly those at low area ratios, are elongated beyond the length of the hub,

there is a more significant rate of increase of the power coefficient as the area ratio is increased. It can be said in the case of this family of diffuser geometries that there is the potential for improved performance with shorter hub lengths to take advantage of the diffusion potential.

At the more extreme area ratios (A_e/A_i>3.7) the performance of the devices tends to fall away once more. This is because the pressure gradient increases to a point where the region of recirculating flow to the rear of the hub, caused by flow separation from the hub surface, begins to have an impact upon the throat velocity.

Comparing Figure 90 with Figure 91, which shows the pressure recovery coefficient of the diffusers over the same region, reveals the extent to which the power coefficient is dependent upon the pressure recovery in the diffuser. The two dimensional correlation coefficient of the two variables is 0.676, indicating that they are highly correlated. The trends are evident in both cases, with longer diffusers of the same area ratio performing better and the hub length effect also present.

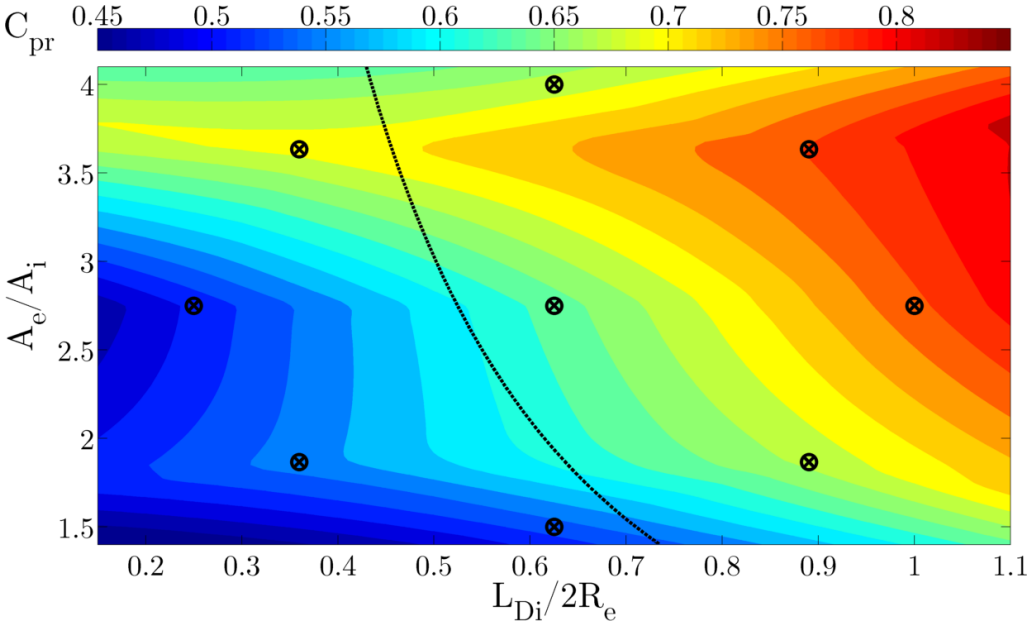


Figure 91: Pressure recovery coefficient against the area ratio and length to diameter ratio at I = 8.91%, with case locations and hub length line

When the power coefficient based upon the diffuser outer area is plotted, as seen in Figure 92, it becomes clear that the most efficient diffuser augmented devices are in fact those with the lower area ratios. This trend for improved performance at lower area ratios can be explained by the diffuser not being able to augment the fluid power at the rotor plane sufficiently to mitigate the increase in

the normalising area. There is a trend for increased performance when the area ratio and length to diameter ratio are increased simultaneously for longer diffusers with $A_e/A_i>2$, which is due to the wall pressure gradients as previously stated.

For the smaller area ratio diffusers ($A_e/A_i<2$) the opposite is found, with the best overall performance being from the low length, low area ratio diffusers. This is due to the fact that the low area ratio diffusers are already at lower diffuser effective angles and so increases in the length of the diffuser only serve to increase the total pressure loss in the diffuser due to the additional wall lengths.

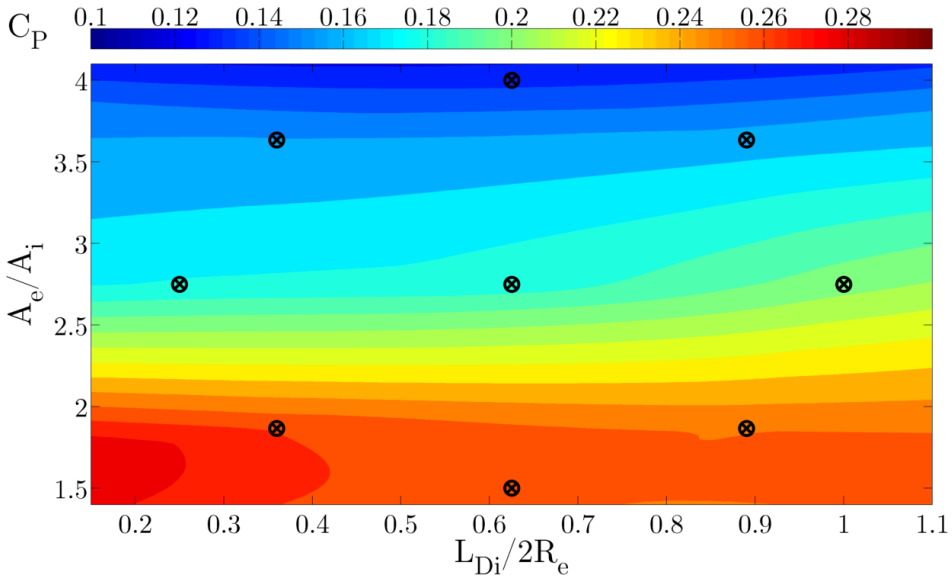


Figure 92: Power coefficient based on the diffuser outer area against the area ratio and length to diameter ratio at a turbulence intensity of 8.91%, with case locations

Interestingly, despite the fact that there are large divergence angles for some of these diffuser cases, in none does the flow separate from the exterior wall due to the strength of the tip gap jets. Instead the flow follows the exterior wall due to the boundary layer momentum being increased by the tip gap flow, similar to the pattern seen in Figure 70. The pressure gradient in the axial direction is still present and has the effect of encouraging earlier separation from the hub and generating a volume of recirculating flow to the rear of the hub along the device centreline.

The area ratio is plotted against the power coefficient based upon the device outer area at a turbulence intensity of 12.71%, which is typical of a tidal power site, in Figure 93. It is evident that for this family of diffuser geometries, there is a correlation between the power coefficient and the area ratio, with lower area ratio diffusers performing better, as shown by Figure 92. It can be seen that the power

coefficient based on the outer area of diffusers with area ratios in the range $1<A_e/A_i<2$ can exceed those of a low thrust bare rotor. The nature of the response in the range $1<A_e/A_i<1.5$ is unclear. As the area ratio returns to unity it could be expected that the power coefficient would tend to that of the bare rotor, the path which it takes through this region is unclear. This area is one which would merit further research as compact, high efficiency diffusers are likely to be the most economic means of diffuser augmented generation due to lower capital costs.

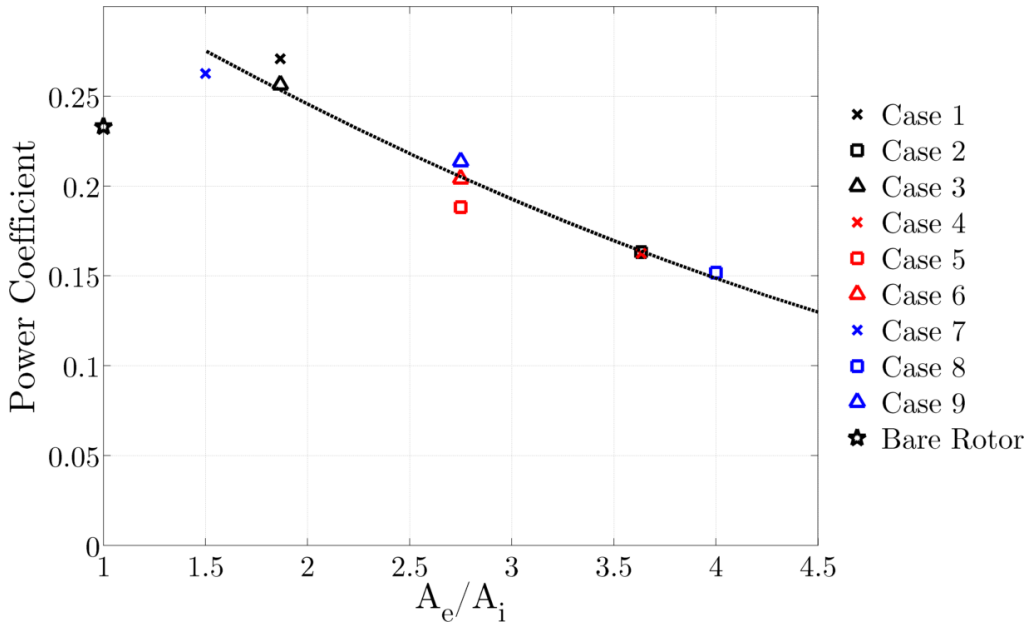


Figure 93: Power coefficient based on the device outer area against the diffuser area ratio at a freestream turbulence intensity of 12.71%

The impact of the level of turbulence on the performance of the devices can be seen in Figure 94 and Figure 95, which show the change in the rotor area power coefficient with changes of the turbulence intensity from 0.99% to 12.71% and 0.99% to 22.42% respectively. These figures include contours of the effective diffuser half angle, which is the angle between the diffuser wall at the rotor plane and the diffuser wall at the exit plane relative to the diffuser axis. At typical operating conditions, with turbulence intensities around 12%, there is a significant variation in the response according to the diffuser geometry, with a maximum variation of 23.09% in the power coefficient when the turbulence level is increased. If the turbulence intensity is increased from 0.99% to 22.42%, the variation in the power coefficient is 22.76%.

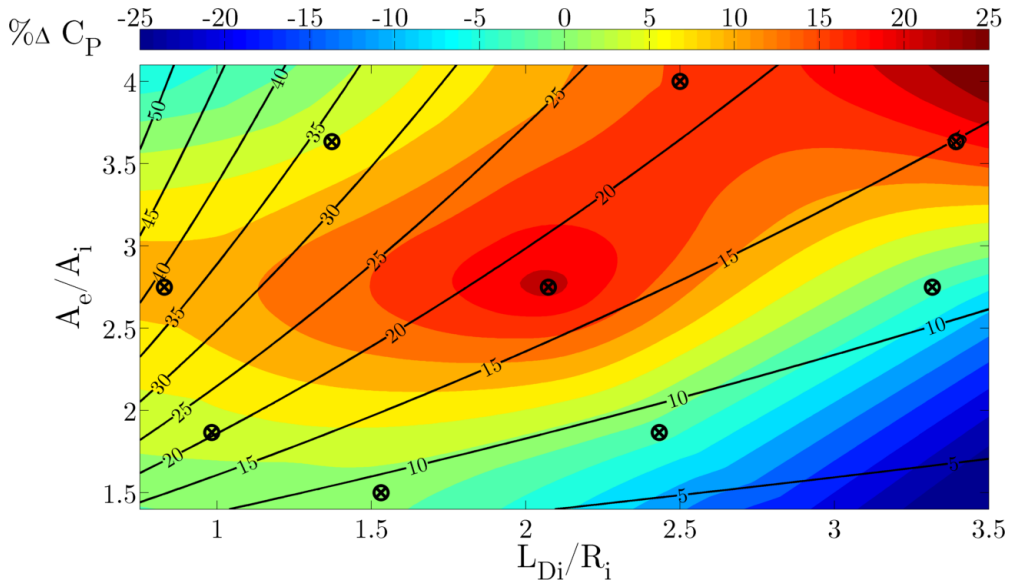


Figure 94: Contour plot of change in the rotor area power coefficient from 0.99% to 12.71% turbulence intensity, with lines of effective half angle and case locations

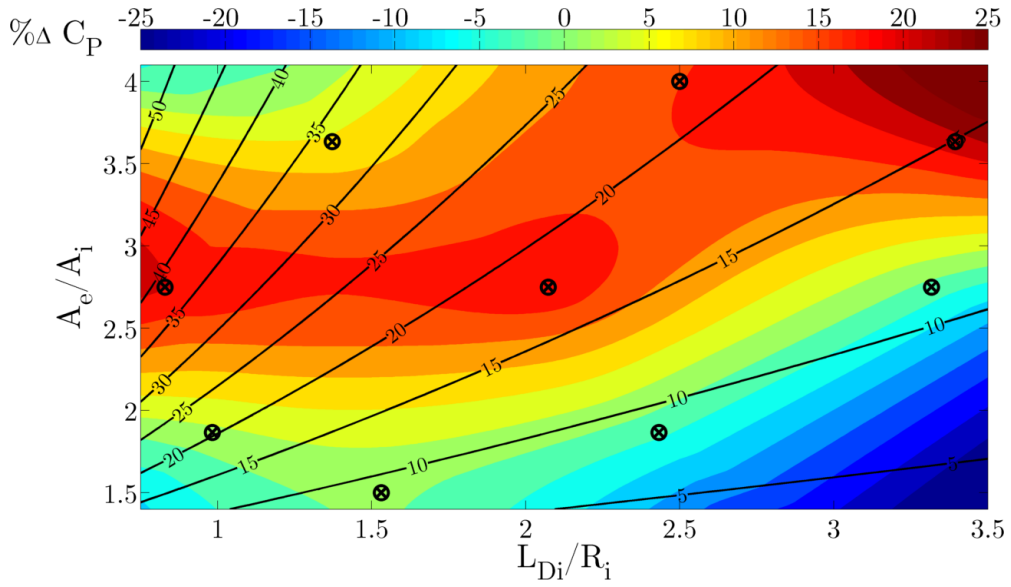


Figure 95: Contour plot of change in in the rotor area power coefficient from 0.99% to 22.42% turbulence intensity, with lines of effective half angle and case locations

From Figure 94 and Figure 95 it is clear that the effective wall angle is the main driver behind the response of diffuser augmented devices to the level of turbulence in the flow. There is a clear peak in the change in the power coefficient around half angles of 20±2°. This trend is due to the ability of the turbulence to promote boundary layer momentum on the hub, where there is a risk of separation. At low angles the flow is attached at low turbulence and so little performance gain is possible. At angles of around 20° the flow is normally detached and the turbulence

acts to suppress this, leading to the peak performance gains. At more extreme wall angles the pressure gradient in the streamwise direction within the diffuser is such that the turbulence level is insufficient to prevent the separation and there are more limited performance gains.

The region $L_{Di}/R_i>2.5$, $1.5<A_e/A_i<2.5$ is an anomaly of the surface plotting. The estimate of the performance here is due to the gradient of the response surface in the centre region being high and being extrapolated outside of the sampled region. This leads to changes in the performance of the device which are not realistic.

The curvature of the peak region from the 20° line to a constant value around $A_e/A_i=2.75$ is due to the turbulence being able to suppress separation better in shorter length diffusers. Diffusion suppresses turbulence and so shorter diffusers, which tend to have lower pressure recoveries, exhibit higher turbulence intensities throughout their length and are able to limit separation at higher angles.

The power coefficient based upon the diffuser outer area at a turbulence intensity of 22.62% is shown in Figure 96. As can be seen the performance changes that are induced by the turbulence do not change the overall trend for improved performance at low area ratios. The changes do however reduce the influence of the length to diameter ratio on the power output, with the shorter, higher angle diffusers benefiting to a greater degree.

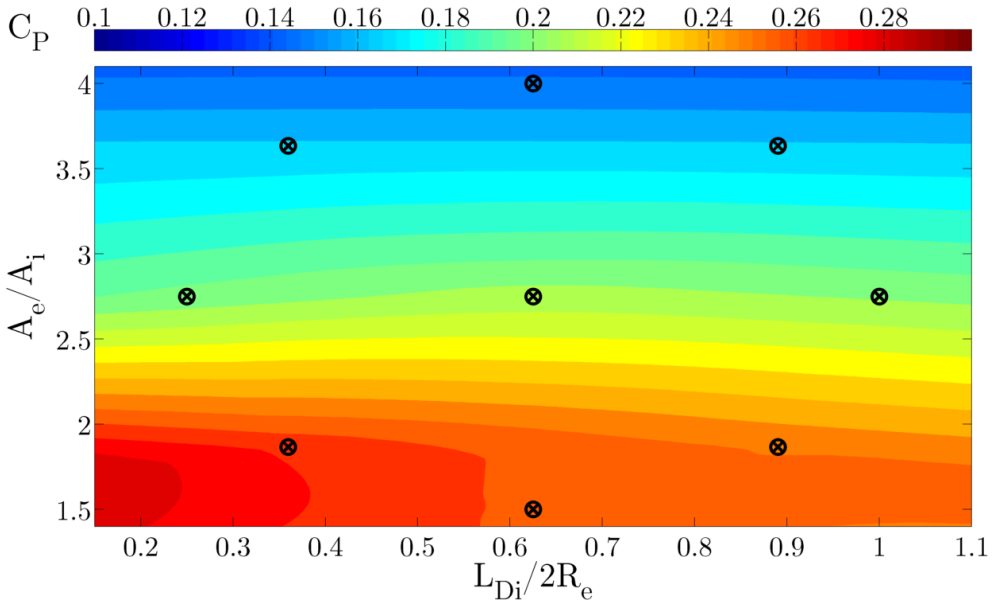


Figure 96: Power coefficient based on the diffuser outer area against the area ratio and length to diameter ratio at a turbulence intensity of 22.62%, with case locations

The conclusion that can be drawn from the results seen above is that the responses of diffuser augmented devices to turbulence vary with the device geometry. There is a trend for diffusers with a large effective half angle to perform better at higher turbulence intensities, but that this gain is not enough to offset the extra size in the radial direction. This means that smaller area ratio diffusers perform better than their larger counterparts regardless of the turbulence conditions.

In order to accurately assess the performance of a device under realistic operating conditions it is important that the device is modelled at the expected turbulence level present at a tidal site. It is evident that in the majority of cases the assumption made during the testing that low turbulence conditions can be used to assess the output of the device is unsuitable. It has been found that deviations of up to 25% in the power coefficient can result from these modelling limitations.

4.6. Concluding Remarks

The key findings from this section are contained primarily within four categories; turbine modelling and geometry, hub modelling and geometry, device optimisation and turbulence modelling.

4.6.1. Turbine Modelling and Geometry

The turbine modelling, through the assessment of a number of different case studies, found that uniform actuator disc modelling is unsuited to diffuser augmented turbine flow. As the uniform actuator disc model omits many of the key outflow characteristics of a turbine wake, such as flow swirl or turbulence, its use in modelling the interaction of the rotor with a diffuser is limited. As can be seen from Section 4.3, the uniform actuator disc model significantly overestimates the power output of a device and is unsuited to diffuser augmented turbine modelling.

As a result of failings within the uniform actuator disc model the blade element actuator disc was used extensively to model the behaviour and interaction of the rotor and diffuser combination. It is recommended that as a much more complete model the blade element actuator disc is used for modelling of diffuser augmented turbines in all cases.

The turbine geometry was found to have a significant impact upon the performance of a diffuser augmented device. High rotor thrust was found to reduce the swallowing capacity of the duct and therefore to reduce the power output. The optimum rotor thrust was found to be around half that of a bare rotor. The

combined effect of the rotor and diffuser was found to bring the device thrust to approximately the same level at the peak power output.

The crucial aspect of the rotor design is to ensure as far as possible that the diffuser and hub wall flows are able to sustain sufficient energy to remain attached and so to maximise the diffusion and power output. The importance of the tip gap jet in the performance of the diffuser augmented device was highlighted. The diffuser wall is the easier of the two surface boundaries to affect as the tip gap size can be controlled with relative ease. The control of the hub flow is more problematic but can be achieved through careful control of the near hub blade profile to minimise thrust in this location. The potential for further performance gains through combined device geometry optimisation is clear from these results.

4.6.2. Hub Modelling and Geometry

The effect of the hub on diffuser augmented devices has been shown to be significant. The necessity for the housing of a drivetrain of large relative size to the rotor when compared to a wind turbine means that the hub region becomes more significant. The adverse pressure gradient, which is by definition present in a diffusing section, tends to induce separation from surface boundaries and reduce the diffusion potential. The modelling of the hub within diffuser augmented turbines is therefore essential to accurately asses the power output and flow dynamics of device.

The effect of the hub shape was found to be relatively limited so long as it does not induce separation too early, which leads to a large volume of recirculating flow which blocks the diffuser exit. It is anticipated that minor performance gains could be made by improved hub shape design but that the majority of any improvements would be concentrated on optimisation of the diffuser.

The effect of hub size was found to be significant in the performance of a diffuser augmented device. The larger hub sizes were found to outperform the smaller device sizes due to the combined effect of streamline displacement and duct swallowing. This increased the velocity at the rotor plane, whilst also passing the fluid through a point further from the turbine axis, increasing the relative flow velocity and therefore the magnitude of the blade forces.

4.6.3. Device Optimisation

The further modelling of the diffuser optimised under the initial optimisation conditions highlighted the modelling limitations of the original approach. In

particular the omission of hub and rotor geometries and the infinitely thin diffuser section limited the routine. The further modelling also showed the extent to which the interaction of the component flows is critical to the performance of the device as a whole. It is therefore likely that a combined optimisation approach, in which the hub, rotor and diffuser geometries are considered simultaneously, would provide geometries with much improved power generation capabilities.

4.6.4. Turbulence Modelling

The modelling of diffuser augmented devices response to turbulence has noted limitations in that the rotor response is not fully modelled and that turbulence specification is limited. The results presented here provide a baseline assessment of the effect of turbulence but more detailed work in the area is needed. In particular the role of turbulence in the performance of the rotor requires clarification.

The complexity of turbulence characteristics and the large spectrum of frequencies and amplitudes over which it occurs within a tidal channel mean that more detailed experimental or modelling work is required. The assessment of turbulence effects would be best achieved through experiments, as full unsteady 3D CFD simulation investigating all parameters would be computationally expensive.

The model does however show that there are potential performance gains to be obtained through the use of diffuser augmentation. There is however a trade off between the potential for performance gains under turbulent conditions and the performance of the device in low turbulence conditions. The effect of turbulence is to suppress separation on diffusers with significant adverse pressure gradients. These diffusers tend to be ones in which there is a large divergence angle and so have a low power coefficient based on the diffuser's outer area. The performance under turbulence is improved for these devices, but not to the point where they are competitive with those diffusers with a smaller cross sectional area.

5. Experimental Methods

5.1. Apparatus

5.1.1. Wind Tunnel

The Durham 2m^2 wind tunnel was used for all of the experimental research conducted as part of this thesis. The tunnel is an open-jet, open return type wind tunnel with an inlet contraction ratio of 7.7:1. The tunnel is powered by two dual entry centrifugal fans housed downstream of the test section in the fan housing. The key features of the wind tunnel are shown in Figure 97. For more detail on the design of the wind tunnel the reader is referred to Sims-Williams et al. [171, 172].

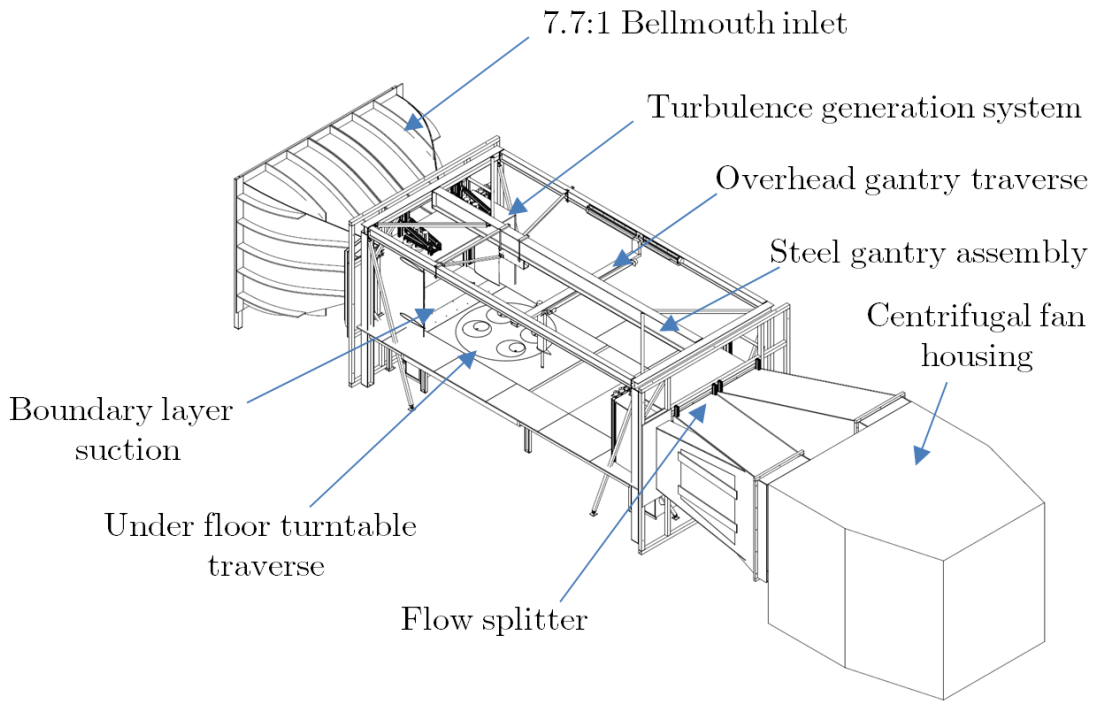


Figure 97: Isometric wind tunnel view detailing the salient features

The wind tunnel is fitted with a three axis overhead gantry traverse system which is used to control the position of the five hole pressure probe. The traverse enables the probe to be moved to any position downstream of the rotor, up to 8 turbine radii downstream of the rotor, 4 turbine radii crosswind in both directions and 2 blade radii above and below the rotor axis. These limits are shown in Figure 98, where the flow enters the section along the x-axis.

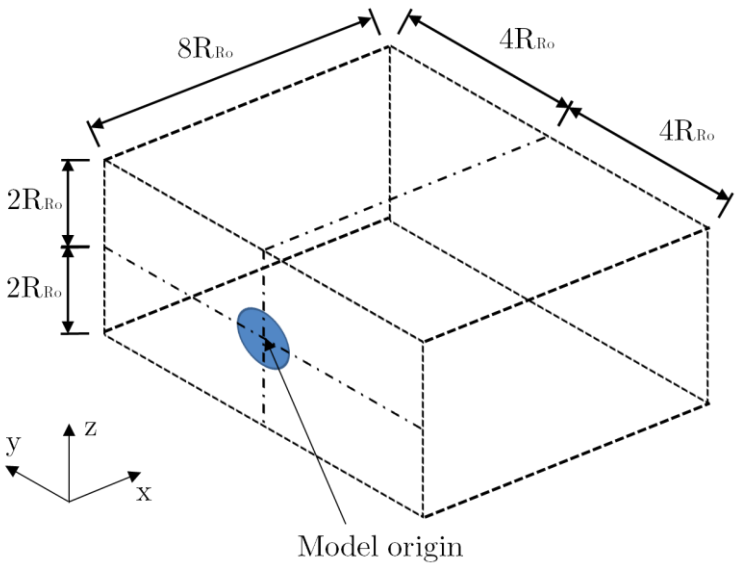


Figure 98: Traverse limits in the wind tunnel as a function of the blade radius

The tunnel has features which were not used in this thesis, the boundary layer suction at the inlet and a turbulence generation system. More details on the TGS and the flow dynamics within the wind tunnel after installation can be found in the work of Mankowski [173]. This study confirmed that the flow through the nozzle is unchanged from the pre-existing nozzle, with no bulk yaw or pitch being induced in the flow when the TGS system is not being actively utilised.

5.1.2. Diffuser & Turbine Experimental Rig Construction

The general arrangement of the combined diffuser and turbine rig with the location of the sub-assemblies can be seen in Figure 99. The details of the experimental rig construction and sub-components are detailed in this section.

5.1.2.1. Diffuser Assembly

The diffuser, the geometry of which was derived using the procedure detailed in Chapter 3 and is defined in Chapter 4, was constructed at $1/40^{th}$ scale for testing in the wind tunnel. This scale was chosen such that realistic Reynolds numbers of up to $Re_{DiU_\infty} = 7.0 \times 10^5$ (based on the throat diameter and freestream velocity) could be achieved whilst ensuring that blockage of the wind tunnel was minimised. The key dimensions of the model scale diffuser can be seen in Figure 100.

The scale used means that the wind tunnel blockage is only 9.8% of the jet area. For the tunnel type and dimensions used the corrections to the velocity field are of the order of 1.18%, or a 3.58% change in the power output [174, 175]. This correction is however conservative as the calculations assume that the combined

device is a solid blockage, rather than having a passage through the centre (albeit one with a degree of thrust blockage). The actual correction factor is thought to be negligible, something backed by Chen & Liou [176], who state that correction to the power output of a wind turbine model is not necessary at blockages of below 10%.

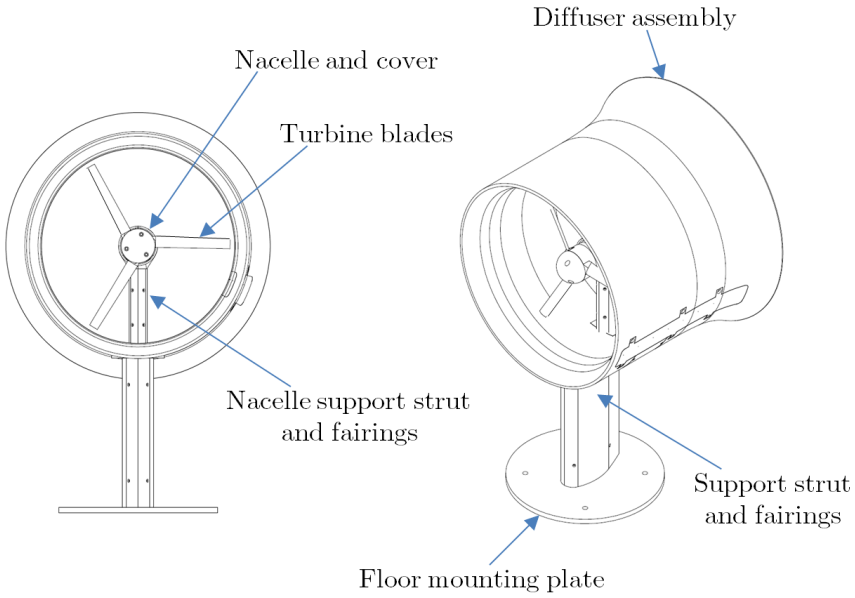


Figure 99: Diffuser and turbine rig salient features

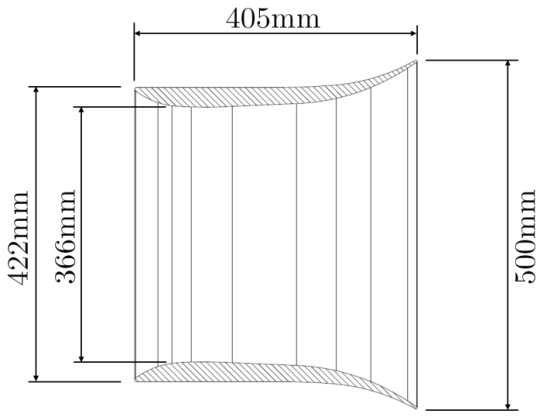


Figure 100: Diffuser body cross section showing key dimenions

The diffuser body was CNC machined from a block of modelboard, which was laminated within the School of Engineering's workshop. The block was constructed from laminated sheets of 1500 mm x 500 mm x 50 mm Alchemie M651 modelboard which were cut to size and joined with Alchemie's Alchemix MG651 adhesive. The block was then CNC machined at Precision 2000 Ltd. in Newcastle-upon-Tyne. The diffuser body was varnished on all surfaces to create a smooth surface.

The diffuser has a number of slots cut into the geometry as seen Figure 101. These slots are to facilitate the fitting of the static pressure tapping insert, allow access for the associated pressure tubing and to provide a mounting area for the diffuser and nacelle strut to the base, which mounts to the under floor force balance.

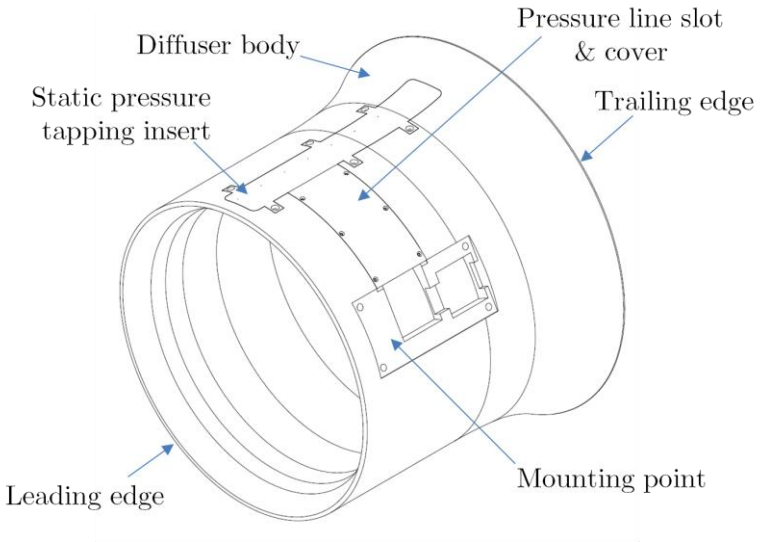


Figure 101: Diffuser assembly details

The details of the static pressure tapping insert can be seen in Figure 102. The insert was constructed using a Stratsys Objet Eden 500V and Fullcure 720 material using a Fullcure 705 support material.

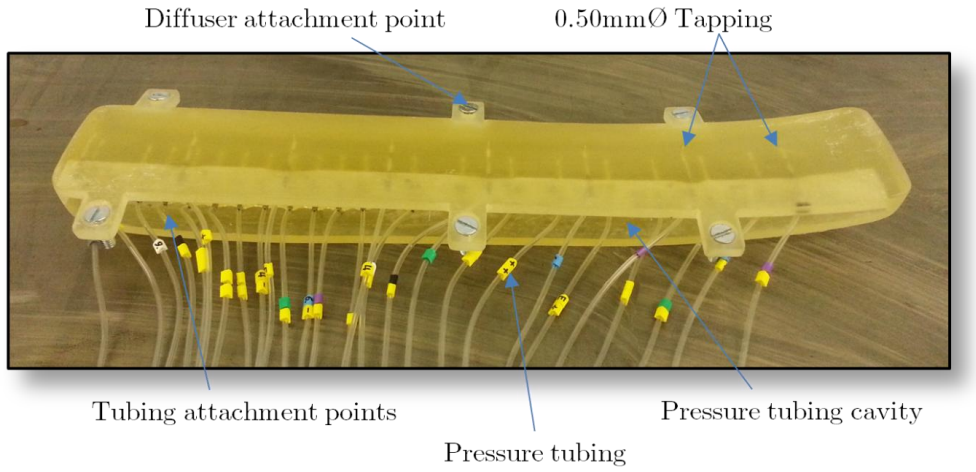


Figure 102: Diffuser static pressure tapping insert details

Once the piece was made, the tapping holes were cleared of the support material using a compressed air supply and hypodermic tubing was inserted into the interior holes to allow attachment of the pressure tubing. The join between the

hypodermic tubing and insert was sealed with epoxy resin and the seal tested. The insert screws into the diffuser body, with the tubing leaving the cavity via a covered slot which runs to the support strut mounting point as seen in Figure 101. The locations of the static pressure tappings are detailed in Figure 119 in Section 5.3.4.

5.1.2.2. Mounting Assemblies

The diffuser body is secured onto a mounting assembly, onto which is also secured the nacelle support strut, which passes through a slot in the diffuser. The overall layout of the structural parts of the model can be seen in Figure 103.

The main mounting assembly is formed of a 40 mm x 80 mm x 3 mm box section and is sized such that the axis of the diffuser is at the centre point of the wind tunnel jet. The mounting assembly sits above the tunnel floor and is fixed onto the under floor force balance pins. On the top of the mounting assembly the diffuser bolts onto the mounting plate and the nacelle strut passes through the diffuser before also being bolted onto the mounting plate. The details and dimensions of the main diffuser mounting assembly can be seen in Figure 104.

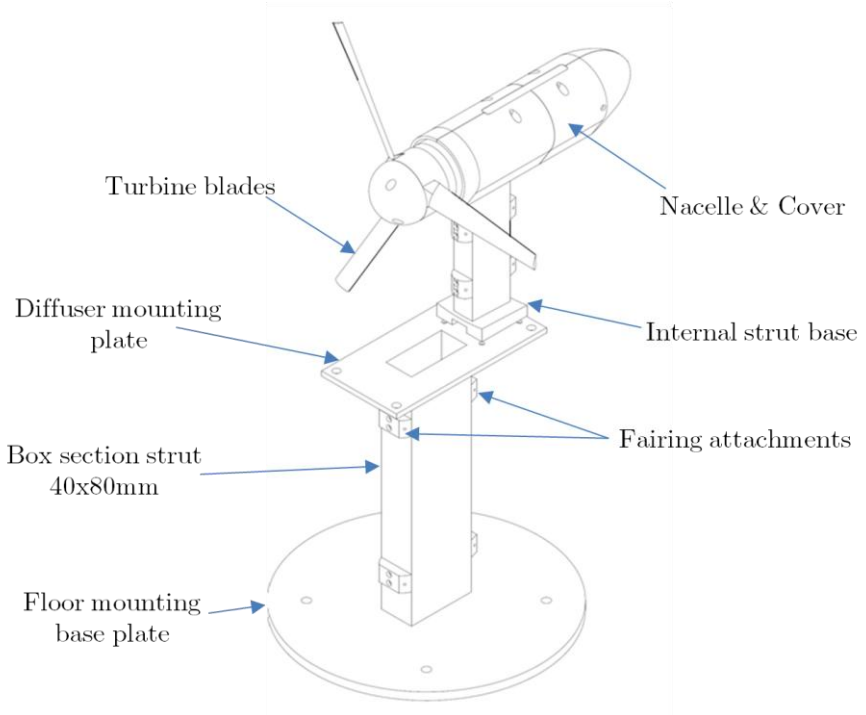


Figure 103: Mounting assemblies shown in rotor only configuartion view

The fairings for the mounting struts were constructed using vacuum forming of 2 mm thick plastic sheeting around profiled wooden moulds cut using a laser. The resulting sections were trimmed to size manually and fitted to the rig.

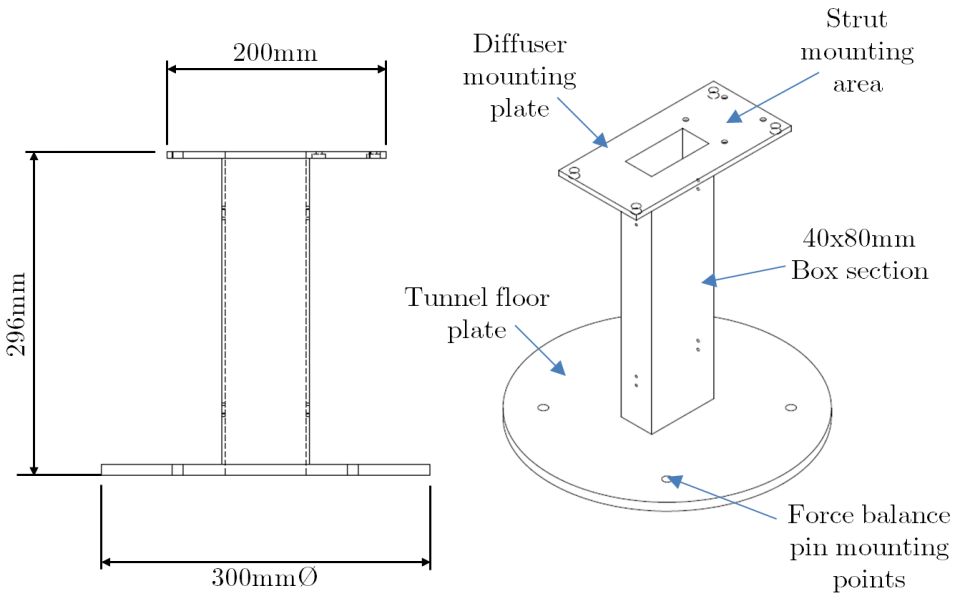


Figure 104: Diffuser mounting assembly details and dimensions

5.1.2.3. Turbine Geometry

The rotor blades were designed as detailed in Chapter 3 using a NACA63818 aerofoil section, with the resulting geometry detailed in Chapter 4. In order to realise lightweight, cost effective blading which would not overly deform at the operational rotational speeds, the blades were constructed using ABS plastic. The blades were manufactured using a Makerbot Replicator, with a printing layer thickness of 0.20 mm. In order to achieve the surface finish necessary for testing the blades surfaces were polished until smooth. The key dimensions and attachment details of the turbine blades can be seen in Figure 105.

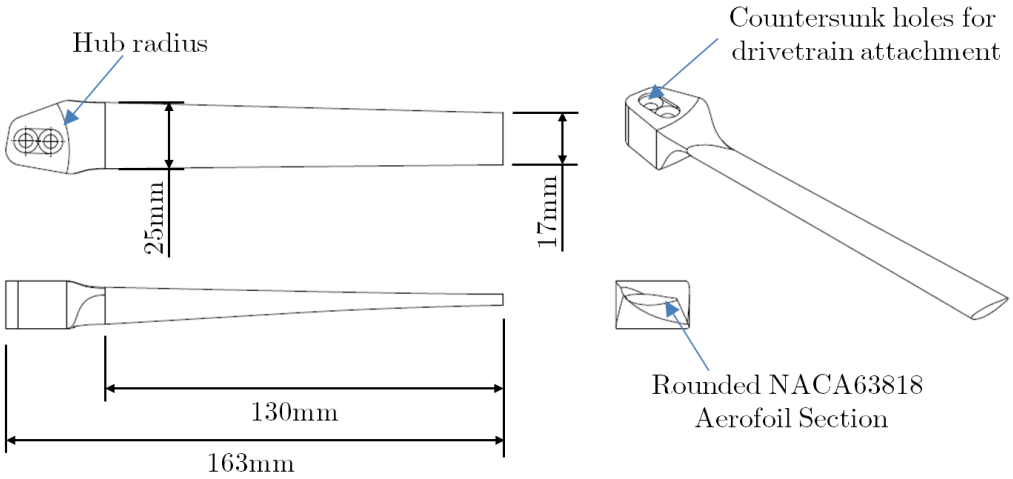


Figure 105: Turbine blade details for non-pitched blade design

Due to manufacturing constraints with the Replicator machine and the small size of the blades, it was not possible to replicate the sharp trailing edge of the NACA63818 aerofoil. As a result, the aerofoil section was rounded at the trailing edge, as seen in Figure 34, such that the blade shape could be accurately constructed. For more information on the rounded aerofoil used here refer to Chapter 4, where the section properties are presented.

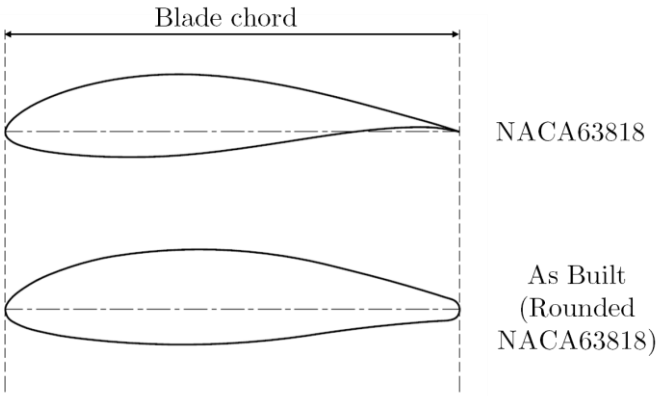


Figure 106: NACA63818 and rounded NACA63818 aerofoil cross sections

There were two separate sets of blades manufactured for testing as detailed in Chapter 4, which are defined for the purpose of this thesis relative to the base case blade, which is referred to as the zero pitched blade set. Both sets of blades use the same aerofoil section and have the same chord distribution, and both maintain a linear relationship for both chord length to blade position and pitch angle to the position along the blade. The distribution of the chord and pitch can be seen in Table 15, with the pitch angle being defined as seen in Figure 107.

r/R	**c/R**	**Pitch (deg)**	
		0° Blade	**-5° Blade**
0.20	0.143	29.490	24.490
0.30	0.1374	26.116	21.116
0.40	0.1318	22.742	17.742
0.50	0.1262	19.369	14.369
0.60	0.1206	15.995	10.995
0.70	0.115	12.621	7.621
0.80	0.1094	9.247	4.247
0.90	0.1038	5.873	0.873
1.00	0.0982	2.500	-2.500

Table 15: Blade geometry details for the experimental blade sets

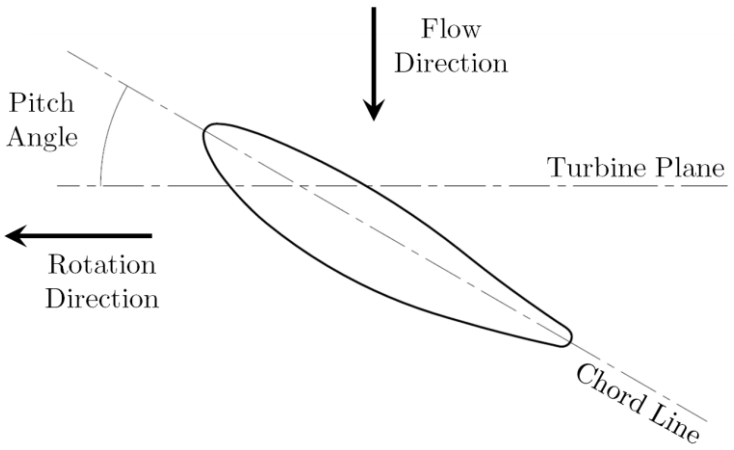


Figure 107: Definition of the blade pitch angle

5.1.2.4. Drivetrain & Nacelle

The drivetrain was based around an AXI5330/24 three phase permanent magnet motor. This motor was designed to power model aircraft and as such has the primary qualities which were required, a small size, high power output and a high shaft speed. The motor has a 63 mm external diameter and is able to supply approximately 1.5 kW at 7000 rpm. During testing the motor was operated as a motor, to overcome the cogging torque of the permanent magnets, and then as a generator. The peak rotational speed for the turbine during testing was 10,000 rpm.

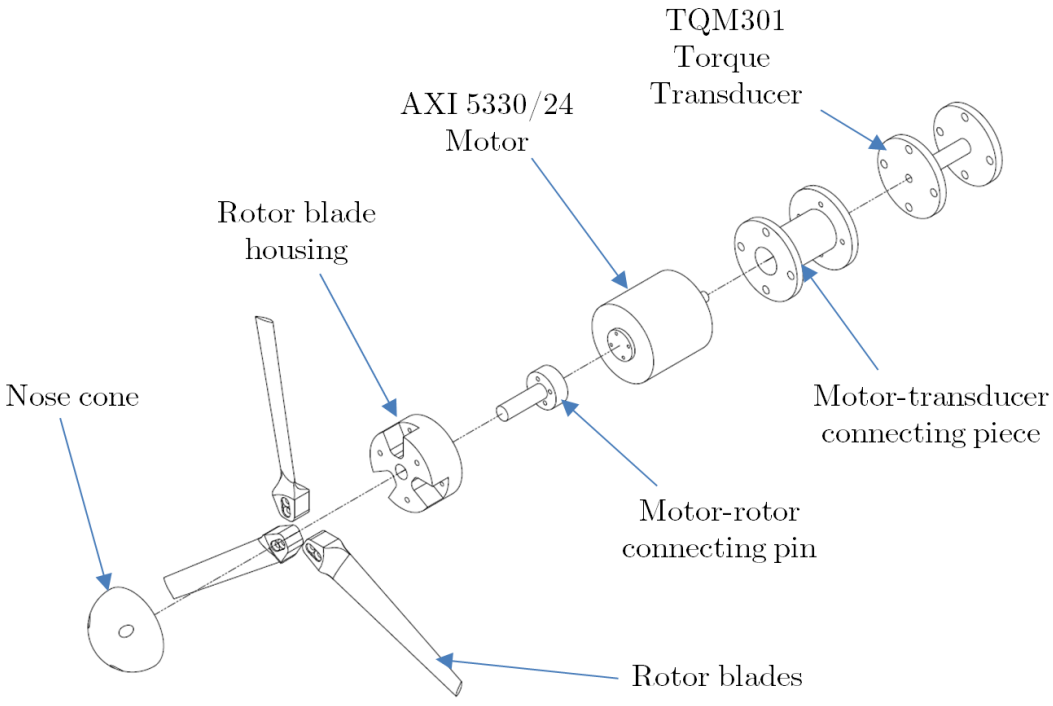


Figure 108: Exploded view of the turbine drivetrain assembly

The rotor was attached within the drivetrain as shown by Figure 108, which shows an exploded view of the complete turbine drivetrain. The rotor blades were secured into the nose cone assembly, which was attached to the motor shaft through a connecting pin. The motor was then secured to an Omega TQM301 reaction torque transducer, full details of which are provided in Section 5.3.1. The torque transducer attached to a supporting base such that the drivetrain was cantilevered from the transducer-base attachment point in order to avoid contact between the drivetrain and base which would have invalidated the torque readings.

The key dimensions and layout of the drivetrain can be seen in Figure 109, along with the fairings and nacelle. The nacelle fairings were constructed in sections using a Makerbot Replicator and were fixed onto the drivetrain support. The fairings were subjected to the same surface treatments as the blades to ensure a good surface finish. The fairings for the nacelle support were manufactured in the same way as those for the main mounting strut fairings detailed in section 5.1.2.2.

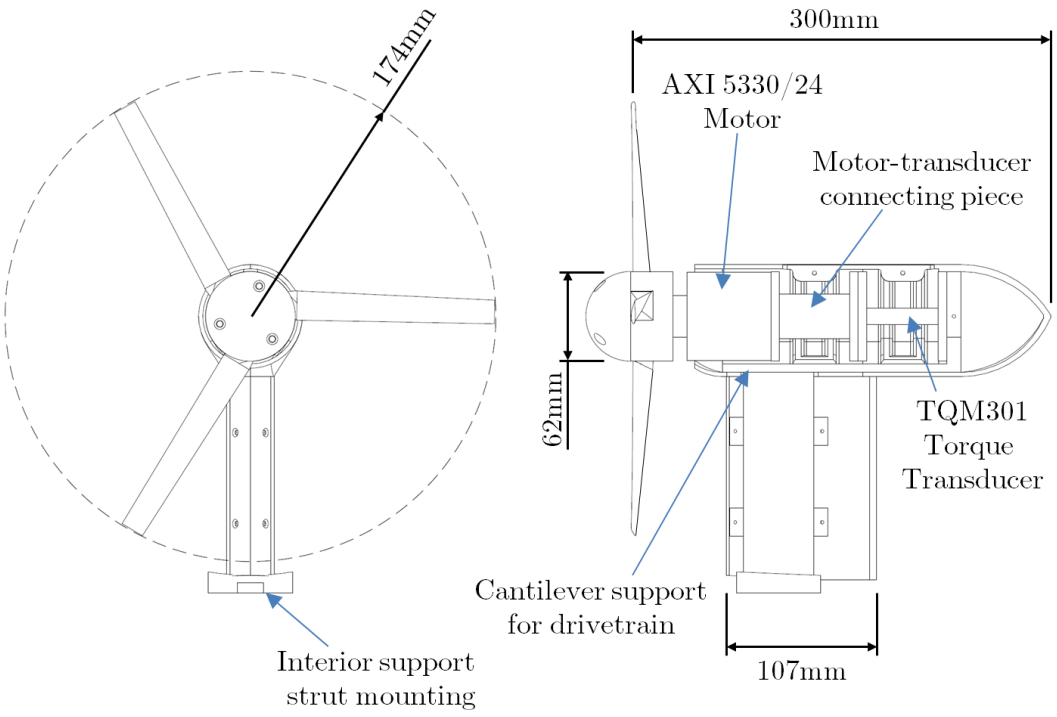


Figure 109: Drivetrain and nacelle details and salient features

The drivetrain and nacelle were secured to the diffuser mounting strut, ensuring that where the diffuser was in place, that the blade clearance within the throat was distributed such that is was uniform circumferentially.

5.1.2.5. Electrical Arrangement

The electrical layout, including the power, control and logging circuits for the experimental rig can be seen in Figure 110. The electrical power system is required to start the rotor in motor mode, dump the electrical power generated during turbine operation and to enable speed control. The switching between motor and turbine operation was achieved through a 3 Phase Double Throw (3PDT) relay switch (Magnecraft 788XCXM4L-12D) which was actuated remotely.

During motor operation, the rectifier and resistor part of the circuit was isolated by the relay and the AXI5330/24 motor was supplied with three phase power via a Jeti Spin 77 Opto speed controller. This acted as an inverter to convert the DC power supplied into three phase AC power for the motor operation. Speed control for the motor operation was achieved via a PWM signal supplied to the controller by the user through the controlling PC.

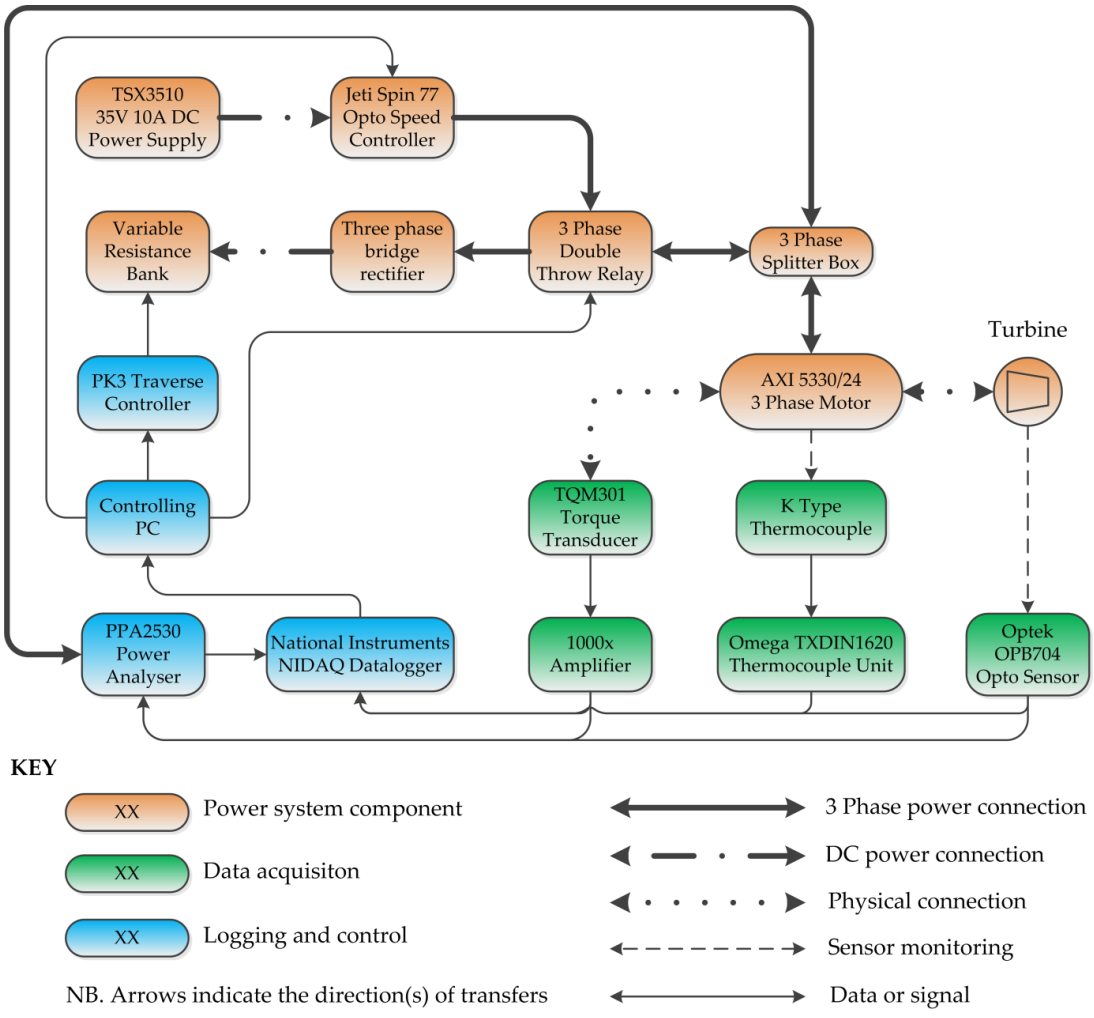


Figure 110: Schematic of the electrical power, logging and speed control circuits

During turbine operation, the inverter part of the circuit was isolated by the relay and the power from the generator was passed to a resistance bank. The layout of this resistance bank can be seen in Figure 111. The three phase power from the generator was converted to DC power to be passed to the resistance bank using a three phase bridge rectifier (IXYS VUO62). The resistance bank was formed of two dual coil variable resistors (Zenith Electrical Company Ltd., 8.2 A, 28 Ω) actuated remotely from the controlling PC by a Unislide traverse unit and stepper motor combination. Speed control of the turbine was enacted using the traverse control of the resistance bank to vary the opposing force to the motion of the rotor.

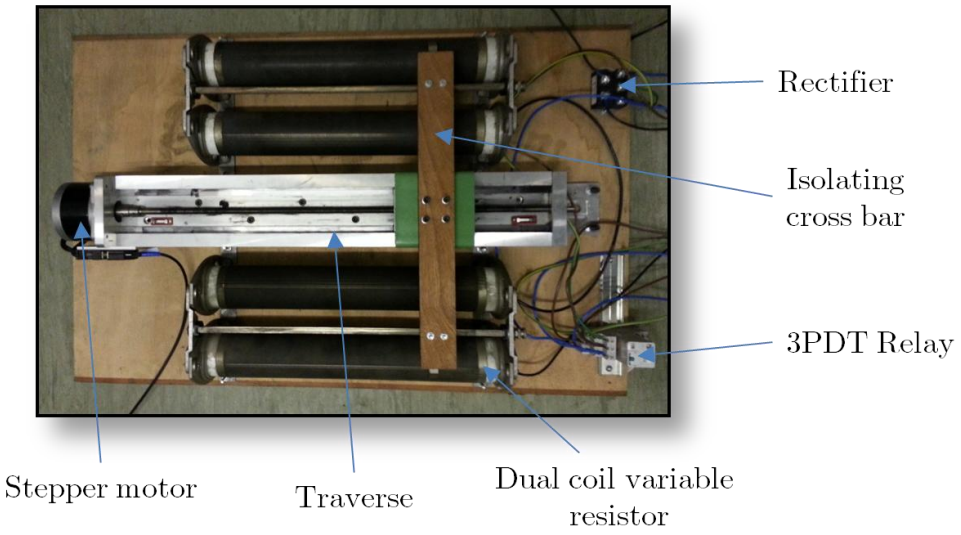


Figure 111: Resistance bank general arrangement

5.2. Experimental Configurations

This section gives an overview of the three separate cases which were examined during the experimentation and the conditions which were tested. The measurement methodologies used for each case are stated and are described in detail in Section 5.3. The experimental rig was placed within the wind tunnel working section, approximately 1/4 of the way into the test section. The position of the rig within the tunnel can be seen in Figure 112.

5.2.1.1. Diffuser Only Experimental Configuration

The diffuser only experimental configuration can be seen in Figure 113. The slot into which the nacelle support strut is placed can be seen open here, during experimentation this slot was covered such that it was flush with the interior surface of the diffuser. In this configuration, only the static pressures from the diffuser and

the aerodynamic forces from the force balance were recorded. The electrical power system was not installed here as it was only required to control the turbine.

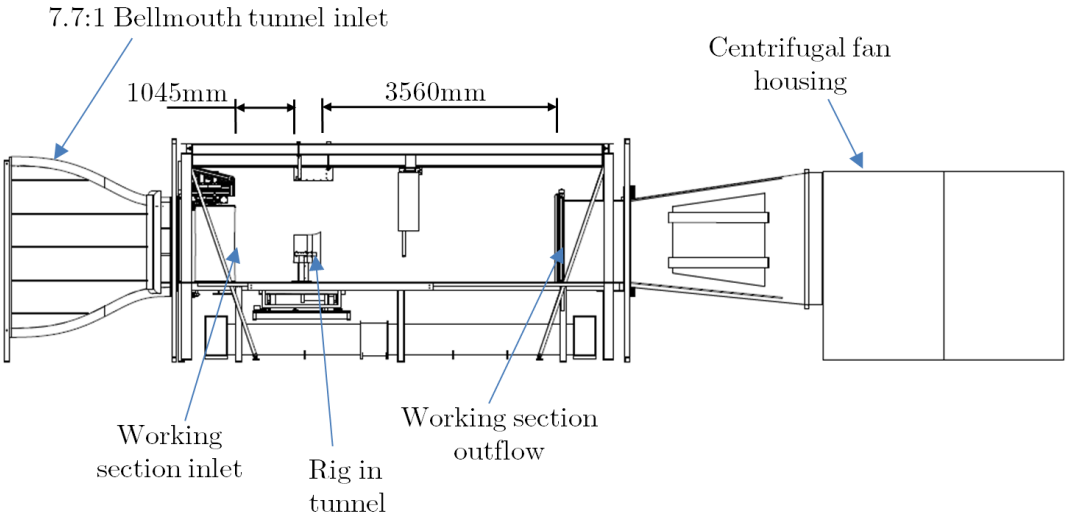


Figure 112: Position of the experimental rig within the wind tunnel

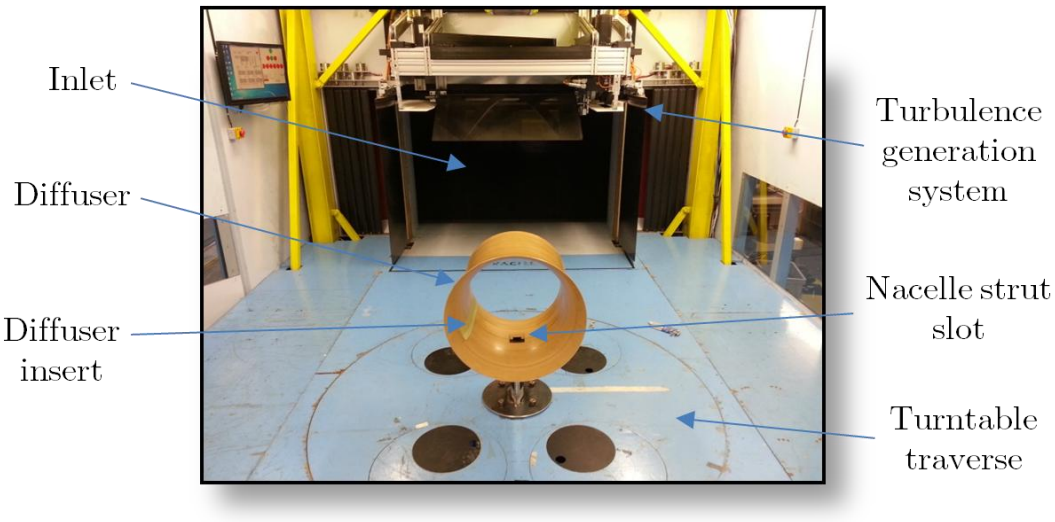


Figure 113: Diffuser only configuration within the wind tunnel looking upstream towards the working section inlet

The experimental runs conducted for the diffuser only case can be seen listed in Table 16, where the Reynolds number is based on the diffuser throat diameter and freestream velocity. These runs were conducted primarily to evaluate the structure of the flow within the diffuser with a variation on the Reynolds number. Additional runs were undertaken to evaluate the impact of the diffuser yaw angle and the interaction between the two factors.

Velocity (m/s)	Reynolds Number	Yaw (Deg)										
		-45.0	-33.8	-31.8	-22.5	-11.3	0.0	11.3	22.5	31.8	33.8	45.0
5.0	1.25E+05						X					
8.7	2.17E+05			X			X			X		
11.3	2.82E+05						X					
14.4	3.60E+05						X					
17.5	4.38E+05	X					X					X
20.6	5.17E+05						X					
23.8	5.95E+05						X					
26.3	6.60E+05			X			X			X		
26.9	6.73E+05						X					
30.0	7.52E+05	X	X		X	X	X	X	X		X	X

Table 16: Experimental tests conducted for the diffuser only configuration

5.2.1.2. Rotor Only Experimental Configuration

The salient features of the rotor only experimental configuration can be seen in Figure 114. The turbine can be seen mounted on the nacelle support strut assembly, which is secured onto the diffuser mounting assembly. The power and data cables from the nacelle can be seen to pass out from beneath the nacelle support assembly and pass through the box section of the diffuser mount and out of the wind tunnel through the floor. In the rear, the five hole probe can be seen mounted on the end of a carbon fibre shaft protruding from the base of the overhead gantry traverse system.

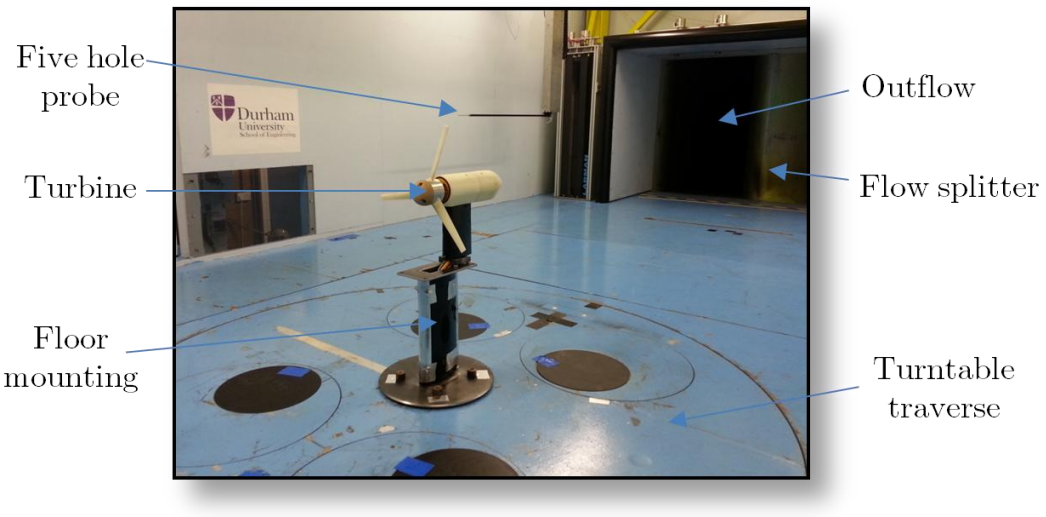


Figure 114: Rotor only configuration within the wind tunnel looking downstream towards the working section outflow

In this configuration, the speed and torque of the motor shaft were recorded as well as the motor temperature, three phase power variables and the aerodynamic

forces from the under floor force balance. Five hole pressure probe traverses were also conducted in the wake of the device as detailed in Section 5.2.1.4.

The experimental runs conducted for the rotor only case for each blade set can be seen listed in Table 17, where the Reynolds number is based on the rotor tip diameter and freestream velocity. These runs were conducted to evaluate the power output from the rotor with variations of the Reynolds number, yaw angle and tip speed ratio. The tip speed ratio range tested varied between cases, being limited by both the mechanical limits of the apparatus and the rotor's $C_P - \lambda_R$ curve. For the zero yaw cases, the rotor was tested up to a minimum tip speed ratio of 5.

Velocity (m/s)	Reynolds Number	Yaw (Deg)									Tip Speed Ratio
		-45.0	-31.8	-30.0	-15.0	0.0	15.0	30.0	31.8	45.0	
15.0	3.76E+05					X					0.5 to Limit
16.8	4.20E+05					X					0.5 to Limit
17.1	4.27E+05		X			X			X		0.5 to Limit
18.5	4.64E+05					X					0.5 to Limit
20.3	5.07E+05					X					0.5 to Limit
22.0	5.51E+05	X		X	X	X	X	X		X	0.5 to Limit
23.8	5.95E+05					X					0.5 to Limit
25.5	6.39E+05					X					0.5 to Limit
26.9	6.75E+05		X			X			X		0.5 to Limit
27.3	6.83E+05					X					0.5 to Limit
29.0	7.27E+05					X					0.5 to Limit

Table 17: Experimental tests for the rotor only configuration with each blade set

5.2.1.3. Diffuser and Rotor Experimental Configuration

The key features of the combined diffuser and rotor experimental configuration can be seen in Figure 115. The turbine can be seen mounted within the diffuser assembly, which is secured onto the diffuser mounting assembly. In this configuration, the speed and torque of the motor shaft were recorded as well as the motor temperature, three phase power variables, diffuser static pressures and the forces from the under floor force balance. Five hole pressure probe traverses were also conducted in the wake of the device as detailed in Section 5.2.1.4.

The experimental runs conducted for the combined diffuser and rotor only case for each blade set can be seen listed in Table 18, where the Reynolds number is based on the diffuser throat diameter and freestream velocity.

The runs detailed in Table 18 were conducted to evaluate the power output from the rotor with variations of the Reynolds number, yaw angle and tip speed

ratio and to investigate the associated aerodynamic effects within the diffuser. The tip speed ratio range tested varied between cases, being limited by both the mechanical limits of the apparatus and the rotor's $C_P - \lambda_R$ curve. For the cases where there was no yaw, the rotor was tested to a minimum tip speed ratio of 6.

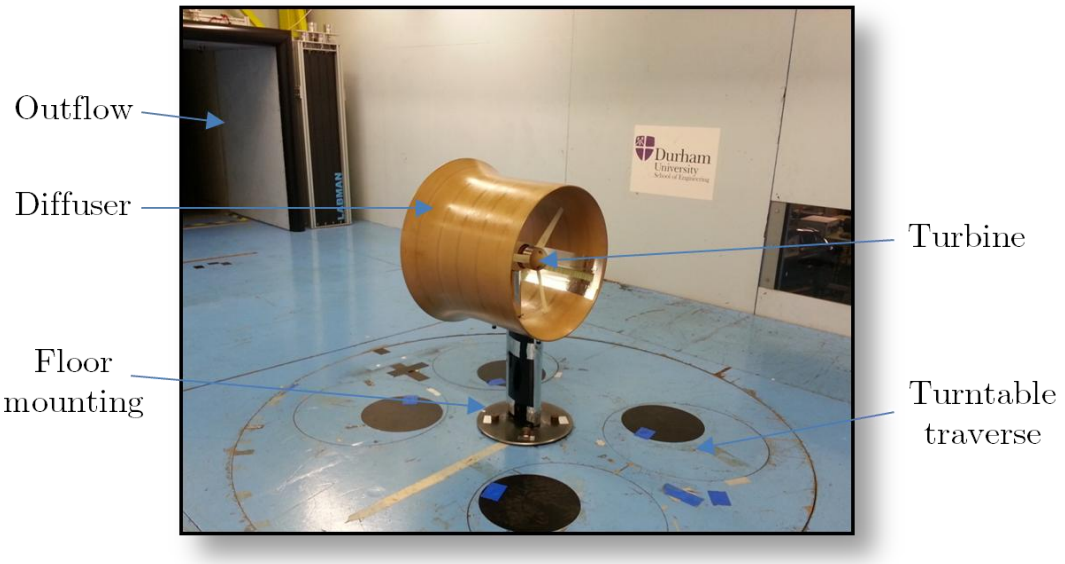


Figure 115: Combined diffuser and rotor configuration within the wind tunnel looking downstream towards the working section outflow

Velocity (m/s)	Reynolds Number	Yaw (Deg)									Tip Speed Ratio
		-45.0	-31.8	-30.0	-15.0	0.0	15.0	30.0	31.8	45.0	
15.0	3.76E+05					X					0.5 to Limit
17.1	4.27E+05		X			X			X		0.5 to Limit
18.5	4.64E+05					X					0.5 to Limit
22.0	5.51E+05	X		X	X	X	X	X		X	0.5 to Limit
25.5	6.39E+05					X					0.5 to Limit
29.0	7.27E+05					X					0.5 to Limit

Table 18: Experimental tests conducted for the combined diffuer and rotor configuration with each blade set

5.2.1.4. Wake Traverses

Wake traverses were conducted for the rotor only and combined diffuser and rotor cases on two separate planes, a longitudinal plane at turbine axis height and a transverse plane parallel to the rotor plane. The planes used were identical for both experimental configurations. The layouts of the planes and the sample points can be seen in Figure 116, where the vertical plane is at x/R=1.6.

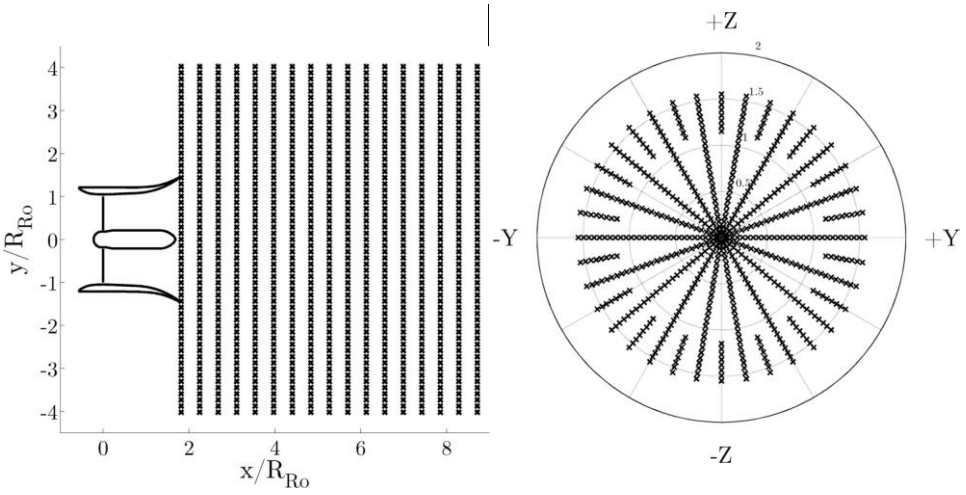


Figure 116: (a) Horizontal and (b) vertical planes and sampling points with coordinates normalised by the blade radius

The wake traverses conducted and the associated conditions are detailed in Table 19. All of the wake traverses were conducted using the -5° pitch blades.

Configuration	Plane	Nominal Re	Tip Speed Ratio
Rotor Only	Horizontal	4.90E+05	5.3
Rotor Only	Vertical	4.90E+05	5.3
Combined	Horizontal	5.30E+05	5.5
Combined	Vertical	5.30E+05	5.5

Table 19: Wake traverse details and flow conditions

5.3. Data Collection and Measurement Techniques

The data collection and measurement techniques used within this thesis are detailed in this section. The layout of the complete setup of the transducers and logging equipment for the combined diffuser and rotor experimental runs can be seen in Figure 117. For the diffuser only or rotor only runs the experimental setup differed as some components were removed, see Section 5.2 for more information.

5.3.1. Torque Sensor Measurements

The torque sensor used was a reaction torque sensor type unit mounted at the rear of the cantilevered drivetrain as seen in Figure 108 and Figure 109. The unit was an Omega TQM301-45N model. This unit has an operating range of 0-45 Nm of torque with a safe overload capacity of 150%. The unit has a stated combined maximum linearity, hysteresis and repeatability error of ±0.2% of the full scale span.

The transducer was amplified with a gain of 1000 using a load cell amplifier which was constructed using a strain gauge amplifier (RS 308-815). The calibration and operation of the torque sensor was undertaken with the same equipment.

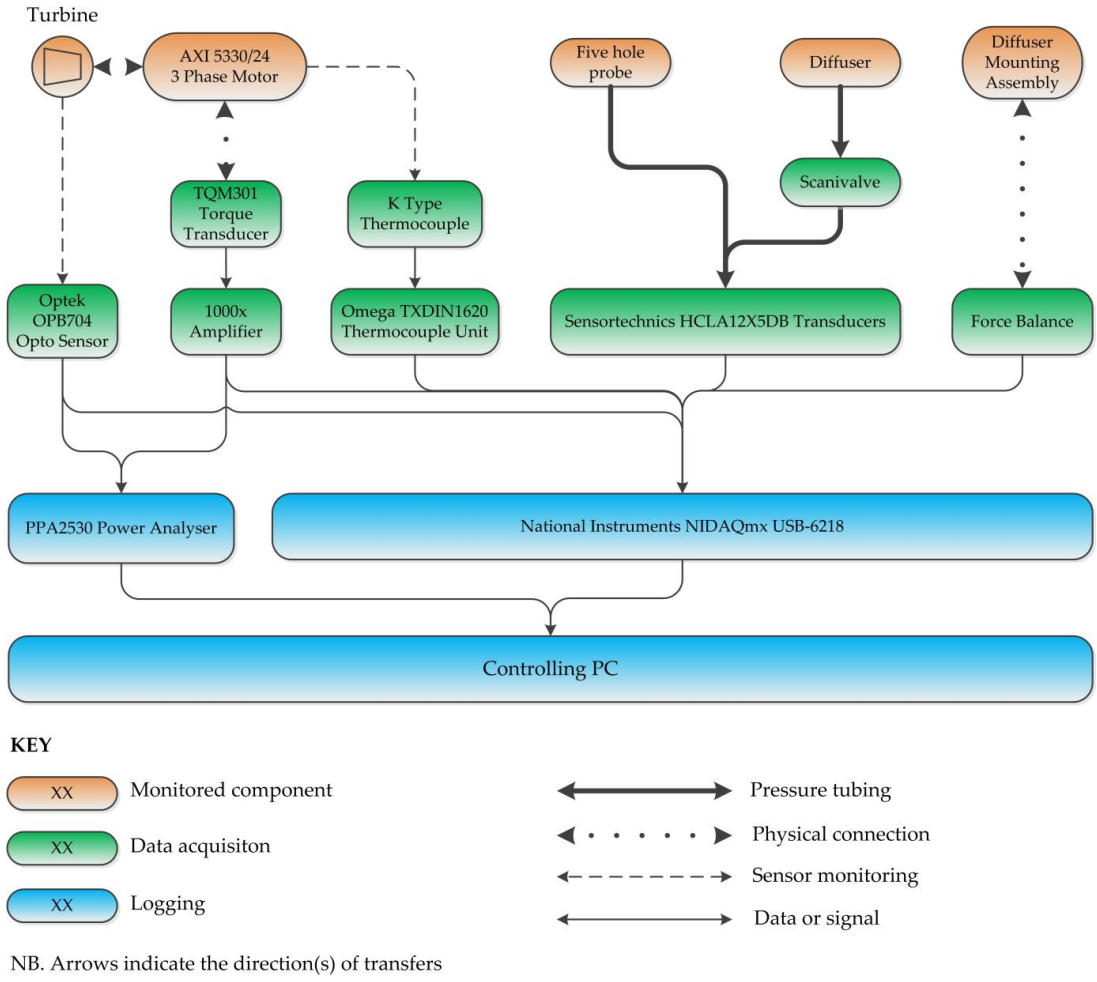


Figure 117: Logging layout for experimental runs

The unit was calibrated in place on the drivetrain to ensure that the addition of the cantilevered drivetrain did not affect the calibration. The calibration was undertaken using known masses applied via a lever arm of a known length. The masses were weighed using scales and recorded to within $1/10^{th}$ of a gram. The length of the lever arm was measured using a pair of Vernier callipers and recorded to $1/10^{th}$ of a millimetre. The voltage output was recorded at 800 Hz in a low noise environment using a National Instruments NIDAQmx USB-6218 logging card and recorded on the controlling PC. The uncertainty in the measurements was calculated from the calibration data and found to be $\pm 1.64 \times 10^{-3}$ Nm [177].

The compensated temperature range of the sensor is 16°C to 72°C, with thermal effects of ±0.0028% of the 45 Nm rating per degree Celsius. The maintenance of the sensor within the thermal operating conditions was verified by the use of the thermocouple installed within the nacelle. To minimise noise, the sensor was also fitted with a screened cable. The components of the torque sensor enable measurement of signal frequencies of up to 200 Hz.

5.3.2. Reflective Phototransistor

The turbine rotational speed was measured by a reflective phototransistor type optical switch. The position of the sensor can be seen in Figure 118.

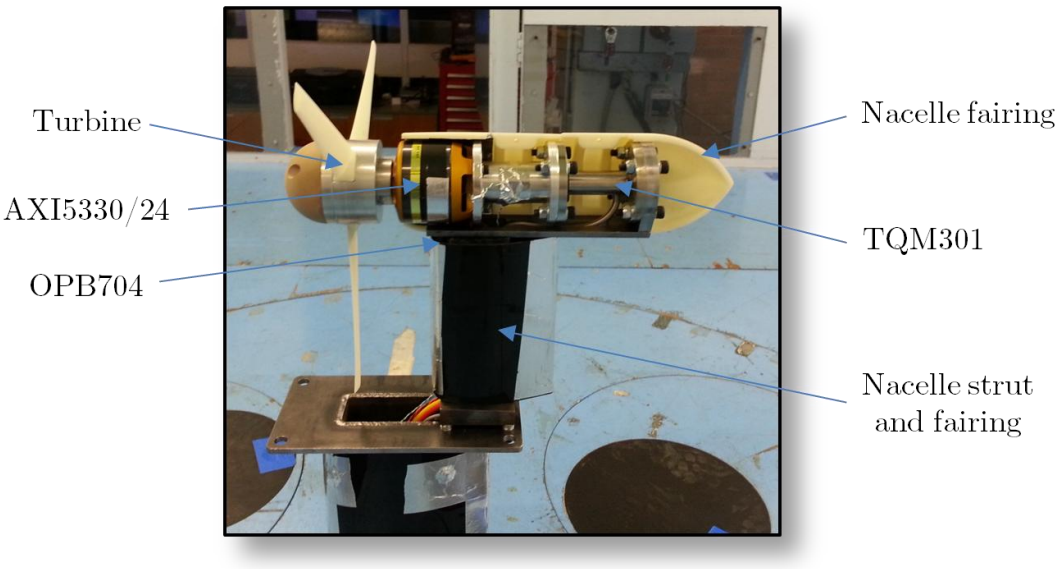


Figure 118: Nacelle layout with location of the OPB704 reflective phototransistor

The model used was an Optek OPB704, which was mounted beneath the motor, between the nacelle support strut and the fairing. The AXI5330/24 motor's exterior was free to rotate with the rotor and nose cone assembly and this was used covered for 50% of the circumference with a matte black finish and 50% with a reflective silvered finish, to trigger the reflective phototransistor.

The OPB704 sensor generates a square wave output signal of 0-5 V with the output dependent upon the surface onto which it is directed. The accuracy of the rotational frequency measurements taken with the OPB704 sensor was verified through comparison with the phase frequency data from the PPA2530 power analyser detailed in Section 5.3.7.

In order to calculate the error in the frequency values captured using the OPB704 sensor an experiment was undertaken using a stroboscope. The stroboscope was set to a range of frequencies over the operating range of the turbine and the errors in the calculation of the frequency were determined. It was found that the combined data collection and processing error was ±0.023 Hz.

5.3.3. Pressure Transducers

Pressure transducers were used to record static pressure measurements from the diffuser surface, pressures from the five hole probe and the wind tunnel's reference pressures. The pressure transducers used in all cases were Sensortechnics HCLA12X5DB transducers. These have an operating range of 0 Pa to 1.25 kPa with a proof pressure of 5 kPa. The peak pressures expected during testing were of the range 0 Pa to 980 Pa, and so they were more than adequate for these experiments. The units have a reported drift of 0.1% of full scale span (FSS) per year, with thermal effects in the range -25°C to 72°C being a maximum of 2.0% of FSS. The error in the pressure readings was calculated from data gathered by supplying the transducers with a range of known pressures from an oil filled manometer. The error in the pressure readings was found to be ±0.169 Pa.

The transducers were formed into banks of two sizes, double transducer banks, intended for pitot-static probes and five transducer banks intended for use with five hole probes. The transducer's calibration was verified using an oil filled micro-manometer prior to testing. All connections to the transducers were made using Thermo Scientific Nalgene pressure tubing.

5.3.4. Static Pressure Tappings

The static pressure tappings on the diffuser surface were connected to a 64 port Scanivalve which was controlled via the Durham Software for Windtunnels suite. The DSW software is a collection of programs written in C code for the automated control and data collection of experiments within the wind tunnels of Durham University. There were a total of 28 static pressure tappings on the diffuser surface, distributed as seen in Figure 119. There were a total of 7 tappings distributed evenly along the exterior surface of the diffuser and 21 tappings distributed along the interior surface. The tappings on the interior are primarily grouped around the turbine plane at $X/L_{Di} \cong 0.2$, with an increased spacing towards the trailing edge. The tappings end at $X/L_{Di} \cong 0.78$ as there is insufficient space within the diffuser cross section to include further tappings.

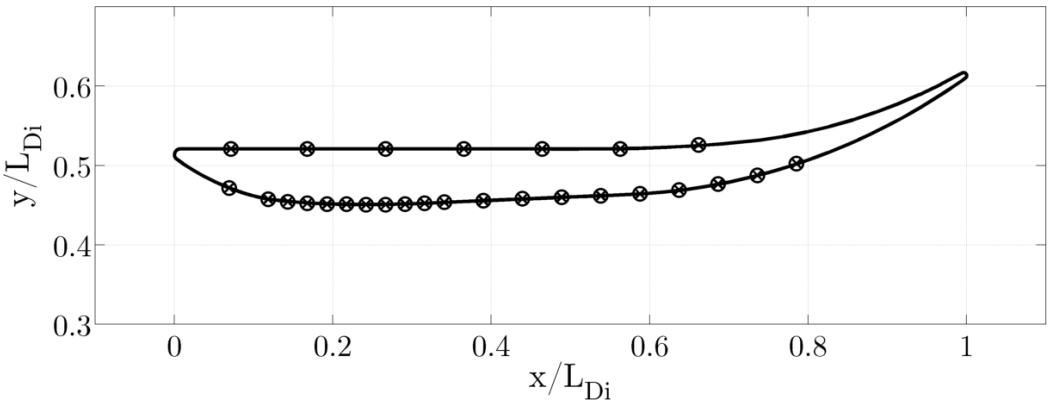


Figure 119: Static pressure tapping locations on the diffuser surface

5.3.5. Five-Hole Pressure Probe

In order to assess the wake of the turbine and diffuser and derive the pressure and velocity fields, a five hole probe was used. The Durham University five hole probe geometry can be seen in Figure 120, along with the hole numbering system. The hole numbering system indicated here is based on the reader looking head on to the tip of the probe. The probes are made of steel, with a rapid prototyped head and a rapid prototyped stay within the steel boss. The pressure is transferred from the head to the pressure tubing attachment points by means of hypodermic tubing, with the head to tube joints being sealed by epoxy resin.

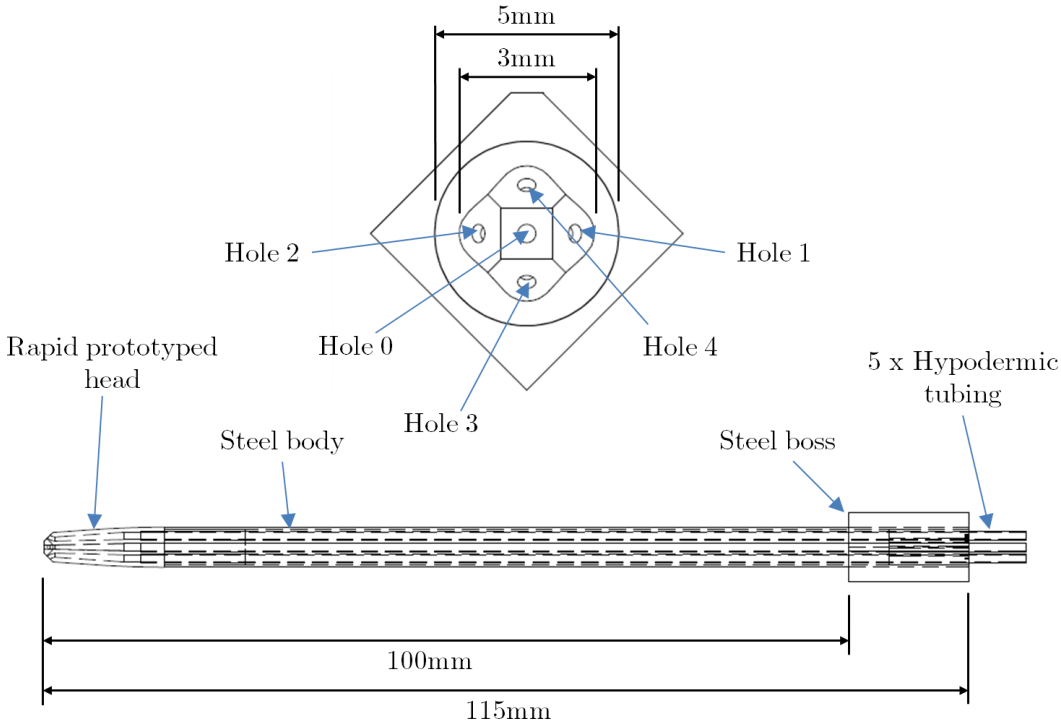


Figure 120: Details of the Durham University five hole probe with hole numbering

Within this work the probe has been used only for the steady state assessment of the wake structure. The probes have sufficient resolution however that they can be used to assess high frequency transients within the flow through the use of transfer function corrections for the tubing attenuation.

The equations used to obtain the average pressure and the flow yaw, pitch, total and dynamic pressure coefficients are given by Equation 81 to Equation 85.

$$p_{AVG} = \frac{p_1 + p_2 + p_3 + p_4}{4} \quad \text{Equation 81}$$

$$C_{YAW} = \frac{p_1 - p_2}{p_0 - p_{AVG}} \quad \text{Equation 82}$$

$$C_{PITCH} = \frac{p_3 - p_4}{p_0 - p_{AVG}} \quad \text{Equation 83}$$

$$C_{p_t} = \frac{p_0 - p_t}{p_0 - p_{AVG}} \quad \text{Equation 84}$$

$$C_{p_{Dyn}} = \frac{p_t - p_{AVG}}{p_{Dyn}} \quad \text{Equation 85}$$

To calibrate a probe, the probe is set to traverse over a high density grid of pitch and yaw angles and the coefficients in Equation 81 to Equation 85 are calculated at each point. The reference velocity was calculated from a nozzle calibration, which used static pressures upstream and downstream of the nozzle to derive the flow velocity. The flow velocity and static pressure were used to calculate the total and dynamic pressures necessary for Equation 84 and Equation 85.

When the probe was used for testing, the coefficients were again calculated and the calibration map was interpolated in two dimensions to recover the actual yaw and pitch angles as well as the total and dynamic pressures.

The probe used in the work contained here was calibrated at a wind speed of 22 m/s over an angle range of ±60° for both pitch and yaw, with a grid density of 2.5°. The probe coefficients tend to breakdown where the magnitude of the flow angle relative to the axis of the probe exceeds 45°, and so flow in these regions cannot be resolved using the five hole probe. Since the wakes of the device configurations examined here were not expected to deviate excessively from the axial direction this was sufficient for the work conducted here.

5.3.6. Force Balance

The under floor force balance employed in the testing was mounted onto the under floor traverse turntable. For further information on the details of the under floor balance the reader is referred to Sims-Williams et al. [171]. The force balance was calibrated using methodology detailed by Mankowski [173].

5.3.7. Three Phase Power Measurements

Three phase power measurements were captured using a Newtons4th Ltd PPA2530 three phase power analyser. This power analyser allows for measurement of power flows with currents of up to 30 A and voltages of up to 3 kV per phase with an accuracy of ±0.04% of the reading. The power analyser is capable of connecting to the reflective phototransistor and torque sensor and hence provides the calculated mechanical power in addition to the basic and derived electrical properties. The device can be connected to a PC via a variety of methods, with a USB connection employed here. The PPA Datalogger software which accompanies the device was used as the main means of providing real time performance data to the user for the operation of the rig as this is relayed to a graphical user interface.

The data from the power analyser was used mainly for the control of the experimental rig but was also saved onto the controlling PC with a time stamp along with the data from the NIDAQmx card. This data was collated with the NIDAQmx data in post-processing and enabled checks to be made on the drivetrain data as stated in Section 5.3.2.

5.3.8. Logging Methodology

The data logging during the experimentation was achieved through the use of the DSW software suite, which has a wide variety of logging and data processing functions. The DSW software is able to interface with all of the necessary hardware detailed in Figure 117 and to log the output data. The NIDAQmx card is able to log up to 16 differential channels at a maximum frequency of 250 kHz.

The experimental data was sampled at a frequency of 1024 Hz, which compared to a peak blade passing frequency for the turbine of 500 Hz (though the frequency was usually far below this). The logging frequency was limited by the response times of the various transducers, with 1024 Hz being able to capture the most rapid changes that these produce. The data contained here is intended to be steady state data. In order to mitigate the proximity of the sampling frequency to

the peak blade passing frequency, the sampling time was extended to 4s for each data point taken. This means that for the fastest turbine rotational speed the data is averaged over a total of approximately 2000 blade passes.

5.3.9. Filtering Methodology

During preliminary testing it was found that there was a large quantity of electrical noise which was present in some of the voltage signals which were entering the datalogger. These signals were treated using one of two possible methods, a low pass filter circuit inserted between the transducer and datalogger and/or numerical low pass filtering applied during post-processing.

The filter circuits used were 250 Hz low pass filters, which were implemented where the anticipated signal frequency was to be below 250 Hz and where the underlying physical significance of the signal would remain unchanged. The reference pressures and the signal from the resistive phototransistor were run through these circuits. The resistive phototransistor was treated, as although the peak blade passing frequency is 500 Hz, the peak rotational frequency, the measured quantity, was only 166Hz. In order to maintain a clear signal, which allowed frequency determination, the higher frequency noise was eliminated.

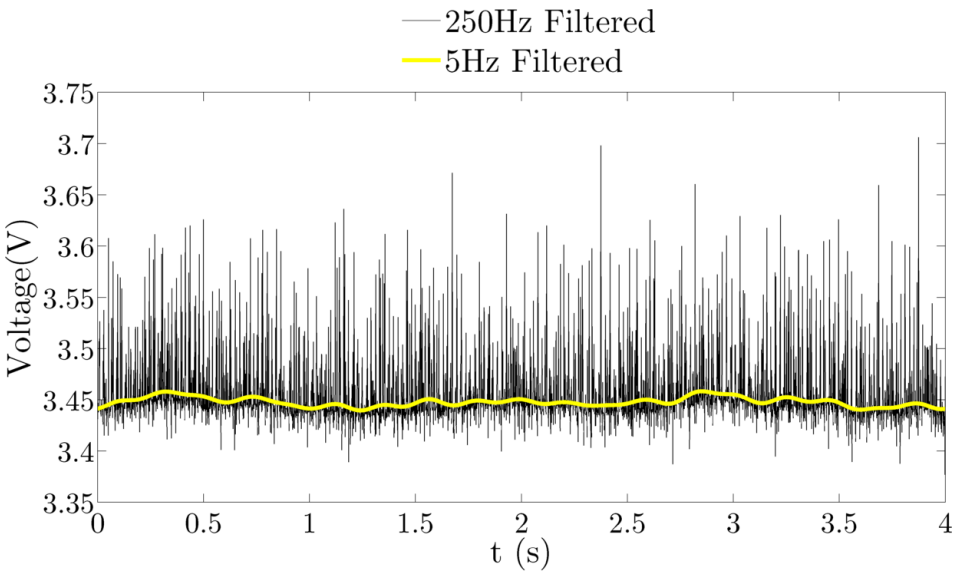


Figure 121: Numerically filtered for example signal using a 5 Hz low pass filter

The reference pressures were treated with numerical filtering using low pass filters which were based upon 3rd Octave Class 0 Bandpass Filters as per ANSI S1.11-2004 [178]. The bandpass filter midpoint was used as the low pass filter design frequency, with the form of the low pass filter remaining identical to the bandpass

above this frequency. Below this frequency the transfer function magnitude employed was set to unity such that lower frequency components are replicated exactly in the filter output. The output from a sample signal which has passed through the 250 Hz filter circuit and then through a numerical 5 Hz low pass filter can be seen in Figure 121.

5.3.10. Overall Estimate of the Uncertainty

The uncertainties in the estimates of the variables used within the experimental sections of this thesis have been calculated and are presented in Table 20. The values have been calculated using methodology detailed by Hughes and Hase [177]. The uncertainties in the measured variables are all below 0.56% of the full scale readings, with derived quantities all below 1.00% of the full scale values.

Variable	Error	Unit
Distance	±0.100	mm
Pressure	±0.169	Pa
Temperature	±0.250	℃
Density	±0.004	kg/m^3
Velocity	±0.066	m/s
Viscosity	$\pm 1.24 \times 10^{-8}$	Pas
Reynolds Number	±1147.896	-
Pressure Coefficient	±0.004	-
Pressure Recovery Coefficient	±0.004	-
Frequency	±0.023	Hz
Rotational Speed	±0.144	rad/s
Tip Speed Ratio	±0.012	-
Torque	±0.002	Nm
Power	±1.051	W
Power Coefficient	±0.003	-

Table 20: Errors in the experimental and derived quantities

The main source of divergence of results from the quantities which could be expected in unbounded flow will be the effect of the wind tunnel blockage. As stated in Section 5.1.2.1, a conservative estimate of the effect of the blockage is a change in the velocity field of the order of 1.18% and a 3.58% change in the power output. It is considered that given the very low overall level of the uncertainties within the

experimental methodology, that the results provide an accurate assessment of the physical phenomenon under investigation.

5.4. Concluding Remarks

This chapter details the experimental methodologies and setups used within this thesis. This chapter contains details of the experimental rig design, apparatus set up and data processing methods such that the results are reproducible. The level of uncertainties within the experiments have been quantified and found to be low enough that the results provide an accurate assessment of the phenomenon investigated. The results from these experiments are detailed in Chapter 6, where they are compared with the numerical results from Chapter 4.

6. Experimental Results

6.1. Diffuser Characterisation

In order to understand the behaviour of the combined diffuser and turbine device it is first necessary to understand the flow through the empty diffuser. In this section, results for the diffuser are presented for the cases tested as detailed in Chapter 5 and compared with the relevant CFD cases detailed in Chapters 3 and 4.

6.1.1. Effect of Reynolds Number

The effects of variations in the Reynolds number of the incoming flow were quantified for the open diffuser by tests performed with a varying inlet flow velocity in the wind tunnel. The inlet speed was varied in the range from 15 m/s to 29 m/s, giving a range of Reynolds numbers from $Re_{DiU_\infty} = 2.7 \times 10^5$ to $Re_{DiU_\infty} = 7.2 \times 10^5$, where the Reynolds number was calculated using the tunnel inlet flow velocity and the diffuser throat diameter. The static pressure coefficient from the experimental results along both the exterior and interior diffuser surfaces can be seen in Figure 122, which also shows the cross section of the diffuser geometry.

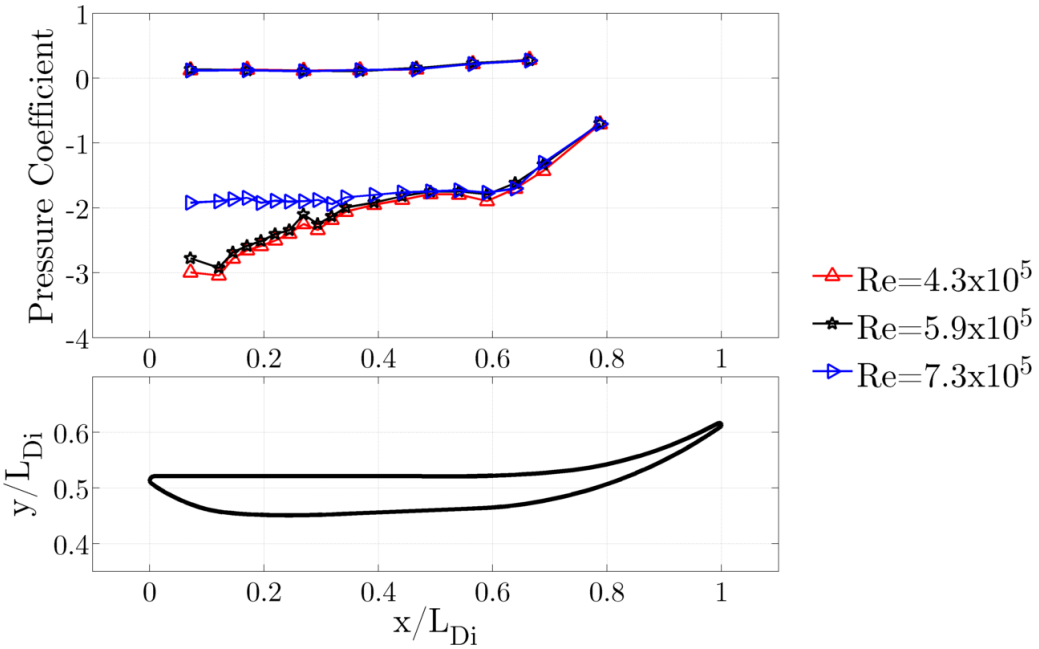


Figure 122: Experimental static pressure coefficient around the diffuser for empty diffuser with variation of the Reynolds number, showing the diffuser geometry

The trends in the pressures which can be seen in Figure 122 show that the majority of the diffusion is occurring in the rear section of the casing due to the

streamwise expansion of the flow. The diffusion occurs over the length $0.2 < \frac{x}{L_{Di}} < 0.8$, where the flow remains attached to the interior of the casing. At $\frac{x}{L_{Di}} \cong 0.8$ the flow has insufficient boundary layer energy and separates from the surface of the casing preventing further flow expansion and diffusion. The static pressure coefficient results are compared with the CFD predictions in Figure 123.

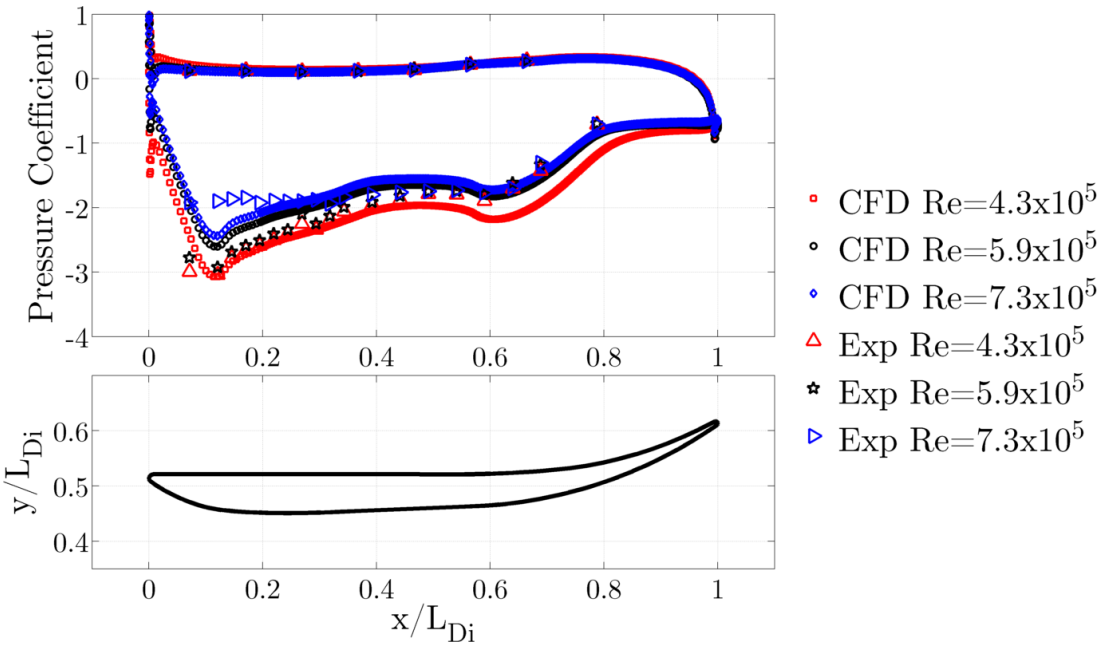


Figure 123: Experimental and CFD static pressure coefficients around empty diffuser with variation of the Reynolds number, showing the diffuser geometry

An increase in the Reynolds number moves the separation point of the flow forward along the interior diffuser surface. This move in the separation point causes a reduction in the flow expansion, reducing diffusion and therefore increasing the pressure coefficient along the interior surface of the casing. The CFD results provide a good approximation to the experimental results at low Reynolds numbers but fail to predict the separation bubble in the range $0.1 < \frac{x}{L_{Di}} < 0.3$ on the interior diffuser surface seen at higher Reynolds numbers.

6.1.2. Effect of the Yaw Angle

The effect of the yaw angle on the diffuser was examined by investigating the static pressure along the diffuser interior surface for a range of flow angles. Figure 124 shows the definition of the yaw angle within the wind tunnel and the location of the static pressure tapping insert within the diffuser. Figure 125 and Figure 126 show the static pressure coefficient around the diffuser geometry for the downwind

and upwind halves of the traverse respectively. Upstream and downstream refer to the location of the static pressure tapping insert relative to the diffuser orientation.

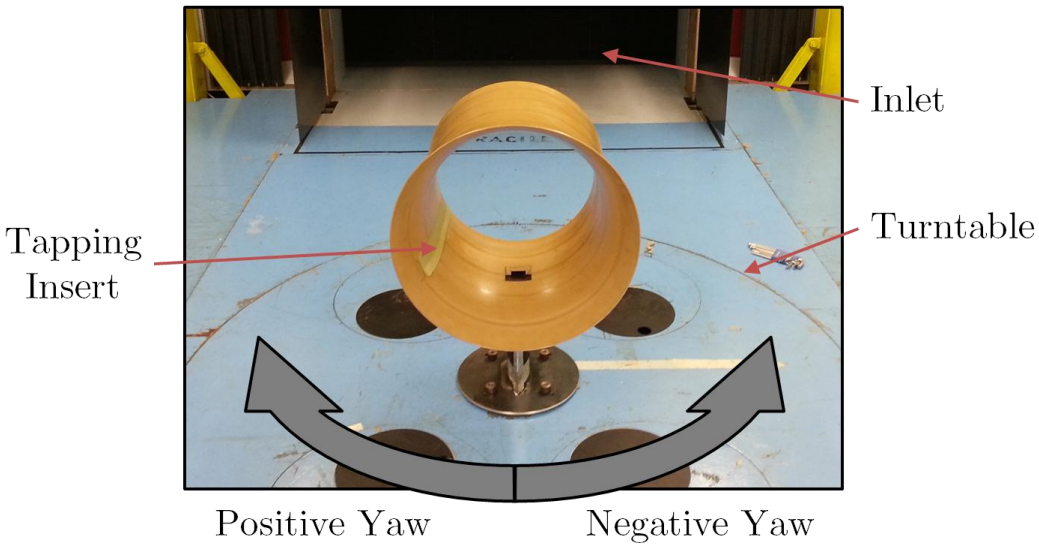


Figure 124: Definition of yaw angle for diffuser only cases

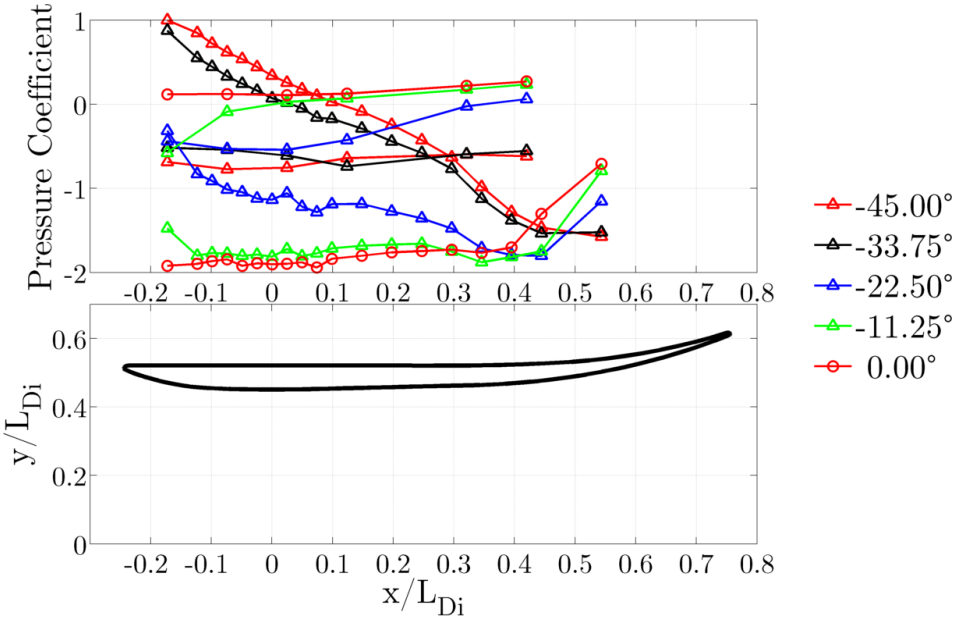


Figure 125: Experimental static pressure coefficient around empty diffuser with variation of yaw angle on downstream section, showing the diffuser geometry

The trends seen in Figure 125 for the downwind section are less revealing about the state of the diffuser flow than the upwind data seen in Figure 126. This is because the turning of the diffuser interior towards the perpendicular of the inflow means that the pressures are a function of the inflow dynamic pressure. As a result the yaw pressures are compared on the upstream section of yaw traverses elsewhere.

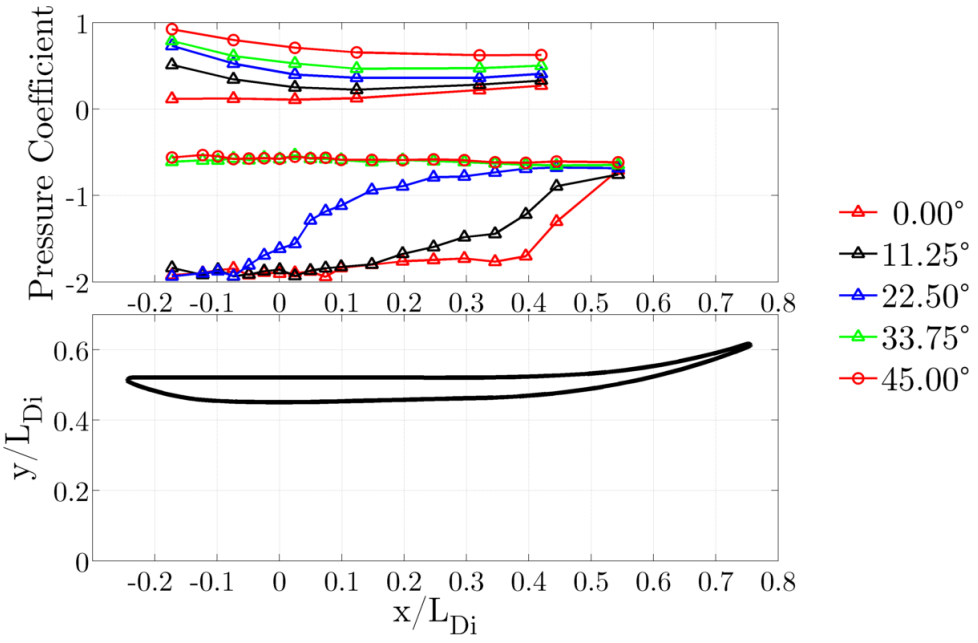


Figure 126: Experimental static pressure coefficient around empty diffuser with variation of the yaw angle on upstream section, showing the diffuser geometry

It can be seen from Figure 126 that even a slight yawing of the flow induces earlier diffuser stall. At 11.25° the separation point begins to move forwards within the diffuser, with the stall process mostly complete by 22.50°. Once the yaw angle passes 33.75° the flow is completely stalled within the diffuser on the upwind side.

6.1.3. Effect of the Nacelle Geometry

The inclusion of the nacelle and the associated support strut, without the rotor, has a significant effect upon the flow within the diffuser. The pressure coefficient distribution around the diffuser can be seen in Figure 127, which also shows an axisymmetric cross section of the diffuser and hub geometries.

It can be seen from the experimental results presented in Figure 127 that the diffuser's ability to sustain a low pressure in the throat has been removed to a large extent by the inclusion of the nacelle and strut. The combined effect is to significantly reduce the diffusion potential of the device by causing a blockage in the rear of the diffuser. The blockage is caused by flow separation from the hub around the expansion at $\frac{x}{L} \cong 0.3$. The exact location of the separation within the experiment is not known, though the separation of the flow at $\frac{x}{L} \cong 0.3$ within the CFD provides a good approximation to the flow conditions experienced in the real device. Normalised velocity contours and streamtraces plotted from CFD data can be seen

in Figure 128 for a Reynolds number, based on the diffuser throat diameter and freestream velocity, of $Re_{DiU_\infty} = 5.9 \times 10^5$.

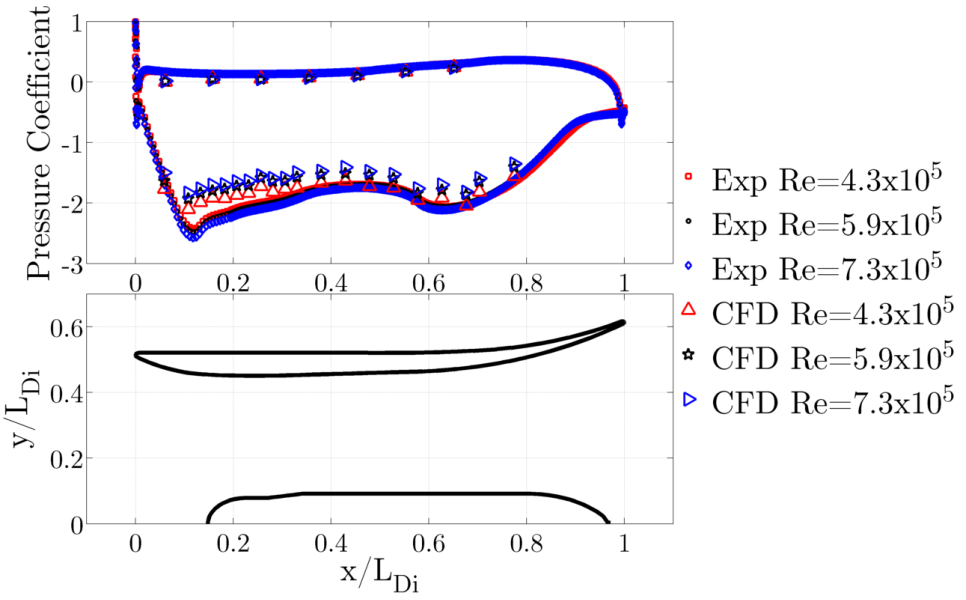


Figure 127: Static pressure coefficient around diffuser for diffuser and nacelle case with variation of the Reynolds number, showing the diffuser and nacelle geometries

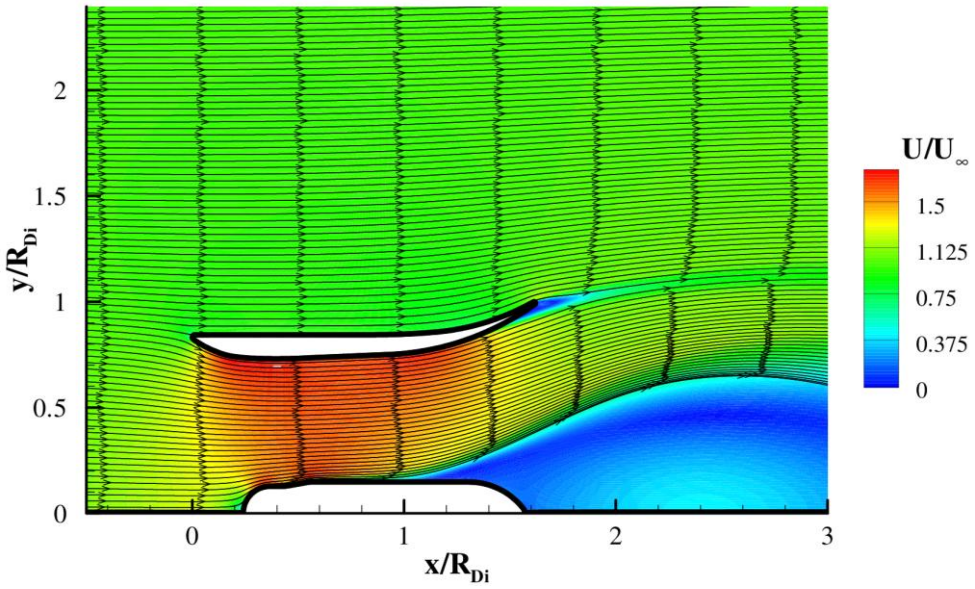


Figure 128: Contours of normalised velocity and streamtraces from CFD for experimental hub and diffuser with no turbine at $Re_{DiU_\infty} = 5.9 \times 10^5$

As can be seen from Figure 128, the separation of the hub flow generates a volume of recirculating flow in the rear of the diffuser, which blocks the diffuser exit and reduces the flow velocity, therefore increasing the pressure within the diffuser throat. The problem of resolution of the separation point in the CFD model means

that the diffusion which occurs is over predicted and as a result so is the swallowing capacity of the diffuser and the pressure reduction in the throat. In contrast to the diffuser only case, the flow does not separate from the interior diffuser wall as it now separates instead from the hub. The reduced swallowing capacity of the duct with the nacelle geometry acts to suppress the separation of the flow from the diffuser in the range $0.1 < \frac{x}{L} < 0.3$ at the higher Reynolds numbers as the flow velocity is reduced and so the state of the boundary layer in this region is changed.

6.2. Rotor Characterisation

The next stage in understanding the behaviour of a combined diffuser and turbine arrangement was to examine the flow around the rotor. In this section, results from the wind tunnel for both rotor geometries detailed in Chapter 4 are presented. In this section, where the Reynolds number is referenced it is based upon the freestream velocity of the flow and the rotor diameter.

6.2.1. Effect of Reynolds Number

The effects of variations in the Reynolds number of the incoming flow upon the performance of a bare turbine were investigated by varying the inlet flow velocity in the wind tunnel. The inlet speed was varied in the range from 15 m/s to 29 m/s, giving a range of $Re_{RoU_\infty} = 2.7 \times 10^5$ to $Re_{RoU_\infty} = 7.2 \times 10^5$. The results for the variation of the rotor power coefficient with the tip speed ratio and Reynolds number are shown in Figure 129 for the two rotors used in the tests.

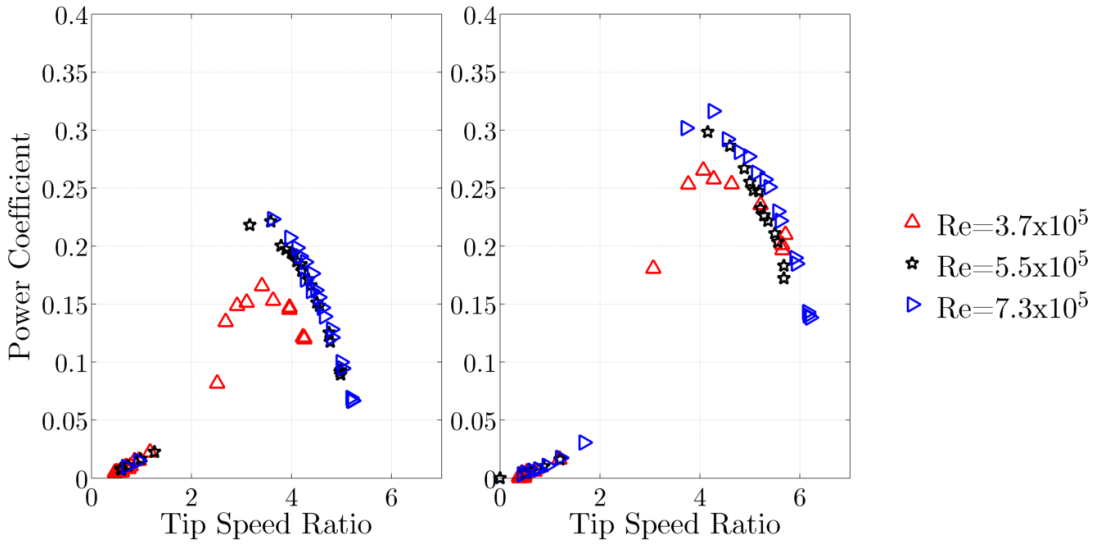


Figure 129: Power coefficient against rotor tip speed ratio for bare rotors with variation of the Reynolds number (a) 0° pitch (b) -5° pitch

Figure 129 shows that at low Reynolds numbers the rotors both suffer from a reduction in the power coefficient, this being particularly marked with the non-pitched rotor. This effect on the performance is caused by laminar separation of the flow from rotor blades at low Reynolds numbers as detailed in Chapter 4. This effect is particularly noticeable at low tip speed ratios due to the lower relative flow velocity. The performance at higher tip speed ratios is improved as the rotational speed of the rotor acts to increase the relative velocity at the blade and therefore the Reynolds number over the blade section. At the full operational device scale these effects would become negligible due to the significantly greater Reynolds numbers experienced by the blades at the operating conditions.

6.2.2. Verification of the Rotor Only Blade Element CFD

The experimental results at a Reynolds number of $Re_{RoU_\infty} = 5.5 \times 10^5$ are compared with those from the blade element momentum model and the implementation of the blade element momentum model within the CFD in Figure 130. Full details of the models and their implementation are presented in Chapter 3.

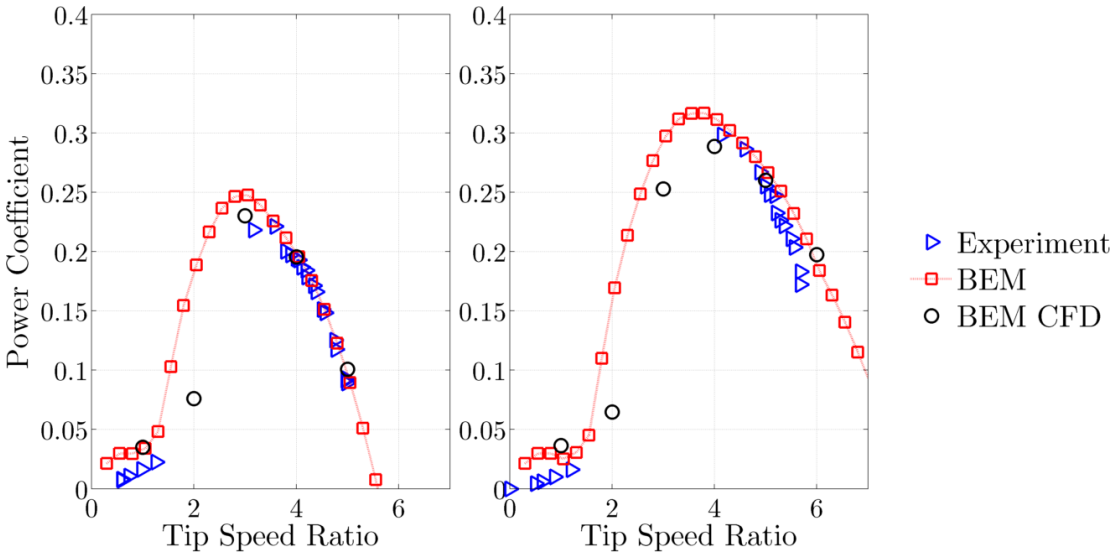


Figure 130: Comparison of blade element momentum, blade element mometum CFD and experimental results at $Re_{RoU_\infty} = 5.5 \times 10^5$ for (a) 0° pitch (b) -5° pitch blades

It can be seen from Figure 130 that both models implemented here provide a good approximation to the power output of a bare turbine. The BEM CFD is the more accurate of the two models as it is a more complete model of the turbine and its operating conditions. The BEM CFD is able to calculate the flow field around the complete turbine and hub arrangement and allows some degree of inclusion of the radial flow component. In contrast, the flow velocities for each blade element

within the BEM model are based upon momentum theory and neglect the hub geometry and the effect of radial flow.

The accuracy of both the BEM and BEM CFD are reduced at low tip speed ratios. This is likely because both models are implemented without post-stall corrections, which would affect the low tip speed ratios more due to their greater relative flow angles. The most commonly used correction is that of Viterna and Corrigan [179], which corrects the lift and drag coefficients in the post stall region.

The results from the BEM CFD model are very close to those which were arrived at experimentally for both rotor geometries as can be seen in Figure 130. It can therefore be said that this method provides an improvement in the calculation of the power coefficient of a bare rotor over the blade element momentum method. The computational expense for the BEM CFD is higher than for the BEM method, as detailed in Chapter 3, and therefore the uses of this model are likely to be confined to more complex problems. Problems where the BEM CFD method may prove beneficial (if the model is extended to 3D) are those where traditionally a fully resolved 3D rotor would ordinarily be used, such as for interactions with bathymetry or array interactions for example. In order to extend the BEM model to 3D and make it suitable for non-axial flow it would be necessary to include compensation in the local relative flow vector for yawing and pitching flows in a manner similar to that detailed for yawed flows in Section 6.2.3.

6.2.3. Effect of the Rotor Yaw Angle

The effect of the flow angle on the rotor was investigated by rotating the complete turbine apparatus about the support strut axis. The yaw angle and the direction of rotation are defined in Figure 131. The results for the variation of the rotor power coefficient with the tip speed ratio and yaw angle are shown in Figure 132 for the two rotors used in the tests.

The results of the variation of the yaw angle seen in Figure 132 show that the power outputs of bare rotors are susceptible to changes in the flow angle. It can be seen that the greater the yaw angle, the more significantly the power coefficient is reduced. This relationship is to be expected, as changing the yaw angle of the rotor will change the local relative flow angle and therefore the blade's angle of attack.

In order to calculate the angle of attack of the blade under yawed flow at any azimuthal position, it is necessary to calculate the angle of relative flow with change

of the yaw angle. The coordinate system used for this calculation is shown in Figure 133. The coordinate transformation can be achieved using Equation 86 and the calculation of the velocity components for a planar rotor using Equation 87 [129].

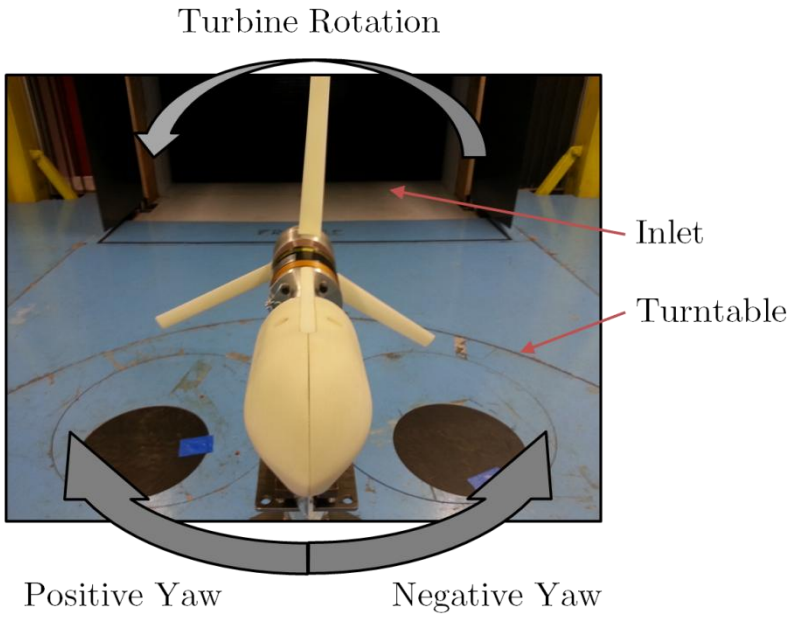


Figure 131: Definition of yaw angle and turbine rotation for rotor only case

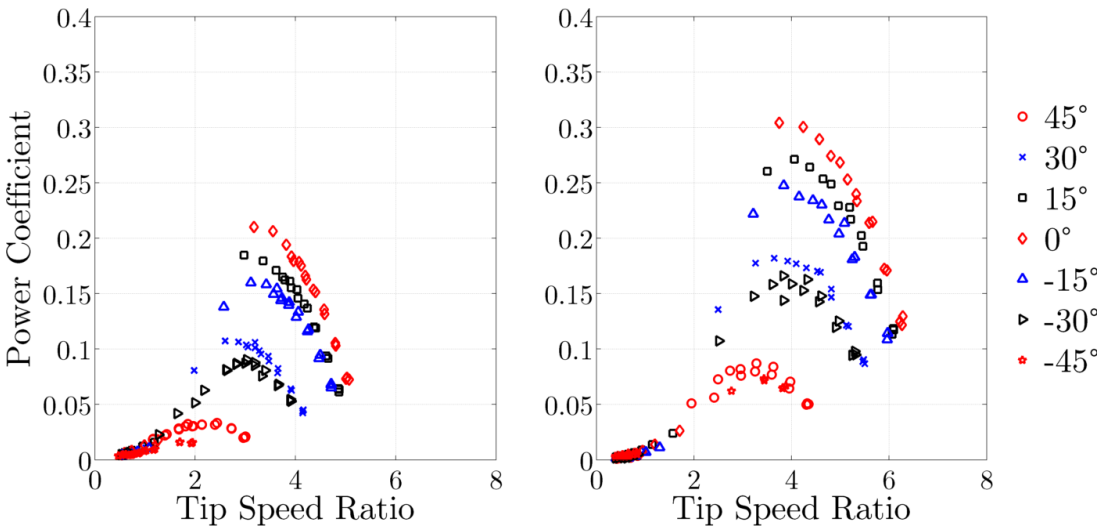


Figure 132: Effect of yaw and tip speed ratio variation on the power coefficient for bare rotors at $Re_{RoU_\infty} = 5.1 \times 10^5$ (a) 0° blade pitch (b) -5° blade pitch

The change in the angle of the local relative flow for a rotor at the yaw angles shown in Figure 132 can be seen in Figure 134 plotted against the azimuth angle. It is evident that there are significant departures in the local relative flow angle from the zero yaw case; this is particularly true when the blade is retreating. These

changing local relative flow angles lead to degraded performance as the blade experiences flow which is incident at angles where the section performance is degraded and in many cases where the section is stalled.

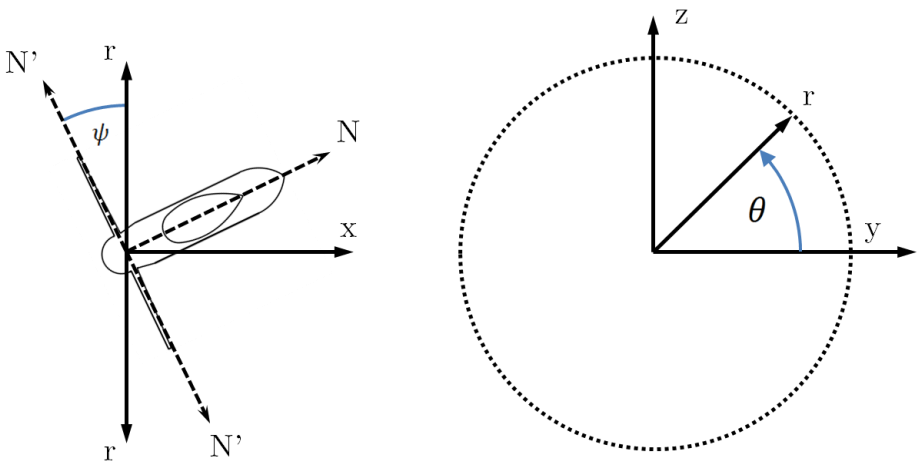


Figure 133: Rotor yaw coordinate system

$$U_{xyz} = \begin{bmatrix} 0 & 0 & 1 \\ cos\theta & -sin\theta & 0 \\ sin\theta & cos\theta & 0 \end{bmatrix} U_{xr\theta} \qquad \text{Equation 86}$$

$$\begin{Bmatrix} U_{\acute{N}} \\ U_N \end{Bmatrix} = \begin{bmatrix} cos\theta sin\theta(1-cos\psi) & cos^2\theta + sin^2\theta cos\psi & sin\theta sin\psi \\ cos\theta sin\psi & sin\theta sin\psi & cos\psi \end{bmatrix} \begin{Bmatrix} U_r \\ U_\theta \\ U_x \end{Bmatrix} \qquad \text{Equation 87}$$

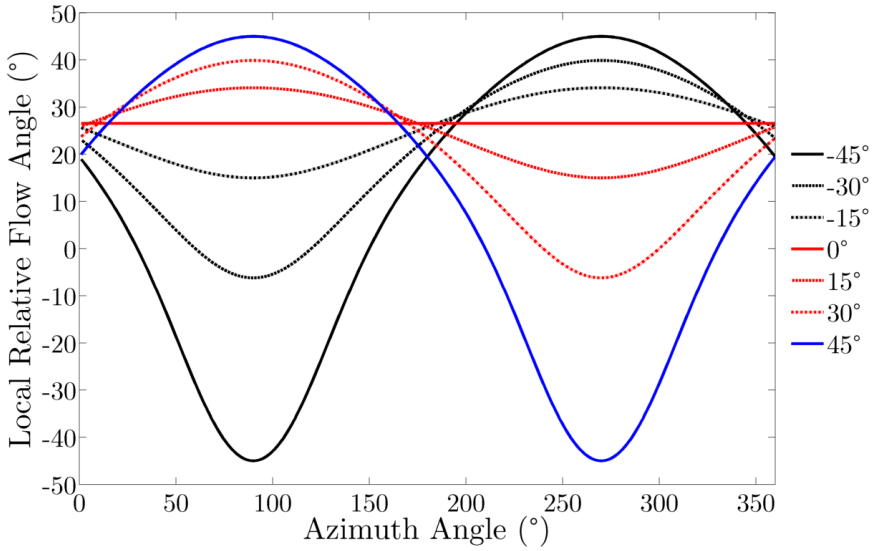


Figure 134: Local relative flow angle against the azimuth angle and yaw angle at mid-span for a planar rotor at a tip speed ratio of 4

In addition to the degraded performance of the rotor due to the local relative flow angle variation, there is also an effect from the normalising power. When the power coefficient is calculated, the power is normalised by the power available to the rotor at a yaw angle of 0°, meaning that yawed flows are penalised more heavily as less frontal area is presented to the flow.

A notable result from Figure 132 is that when the yaw angle of the device is positive the power coefficient is greater than when the device is yawed to the corresponding negative angle. This runs counter to that which might be expected given the ideal symmetric distribution of the local relative flow angle with azimuthal position seen in Figure 134. This effect is thought to be due to the effect of the nacelle support on the flow in the range of azimuth angles $250° < \theta < 290°$. The support fairing, when misaligned with the flow, induces streamline curvature in the incoming fluid. The effect of this geometry would be to further misalign the flow due to inducing transverse flow as well as acting to reduce the local relative flow velocity. The transverse velocity is induced such that the flow is aligned to some extent with the support fairing as seen diagrammatically in Figure 135.

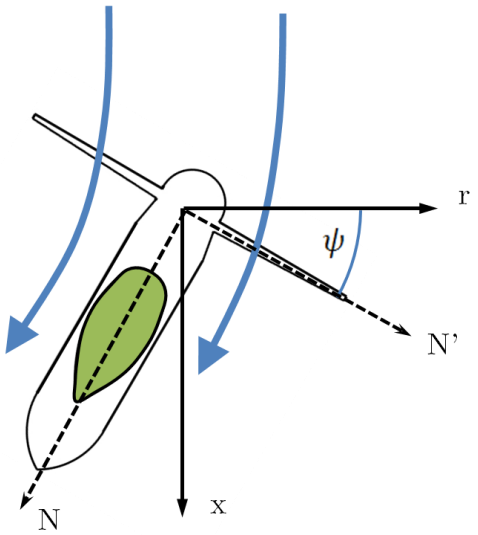


Figure 135: Diagrammatic representation of the effect of the hub support fairing on the flow direction at the rotor plane

The aligning of the flow with the normal of the rotor plane acts to reduce the effective yaw angle onto the rotor plane in front of the support. The performance of the rotor in this region is improved for both positively and negatively yawed rotors, though as this is where the positively yawed rotors experience their greatest departures in the local relative flow angle they have the most to gain.

If the power coefficient of the rotor at each yaw angle normalised by the peak power coefficient is plotted for both rotors, as seen in Figure 136, it is evident that the -5° pitch blades perform better under yawed flows.

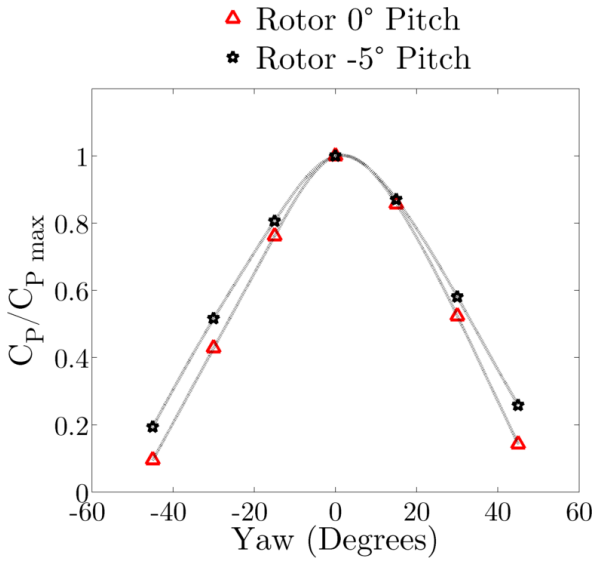


Figure 136: Normalised peak power coefficient against yaw angle for both blades

When the angle of attack is plotted against the azimuthal position as seen in Figure 137, it becomes clear that this is because the angle of attack remains closer to the optimum angle of attack during rotation due to the blades' pitch distribution. The performance characteristics of the blades are therefore more favourable with the -5° pitch and the rotor's power output is increased.

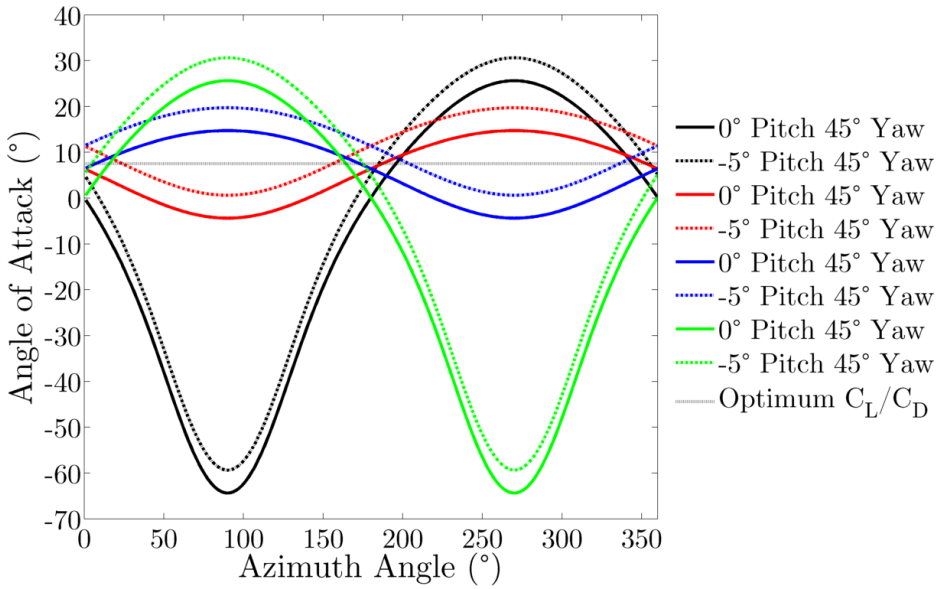


Figure 137: Angle of attack against the azimuth angle and yaw angle at mid-span for a planar rotor at a tip speed ratio of 4

6.2.4. Rotor Wake Flow Structure

Understanding of the interaction between the turbine and diffuser requires knowledge of the propagation of the rotor wake. In order to investigate this wake, traverses were conducted on planes parallel and perpendicular to the flow.

6.2.4.1. Offset Transverse Plane Parallel to the Rotor Plane

The flow field on an offset transverse plane in the rotor wake at TSR=5.3 and $Re_{RoU_\infty} = 4.9 \times 10^5$, on the Y-Z plane at 1.8 blade radii downstream of the rotor plane is presented here. The location of the traverse plane and directions of motion are presented in Figure 138. The offset of the traverse plane is such that the traverse plane is identical to the diffuser exit traverse plane used in Section 6.3.4.

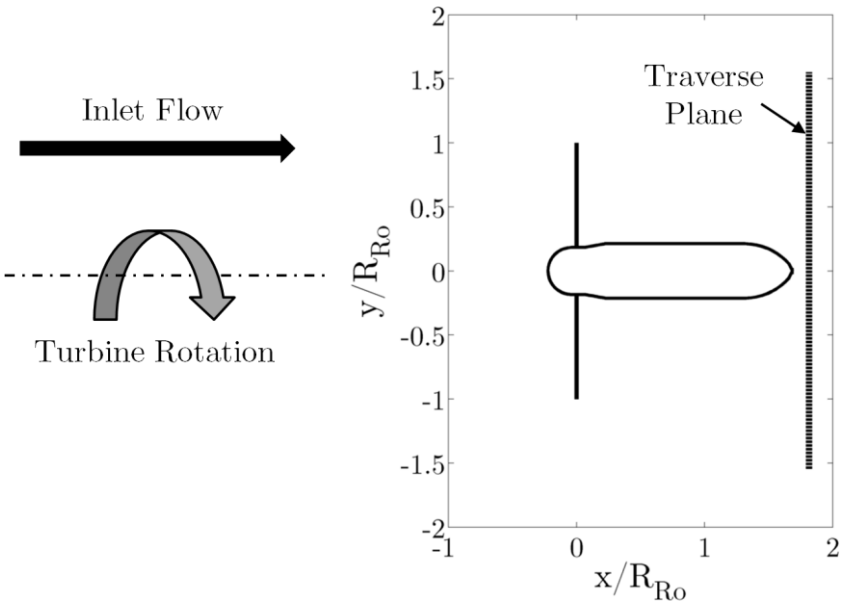


Figure 138: Location of the downstream offset plane relative to the bare rotor

The radius used for the normalisation is the blade radius, with the -5° pitch blades used. The time averaged images are looking upstream towards the rotor plane, with the turbine rotating in the counter-clockwise direction. Figure 139 shows total and static pressure coefficient distributions, where the total pressure coefficient is defined as in Equation 88. Figure 140 shows the normalised velocity in the wake.

$$C_{p_t} = \frac{p_t - p_{t\infty}}{1/2 \rho U_\infty{}^2} \qquad \text{Equation 88}$$

In Figure 139 and Figure 140, the main features of the time averaged rotor wake, such as the hub wake, tip losses and wake expansion can be distinguished. The hub wake is clearly visible in the velocity deficit at the plane's centre. The

effect of the tip vortices, with the reduced velocity and stagnation pressure losses can be clearly seen around the circle at $r/R_{Ro}\approx1.05$. The wake expansion is limited in scale due to the thrust of the rotor, but can also be seen due to the wake's expansion to $r/R_{Ro}\approx1.15$ at the traverse plane. The support strut is also visible in the lower half of the wake at $y/R=0$, with a reduced total pressure, velocity and weakening of the tip vortex induced turbulence around $r/R_{Ro}\approx1.05$.

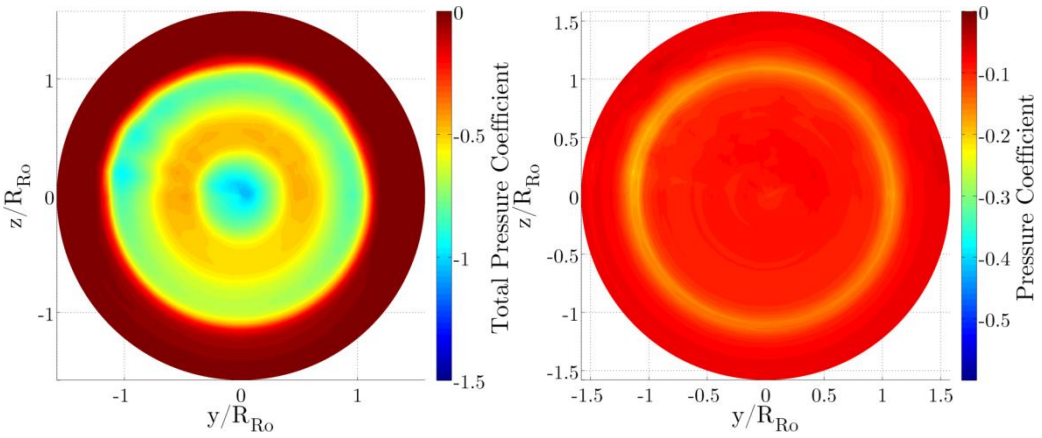


Figure 139: (a) Total and (b) static pressure coefficients for -5° blade pitch rotor at TSR=5.3 and $Re_{RoU_\infty} = 4.9 \times 10^5$, on Y-Z plane at 1.6 blade radii downstream of the rotor

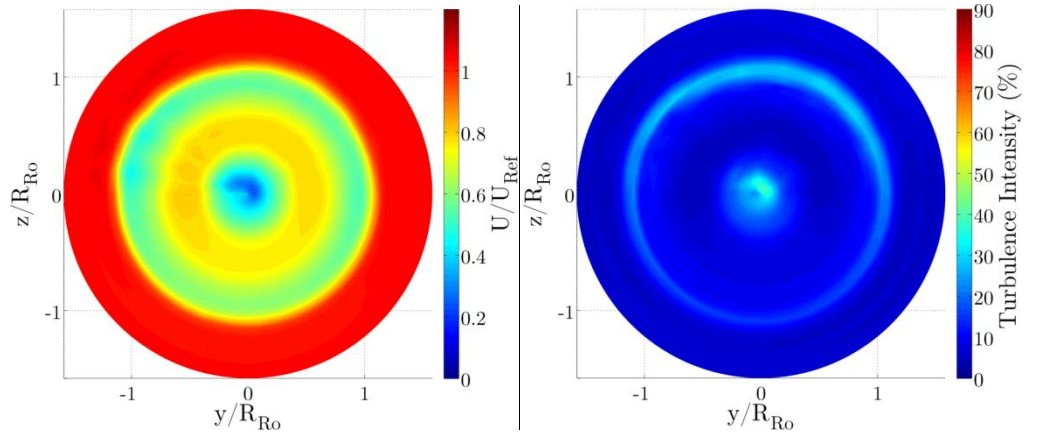


Figure 140: (a) Normalised velocity (b) turbulence intensity with -5° blade pitch at TSR=5.3 and $Re_{RoU_\infty} = 4.9 \times 10^5$, on Y-Z plane at 1.6 blade radii downstream of the rotor

Figure 141 shows the radial and tangential velocity components in the rotor wake. The rotor generated wake swirl is visible in Figure 141(b) as a bulk negative tangential velocity in the clockwise direction, counter to the turbine rotation, where $r/R_{Ro}<1$. The swirl velocity is particularly strong towards the centre of the plane,

indicating that a vortex was formed around the rear of the nacelle similar to that seen within the CFD results presented in Section 4. This explaining why the hub wake's extent has reduced by the traverse plane.

The effect of the strut is visible here, as due to the length of the fairing, the swirl velocity is distorted in the lower half of the plot and is no longer axisymmetric, as the flow is forced around the fairing. This leads to a high swirl velocity in the region $y/R_{Ro}<0$, $z/R_{Ro}<0$ and a lower swirl velocity in the region $y/R_{Ro}>0$, $z/R_{Ro}<0$, where the swirling flow from the rotor is directed towards the fairing. The radial velocity distribution shows that the wake closes around the rear of the nacelle and that the wake is contracting by this distance downstream of the rotor plane.

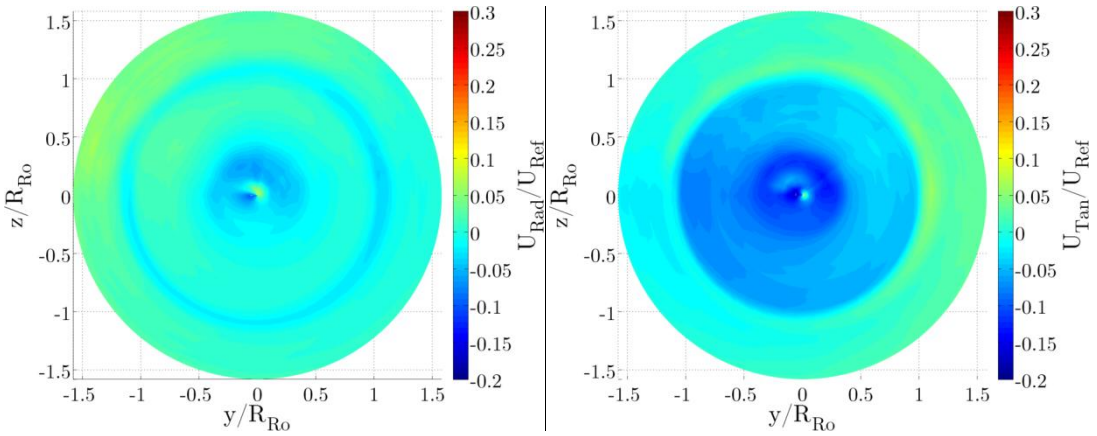


Figure 141: Normalised (a) radial and (b) tangential velocity with -5° blade pitch at TSR=5.3 and $Re_{RoU_\infty} = 4.9 \times 10^5$, on Y-Z plane at 1.6 blade radii downstream of the rotor

The velocity deficit in the turbine wake is compared to that calculated using the blade element momentum CFD in Figure 142. This shows broad agreement with the experimental results, meaning that the major flow structures of the wake are being resolved. This agreement means that the near wake, the region of flow which will interact with the diffuser, is represented faithfully. This then means that the BEM CFD implementation for the diffuser should maintain accuracy.

The large kink that is evident in the velocity distribution seen in Figure 142 is due to the spanwise distribution of the power contribution from each blade element, which can be seen in Figure 143. It is clear that the section towards the tip of the blade at this tip speed ratio is doing the majority of the work of the rotor. This increased tip work acts to increase the axial induction factor at the blade tip and so results in the region of velocity deficit seen in the wake. Conversely, the lower power

output from the central portion of the blade leads to a lower axial induction factor and therefore a higher wake velocity.

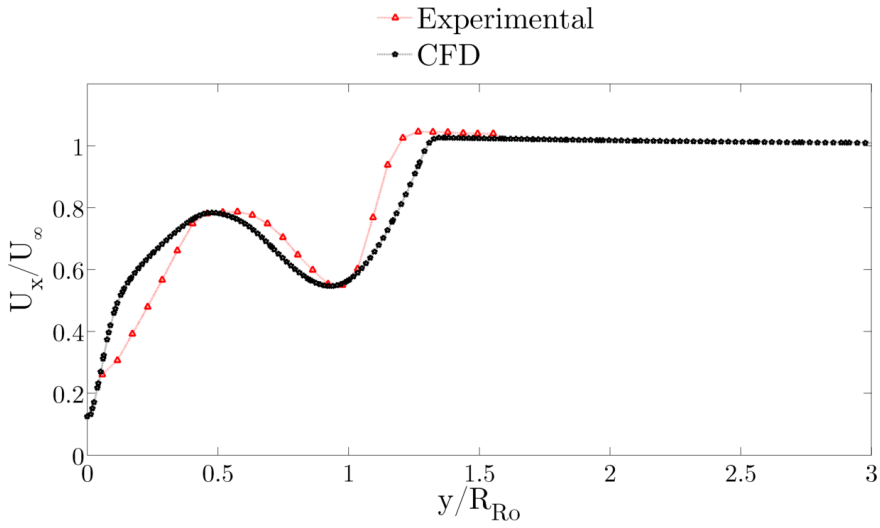


Figure 142: Comparison of computed normalised axial velocity distribution at traverse plane with experimental data for the bare rotor with -5° blade pitch

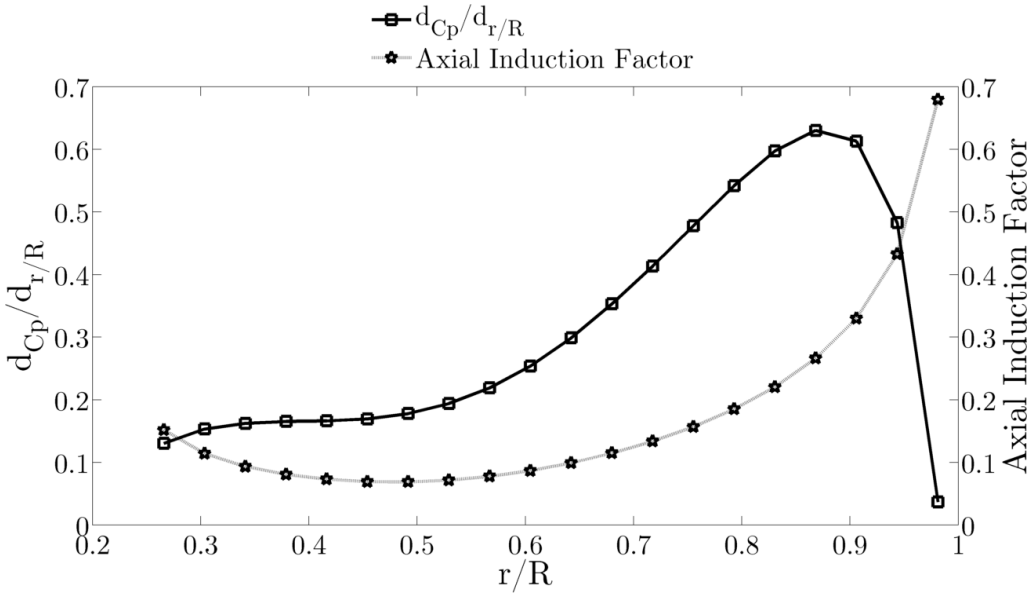


Figure 143: Spanwise distribution of blade elements' contribution to rotor power coefficient and axial induction factor for the -5° blade pitch rotor at TSR=5.5 and $Re_{RoU_\infty} = 4.9 \times 10^5$, calculated using the BEM model

6.2.4.2. Longitudinal Plane at the Rotor Axis

In addition to the transect parallel to the rotor plane a longitudinal transect was taken on the X-Y plane of the wind tunnel at the turbine axis height. This transect was taken in the rotor wake at TSR=5.3 and $Re_{RoU_\infty} = 4.9 \times 10^5$. The

normalising radius is the blade radius, with the -5° pitch blades being used. Figure 144 shows the wake pitch and yaw distributions.

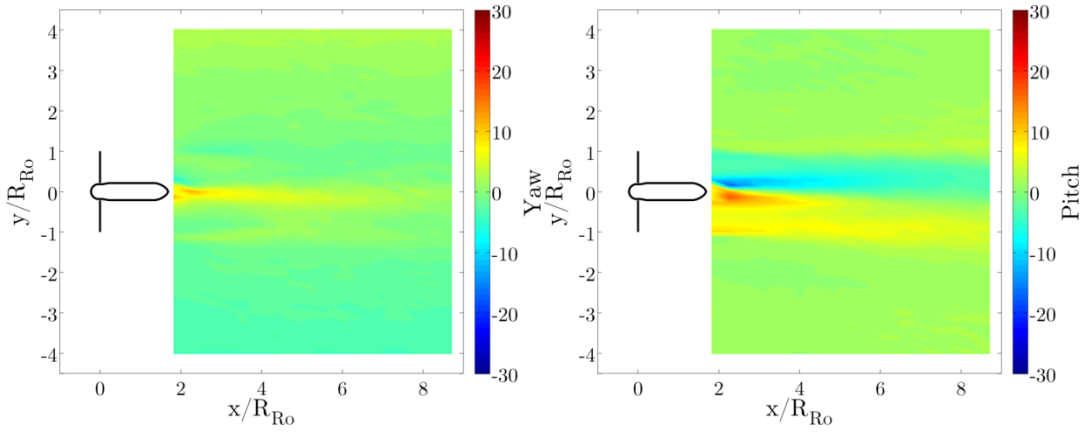


Figure 144: (a) Yaw and (b) pitch angles in degrees in the rotor wake for -5° blade pitch rotor at TSR=5.3 and $Re_{RoU_\infty} = 4.9 \times 10^5$, on X-Y plane at axis height

The wake structure seen in Figure 144 exhibits only limited yaw, meaning the area of the wake is not changing to a notable extent in the streamwise direction. The pitch distribution indicates a wake which is swirling heavily around the rear of the nacelle and exhibits the velocity distribution of a vortex, with increasing swirl velocities towards the vortex core. Figure 145 shows the total and static pressure coefficients, with Figure 146 showing the normalised velocity.

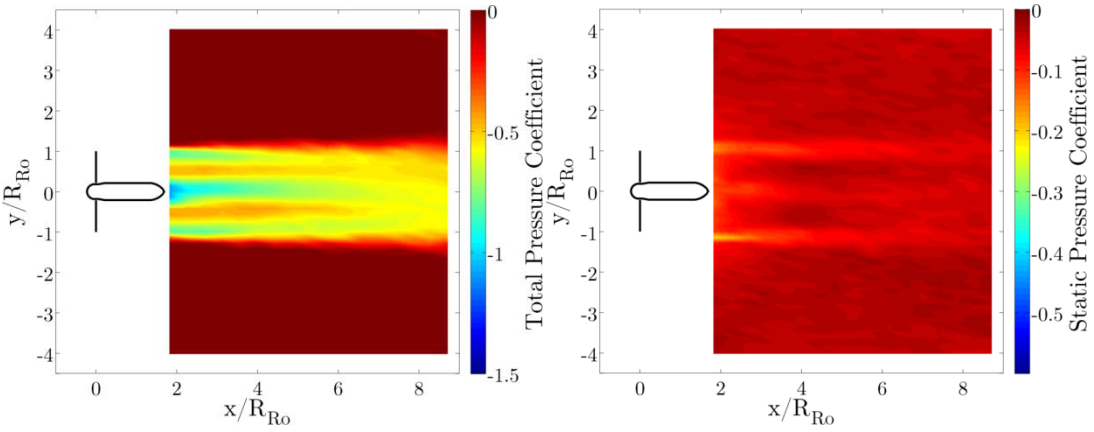


Figure 145: (a) Total and (b) static pressure coefficients in the rotor wake for -5° blade pitch rotor at TSR=5.3 and $Re_{RoU_\infty} = 4.9 \times 10^5$, on X-Y plane at axis height

Figure 145 and Figure 146 show the strength of the tip vortices and the associated velocity deficit and stagnation pressure losses seen in the tip region as well as the turbulence in the wake. These distributions are to be expected as the blade geometry has a flat tip, meaning that the tip vortex strength will be relatively

high. The level of turbulence in the test environment means that the wake takes some time to break down, as detailed in Section 6.2.4.3. The level of turbulence will impact upon the performance of the diffuser as it is one of the main drivers of the ability of the flow to remain attached to the diffuser casing.

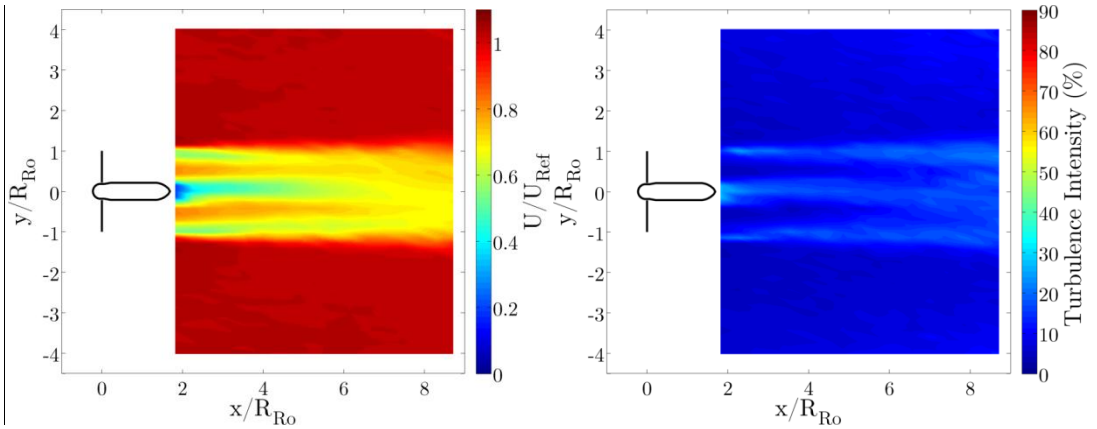


Figure 146: (a) Normalised velocity and (b) turbulence intensity in the wake for -5° blade pitch rotor at TSR=5.3 and $Re_{RoU_\infty} = 4.9 \times 10^5$, on X-Y plane at axis height

6.2.4.3. Wake recovery

The wake recovery is an important parameter within the study of tidal stream turbines since it will effect the interaction of devices within an array and the spacing between devices which is necessary. Wake recovery is quantified through assessment of the axial velocity deficit in the wake along the device centreline [180]. The velocity deficit on the centreline of the -5° pitch rotor wake is shown in Figure 147.

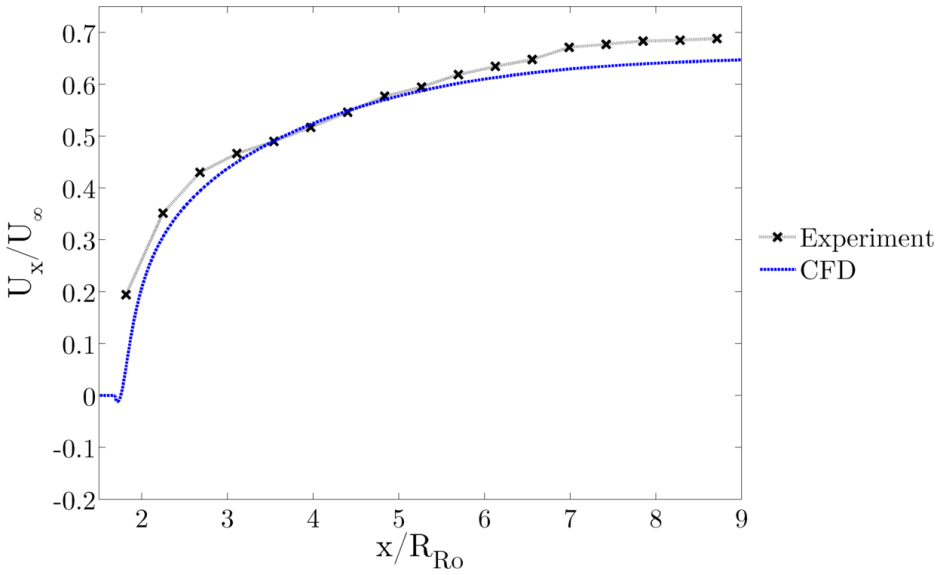


Figure 147: Comparison of experimental and BEM CFD predicted wake recovery for -5° blade pitch rotor at $Re_{RoU_\infty} = 5.5 \times 10^5$, with a turbulence intensity of 4.71%

It can be seen from Figure 147 that the bare rotor wake recovers to 65% of the freestream velocity by 9 rotor radii downstream of the rotor plane. It can also be seen that the BEM CFD model provides an accurate assessment of the magnitude of the wake recovery. As can be seen from the results seen in Section 4, the turbulence in the freestream has a large impact upon the expected wake recovery.

6.3. Combined Diffuser and Rotor Characterisation

In this section, where the Reynolds number is referenced it is based upon the freestream velocity of the flow and the diffuser throat diameter.

6.3.1. Effect of Reynolds Number

To quantify the effects that a variation of the Reynolds number has on the performance of the rotor and diffuser combination, a set of experimental runs were conducted using the two blades sets over a range of operating speeds. The results of these experimental runs can be seen in Figure 148, which shows the effect of the Reynolds number and tip speed ratio on the power coefficient of the two rotor pitches used in this study. The Reynolds number here is based upon the freestream velocity of the flow and the diffuser throat diameter. The tip speed ratio is defined as the ratio of the tip speed of the blades to the freestream velocity, in the case of a diffuser augmented device, the direct relation of this quantity to the relative flow angle is convoluted. As the flow speed in the diffuser throat will in most cases be above that in the freestream and significantly above that found at the rotor plane of a bare turbine, the real tip speed that the rotor experiences will be reduced.

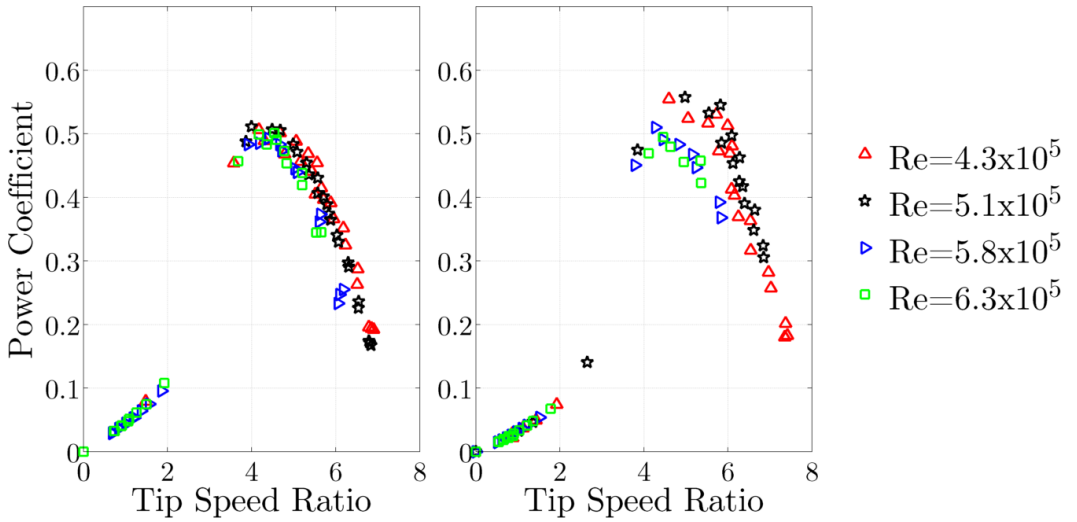


Figure 148: Effect of Reynolds number and tip speed ratio on the power coefficient of (a) 0° blade pitch (b) -5° blade pitch diffuser and rotor combinations

The increased power coefficient seen in the case of the -5° pitch rotor at low Reynolds numbers is due to the blade construction. The higher Reynolds numbers ($> 5.6 \times 10^5$ in both blade cases) were tested with a stiffer set of blades than the lower Reynolds number runs as the original sets of blades were found to be too structurally weak for safe testing at the increased testing velocities. The effect of this change of blades is limited in the case of the 0° pitch rotor as there is less thrust, though the performance is slightly degraded at higher tip speed ratios. With the -5° pitch rotor the stiffer blades cause a large drop in the performance over the higher range of tip speed ratios, where there is a higher turbine thrust.

The increased stiffness acts to suppress blade deformation during operation. The increased performance in the case of the more deformable blades is thought to be due to rotor coning. The effect of the thrust on the lightweight blades will be to induce what is essentially downstream rotor coning on the blade during operation. This coning acts to increase the local relative flow angle [129], which in turn increases the angle of attack of the blades, the rotor thrust and the power output.

Figure 149 and Figure 150 show the pressure coefficients for the 0° pitch and -5° pitch blades respectively over a range of Reynolds numbers. The reduced thrust from the stiffer blading is clearly visible in Figure 150, through the reduced exterior separation and smaller pressure drop across the rotor plane.

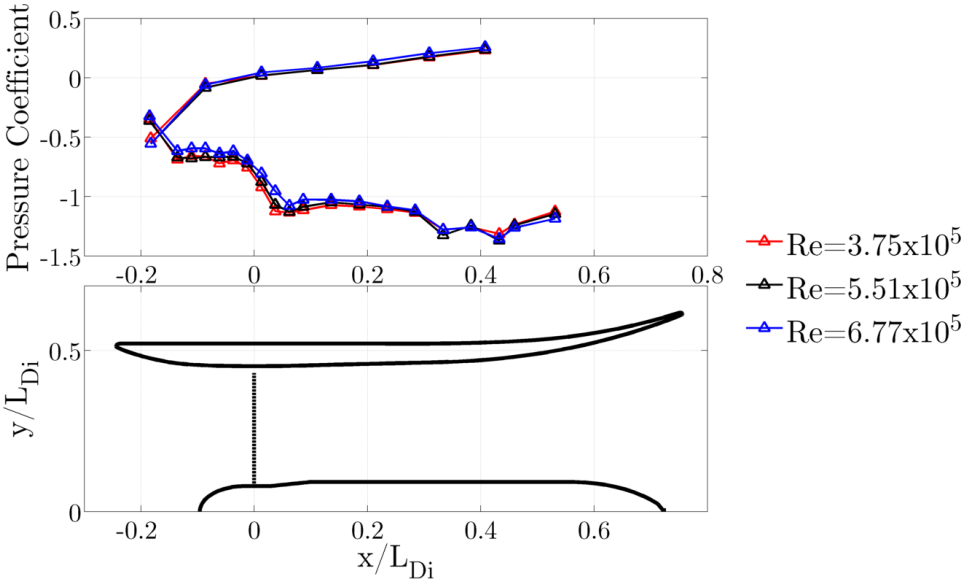


Figure 149: Pressure coefficient around diffuser for diffuser and rotor case with 0° blade with variation of Reynolds number at TSR = 5

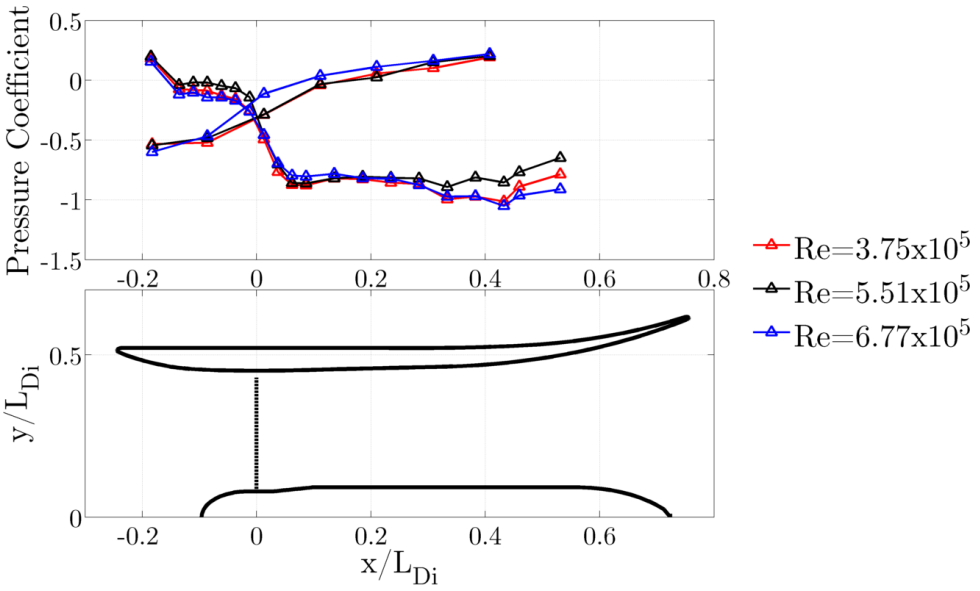


Figure 150: Pressure coefficient around diffuser for diffuser and rotor case with -5° blade with variation of Reynolds number at TSR = 5

The results seen in Figure 148 show the diffuser tends to reduce the relative magnitude of the variations in the power coefficient caused by changes in the Reynolds number. This effect is caused by the accelerating effect of the diffuser on the flow, which increases the velocity at the rotor plane and therefore the Reynolds number over the blade. At the full device scale the Reynolds number effects on the blades would be negligible due to the significantly higher Reynolds numbers present.

It can be seen from Figure 148 that the diffuser acts to increase the turbine power coefficient to a varying extent. For the non-pitched rotor, which when run bare has a lower peak power coefficient and hence a lower thrust, the potential gains are greater. For the non-pitched rotor the power coefficient is 126% greater than for a bare turbine (9% greater when based on the diffuser outer diameter), whereas for the -5° pitch rotor the gain is 84%. The latter representing an 11% decrease in the power coefficient compared to a power coefficient based on the diffuser outer diameter. This decrease in the peak power coefficient is caused by the thrust of the rotor acting to cause a blockage of the diffuser throat, reducing the swallowing capacity of the duct and therefore the throat velocity and power output.

The effects of the rotor thrust can be clearly seen when the pressure coefficients around the diffuser surface are compared for a prescribed tip speed ratio. It can be seen immediately from Figure 149 and Figure 150 that there is a significant difference between the two, with the -5° pitch blades producing a higher

thrust. This thrust is visible as a result of the enlarged region of exterior separation at the diffuser leading edge and the increased pressure gradient across the rotor plane. The power outputs for the diffuser and rotor combinations are approximately equal at the Reynolds numbers being investigated, which seems counterintuitive.

The 0° pitch rotor is a lightly loaded rotor, meaning that the pressure drop across the rotor is small, and that the mass flow rate through the duct will be larger. The -5° pitch rotor is more heavily loaded, inducing a larger pressure drop across the rotor, but retards the flow and so has a reduced swallowing capacity. Since the power output is proportional to the product of the pressure drop and mass flow rate the two rotors produce approximately the same power output with differing flow regimes. The duct and rotor combination is therefore acting to limit the power at higher thrusts due to the reduced ability to sustain an augmented throat velocity.

This change in the flow regime is again evidenced by Figure 151, which shows the pressure coefficient around the diffuser surface for a selection of tip speed ratios. It is apparent from Figure 151 that when the rotor thrust is low and the power coefficient is limited, the blockage effect of the rotor is low. This low blockage increases the swallowing capacity of the duct. This flow regime is characterised by high throat velocities and low pressures along the diffuser interior surface, with a small pressure drop across the rotor plane due to a low power output.

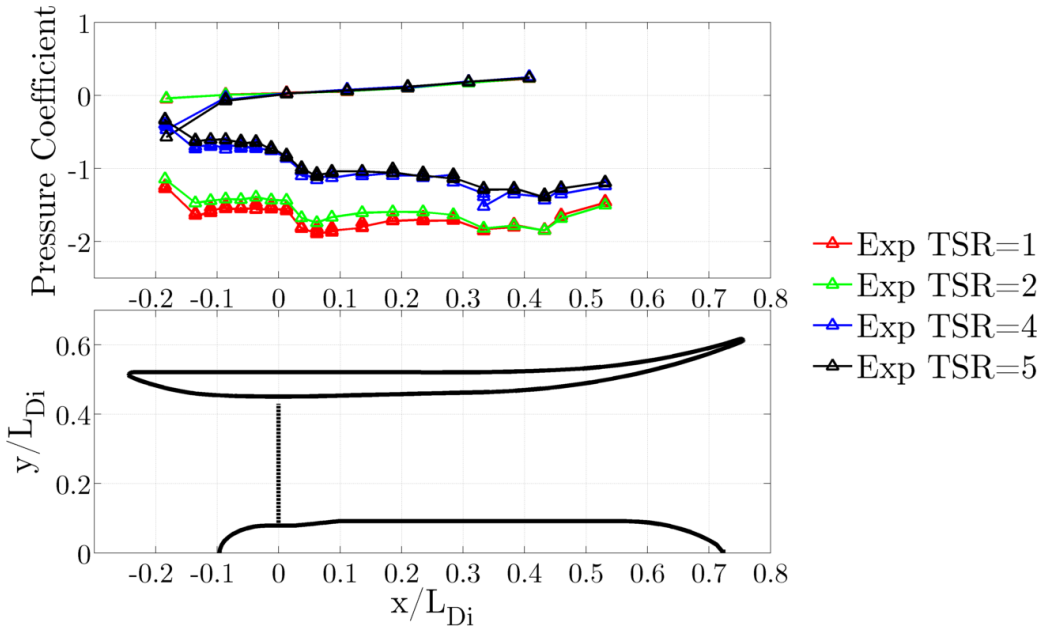


Figure 151: Pressure coefficient around diffuser for diffuser and rotor case with 0° blade with variation of the tip speed ratio at $Re_{DiU_\infty} = 6.3 \times 10^5$

At high thrusts, when the power coefficient of the turbine is at a maximum, the blockage effect of the rotor is significant. The flow regime in this state is characterised by a heavily thrusting rotor, causing a large pressure drop across the rotor and forcing flow around the diffuser. This flow re-direction can be seen through the separation around $-0.2 < x/L_{Di} < 0.0$ on the diffuser's exterior, caused by flow approaching the leading edge with large radial velocity due to the blockage.

6.3.2. Verification of the Combined Blade Element CFD

The experimental results at $Re_{DiU_\infty} = 5.8 \times 10^5$ are compared with those from the blade element momentum model within the CFD in Figure 130. Full details of the models and their implementation are presented in Chapter 3.

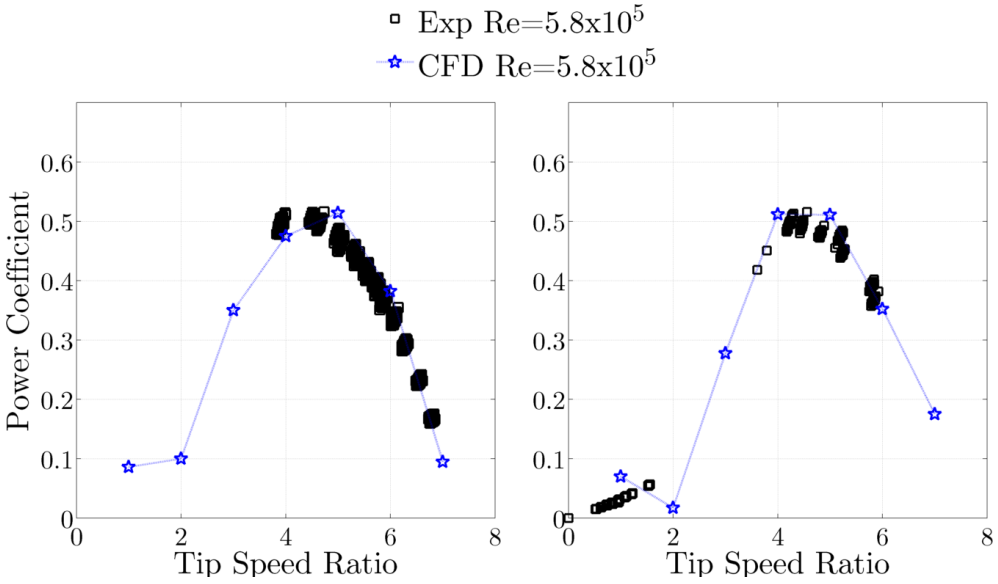


Figure 152: Comparison of blade element mometum CFD and experimental results at $Re_{DiU_\infty} = 5.8 \times 10^5$ for (a) 0° pitch (b) -5° pitch blades

The blade element momentum CFD results seen in Figure 152 show a good agreement with the experimental power coefficient curves. The power coefficient at the lower tip speed ratios is, as with the bare rotor, the weak point of the model. This is again thought to be due to the lack of inclusion of a post-stall model of the blade section performance on the lift and drag data of the section.

These results indicate that the model sufficiently represents the rotor wake characteristics such as the velocity deficits, tip losses, swirl and turbulence generation over the range of tip speed ratios, such that the flow in the diffuser is

realistic. This allows for accurate determination of the diffusion and swallowing capacity of the duct and therefore of the overall power coefficient of the device.

The pressure coefficient around the diffuser surface from both the experimental results and the CFD, at TSR=5 & $Re_{DiU_\infty} = 5.8 \times 10^5$ can be seen in Figure 153. The trends in the CFD calculation of the static pressure distribution through the duct using the blade element momentum model can be seen to match the experimental data well. The main flow features are clearly replicated in the CFD, with the large area of recirculating flow on the diffuser's exterior leading edge and the pressure drop across the rotor plane both clearly visible. The CFD predicts a larger pressure drop across the rotor, which would explain the overestimation of the power coefficient at this tip speed ratio. The CFD also predicts a much steeper drop in pressure, something which was expected as the turbine model has a very clearly defined, steady tip gap. Within the experimental data the pressure transition takes place over a greater distance due to the transience of the rotor.

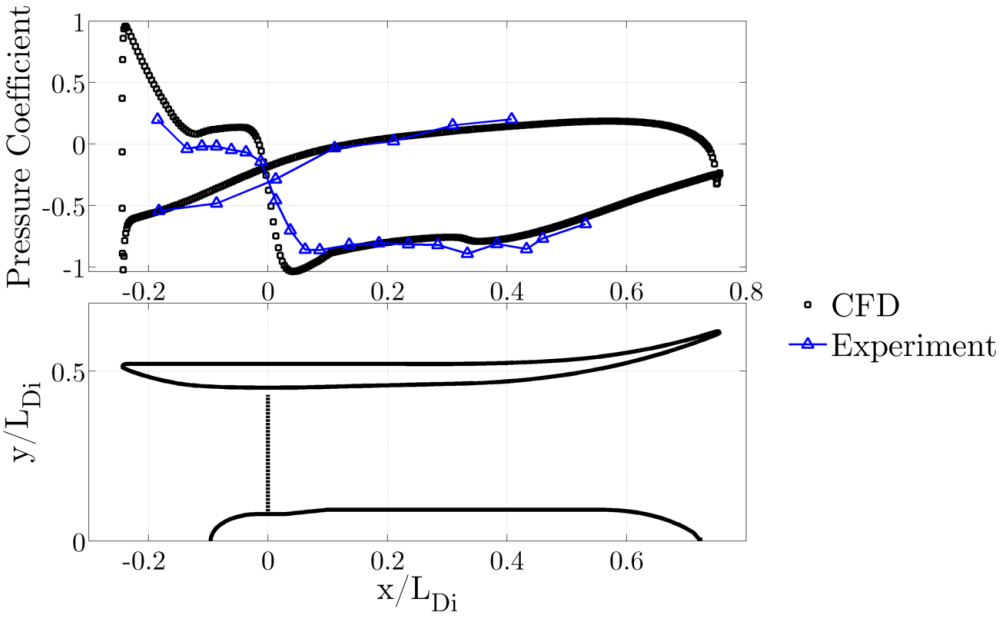


Figure 153: Pressure coefficient around diffuser for diffuser and rotor case with -5° pitch blade, TSR=5, $Re_{DiU_\infty} = 5.8 \times 10^5$, showing the component geometries

The predictions at the higher tip speed ratios provide a good match to the experimental data in the diffuser behind the rotor plane. At lower tip speed ratios, where large parts of the rotor are stalled, the predictions of the performance diverge. Figure 154 shows the static pressure coefficient distribution around the diffuser for TSR=1 & $Re_{DiU_\infty} = 5.8 \times 10^5$. It can be seen that the CFD pressure distribution

more closely resembles that of the diffuser without the rotor, as seen in Figure 154. Due to the divergence of the lift and drag data of the blade section from the actual post stall behaviour, there is an under prediction of the turbine thrust. This reduced thrust is visible here from the lack of a clearly defined pressure drop across the rotor plane and an elevated exterior leading edge surface pressure caused by complete flow attachment at this point. It is thought that incorporation of a post stall model within the BEM CFD would remove these errors at low tip speed ratios.

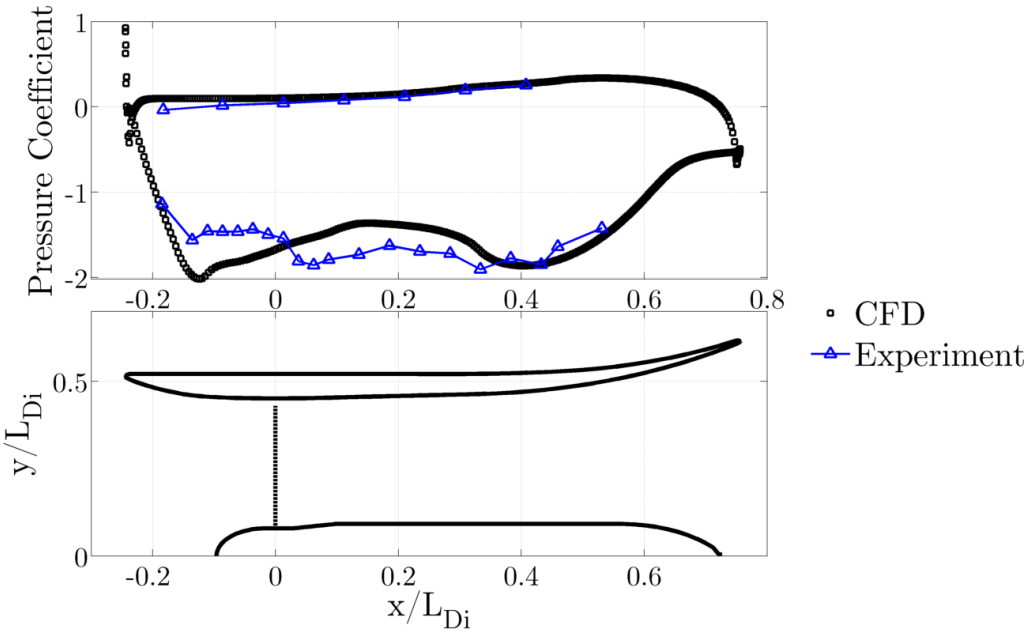


Figure 154: Static pressure coefficient around diffuser for diffuser and rotor with -5° pitch blade, TSR=1, $Re_{DiU_\infty} = 5.8 \times 10^5$, showing component geometries

Ahead of the rotor plane, on the interior surface of the casing, the CFD tends to diverge from the experimental data, over predicting the pressures when heavily loaded, and under predicting them when lightly loaded. These differences are, as with the diffuser only cases presented in Section 6.1.1, the result of the CFD's inability to accurately determine the separation from the interior surface of the casing ahead of the rotor plane at $\frac{x}{L_{Di}} \cong -0.15$.

The model can be seen to accurately replicate the power coefficients and pressure distributions seen within a diffuser augmented tidal stream turbine. These results give confidence that the model is sufficiently accurate to assess the behaviour and power generation potential of diffuser augmented tidal stream turbines.

6.3.3. Effect of the Device Yaw Angle

The effect of the flow angle onto the combined rotor and diffuser device was investigated by rotating the complete assembly about the support strut axis. The yaw angle and the direction of rotation are defined in Figure 155.

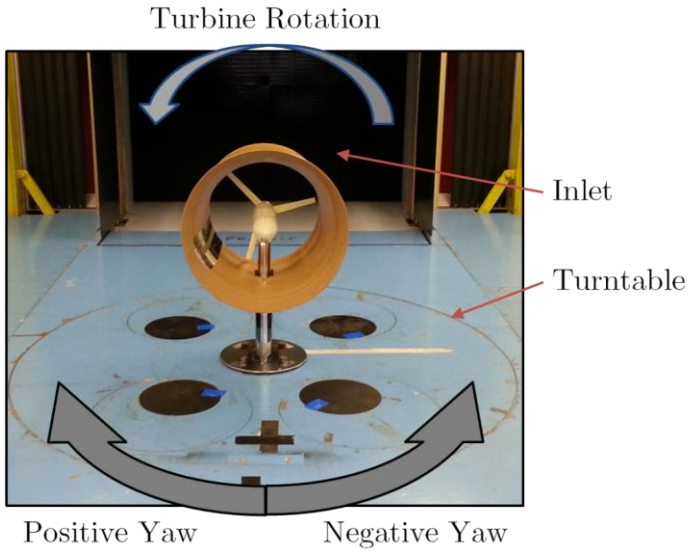


Figure 155: Definition of yaw angle and turbine rotation for diffuser and rotor

The results for the variation of the rotor power coefficient with the tip speed ratio and yaw angle are shown in Figure 156 for the two rotors. The results seen here clearly show the duct's ability to sustain performance of the rotor at flows with yaws of up to 30°. This effect is due to the duct acting to maintain the flow axial direction around the rotor until the diffuser stalls.

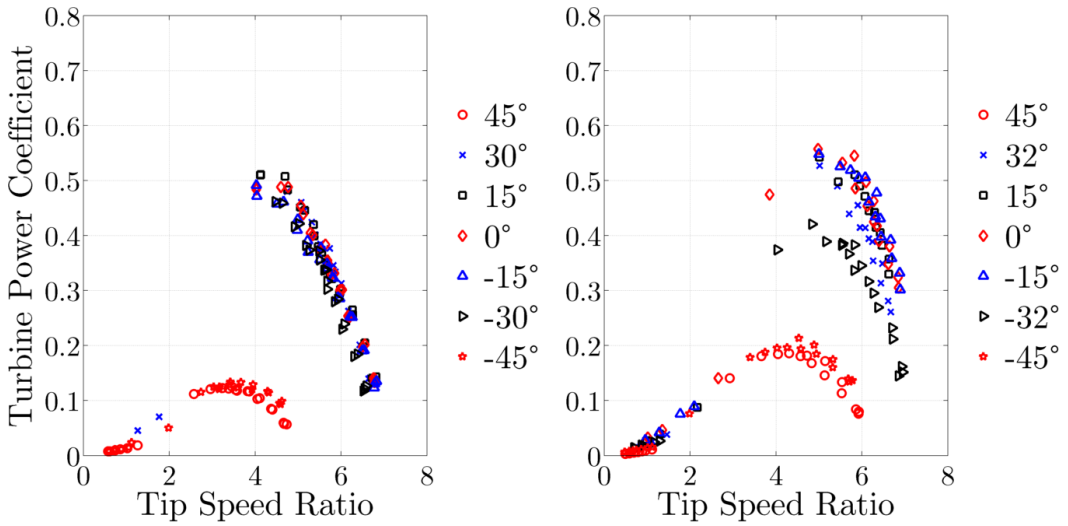


Figure 156: Effect of the yaw angle and tip speed ratio on the power coefficient with (a) 0° blade pitch (b) -5° blade pitch rotors

The static pressure coefficient around the diffuser for a range of yaw angles can be seen in Figure 157. Only one half of the rotation (0° to 45°) is shown here, for the reasons stated in Section 6.1.2. It can be seen that the exterior pressure increases with the yaw angle, which would be expected as the tappings are turning in such a way that the flow moves increasingly towards the perpendicular.

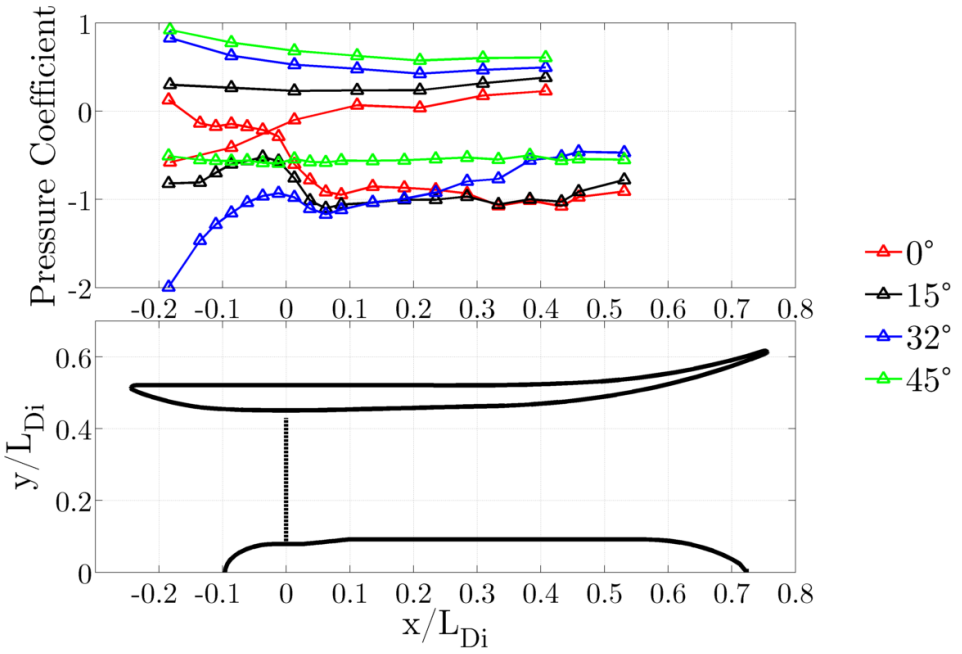


Figure 157: Pressure coefficient around diffuser for diffuser and rotor case over yaw angle range, with -5° pitch blade, TSR=5, $Re_{DiU_\infty} = 5.5 \times 10^5$

At low yaw angles the pressure coefficients within the rear of the diffuser ($x/L_{Di}>0$) can be seen to remain similar. Diffuser stall occurs at a yaw angle of just over 30°, with the start of stall being visible for the -5° blade pitch rotor at a diffuser yaw angle of 32°. This stall is evidenced by the separation of the flow from the diffuser at $x/L_{Di}\approx0.46$ and the resulting reduced peak power coefficient. At a yaw angle of 45° the diffuser can be seen to be fully stalled along the interior, leading to a significantly reduced power coefficient.

The separation is prevented at low yaw angles by the effect of the tip gap jet, which acts to increase boundary layer momentum. The performance enhancement of diffuser augmented turbines under yawed flows has been noted by Igra [94] and Phillips [25]. Igra stated that the performance is due to an increase in lift generated by the annular wing section under yawed flows of up to 15°. This explanation makes the assumption that the annular wing's lift increases up to the point at which the diffuser stalls, which cannot explain the performance here up to ±30°. The diffuser

here can be seen to stall at angles of between 11° and 22°, as shown in Figure 126, and so there must be another mechanism inducing the performance boost.

Phillips [25] stated that the performance was due to the slotted design of the diffuser, with the slots adding momentum to the boundary layer flow. This explanation would partially explain the results seen by Phillips, but would again not explain the performance seen here as no slots are present. The separation suppression seen here must then be due to the tip gap jet formed between the diffuser and the rotor, and it is suggested that a large part of the performance improvements noted by both Igra and Phillips were due to this same mechanism.

The stall phenomenon causes progressively decreasing power coefficients for yaw angles which increase beyond 30°, with a 2/3 reduction in the power coefficient being noted by 45° yaw. This ability to maintain performance at off angle flows is in contrast to the performance of a bare rotor as seen in Figure 132. In this case, the decrease in the peak power coefficient relative to the perpendicular flow condition is greater at all angles than for a diffuser augmented device. The normalised peak power coefficient's relationship to the yaw angle can be seen in Figure 158 for both the bare and diffuser augmented cases.

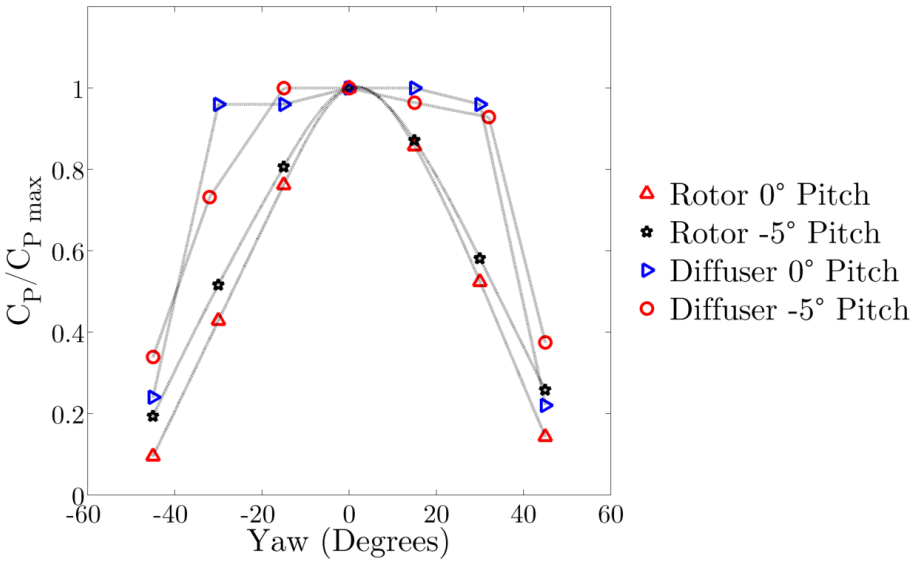


Figure 158: Normalised peak power coefficient against the device yaw angle for both rotors with and without diffuser augmentation

Figure 158 shows that the use of a diffuser allows for efficient power extraction over a wide range of yaw angles and continues to outperform the bare rotor even after the diffuser has stalled. This behaviour may allow a diffuser augmented device

to outperform a static bare rotor in a flow whose yaw behaviour is transitory. It would also allow the use of a static diffuser where some form of yaw compensation mechanism may be necessary for a bare rotor.

6.3.4. Diffuser and Rotor Wake Flow Structure

This section examines the interaction between the rotor wake and the diffuser and how this will affect the power output of the coupled device. In order to investigate the wake, traverses of the device wake were conducted on planes parallel and perpendicular to the direction of flow.

6.3.4.1. Offset Transverse Plane Parallel to the Rotor Plane

The flow on a transverse plane in the wake at TSR=5.5 and Reynolds number of $Re_{DiU_\infty} = 5.3 \times 10^5$, on the Y-Z plane at 1.6 blade radii downstream of the rotor are presented here. The location of the traverse plane and directions of motion are presented in Figure 159.

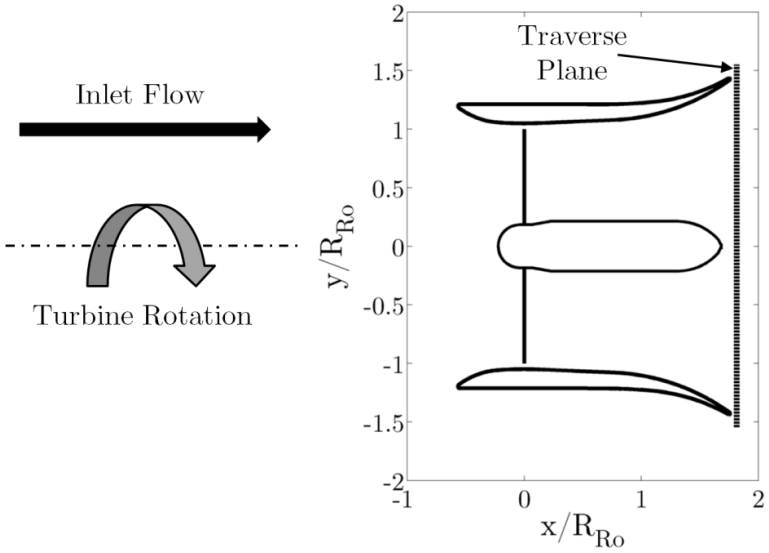


Figure 159: Location of the downstream offset transect plane relative to the diffuser

The radius used for the normalisation of data is the blade radius, with the -5° pitch blades being used. The time averaged images are looking upstream towards the rotor plane, with the turbine rotating in the counter-clockwise direction. Figure 160 shows total and static pressure coefficient distributions on the plane, where the total pressure coefficient is defined as in Equation 88. Figure 161 shows the normalised velocity and turbulence intensity in the wake.

It can clearly be seen from Figure 160 and Figure 161 that the flow structure of the wake has changed markedly from that seen with the bare rotor in Section

6.2.4. The most significant effects are that the pressures and velocities at exit are significantly below those found in the bare rotor case. The pressure drop is expected as the motivation for the use of a diffuser for power augmentation is to reduce the pressure behind the rotor plane to increase the swallowing capacity of the duct. The velocity drop is caused by the diffusion of the flow and the necessity of the flow velocity to drop as the pressure rises. The overall wake structure has also changed, with the region of velocity deficit in the hub wake being significantly increased. The wake expansion, primarily following the diffuser surface due to the higher energy flow at the exterior, leads to a low velocity in the hub wake region.

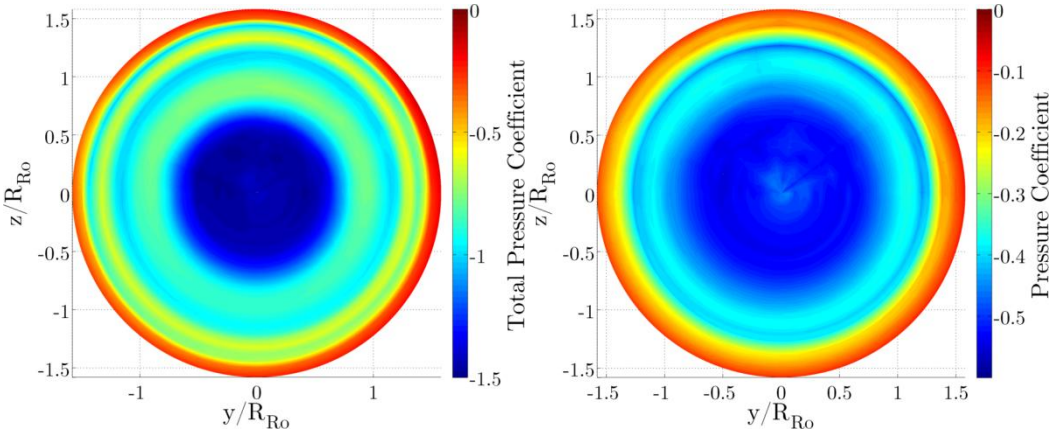


Figure 160: (a) Total and (b) static pressure coefficients with -5° blade pitch at TSR=5.5 and $Re_{DiU_\infty} = 5.3 \times 10^5$, on Y-Z plane at 1.6$R_{Ro}$ downstream of the rotor

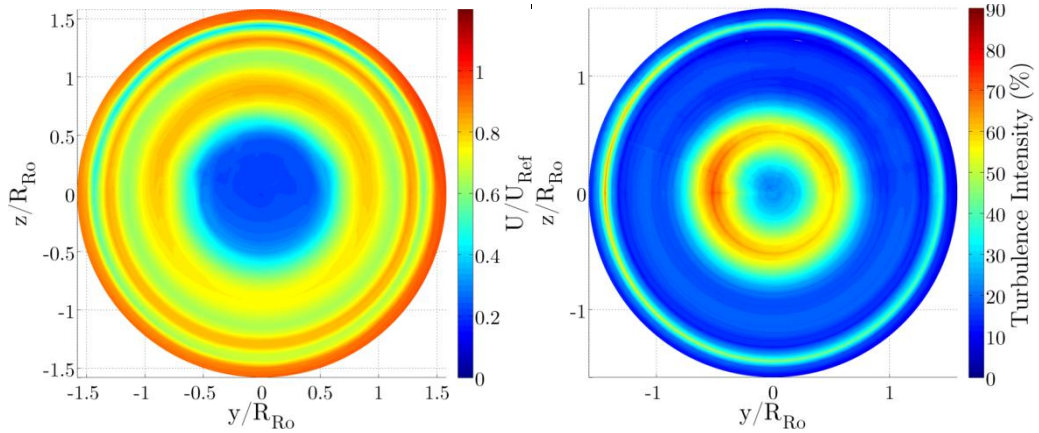


Figure 161: (a) Normalised velocity and (b) Turbulence intensity with -5° blade at TSR=5.5 and $Re_{DiU_\infty} = 5.3 \times 10^5$, on Y-Z plane 1.6$R_{Ro}$ downstream of rotor

From the velocity distribution seen in Figure 161 it can be seen that the tip vortices propagate downstream radially outward, following the expansion of the diffuser. The high velocity tip gap jet, formed between the rotor and casing, can be

seen around the circumference of the wake at $r/R_{Ro} = 1.3$. The shadow of the diffuser trailing edge and associated velocity deficit is also visible around $r/R_{Ro} = 1.4$. The structure of the flow from the rotor tips has changed, with the greater wake expansion in the diffuser and the high shear with the tip gap jet flow, the tip structure has dissipated to some extent by exit.

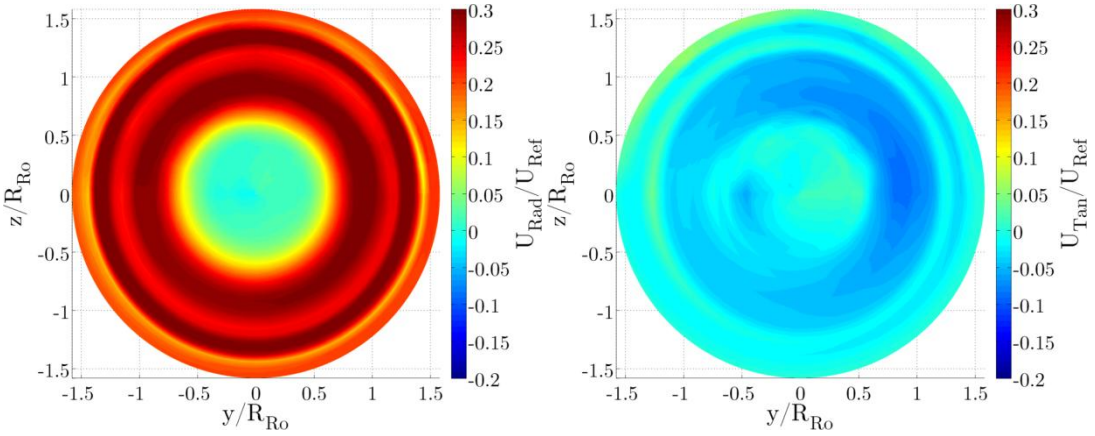


Figure 162: Normalised (a) radial and (b) tangential velocity with -5° blade pitch at TSR=5.5 and $Re_{DiU_\infty} = 5.3 \times 10^5$, on Y-Z plane at 1.6$R_{Ro}$ downstream of the rotor

Diffuser augmentation causes the flow at the traverse plane to become more uniform circumferentially due to the increased turbulence intensity. As can be seen from Figure 140(b) and Figure 161(b) there is a large increase in the turbulence intensity in the near hub region in the diffuser. The large turbulence intensity acts to increase the level of mixing which occurs within the rear of the diffuser and hence to smooth out circumferential variation. In order to quantify the circumferential non-uniformity, the RMS variation of certain variables was taken circumferentially for a number of radial stations and averaged across the traverse plane. The RMS variation was calculated using Equation 89, with the results shown in Table 21.

$$RMS_U = \sqrt{\frac{(U_1-\bar{U})+(U_2-\bar{U})+\cdots+(U_n-\bar{U})}{n}} \qquad \text{Equation 89}$$

Variable	Units	Rotor	Diffuser	Delta (%)
P_0	Pa	20.861	23.428	12.302
U_r/U_∞	-	0.039	0.023	-40.025
U_ϑ/U_∞	-	0.035	0.021	-41.078

Table 21: Circumferential RMS variations in the traverse plane flow properties

As can be seen there is a significant increase in the uniformity of the velocity field due to the enhanced mixing within the diffuser. The total pressure exhibits marginally greater non-uniformity across the traverse plane due to the proximity of the diffuser trailing edge to the measurement plane and the circumferentially varying extent to which the wake is visible. If the RMS variation is averaged instead over the range $0<r/R<1.4$, then the percentage change is actually -31.129%, again showing that the turbulence is reducing the non-uniformity across the exit plane.

The flow patterns seen in Figure 162(a) show that the radial velocity components of the diffuser flow are greater than in the rotor only case seen in Figure 141. The tendency of the flow to follow the tip gap flow along the diffuser's interior surface in preference to flowing axially along the hub is also seen. This is an illustration of the Coanda effect [181], with the high velocity flow along the wall encouraging the bulk flow to follow along the same path. The effect of the tip losses on this flow pattern is to introduce a division between the tip gap jet and bulk flow, the strength of which is dependent upon the velocity deficit in the tip region.

The tangential velocity distribution seen in Figure 162(b) exhibits broadly the same structure as in the rotor only case. The wake swirls counter-clockwise, opposed to the rotation of the rotor, but with a lower magnitude than in the rotor only case. This reduction is due to the diffuser's slowing of the wake flow. The extent to which the strut is visible is greater in this case than in the rotor only case. Here the tangential velocity can be seen to increase from a minimum in the strut shadow in the bottom left sector and gradually increase as the flow swirls circumferentially around to the bottom right sector and the pressure side of the strut fairing.

Figure 163 shows the circumferentially averaged axial velocity at the traverse plane from the experiments against the results of the BEM CFD for the equivalent run. It can be seen that the CFD predicts a much greater extent of mixing between the tip gap jet and the bulk flow, with the jet barely evident by the traverse plane. The jet within the experimental results can also be seen to diverge from the duct casing, resulting in a velocity peak at $y/R_{Ro} \approx 1.3$. The mixing seen between the jet flow and bulk flow causes the velocity of the bulk flow to increase, with a peak velocity reaching almost that seen in the freestream.

The CFD predicts that the hub wake at this tip speed ratio is characterised by an area of recirculating flow, whereas the experimental results show a region of

flow which is slow moving but at a constant velocity. The difference between these flow regimes is likely to be caused by limitations in the modelling of the near hub fluid dynamics and the rotor turbulence. In the experimental case the situation is complicated by flow being bled behind the rotor for the generator cooling flow. This bleed acts to suppress the boundary layer behind the rotor plane, which suppresses trailing separation from the hub and the region of flow recirculation in the wake.

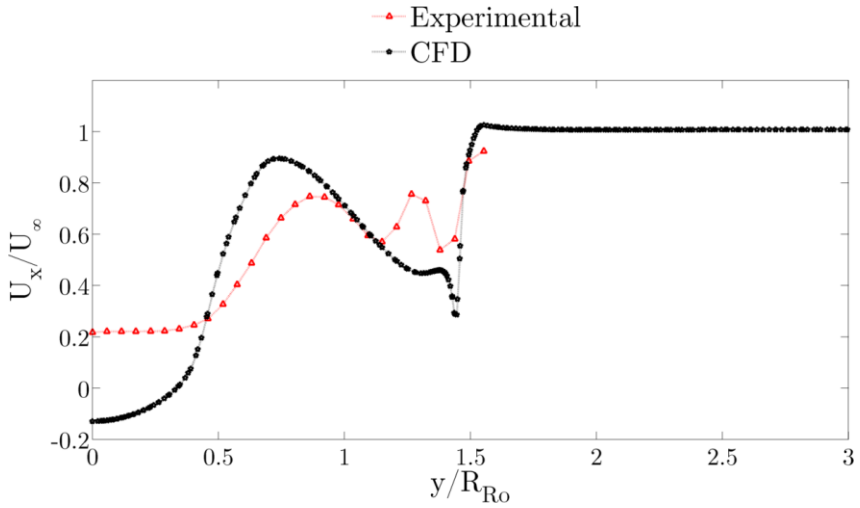


Figure 163: Comparison of CFD normalised axial velocity distribution at traverse plane with experimental data for diffuser augmented rotor with -5° blade pitch

The turbulence generation model used within the BEM CFD is likely to be the prime driver of the diverging results seen here. The model, which ties the turbulence intensity to the axial induction, as detailed in Section 3.2.4.2, is an empirical relation for bare turbine rotors. The magnitude of the turbulent kinetic energy is likely to be comparable, but as detailed in Section 2.3.4, flows within diffusers are sensitive to the intensity, length scales and orientation of turbulent eddies. The model here over predicts the overall mixing, as can be seen by the joining of the jet and bulk flows. In order to gain a more detailed picture of the flow within the diffuser from the CFD a more detailed turbulence generation model is needed.

6.3.4.2. Longitudinal Plane at the Rotor Axis

In addition to the transect parallel to the rotor plane, a longitudinal transect was taken on the X-Y plane of the wind tunnel at the turbine axis height. This transect was taken in the rotor wake at a TSR=5.5 and $Re_{DiU_\infty} = 5.3 \times 10^5$. The radius used for normalisation is the blade radius, with the -5° pitch blades being used. Figure 164 shows the pitch and yaw distributions in the wake.

What can be seen in Figure 164 is that the diffuser has a significant impact upon the wake structure of the device. The yaw distribution shows that the wake continues to expand after exit from the diffuser, aided by the radial direction of the flow around the duct's external surface, until $x/R_{Ro} \cong 2.3$. Past this point the wake flow contracts around the hub wake region and closes.

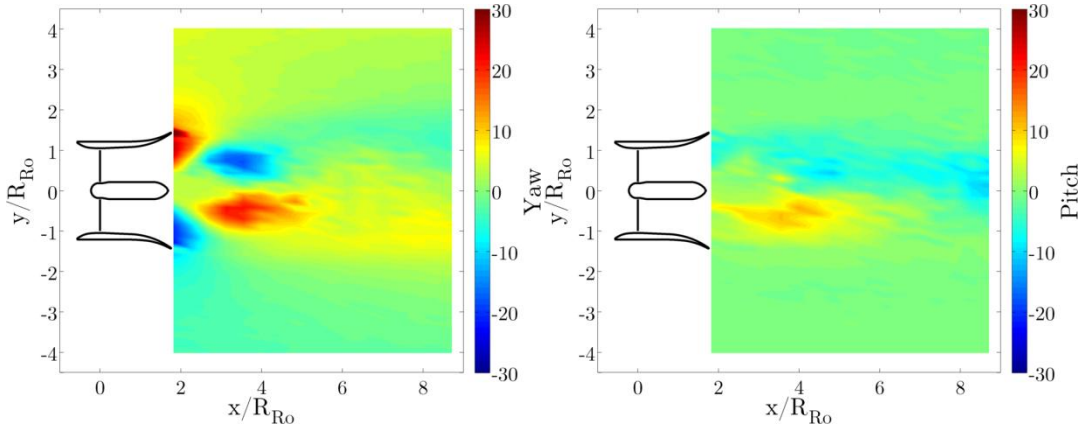


Figure 164: (a) Yaw and (b) pitch angles in degrees in the diffuser wake for -5° blade pitch rotor at TSR=5.5 and $Re_{DiU_\infty} = 5.3 \times 10^5$, on X-Y plane at axis height

The pitch distribution seen in Figure 164(b) shows a wake where the overall swirl level is consistent with that seen in the rotor only case, the overall magnitude being reduced, but the swirling volume being higher. The wake can be seen to swirl around the rear of the hub wake and when the flow closes around the rear of this region the entire cross section of the wake continues to swirl, with the overall wake pitching downwards as it moves downstream.

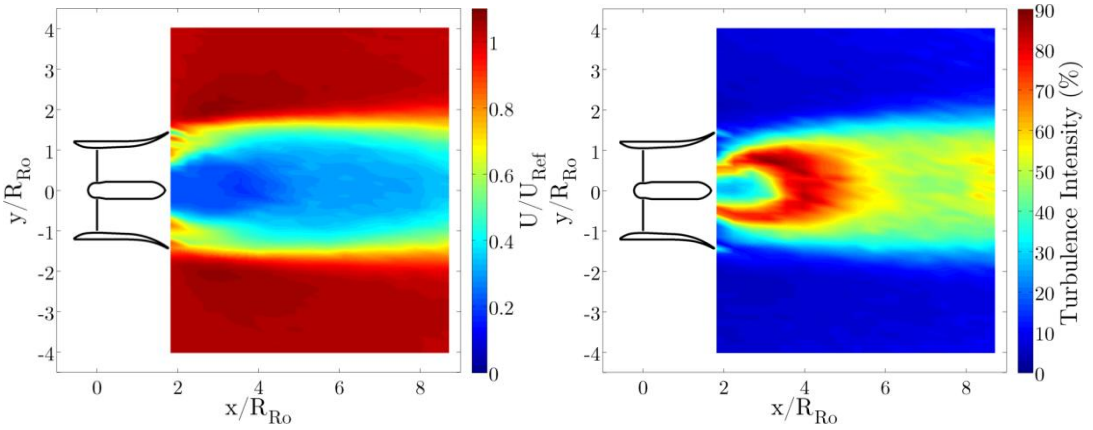


Figure 165: (a) Normalised velocity and (b) turbulence intensity in the wake for -5° blade pitch rotor at TSR=5.3 and $Re_{DiU_\infty} = 5.3 \times 10^5$, on X-Y plane at axis height

The freestream flow mixes with the exterior of the wake, where the majority of throughflow passes. The bulk flow through the rotor interacts transiently with the slow moving region of flow around the hub at the diffuser exit. This causes the generation of both a distinct shear layer and very high levels of turbulence.

The overall pattern of the flow through the diffuser can be inferred from Figure 165. It shows a flow which is attracted to the interior diffuser walls by the jet flow and through this mechanism is pulled from the hub surface. The tendency of the bulk flow to radiate outwards from the axis leads to the region of slow moving flow behind the hub, around which the bulk of the rotor wake tends to flow.

As seen in Figure 165, the overall wake velocity deficit is significantly greater than for a bare turbine. In addition the pressure distributions seen in Figure 166 show that the wake is significantly less energetic than in the rotor only case.

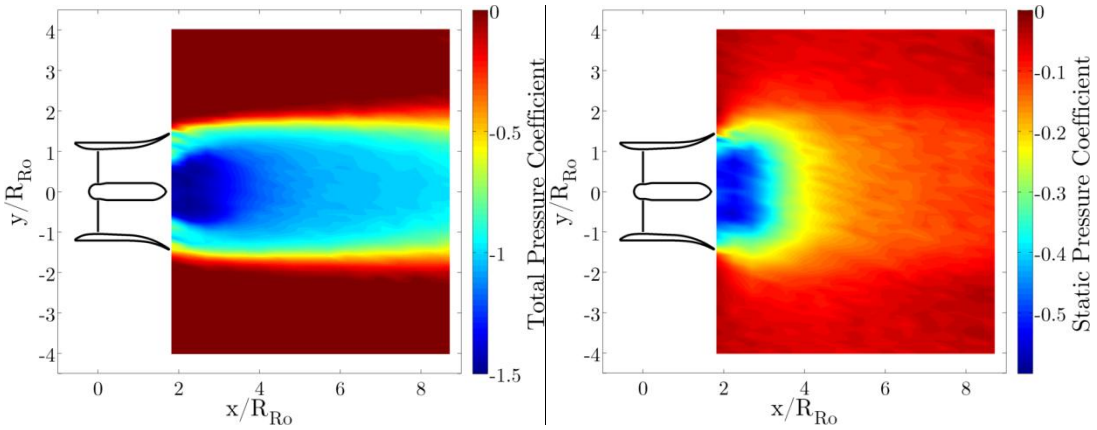


Figure 166: (a) Total and (b) static pressure coefficients in the diffuser wake for -5° blade pitch rotor at TSR=5.5 and $Re_{DiU_\infty} = 5.3 \times 10^5$, on X-Y plane at axis height

As seen from Figure 165 and Figure 166, the amount of energy captured by the device compared to that which is lost to the flow as a result of the device is lower than for a bare rotor. As a result of this a diffuser augmented device would be less effective as part of an array than a bare rotor as there would be less energy remaining in the flow for a downstream device in this case.

6.3.4.3. Wake Recovery

The axial velocity deficit along the centreline of the wake of the -5° blade pitch rotor and the same rotor within the diffuser is shown in Figure 167. It can be seen immediately that the wake recovery is considerably slower in the case of the diffuser augmented turbine than the bare rotor. The velocity deficit in the diffuser

augmented case was $\sim 0.65U_\infty$ at x/R=9, whereas with the bare rotor the velocity deficit was only $\sim 0.30U_\infty$ at x/R=9. This reduction in the wake recovery is due to the higher energy losses seen in the diffuser wake and the wake structure.

In the bare rotor wake the hub wake region is de-energised but with a moderate turbulence intensity of around 20% as can be seen from Figure 146. The flow surrounding the hub wake is more energetic, although with a lower turbulence intensity. The proximity of the more energetic flow to the turbulent hub wake means that the two regions mix and the wake recovers relatively rapidly.

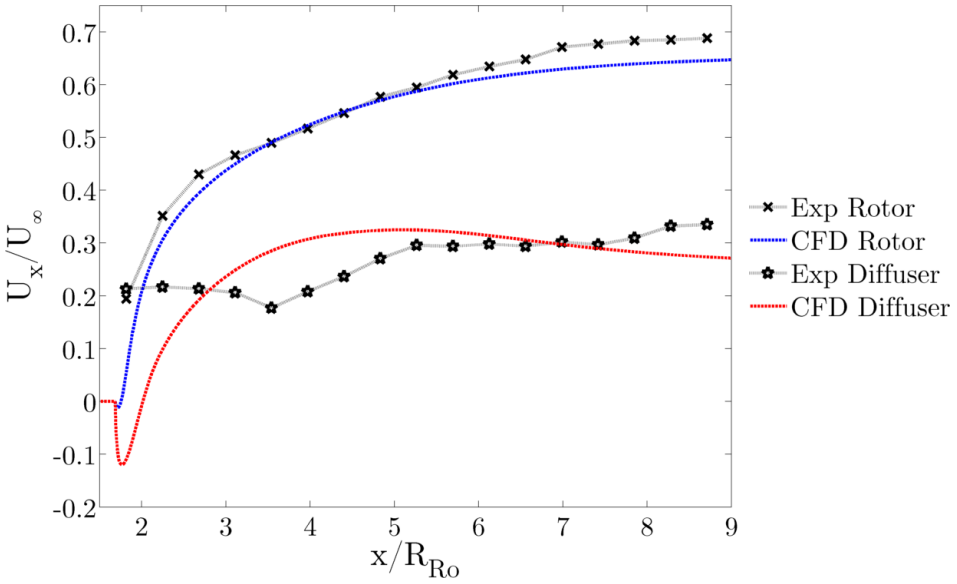


Figure 167: Experimental and BEM CFD wake recovery for -5° blade pitch bare rotor and diffuser augmented rotors at $Re_{DiU_\infty} = 5.5 \times 10^5$, with a turbulence intensity of 4.7%

In the case of the diffuser augmented turbine, the flow separates from the hub closer to the turbine plane and there is a large region of slow moving flow behind the hub as can be in Figure 165. Although this region has higher turbulence levels than with the bare turbine, the surrounding flow also possesses low energy and so the mixing effect, whilst strong, limits effective recovery of the wake.

The departure of the CFD results from the experimental data is caused by the prediction of the wake structure. As seen from Figure 163, the CFD predicts a region of flow recirculation behind the hub when the experimental results suggest that this region is slow moving flow. This inaccurate prediction of the near wake propagates downstream to the far wake causing erroneous flow patterns.

The results show that diffuser augmented turbines will need considerably greater axial spacing distances in array formations than would bare rotors due to the inability of the wake to recover. Given that optimum power generation conditions in tidal power sites tend to be located within a relatively small geographical area, this would lead to inefficient extraction of the available power.

6.4. Concluding Remarks

The key findings from the experimentation can be categorised into three sections; verification of the turbine modelling methodology, wake recovery performance and yaw effects.

6.4.1. Verification of Blade Element Momentum Turbine Model

The key finding of the experimental campaign was the verification of the blade element momentum based computational fluid dynamics model for the estimation of the power output of a diffuser augmented device. The model has been shown to represent the power output of the device well for both power outputs tested.

The limitations of the current model have been noted at low tip speed ratios, where the blade section is largely stalled or close to the stall point along the blade length. A simple correction for post-stall section behaviour, such as that proposed by Viterna and Corrigan [179], to the blade section performance data should correct this divergence. It should be noted that the accuracy of the section data is the prime driver of the model fidelity as with any blade element based model. It is therefore of significant importance to ensure as far as possible that the data is accurate for the flow conditions that will be experienced by the rotor at all points.

The BEM CFD model was shown to predict the approximate pressure distribution around the diffuser section but only replicated the downstream flow field with limited success. This was primarily due to the over prediction of mixing as a result of the turbine's turbulence generation model. It is therefore recommended that further work is conducted to ascertain the turbulence structure generated within the diffuser by the turbine and to tie this back to the turbine's geometric properties. An empirical relation can then be arrived at to represent the complex turbulence field within the simplified BEM CFD model.

The model, despite it's limitations in wake prediction, has been shown to be accurate for the prediction of device performance at the design stage. Whilst this model cannot supplant 3D CFD and experimental work for later stage development,

it does effectively fill a niche for the rapid assessment of device performance. It is therefore ideally suited to the comparison of component geometry effects.

6.4.2. Wake Recovery

The wake recovery for a diffuser augmented turbine has been assessed experimentally for the first time as a part of this thesis. It has been found that the wake of a diffuser augmented turbine is less energetic than for the equivalent bare rotor. The velocity deficit in the diffuser augmented case was $\sim 0.65 U_\infty$ at x/R_{Ro}=9, whereas in the bare rotor case the velocity deficit was only $\sim 0.30 U_\infty$ at x/R_{Ro} =9.

The significantly reduced wake recovery means that diffuser augmented devices would need to be spaced over much larger axial distances within arrays. This increased spacing, coupled with the reduced power coefficient, means that diffuser augmented arrays make less efficient use of the available power than bare rotors. As optimal conditions in tidal power sites tend to be concentrated within a limited geographic area this is a significant limitation.

6.4.3. Effect of Yaw

The effect of yaw on diffuser augmented turbines has been investigated before [25, 53, 94], but there have been questions about the validity of the obtained results raised by the authors themselves as a result of the excessive wind tunnel blockages. The results obtained here, with blockage ratios of only 9.8% and in an open jet type tunnel show that diffusers can produce performance benefits with yawed flows.

The results seen in this chapter show that the diffuser augmented turbine is capable of maintaining device performance at around the peak, with yaw angles in the range ±30°. The main driver of this performance is the tip gap jet flow, generated between the rotor and diffuser, which acts to suppress boundary layer separation. The lack of separation means the swallowing effect of the diffuser remains broadly similar with yawed flows and as a result of the diffuser geometry the flow is largely aligned with the rotor at the rotor plane. At large yaw angles of greater than ±30°, the diffuser begins to stall and the performance drops rapidly.

7. Diffuser Augmented Device Costs

The adoption of diffuser augmented devices in the tidal stream generation industry will be driven by the costs and generation potentials associated with them. Since the energy provided to these devices is free, the main factor which will affect their uptake is the relationship between the device capital cost and the power output. Using data gathered from a variety of sources and the experimental and numerical data contained within this thesis, calculations of the generation and economic aspects of full scale devices have been made.

7.1. Tidal Stream Turbine Cost Model

The basis of the cost model, derived here for diffuser augmented and bare tidal stream devices, is the NREL wind turbine design cost and scaling model of Fingersh et al [182]. This model uses a range of wind turbine metrics to estimate the cost of energy of a device design based on a number of underlying assumptions.

7.1.1. Assumptions of the Tidal Stream Turbine Cost Model

There are a number of assumptions made by NREL in the construction of the wind turbine design costs and scaling model, which are that:

1. The base device is a three bladed, upwind, variable speed turbine
2. The results are based on a mature design with mature components
3. The device is installed as part of a 50MW farm
4. A fixed charge rate of 11.58% is applied

These assumptions of the overall configuration are sensible given trends in the tidal industry [21], and so this model can broadly be adapted for use for the cost estimation of tidal stream devices. The assumption of the 50MW farm size is also a sensible scale for the estimation of costs as it represents a medium scale array [183].

At this stage in the development of the tidal stream generation industry the assumption of mature designs and mature component specification is unlikely to hold. In order to overcome this limitation adaptations have been made to the NREL model as detailed later in Section 7.1.2.

The fixed charge rate was calculated by NREL and covers items such as return on debt and equity, financing, depreciation, income tax and insurance. The rate was calculated based on a spreadsheet model of the likely project cashflows for

a hypothetical wind farm. The exact value for this figure will have changed over time, but for the purposes of this model it is deemed that in order to facilitate a fair comparison no change is necessary since it represents a percentage adjustment. If the absolute rather than the relative values from this model are to be used then the fixed charge rate must be updated.

The configuration used for estimation within this thesis is a monopile foundation in a water depth of 30m, with a cross beam and two devices (bare or diffuser augmented) mounted onto this. It is therefore the same as the configuration used by Bir et al. [184], similar to the configuration used by Marine Current Turbines [185] and also resembles the diffuser mounting foreseen by Luquet et al. [103]. The layout can be seen schematically in Figure 168. Although the work contained within this thesis assumes this device layout, many of the aspects of the scaling model are applicable to a variety of tidal stream turbine configurations.

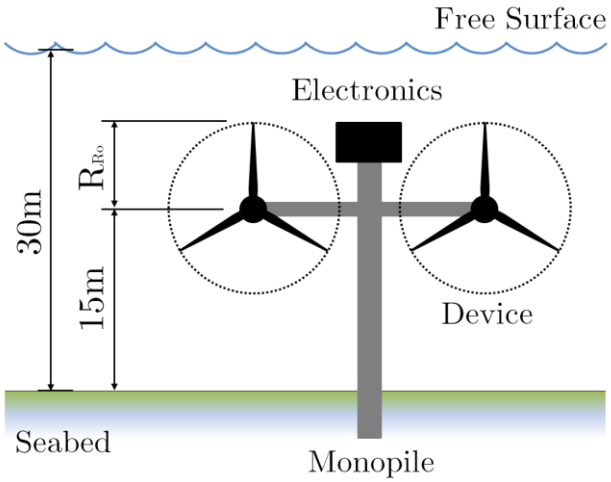


Figure 168: Assumed configuration for the present study cost model

There are a number of further assumptions or assertions made in the construction and adaption of the cost model, these are that:

1. The baseline blade radius is 8 m
2. The design wind velocity is 8.5 m/s
3. The design tidal velocity is 2 m/s
4. Survival speeds are 60 m/s for wind and 6 m/s for tidal
5. The density of air is 1.225 kg/m^3 and that of seawater is 1028 kg/m^3

It should be noted that the models detailed here use kW as the base unit for power, kWh for energy and kNm for torque.

All costs within the model are in pound sterling (GBP) as of July 2014. Price inflation was calculated in the source currency and then converted to GBP using rates of £1=€1.26 and £1=$1.69. Inflation rates were taken from the UK Office for National Statistics [186], the United States Bureau of Labor Statistics [187] and the European Central Bank [188]. All cost formulae which have been directly adopted, unless otherwise stated, have been multiplied by factor of 0.778 to convert from December 2002 USD to July 2014 GBP.

The cost model is formed of two parts, the capital cost model and the operating and maintenance cost model. The capital cost model is the more involved part of the model and is based upon a summation of the costs of a number of parts within the device. The operation and maintenance cost model uses a more simplistic approach to estimation, which is based upon the annual energy production.

7.1.2. Capital Cost & Mass Model

The capital cost and mass models are formed on the basis that the cost or mass are the sum of the project component costs or masses. NREL derived cost and mass scaling models for the components found within a typical wind turbine. There is a significant degree of crossover between the wind and tidal industries, the functions however will not remain the same in all cases. Within this section the NREL model is presented along with corrections, where relevant, made to enable estimation of the costs and masses for tidal stream turbines in the present study.

7.1.2.1. Rotor Components

The rotor comprised of three components within the model, the blades, hub and nose cone. The masses in the NREL rotor model are detailed in Table 22.

Part	Model	Equation
Blades (Each)	NREL	$m_{Blade} = 0.1452 {R_{Blade}}^{2.9158}$
	Present Study	$m_{Blade} = 4.899 {R_{Blade}}^{2.9158}$
Hub	NREL	$m_{Hub} = 0.954 m_{Blade} + 5680.3$
	Present Study	$m_{Hub} = 0.954 m_{Blade} + 5680.3$
Nose Cone	NREL	$m_{Nose} = 37 R_{Blade} - 520.5$
	Present Study	$m_{Nose} = 310.504 R_{Blade} - 520.5$

Table 22: Masses of the rotor components in the two mass models

The blade mass estimation for the present study was based upon the NREL mass with an adjustment factor computed using the blade design of Bir et al. [184]. This blade has a 9 m radius, and is a composite blade with epoxy slurry filler and a mass of 3413.2 kg. It was assumed that the relationship of mass to length retains its almost cubic, geometric nature, and the constant was amended so that the present study's blade mass model was equal to that of the Bir blade at a radius of 9m.

The hub mass relationship was assumed to remain the same as any necessary correction was assumed to have been accounted for by the change in the blade mass.

The nose cone mass was amended from the NREL model, as the nose cone mass would otherwise be negative at the relatively small device radii found in tidal stream turbines. To account for this, the mass was altered by taking into account the bending moments at the blade root. The root bending moment on a cantilevered beam subject to a uniformly distributed load is given by Equation 90. Assuming that the turbine thrust can be approximated as the pressure difference across the rotor and that this is the product of the dynamic head and the power coefficient, the idealised root bending moment on each blade can be calculated using Equation 91.

$$M = \frac{wR_{Ro}{}^2}{2} \qquad \text{Equation 90}$$

$$M = \left(\frac{1000}{4}\right)\left(\frac{C_P \rho U^2 \pi R_{Ro}{}^3}{B}\right) \qquad \text{Equation 91}$$

Assuming that the power coefficient is constant, and using the values specified in Section 7.1.1, the difference between the bending moments for any given rotor radius is a constant factor of 8.392 applied to the blade radius.

The cost models for the rotor are given in Table 23. As can be seen, the costs of the hub and nose were assumed not to have changed, beyond the currency and temporal change, as this was accounted for in the change of the masses. The rotor cost has changed markedly, as the NREL cost model would mean a cost which would be negative at the radii under consideration. The cost here has been calculated based upon the average proportion of the total capital cost that the rotor represents for wind turbines from a survey of models by Engels et al. [189]. To convert this to a value tied to the device's characteristics, the cost per rated kW for the MCT SeaGen, as given by Fraenkel [185] for a 10MW array was used.

Part	Model	Equation
Blades (Each)	NREL	$\$_{Blade} = \frac{0.04019{R_{Blade}}^3 + 2.745{R_{Blade}}^{2.5025} - 955.24}{1 - 0.28}$
	Present Study	$£_{Blade} = 139.26P_{RATED}$
Hub	NREL	$\$_{Hub} = 4.25m_{Hub}$
	Present Study	$£_{Hub} = 4.25m_{Hub}$
Nose Cone	NREL	$\$_{Nose} = 5.57m_{Nose}$
	Present Study	$£_{Nose} = 5.57m_{Nose}$

Table 23: Capital costs of the rotor components in the two cost models

7.1.2.2. Drivetrain Components

The purpose of the drivetrain is to transfer the rotational energy of the rotor through to the generator. The drivetrain is made up of a set of five components within the model, the pitch bearings, low speed shaft, main bearings, gearbox and the brake. The masses of these components are given in Table 24.

Part	Model	Equation
Pitch Bearing	NREL	$m_{Pitch} = 0.1719m_{Blade} + 1207.47$
	Present Study	$m_{Pitch} = 0.1719m_{Blade} + 1207.47$
Low Speed Shaft	NREL	$m_{LSS} = 0.0142(2R_{Blade})^{2.888}$
	Present Study	$m_{LSS} = 48.920{R_{Blade}}^{2.888}$
Main Bearings	NREL	$m_{Bearing} = \left(\frac{16}{600}R_{Blade} - 0.033\right)0.0092(2R_{Blade})^{2.5}$
	Present Study	$m_{Bearing} = 2.374{R_{Blade}}^{3.5} - 0.350{R_{Blade}}^{2.5}$
Gearbox	NREL	$m_{Gear} = 70.94T^{0.759}$
	Present Study	$m_{Gear} = 70.94T^{0.759}$
Brakes	NREL	$m_{Brakes} = 1.989P_{RATED} - 0.1141$
	Present Study	$m_{Brakes} = 1.989P_{RATED} - 0.1141$

Table 24: Masses of the drivetrain components in the two mass models

The masses of the pitch bearings, gearbox and brakes are assumed to remain the same in both models as the relationships are either derived from previously

amended values or are calculated directly with tidal data. NREL provide a number of options for the gearbox type, the type specified within the present study was selected as being a planetary or helical gearbox as informed by the generator choice detailed in Section 7.1.2.3. The mass of the gearbox is calculated using the torque on the low speed shaft. The masses of the low speed shaft and main bearings were modified from the NREL model and corrected for the blade root bending moments.

The costs associated with the drivetrain components can be seen in Table 25. Alterations were made to the cost model in the same way as with the mass model, with the pitch bearings, gearbox and brakes only altered to change to 2014 GBP. The cost of the low speed shaft and the main bearings were again corrected for the blade root bending moments and amended for 2014 GBP.

Part	Model	Equation
Pitch Bearing	NREL	$\$_{Pitch} = 3.030 R_{Blade}^{2.6578}$
	Present Study	$£_{Pitch} = 2.356 R_{Blade}^{2.6578}$
Low Speed Shaft	NREL	$\$_{LSS} = 0.010(2R_{Blade})^{2.887}$
	Present Study	$£_{LSS} = 34.354 R_{Blade}^{2.888}$
Main Bearings	NREL	$\$_{Bearing} = 35.2 m_{Bearing}$
	Present Study	$£_{Bearing} = 27.386 m_{Bearing}$
Gearbox	NREL	$\$_{Gear} = 16.450 P_{RATED}^{1.249}$
	Present Study	$£_{Gear} = 12.798 P_{RATED}^{1.249}$
Brakes	NREL	$\$_{Brakes} = 10 m_{Brakes}$
	Present Study	$£_{Brakes} = 7.78 m_{Brakes}$

Table 25: Capital costs of the drivetrain components in the two cost models

7.1.2.3. Generator and Electrical Components

A three stage drive with a high speed generator was selected for the drivetrain as it most closely resembles those used by wind turbines and is a proven, high efficiency, fault resistant technology [190]. This drive type is similar to that employed on the MCT SeaGen device [191]. The masses of components within the model can be seen in Table 26.

The mass of the generator within the model is assumed to be the same as for the NREL model as the cost should retain its relationship to the rated power of the device. The masses of the other components are either negligible within the scale of

the model or the components are assumed to be sited at the sub-station and not contribute to the device mass.

Part	Model	Equation
Generator	NREL	$m_{Gen} = 6.47 P_{RATED}{}^{0.9923}$
	Present Study	$m_{Gen} = 6.47 P_{RATED}{}^{0.9923}$
Variable Speed Electrics	NREL	–
	Present Study	–
Electrical Connects	NREL	–
	Present Study	–
Electrical Interface	NREL	–
	Present Study	–

Table 26: Masses of the generator and electrical components in the two mass models

The costs within the models are detailed in Table 27. The costs are taken directly from the NREL model for offshore turbines and amended to 2014 GBP. The assumption that the prices do not need amending is justified by the listed prices reflecting the offshore nature of the devices. Necessary allowances for the cost of encapsulating and sealing these components are made elsewhere within the model.

Part	Model	Equation
Generator	NREL	$\$_{Gen} = 65 P_{RATED}$
	Present Study	$£_{Gen} = 50.57 P_{RATED}$
Variable Speed Electrics	NREL	$\$_{VSE} = 79 P_{RATED}$
	Present Study	$£_{VSE} = 61.46 P_{RATED}$
Electrical Connects	NREL	$\$_{EInt} = 40 P_{RATED}$
	Present Study	$£_{EInt} = 31.12 P_{RATED}$
Electrical Interface	NREL	$\$_{ECon} = 260 P_{RATED}$
	Present Study	$£_{ECon} = 202.28 P_{RATED}$

Table 27: Costs of the generator and electrical components in the two cost models

7.1.2.4. Electronics & Control Components

The electronics and control components are those which manage the power conversion process. This covers the automation and actuation of the blade pitching and yawing of the device to face the oncoming tidal current. The masses of the

electronics and control components are detailed in Table 28. The mass of the yaw mechanism has been altered to reflect the level of loading during operation and has been corrected by a factor relating the freestream dynamic pressures at the design speeds. This factor was calculated as being the freestream dynamic pressure at the design speed of the tidal stream turbine normalised by that of the wind turbine. The mass of the hydraulics and cooling is assumed to remain the same and the mass of the control system is assumed to be negligible in relation to the overall device mass.

Part	Model	Equation
Yaw Mechanism	NREL	$m_{Yaw} = 0.0143{R_{Blade}}^{3.314}$
	Present Study	$m_{Yaw} = 6.644{R_{Blade}}^{3.314}$
Hydraulics & Cooling	NREL	$m_{Hyd} = 0.08P_{RATED}$
	Present Study	$m_{Hyd} = 0.08P_{RATED}$
Control System	NREL	–
	Present Study	–

Table 28: Masses of the electronics & control components in the two mass models

The capital costs of the electronics & control components are given in Table 29. The costs have been amended in the same way as the mass model, with the hydraulics and yaw costs taken directly from the NREL model, and the currency converted. The yaw cost has again been amended by a factor relating the dynamic pressures at the design speeds as done previously to the mass.

Part	Model	Equation
Yaw Mechanism	NREL	$\$_{Yaw} = 0.529{R_{Blade}}^{2.964}$
	Present Study	$£_{Yaw} = 24.577{R_{Blade}}^{2.964}$
Hydraulics & Cooling	NREL	$\$_{Hyd} = 12P_{RATED}$
	Present Study	$£_{Hyd} = 9.34P_{RATED}$
Control System	NREL	$\$_{Cont} = 55000$
	Present Study	$£_{Cont} = 42790$

Table 29: Costs of the electronic & control components in the cost models

7.1.2.5. Structural Components

The structural components category covers the supporting elements of the design as well as the covering for the nacelle. The selection of the frame type from

the NREL model depends on the generator and gearbox configuration, the relationships here being those for a three stage drive with a high speed generator. The masses in the two models are presented in Table 30.

Part	Model	Equation
Frame	NREL	$m_{Frame} = 8.646 R_{Blade}^{1.953}$
	Present Study	$m_{Frame} = 550.709 R_{Blade}^{1.953}$
Nacelle Cover	NREL	$m_{Nacelle} = 1.154 P_{RATED} + 384.97$
	Present Study	$m_{Nacelle} = 1.154 P_{RATED} + 384.97$
Tower	NREL	$m_{Tower} = 0.2694 A_{Ro} h_{Tower} + 1779$
	Present Study	$m_{Tower} = 24.981 A_{Ro} h_{Tower} + 1779$
Crossbeam	NREL	–
	Present Study	$m_{XBeam} = 9.460 A_{Ro} h_{Tower} + 676$

Table 30: Masses of the structural components in the two mass models

The model for the tower mass was scaled using the 242 tonne mass of the MCT SeaGen tower reported by Douglas et al. [192]. The crossbeam mass, which did not previously exist in the NREL model, was based upon the tower scaling relationship, but is calibrated using the 92 tonne mass of the MCT SeaGen crossbeam. The frame mass was amended by the ratio of the dynamic pressures at survival speed, with the nacelle cover mass assumed to remain constant. The capital costs of the structural components can be seen in Table 31.

Part	Model	Equation
Frame	NREL	$\$_{Frame} = 36.74 R_{Blade}^{1.953}$
	Present Study	$£_{Frame} = 470.22 R_{Blade}^{1.953}$
Nacelle Cover	NREL	$\$_{Nacelle} = 10 m_{Nacelle}$
	Present Study	$£_{Nacelle} = 15.56 m_{Nacelle}$
Tower	NREL	$\$_{Tower} = 1.5 m_{Tower}$
	Present Study	$£_{Tower} = 1.167 m_{Tower}$
Crossbeam	NREL	–
	Present Study	$£_{XBeam} = 1.167 m_{XBeam}$

Table 31: Capital costs of the structural components in the two cost models

The tower and crossbeam costs are assumed to maintain the same relationship as with the NREL model and so only the currency has changed. The cost for the frame has been updated in the same way as the mass, with the ratio of the survival speed dynamic pressures being used. The nacelle cover cost has been doubled to reflect the extra strength which is required to withstand the external pressures and the need for it to remain watertight.

7.1.2.6. Diffuser

The capital cost and the mass of a diffuser for tidal stream augmentation are not something which has previously been estimated to the author's knowledge. The starting point here was the estimate made by Foreman of the diffuser cost for a diffuser augmented wind turbine [89]. The total cost given by Foreman for the construction of a fibre reinforced polymer, balsa core, diffuser for a 36ft diameter rotor was $62969 in 1981. Foreman states that the fibre reinforced polymer cost is a function of the surface area of the diffuser. The surface area of the diffuser was approximately 654m^2, making the cost at the time of writing £365.14/m^2.

In order to amend the cost for use with diffuser augmented tidal stream turbines, the cost of the diffuser was corrected for the stresses that it is likely to experience. The stress was estimated using sandwich plate theory and forces based on the freestream dynamic pressures at survival speed. This led to the conclusion that the stresses in the upper and lower laminates would grow by a factor of 4.196. Assuming that axial strain varies linearly across the section, the thickness of the exterior sheets must be raised by this factor. No breakdown was given by Foreman and so the skin's fraction of the material cost is assumed to be 2/3 of the cost of the laminate. The material cost is therefore increased by a factor of 2.798.

The total cost is formed of two components, the labour and manufacture costs and the material costs. The cost split was calculated for the labour and material cost split for a baseline material blade of 50m radius from the NREL model turbine model. The cost split was labour at 49.8% of the total cost and material at 50.2% of the total cost. It was assumed that the cost of the labour would remain constant as the degree of complexity is approximately equivalent. The final cost factor was therefore 1.902, giving a total cost for the diffuser of £691.28/m^2.

In order to check the estimate was within an acceptable margin of error, the cost was compared to that for FRP bridge decking as provided by Nystrom et al

[193]. The cost in this study was found to be £652.41/m^2. The bride decking in this case was 600mm sandwich panels with a honeycomb core. The complexity of the honeycomb centre is assumed to be comparable to the radius and assembly of the diffuser. The calculated cost of the diffuser for the tidal stream model is therefore thought to be sufficiently detailed for the purposes for which this model is intended.

The mass of the diffuser was estimated using a construction based on a 15mm thick fibre reinforced skin and a balsa wood core. The densities of the skin and balsa are taken as 1661 kg/m^3 and 160 kg/m^3 respectively. The mass is now both a function of the thickness of the diffuser and the surface area as seen in Table 32.

Variable	Equation
Mass	$m_{Di} = A_{DSurf}[160(z_{Skin} - 0.03) + 49.824]$
Cost	$£_{Di} = 694.71A_{DSurf}$

Table 32: Mass and capital cost of the diffuser in the present study

7.1.2.7. Turbine and Tower Costs

The turbine and tower capital costs and masses are the sum of those from Table 22 to Table 32. The cost ($\$_{T\&T}$ or $£_{T\&T}$) is used as an input for the calculation of the warranty premium and the marinisation cost, as detailed in Section 7.1.2.9.

7.1.2.8. Foundations and Civil Engineering Works

The foundations and civil engineering works include all the tasks necessary to install, secure and protect the device. The costs of these works have been taken directly from the NREL model as it is assumed that the complexity of the tasks remains the same. The costs can be seen in Table 33.

Part	Model	Equation
Foundations	NREL	$\$_{Found} = 300P_{RATED}$
	Present Study	$£_{Found} = 233.4P_{RATED}$
Turbine Installation	NREL	$\$_{Inst} = 100P_{RATED}$
	Present Study	$£_{Inst} = 77.8P_{RATED}$
Scour Protection	NREL	$\$_{Scour} = 55P_{RATED}$
	Present Study	$£_{Scour} = 42.8P_{RATED}$

Table 33: Capital costs of civil engineering works in the two cost models

7.1.2.9. Other Costs

This section of the model covers a range of other costs associated with the initial project set up. The costs related to the obtaining of permissions from the relevant authorities, transportation of the turbine to the site by sea, access equipment and port facilities are covered.

There is an additional factor included within the models for the marinisation of components to make them suitable for the harsher environment relative to that for wind turbines. This factor covers things such as the need for improved sealing and improved surface protection. The costs, which can be seen in Table 34, have been taken directly from the NREL model with the exception of the marinisation factor. This factor has been increased by 50% to reflect the additional problems faced as a result of the submergence of the device. The magnitude of this factor will become clearer as the tidal energy industry develops.

Part	Model	Equation
Permits	NREL	$\$_{Permit} = 37P_{RATED}$
	Present Study	$£_{Permit} = 28.8P_{RATED}$
Marinisation Factor	NREL	$\$_{Marine} = 0.135\$_{T\&T}$
	Present Study	$£_{Marine} = 0.202£_{T\&T}$
Transport	NREL	$\$_{Transport} = 1.58 \times 10^{-5}{P_{RATED}}^3 - 0.038{P_{RATED}}^2 + 54.7P_{RATED}$
	Present Study	$£_{Transport} = 1.23 \times 10^{-5}{P_{RATED}}^3 - 0.029{P_{RATED}}^2 + 42.6P_{RATED}$
Port & Staging	NREL	$\$_{P\&S} = 20P_{RATED}$
	Present Study	$£_{P\&S} = 15.6P_{RATED}$
Access Equipment	NREL	$\$_{Access} = 60000$
	Present Study	$£_{Access} = 46680$

Table 34: Other capital costs in the two cost models

There are two additional costs which are accounted for in the models, these are the warranty premium and the surety bond. The costs for these, which have both been taken directly from the NREL model, can be seen in Table 35. The warranty premium covers the additional cost which suppliers will charge for the provision of a warranty on the device. The surety bond covers the cost of decommissioning and the removal of foundations.

Part	Model	Equation
Warranty Premium	NREL	$\$_{WP} = 0.15\$_{T\&T}$
	Present Study	$£_{WP} = 0.15£_{T\&T}$
Surety Bond	NREL	$\$_{Surety} = 0.03(\$_{Capital} - \$_{WP})$
	Present Study	$£_{Surety} = 0.03(£_{Capital} - £_{WP})$

Table 35: Insurance and fiancial costs in the two cost models

7.1.2.10. Total Masses and Capital Costs

The total mass, m_{Total}, and initial capital cost, $£_{ICC}$, are now a sum of the individual itemised masses and costs in Table 22 to Table 35.

7.1.3. Operation and Maintenance Cost Model

The operation and maintenance cost within both models is a simplified assessment of the costs of operation, significant overhauls and lease of the seabed. The extent of the costs from the operation of tidal stream device arrays is not known and so adaption of the NREL model is seen as adequate given the current status. The costs for operation and maintenance can be seen in Table 36.

Part	Model	Equation
Levelised Replacement	NREL	$\$_{LRC} = 17P_{RATED}$
	Present Study	$£_{LRC} = 13.3P_{RATED}$
Bottom Lease	NREL	$\$_{Lease} = 0.00108E_{AEP}$
	Present Study	$£_{Lease} = 8.4 \times 10^{-4}E_{AEP}$
Maintenance	NREL	$\$_{Maint} = 0.02E_{AEP}$
	Present Study	$£_{Maint} = 0.024E_{AEP}$

Table 36: Operation and maintenance costs in the two cost models

The costs for the bottom lease and levelised replacement cost have both been taken directly from the NREL model for offshore wind turbines. The bottom lease is a factor independent of the device type and the levelised replacement cost is assumed to maintain the same relation. The O&M item has been increased by 50% to reflect the likely need for higher levels of intervention in an as yet relatively unproven area. The annual operation and maintenance costs for the tidal stream turbine, $£_{O\&M}$, are now a sum of the items in Table 36.

7.1.4. Model Verification

The model was verified in two parts, in the first stage the mass model was verified against the MCT SeaGen device, using data from Douglas et al. [192]. In the second stage the cost model was again verified against cost data from the MCT SeaGen model as provided by Fraenkel [185] and Matthews [194].

The mass of the MCT SeaGen device was reported by Douglas et al. [192] as being a total of 465 tonnes. The mass of the device as predicted by the present model is 464.78 tonnes. The accuracy of this prediction is largely because the model was calibrated for the two main masses in the model, the 242 tonne pile structure and the 92 tonne crossbeam. This result does show however that the mass estimation for the remainder of the components also bears a good correlation with that which would be expected on a real device.

The cost of an MCT SeaGen device array was estimated by Fraenkel [185] and Matthews [194]. Fraenkel based the estimate upon the cost of a 10MW array using proven technology, whereas Matthews provides the cost of the 8MW Kyle Rhea array project. The cost estimates and their parameters are detailed in Table 37.

Study	**Year**	**Array Size (MW)**	**Estimated Cost £/kW**
Fraenkel	2007	10	2347
Matthews	2011	8	4375
Present Study	2014	50	2331

Table 37: Estimates for the cost of array installation for MCT SeaGen devices

The model in the present study is based upon a 50MW array size, using proven technology. The model estimates the cost given by Fraenkel to within 0.1%. The estimate given by Matthews for the Kyle Rhea project reflects that the technology is not as developed as was assumed by Fraenkel, or as is assumed by the model. Given the proximity of the model estimate to the prediction of the cost made by Fraenkel and the similarity of the underlying assumptions, the model is thought to be accurate for the prediction of mature tidal stream turbine technology costs.

There is little available data on the cost per rated kW and the exact economics of tidal stream arrays are still relatively unknown, though there is clear potential for the reduction of costs with larger array sizes and more mature device

technology [195, 196]. It is therefore likely that the costs predicted by the model and those of commercial arrays will tend towards each other as the industry develops.

7.1.5. Tidal Stream Turbine Test Cases

There were three devices assessed as part of the annual energy production analyses, a bare rotor, the diffuser augmented device derived as a part of this thesis and the diffuser augmented tidal stream device of Sun and Kyouzka [122]. The bare rotor assessed was based upon the characteristics of the MCT SeaGen rotor, with data being taken from or derived from that presented by MacEnri et al. [159].

The devices are compared here such that the outer diameter of all three devices is the same, i.e. the outer duct radius in the diffuser augmented cases is the same as the blade radius for the bare rotor. This comparison is made as it reflects the need to make best use of the available channel cross section. The sizes of each device and the power coefficients used in the calculations are shown in Table 38.

Characteristic	**Bare Rotor**	**Cresswell Diffuser**	**Sun Diffuser**	
			Literature	**BEM CFD**
C_P	0.372	0.252	0.376	0.190
R_{Ro} (m)	8.000	5.563	5.984	5.984
R_{Di} (m)	-	8.000	8.000	8.000

Table 38: Device sizes and power coefficients of the tidal stream turbine test cases

The effect of the choice to compare devices based upon the outer diameter is that the rated power of the three devices differs with the power coefficient (assuming the same rated speed). The effect of the change in the rated power will be to influence the cost of many of the components within the cost model since this is one of the main variables. Due to the necessity to make best use of the channel cross section the cost per kWh for a given device radius is the best comparator as there are physical limits on device size imposed by channel cross section limitations.

The Sun and Kyozuka [122] device is based upon the diffuser augmented wind turbine design of Ohya and Karasundi [96]. Both studies give a power coefficient in the region of 0.48 based upon the device's outer area. This power output is thought by the author to be on the high side. Calculations were performed on this geometry using the BEM CFD model detailed in Chapter 3, the results of which are presented in Chapter 4. It was found that the diffuser and rotor geometry of Sun and Kyozuka,

with the rotor designed for use within a duct, had a power coefficient based upon the device outer area of 0.190. As a result of this lack of clarity regarding the power output of the Sun and Kyozuka device, the findings of the model detailed within this chapter for that device should be treated with caution.

7.1.6. Cost Model Results

7.1.6.1. Part Breakdown

The breakdown of the device and project components' costs for the device configuration presented in Table 38, are detailed in Figure 169. These results show that the cost of the device is heavily tied to the rotor diameter and also that a large diffuser provides a large cost overhead. The relationship of the cost of the rotor and drivetrain components to size could be expected and has been stated previously by Kirke [197] to be one of the main likely advantages of ducted units.

For a diffuser augmented device, such as that devised within this thesis, the cost of the diffuser will prove to be a significant proportion of the overall device capital cost. There is therefore merit in the reduction of the size of the diffuser in order to make the economics of the device improve. The diffuser of Sun and Kyozuka is, according to the estimation methodology adopted here, cheaper than the diffuser presented in this thesis by a factor of 5.5. The implication of this is that the power production of the larger diffuser would have to significantly outperform the smaller device in order for the cost of energy to be favourable.

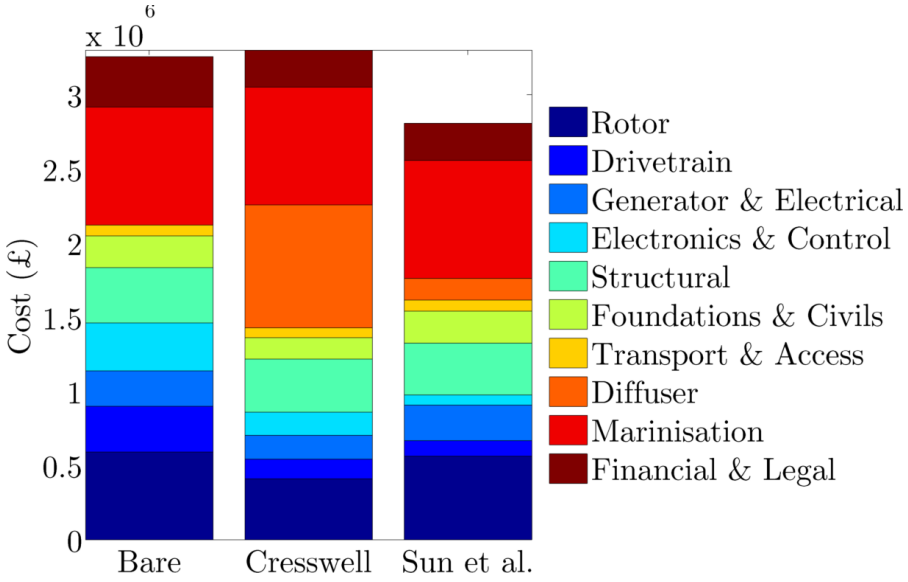


Figure 169: Cost breakdown for dual 16 m outer diameter devices on monopile foundation at a rated speed of 2.5 m/s

The levelised cost of energy component breakdown for the three devices for an example site (Site 1 from Section 7.2.2) can be seen in Figure 170. The predicted component costs from an estimation exercise by the Carbon Trust can be seen in Figure 171 for both wave and bare rotor tidal stream devices. Although comparison is hindered by the limited breakdown in the Carbon Trust data is evident that the model provides a comparable estimate of the capital cost to O&M cost ratio at 28% as compared to 23%. The capital cost of the device itself is estimated as being 63% of the total cost of energy as opposed to 74% as estimated by the Carbon Trust. These differences can be explained by the differing approaches taken to the estimation but ultimately at this stage in the commercialisation of tidal stream technology the true costs are unknown.

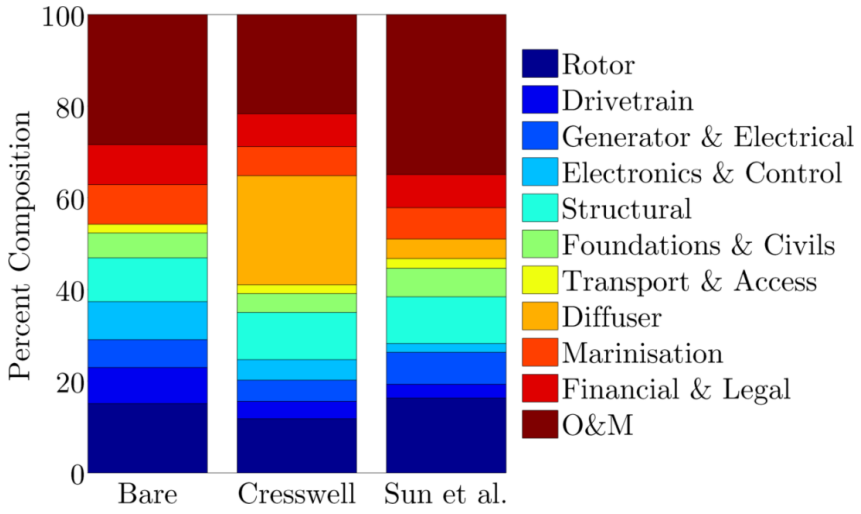


Figure 170: Levelised cost of energy components for a dual 16m outer diameter devices on a monopile foundation with a rated speed of 2.5 m/s

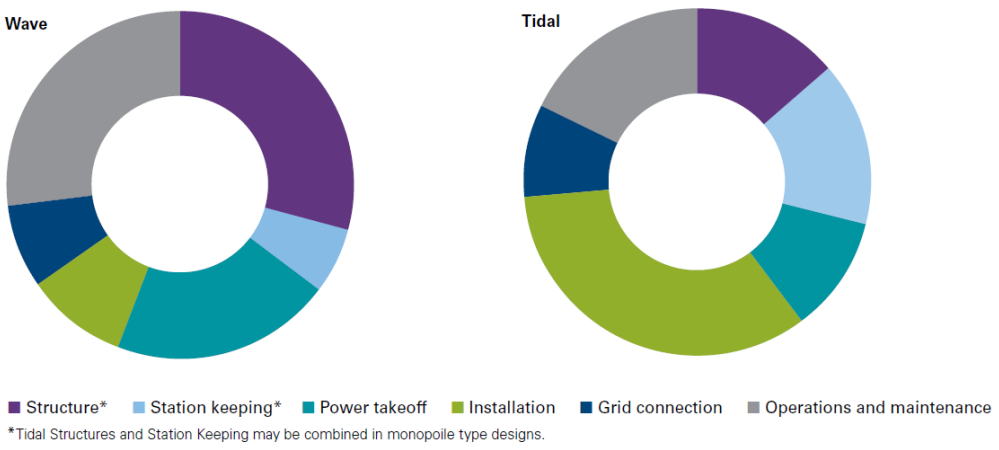


Figure 171: Indicative levelised cost of energy components for early commercial wave and tidal energy arrays [195]

7.1.6.2. Effect of the Device Size and Rated Power

The scale of the devices deployed will have an impact upon the economics of the devices as it will affect both the rated power of the devices and rotor diameter. With these two factors being the prime drivers of the device cost model the capital cost will be strongly linked to these. Figure 172 shows the effect that the device radius has on the project capital cost for dual devices mounted on a monopile foundation at a rated speed of 2.5 m/s.

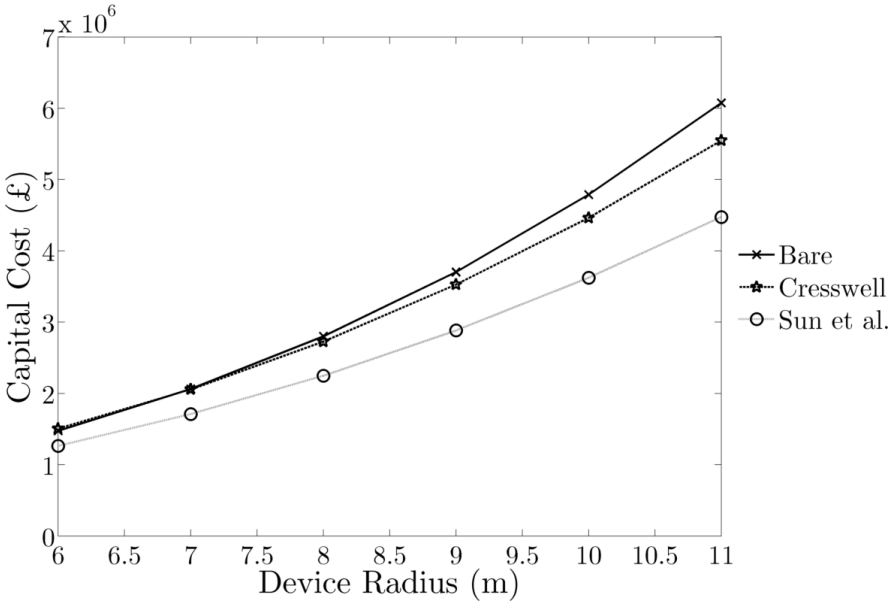


Figure 172: The effect of device radius on capital cost

The trends seen in Figure 172 are what would be expected from the scaling up of a device, with an increasing capital cost which is related to an exponential function of the device radius. The drivetrain cost is the deciding factor in the overall capital cost of the devices, with the larger rotor and therefore more costly drivetrain of the bare rotor being penalised here. As the diffuser cost is scaled per unit area of diffuser surface, the scaling causes an increase in the cost to the square of the device radius rather than the cube as is the case with the rotor. This means that as the device radius increases diffuser augmented cases tend to become more competitive. This analysis does however overlook the increased structural requirements of the larger diameter devices, which is likely to lead to an increased cost.

7.2. Annual Energy Production Analyses

Annual energy production analyses were conducted using real tidal flow data to examine the performance of tidal stream devices under realistic conditions. Four

devices were examined, a bare rotor, the device derived as a part of this thesis and the diffuser augmented tidal stream device of Sun and Kyouzka [122] using both the literature power coefficient and that derived here with the BEM CFD.

7.2.1. Annual Energy Production Methodology

The basis of the annual energy production analysis is the coupling of Equation 92, which relates the rotor's power coefficient with the available energy in the freestream flow and Equation 93, which enables the calculation of the energy output.

$$P = {}^{1}/_{2}\, C_p \rho A U^3 \qquad \text{Equation 92}$$

$$E = P\delta t \qquad \text{Equation 93}$$

In order to assess the power output from a device it is necessary to include a number of losses as detailed in Sections 7.2.1.1 to 7.2.1.3. Once these have been decided the power output is now calculated using Equation 94.

$$P = {}^{1}/_{2}\, (\kappa_{Gen}\kappa_{Trans}\Lambda_{Avail}\Lambda_{YAW}\Lambda_{Turb}) C_P \rho A U^3 \qquad \text{Equation 94}$$

In a tidal stream device there is typically both a cut-in and a rated velocity. The cut-in velocity is that below which no power will be generated and the device will be idle. The rated velocity is that at which the device produces its rated power and above which further increases in velocity will not affect the power output. The cut-out velocity is not usually given for tidal devices but is related to shutdown of the device under extreme conditions to prevent damage. The idea of the cut-in and cut-out velocities and the rated power are illustrated in Figure 173.

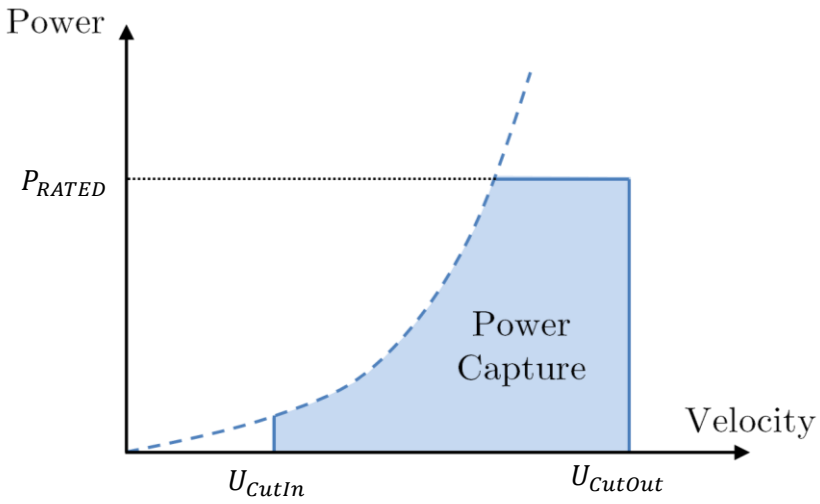


Figure 173: Diagrammatic representation of power capture against current velocity

The power calculated using Equation 94 is set to zero when the velocity is below the cut-in velocity, limited to the rated power above the rated velocity and set to zero if the cut-out speed is exceeded. The energy for each sample period can now be calculated using Equation 93 and the resulting outputs summed across the year. If the tidal velocity input data does not extend for a full year, but does cover a full lunar month, then the assumption that the energy output can be annualised should not cause an excessive error in the results.

7.2.1.1. Power Transfer and Availability Losses

The power is calculated using Equation 92, with a number of correction factors applied for losses in the system and flow effects. There are three sets of losses commonly accounted for in AEP models, availability losses, generation losses and transmission losses. The availability of tidal energy devices has been suggested by Entec [198] to be around 95% and so a 5% correction was applied for downtime. Generator and gearbox losses are assumed to be 3% of the generated power, which is seen as being an optimistic value by Bahaj and Myers [199] for tidal stream generation. The correction for transmission losses was taken as being the average of a number of case studies of wave energy scenarios conducted by Henfridsson et al. [200], which comes to a loss of 7.5%.

7.2.1.2. Flow Yaw Losses

There are two additional factors taken into consideration during this analysis, the effects of the yaw angle and the turbulence intensity on the power output of the devices. The effect of the yaw angle on the power output of the device was taken from the results presented in Section 6.3.3 in the cases of the diffuser devised as a part of this thesis and the bare rotor. The device of Sun and Kyouzka [122] has unknown yaw characteristics and so the performance was estimated. In order to do this the literature on diffuser augmented wind turbines was examined and it was found that there was a correlation between the length to diameter ratio and the yaw performance. Figure 174 shows the maximum unaffected yaw angle of a variety of diffusers which have previously been tested at yaw. Presented are results from Igra [94], Phillips [25] and Foreman and Gilbert of Grumman Aerospace [201].

The effect seen in Figure 174 is likely to be due to the increased strength of the tip gap jets, which as detailed in Chapter 6 are the main drivers of the yaw performance. The increased length enables a lower cavity pressure due to enhanced diffusion potential and greater rotor plane vleocity. With the reduced base pressure

behind the rotor stronger tip gap jets are generated and the diffuser is then able to perform better under yawed flow.

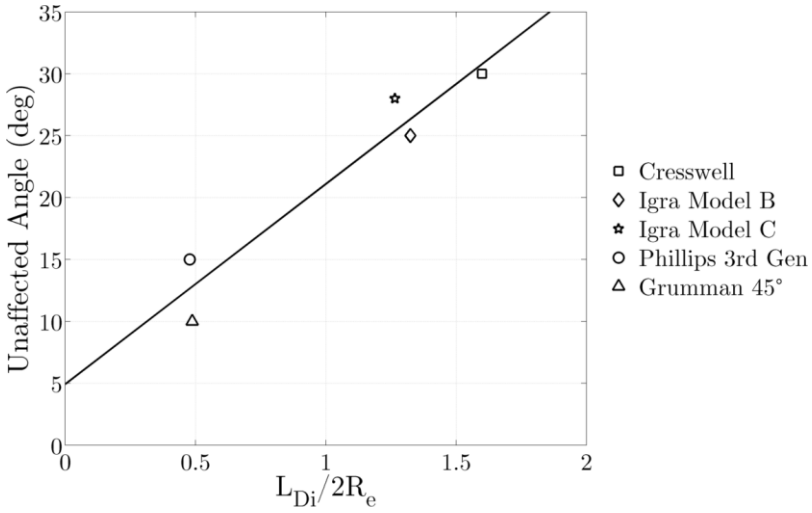


Figure 174: Unaffected yaw angle against the diffuser length to diameter ratio

Using the relationship derived from the data presented in Figure 174 the performance chart for the Sun and Kyozuka diffuser under yaw was estimated. The estimated performance is plotted in Figure 175, along with the performance results for the diffuser devised as a part of this thesis and the bare rotor.

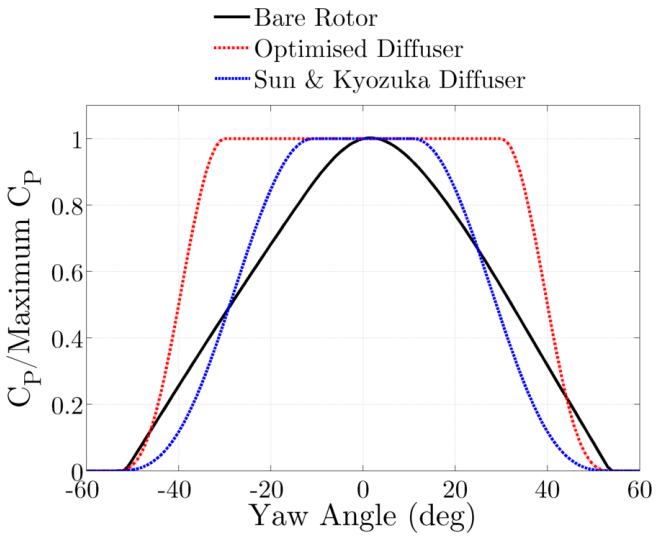


Figure 175: Power reponses to the flow yaw angle for the devices examined

7.2.1.3. Flow Turbulence Losses

The performances of the devices at different levels of ambient turbulence were considered based upon the numerical results detailed in Section 4.5.3. The turbulence response data used here is summarised in Figure 176.

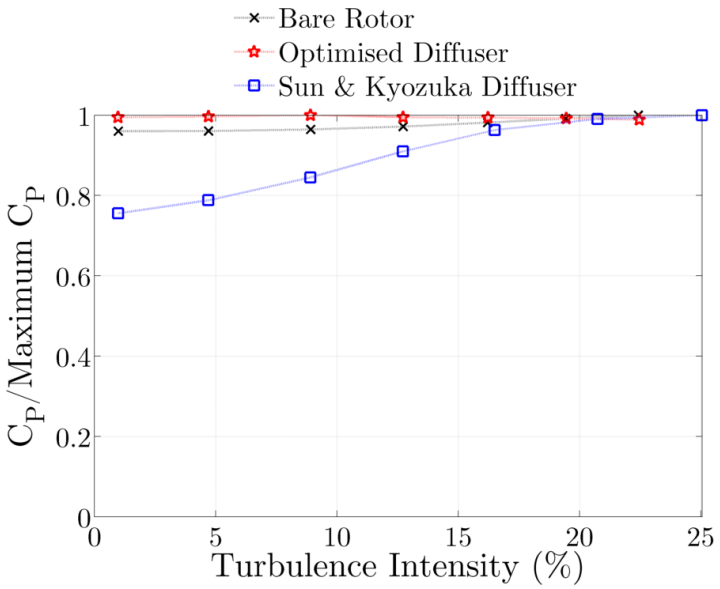


Figure 176: Turbulence performance data for the devices examined

7.2.2. Tidal Channel Data

The annual energy production analyses were conducted using data from the Bedford Institute of Oceanography of the Canadian Government. The data presented here has been used previously as part of Cornett's [32] guide to tidal energy resource assessment. The site examined was the Minas Passage in Nova Scotia, Canada, as seen in Figure 177.

There were six locations analysed as a part of this study as shown in Figure 178. These locations are all very close to the Fundy Ocean Research Centre for Energy (FORCE), which is a test facility for tidal stream devices. Location 1 is the closest location, being 2km to the south east of the FORCE site, which is located approximately 3.5km due west of Cape Sharp. The data was collected using a bottom mounted acoustic Doppler current profiler.

The sampling periods, with the exception of location 1, are long enough to extend over a the lunar month and therefore cover both spring and neap tides [27]. The sampling frequency is in all cases sufficient to capture the trends present in tidal flow velocities present but inadequate to gain any understanding of shorter scale transient structures present within the flow.

The water depths are beyond those which are seen as being acceptable for a monopile foundation as is assumed within the context of the cost of energy analyses as presented in Section 7.3. An assumption is made in these cases that there is a floating support structure for the device, secured via tethers to a foundation

structure. The cost of this component is assumed to scale with the same relationship to the devices rated power. This is seen as being conservative as the cost of floating platforms is likely to be lower than fixed bottom mountings [196, 202].

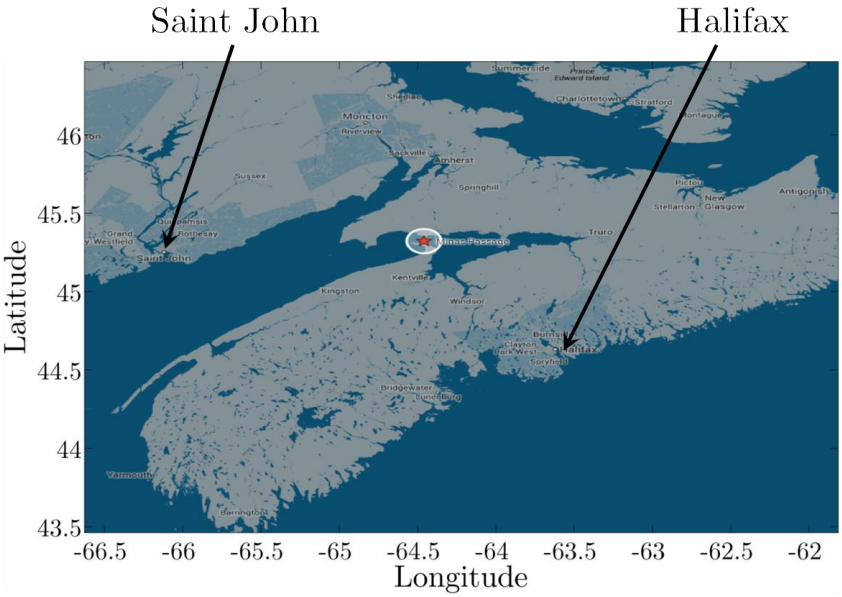


Figure 177: Map showing the the Minas Passage, Map data ©2014 Google

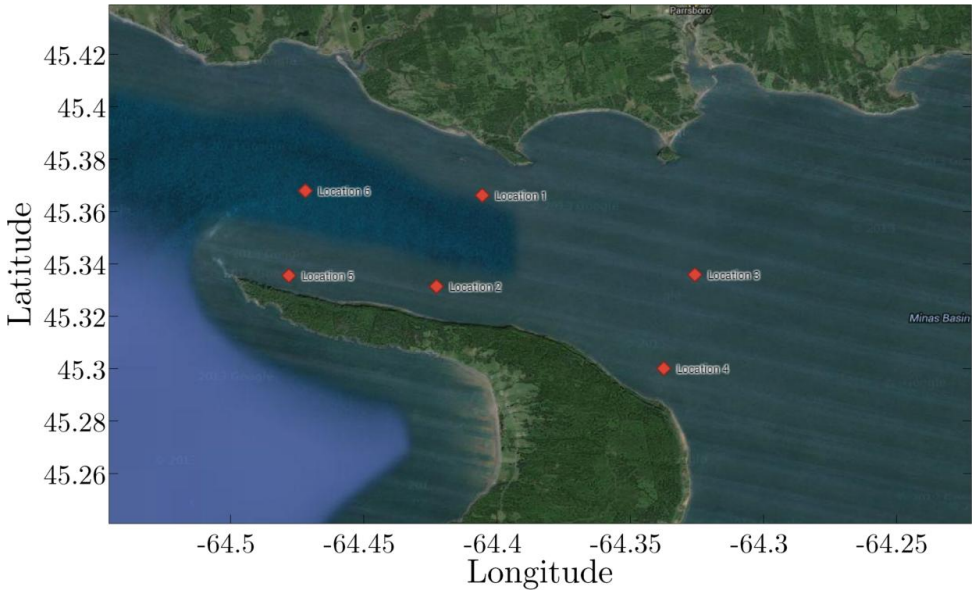


Figure 178: Aerial Image showing the six site locations within the Minas Passage, Map data ©2014 Google, Google Imagery ©2014 TerraMetrics

The tidal current data at each site is expressed in the series of hodographs in Figure 179 to Figure 184. These hodographs also include the optimal heading of the device for power capture during both the flood and ebb tides. These headings were calculated using the velocity weighted average tidal heading for each tidal phase.

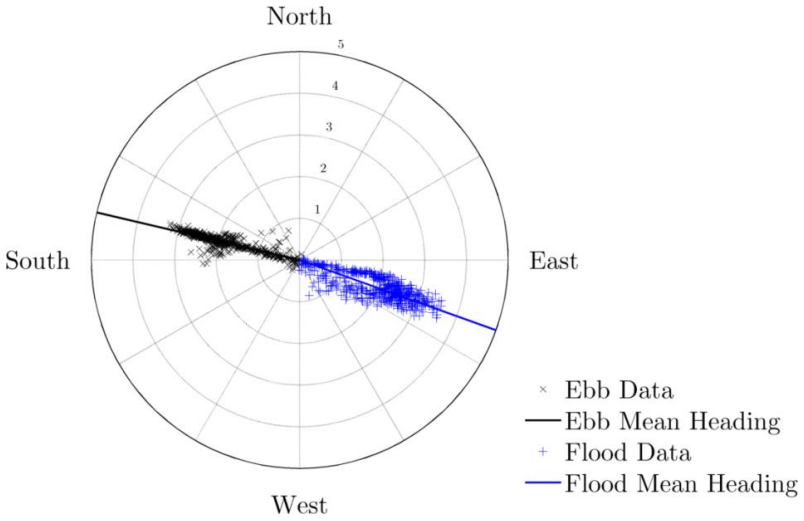


Figure 179: Hodograph of the sample tidal velocities for Location 1

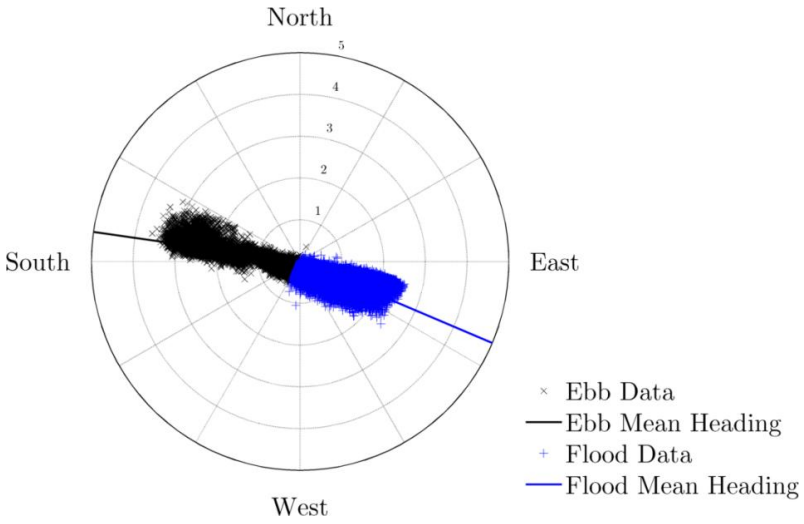


Figure 180: Hodograph of the sample tidal velocities for Location 2

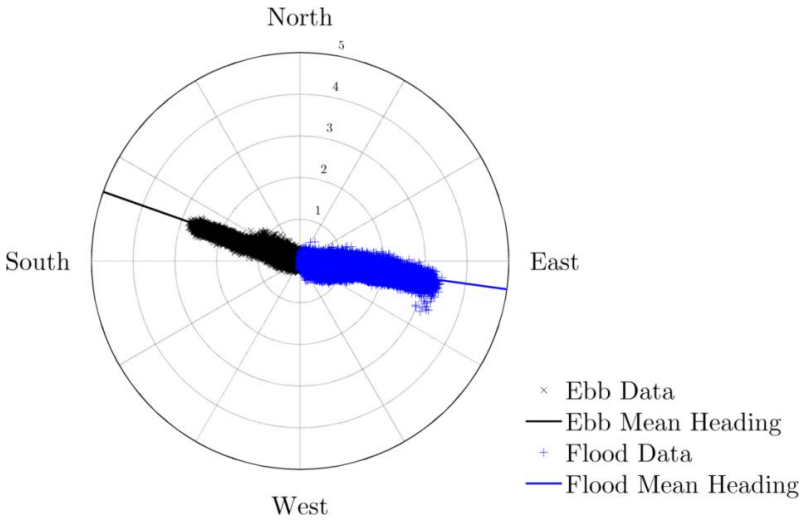


Figure 181: Hodograph of the sample tidal velocities for Location 3

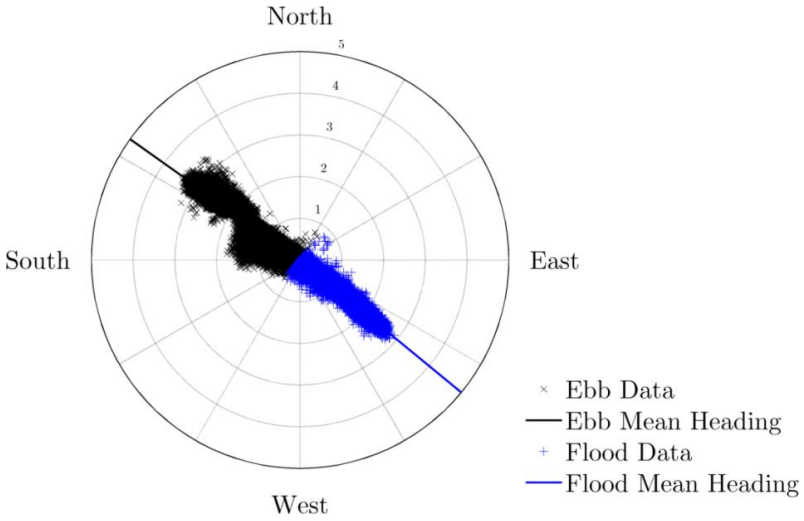


Figure 182: Hodograph of the sample tidal velocities for Location 4

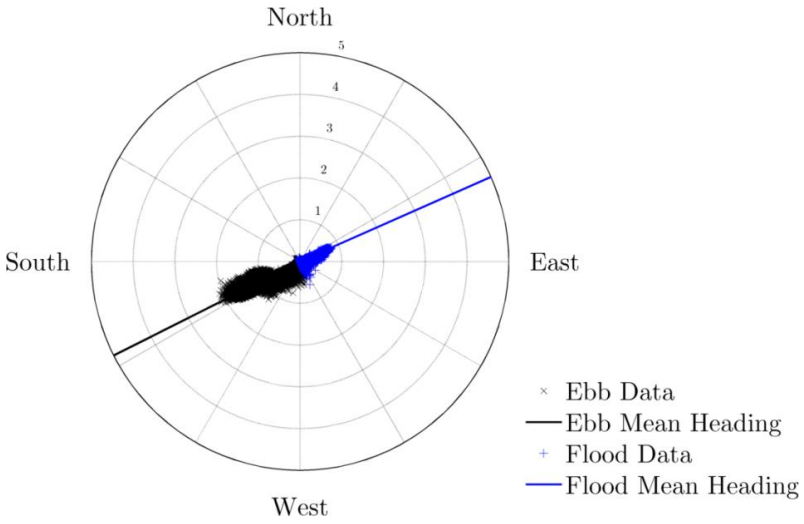


Figure 183: Hodograph of the sample tidal velocities for Location 5

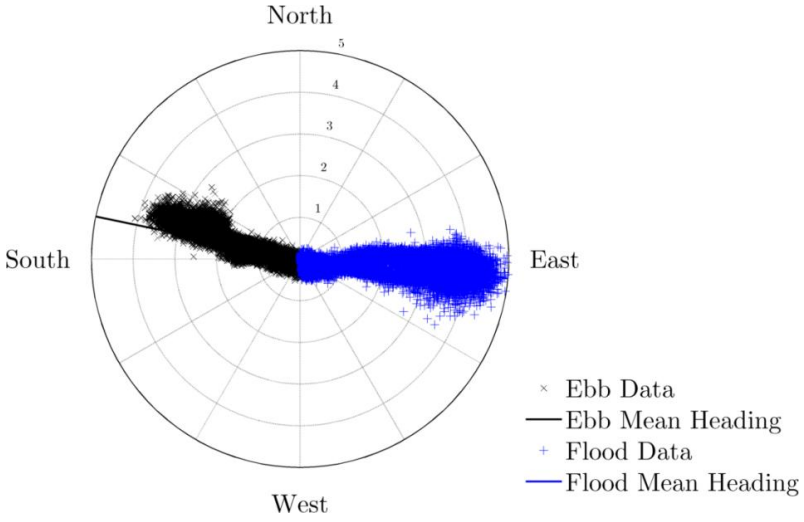


Figure 184: Hodograph of the sample tidal velocities for Location 6

As can be seen immediately from Figure 179 to Figure 184, some of the sites are better suited to tidal power extraction than others. It can be seen for example that Location 5, as a result of being behind the headland experiences only low velocity flows, with a large deviation between the ebb and flood velocities.

It is worth noting that the assumption of rectilinear flow in a tidal channel, which is often made when performing AEP analyses, does not hold. There is a clear variability evidenced in the flow yaw at all of the sites. Some of these sites exhibit flow angles of up to ±30° even at higher tidal velocities. This yaw effect is likely to be further compounded by the presence of large scale eddies in the flow further altering the relative flow angle. Given the large yaw effects seen for devices in Section 7.2.1.2, there is therefore a clear necessity to account for the effects of flow yaw on device performance whilst performing annual energy production analyses.

7.2.3. AEP Model Input Data

As detailed in Section 7.1.5, there were four device types assessed as part of the annual energy productions analyses, a bare rotor, the diffuser augmented device derived as a part of this thesis and the diffuser augmented tidal stream device of Sun and Kyouzka [122] with the literature C_P and the BEM CFD derived C_P. The sizes of the devices and their power coefficients are detailed in Table 38, and the velocity parameters are detailed in Table 39.

Characteristic	**Bare Rotor**	**Cresswell Diffuser**	**Sun Diffuser**	
			Literature	**BEM CFD**
v_{CutIn} (m/s)	0.800	0.800	0.800	0.800
v_{CutOut} (m/s)	6.000	6.000	6.000	6.000
v_{Rated} (m/s)	2.500	2.500	2.500	2.500

Table 39: Device velocity parameters for the AEP model

The cut-in and rated velocities of the turbines were chosen as being representative of existing tidal devices [56, 159]. The cut-out velocities were chosen as being the survival speed of a tidal device as defined in Section 7.1.1. A cut-out velocity is thought to be useful in the event of extreme wave loadings, but since the tidal velocities are largely predictable, devices should be able to continue to operate at rated power in the majority of cases [203].

The material properties of seawater were assumed to be as detailed in the numerical methods in Section 3.2.3.

The correction for the freestream turbulence intensity was based upon the analysis of the performance of the devices as presented in Section 4.5.3. The correction was made by interpolation of the data presented in Figure 175. The correction factor at the turbulence of interest was normalised by the factor at the turbulence of experimental testing to arrive at the correction.

The correction for the yaw angle was made from the experimental results, using the data presented in Chapter 6. The yaw angle amendment was applied as a correction factor relative to the zero device yaw condition.

7.3. Tidal Stream Turbine Cost of Energy

The levelised cost of energy provides a measure of the generation cost per unit of useful electrical energy which a device outputs. The levelised cost of energy is ultimately the metric by which an electricity generating technology is judged as it reflects the overall economic competiveness of a technology [204]. In order for tidal stream energy to gain acceptance it will be necessary to reduce this to a point where it is competitive with both other renewable and conventional energy sources. As a result there is a push for the capital and operating costs to be brought down and the generation potential to be increased [205]. The levelised cost of energy per kWh for a device can be calculated using Equation 95.

$$£_{COE} = \frac{\%_{FCR} £_{ICC}}{E_{AEP}} + \frac{£_{O\&M}}{E_{AEP}} \qquad \text{Equation 95}$$

The results of the annual energy production analysis indicate that as a result of certain flow patterns, the device type significantly influences the power production capabilities and hence the levelised cost of energy of a tidal stream array for a given set of tidal flow conditions. The effect that flow yaw and the freestream turbulence intensity have on the generated power is quantified here.

7.3.1. Effect of Flow Yaw

The yaw sensitivity of the model was assessed by using a semi-diurnal tide, idealised as a sinusoidal tidal velocity with amplitude of 3.5 m/s and a tidal period of 12.4 hrs. The velocity of the input data was described by the function in Equation 96. This input was sampled with a 1 minute sampling interval, and this was then used as the input for the annual energy production analysis. In order to

include a measure of yaw, a random number generator was used to assign a heading to the velocity within a certain band of angles. The band of angles was set to give a prescribed standard deviation of the headings of between 0° and 30°, rising in 5° increments. In order to ensure that the distribution of the yaw was uniform a sample period of 30 days was used.

$$U = U_{max}\sin\left(\frac{\pi t}{12.4 * 3600}\right) \qquad \text{Equation 96}$$

The effect that the flow yaw has on the annual energy production and the cost of energy can be seen in Figure 185 and Figure 186 respectively. It is clear that the presence of flow yaw can have a significant impact upon the generation potential and therefore the generation cost. This is as result of the diffuser augmented device's response to the effects of flow yaw as a result of the aligning effect detailed in Section 6.3.3. The diffuser devised as a part of this thesis is insensitive to yaw to a large extent, though the device is hampered by its low power coefficient based on the diffuser outer area. The shorter diffuser of Sun and Kyozuka performs well in the low yaw range ±18°, but at larger yaw angles the performance rapidly degrades. It should be noted that as the exact nature of the yaw response of the Sun and Kyozuka diffuser is unknown, this pattern of performance represents a best estimate only. The effect of the estimate of the power coefficient on the performance of the Sun and Kyozuka device is highly visible, with the power output being almost three times higher where the published data is used.

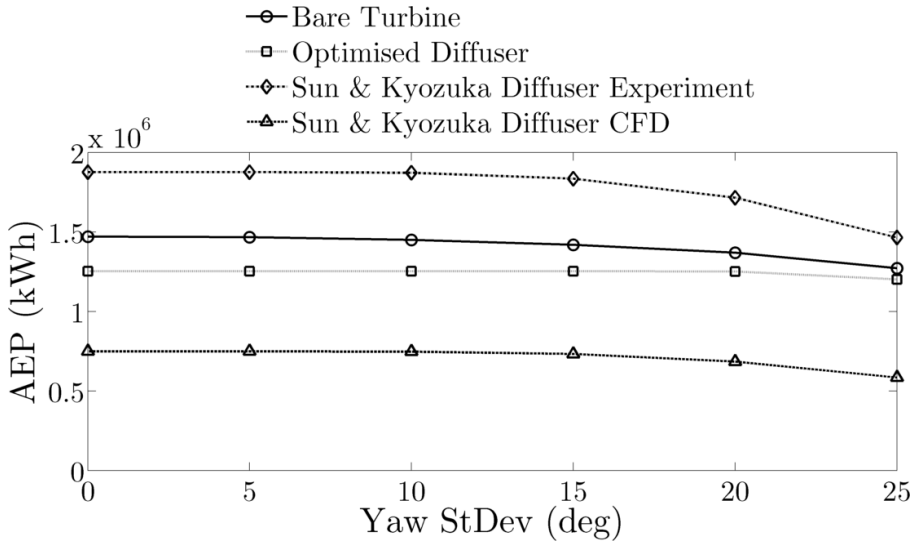


Figure 185: Annual energy production for the trialled devices with a randomly yawed siusoidal input flow

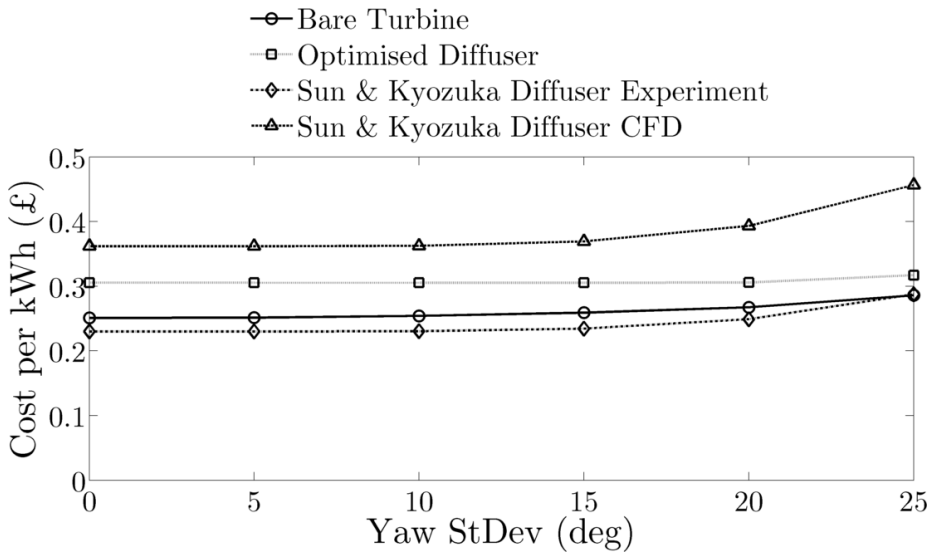


Figure 186: Cost per kWh for the devices with a yawed siusoidal input flow

These results show the dependence of all of the devices on the flow yaw angle. It can be concluded that a bare rotor is best suited for tidal flows which have rectilinear flow or at least very little flow yaw. The performance characteristics of the diffuser augmented devices makes them better suited to the acceptance of flow yaw. The lower power coefficients of the diffuser augmented turbines means that the bare rotor performs relatively favourably at off design flow angles.

The dependence of the yaw response of a diffuser augmented device on the length to diameter ratio of the diffuser means that there will be a length to diameter ratio which will maximise the energy production for a prescribed flow yaw standard deviation. As a result of the performance trends seen in Figure 174, this would be a longer diffuser for flows with a greater degree of yaw. In order to minimise the levelised cost of energy however there is clearly a balance to be drawn with the cost of the diffuser structure. The results show that unless a particularly high power coefficient is achievable for the diffuser augmented turbine, the likelihood is that the most economical means of generation under yawed flow is a bare rotor.

It should be noted that no account has been made in the energy production for active yawing of a device during operation. The bare rotor's power capture performance would undoubtedly be improved by this effect, though the costs associated with this yawing will also impact upon the cost of energy.

The results seen in Figure 185 and Figure 186 show that for a flow with a simple, sinusoidally varying flow velocity magnitude and a varied heading, bare

rotors are likely to provide the lowest cost of energy. Although the Sun and Kyozuka experimental results place their diffuser in a better position, there is a lack of clarity over whether a diffuser augmented device can attain a power coefficient of that magnitude. This means that a bare rotor is the most likely of the devices examined to provide energy at the lowest cost.

7.3.2. Case Study Location AEPs

The final stage of the cost of energy analysis is applying the models to the analysis of real world tidal flow data. The analysis was performed on the six tidal energy sites in the Minas Passage detailed in Section 7.2.2. The standard deviation of the yaw angle from the velocity averaged optimal device heading for each tidal phase was calculated for each of the sites, with the results presented in Figure 187. It is evident from this data that these tidal sites have yaw angles which are typically in the range from 0° to ±12-20°. With a high level of yaw such as this, the performance of a bare rotor would be hindered as the yaw characteristics in this range are poor compared to those of the diffuser augmented cases as seen in Figure 175. At the extreme angle of 20° the performance is 84% of the longer diffuser performance for the Sun and Kyozuka diffuser and only 68% for the bare rotor.

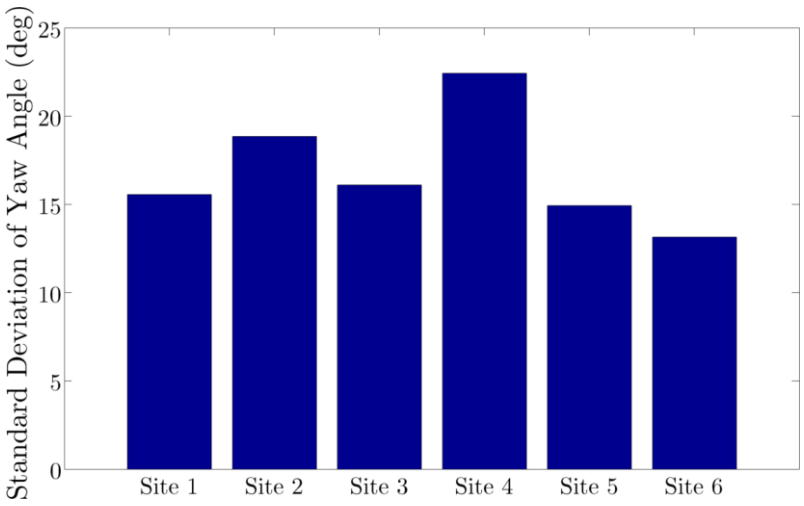


Figure 187: Yaw angle characteristics for the six case study sites

The extent to which the yaw affects the power output of the device will be tied not to the yaw angle distribution but to the distribution of the velocity weighted yaw angle distribution. This is because it is the high velocity flows which tend to produce the most power due to the cubic relationship of the velocity to the power output. The magnitude of the axial velocity component increases relative to the transverse component at higher flow velocities. This means that the higher

velocity sites will tend to have a lower response to the yaw characteristics of a device than the lower velocity ones.

The levelised cost of energy for each of the devices, calculated at each of the six case study sites for a turbulence intensity of 10% can be seen in Figure 188. It is evident from these results that there is clear hierarchy of the devices regardless of the flow at the site. The performance of the devices depending so heavily on the estimate of the power coefficient is highly visible in the two estimates of the Sun and Kyozuka diffuser. If it is assumed that the real value of the power coefficient lies somewhere between the two then it is more than likely the case that the bare rotor is the best configuration at all sites tested.

The failure of the longer diffuser to provide competitively priced energy is tied to the cost of the diffuser itself. When this is coupled with the relatively low performance of the device based on its outer area, the benefits of its yaw performance cannot make up for the shortfall. In contrast, if the higher estimate of the power coefficient is used, the Sun and Kyozuka diffuser, with its lower cost and improved yaw and turbulence characteristics, outperforms in all cases.

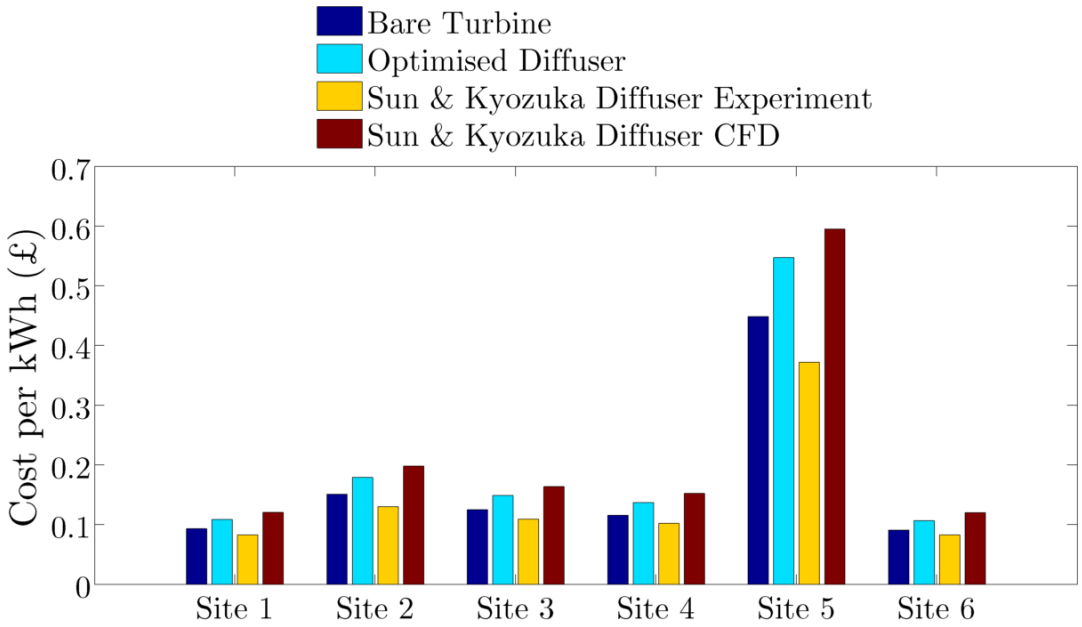


Figure 188: Levelised cost of energy for the devices at the six case study sites

The performance at site 5 is by far the poorest, although this would be expected given that the tidal velocities at this site are very low and for most of the flood phase the unit would not be generating. The remainder of the sites are broadly comparable in terms of the levelised cost of energy and would be considered to be

good sites for the deployment of tidal stream devices. It is evident that the main factor which affects the cost of energy is the tidal velocity, but there is also evidence of the effect of the flow yaw. The performance at site 6 for example shows that in flows where the yaw angle is limited and the flow velocity is high, the difference between the shorter diffuser device and the bare rotor is minimised.

7.4. Summary of the Factors Affecting Device Cost

It has been found that the cost of energy from a tidal stream device is tied to a number of factors which characterise the flow. The key aspect of the flow is the tidal stream velocity, which as being one of the key determinants of the power output is to be expected. The main determinant of the device's merit is the power coefficient, which again would be expected. Other factors which have been explored here are the effects that yaw and turbulence characteristics have on the generation potential and their implications. Despite diffusers having favourable characteristics under these conditions, the lower value of the power coefficient means that their cost of energy will continue to remain above that of a bare rotor.

The underlying assumptions of the calculations performed here are a tidal stream turbine cost model. The absolute values of the costs from this model are designed to give guidance to the reader as to the likely scale of the costs associated with certain components and tasks, and to build a representative basis for relative cost comparison. There is still uncertainty within this model and as such the results should be interpreted with some degree of caution by the reader.

The flow yaw has been found previously [25, 94] to affect diffuser augmented devices in a different way to bare rotors. A survey of historical and present data has found that the performance of the diffuser augmented devices under yaw is tied to the length to diameter ratio of the device, with longer diffusers able to sustain the performance at larger off design flow yaw angles. This can be attributed to the effect that the length has on the ability of the diffuser to sustain sub-ambient pressures as stated in 7.2.1.2, and therefore generate tip gap jets which increase boundary layer momentum.

Flow turbulence can have a significant impact upon the generation potential of diffuser augmented devices. Diffuser augmented devices which have a large potential for improvement of the degree of separation from the interior diffuser wall

have the most to gain. It has been shown that one such device has the potential for improvements of up to 33% relative to low levels of freestream turbulence.

Overall it has been shown that diffuser augmented devices could potentially generate energy at prices which are comparable with and potentially better than those of bare rotors. The lack of clarity regarding the power output of the Sun and Kyozuka [122] device means that these results should be treated with caution and the evidence points to the bare rotor being a more economical means of generation.

The cost of generation is primarily tied to the local flow environment and the device's peak power coefficient. Other factors, which are often overlooked, can also have significant effects upon the cost of energy and should be considered at the design stage when estimating the likely power outputs from devices.

8. Conclusions

This thesis aimed to investigate the key factors which affect the use of diffuser augmented turbines for the economic generation of power from tidal streams. To this end, work was conducted investigating the key parameters which affect the power output of such devices, and how these affect the cost of energy.

Work was conducted both numerically and experimentally, with the aim of gaining an understanding of the device fluid dynamics and allowing the numerical modelling thereof. Conclusions about the performance and fluid dynamics of diffuser augmented tidal stream turbines and the efficacy of their use for economical power generation are separated here.

8.1. Fluid Dynamics of Diffuser Augmented Turbines

There are several key findings of this thesis that relate to the power conversion performance of diffuser augmented devices and the modelling thereof. The most important of these is the derivation of an experimentally verified numerical method for the assessment of the power output of diffuser augmented turbines. This allows for the modelling of the power capture and flow field of diffuser augmented devices within 2D axisymmetric CFD, at low computational expense. This model could be extended with relative ease to 3D geometries and allowed to incorporate effects such as flow yaw, rotor coning or rotor tilting.

The necessity for the derivation of a numerical model for diffuser augmented turbines was highlighted by the study of uniform actuator disc modelling. It was found that uniform actuator discs are entirely unsuited to the assessment of diffuser augmented devices as a result of the omission of flow features such as flow swirl, turbulence and tip losses. It is the interaction of these flow features with the diffuser which is the primary driver of the overall device performance and so they must be modelled to replicate realistic flow and power capture conditions.

The effect of the hub was shown to be significant to the power capture of the overall device. The shape of the hub was shown to have a less significant effect than the hub radius, as long as the shape does not induce early boundary layer separation. An increased hub radius was found to increase the power output potential of the device due to shifting of the streamlines towards the centre of the blade. This allows

for increased relative flow velocities in this region and so higher blade forces. The limitations of this effect require further clarification.

The effect of turbine thrust on the performance of the overall device was investigated using the derived BEM CFD model. It was found that for diffuser augmented cases, the ideal rotor thrust is around half that of an ideal bare rotor. This effect is due to the interaction of the rotor thrust and the duct's swallowing capacity and hence the rotor plane velocity and available power. The overall device thrust at peak power capture was found to be approximately equivalent for both the diffuser augmented and bare rotor cases. The reduction in the rotor thrust force, coupled with the reduced blade radius means that the blade bending moments will be reduced and there is therefore potential for cost savings.

The impact of the diffuser area ratio on the outer area based power coefficient was highlighted. This suggested that although the overall power output can be increased by increasing the area ratio the efficiency of conversion suffers. It was found that the region in which the peak power coefficients occur for diffuser augmented devices was the region $1 < A_e/A_i < 2$.

The impact of flow yaw on the power output of the device was investigated. It was found that the diffuser augmented device was able to sustain power coefficients at around the peak value up to flow yaw angles of ±30°. This effect was caused by the ability of the diffuser to sustain sub-ambient cavity pressures and so to drive the formation of strong tip gap jets to add momentum to the diffuser boundary layer. Analysis of the results from the experiments contained here and those seen in the literature suggest that the yaw performance of a diffuser augmented turbine is correlated to the diffuser length. Since the cost of the diffuser is also correlated to the overall length, there is clearly a trade off to be made in the diffuser design here.

The interaction of the rotor geometry with the augmentation potential was highlighted, with rotors which performed poorly bare performing well for diffuser augmentation. This effect was due to the turbine thrust as discussed above and the rotor outflow profile. The careful design of the rotor to optimise the thrust distribution would allow for elevated velocities and turbulence in the near boundary regions. This momentum transfer to the boundary layer flow is the essential driver of the diffuser performance and hence the swallowing capacity of the duct.

The interaction effects detailed within this thesis suggest that there is further potential for the augmentation of the power output of diffuser augmented devices. The extent of these potential gains is unclear, but figures of 17% have been quoted in the literature for simple changes to rotor geometry alone [116].

The fluid dynamics results obtained within this thesis and those from the literature which were analysed suggests that the performance of diffuser augmented devices is currently lower than for equivalently sized bare rotors. This thesis has highlighted some potential areas for improvements in the overall performance which have the potential for the devices to reach parity.

8.2. Generation Potential of Diffuser Augmented Turbines

The economic assessment of the device performance suggests that diffuser augmentation of tidal stream turbines is not economically viable at the current time. The main drivers of this are the diffuser cost, the array scale dynamics of the devices and the low power coefficient values attained.

There are some potential questions around the cost model derived within this thesis which require further investigation, in particular the blade and diffuser costings. The finding that the blade bending moments are reduced for diffuser augmented turbines has the potential for cost savings, whilst the costs of the diffuser is estimated based upon a single manufacturing methodology. Further investigation of the likely structure and manufacturing methods of the diffuser are needed to gain a clearer understanding of these costs.

The diffuser augmented devices were found within this thesis to suffer from poor wake recovery characteristics when compared to bare rotors. The overall level of device thrust was found to be comparable however. The implications of this are that array shapes for diffuser augmented devices would be characterised by rows of turbine with the same transverse spacing but increased axial spacings. This reduced array density makes poor use of concentrated tidal stream energy, increases bottom lease costs and has cost implications for grid connections.

The potential for generation increases as a result of the yaw and turbulence characteristics of diffuser augmented tidal stream devices was analysed. It was found that these effects will contribute in a positive way towards the power capture of the device, especially at low tidal velocities. The example tidal stream sites evaluated here however highlight the fact that at higher tidal velocities the yaw and

turbulence intensity levels are not significant enough to favour diffuser augmented devices. The power capture was found to be higher for bare rotors unless generous assumptions are made of the power coefficient of the diffuser augmented device.

The research contained here suggests that there is remaining potential for the performance improvement of diffuser augmented turbines. The current status of diffuser augmented devices however is such that economic generation of energy from tidal streams is best achieved via bare rotor power capture.

9. Further Work

During the course of this research the need for further investigation of a number of the aspects of the behaviour of diffuser augmented turbines became apparent. The key aspects which warrant further investigatory work are:

1. Investigation of the potential gains of a full system optimisation
2. Investigation into turbulence effects on diffuser augmented devices
3. Cavitation inception in diffuser augmented devices
4. The effect of shear profiles and wave effects on diffuser augmented devices

9.1. Component Interaction Effects

The work undertaken here has shown that there are areas of interaction between components in which there are gains to be made. The interaction of the rotor wake with the diffuser surface boundaries is of particular interest. To this end it is recommended that a full device optimisation is conducted to ascertain the extent of the possible gains. This optimisation should allow variation in the geometry of the hub, diffuser and rotor. It is envisaged that the methodology utilised here can be coupled with the blade element CFD model through relatively simple extensions of the overall procedure.

A full device optimisation should use an objective function based upon the cost of energy of the device rather than simply the power output alone. The interaction of the cost of the diffuser and the size needed for adequate power augmentation being of primary concern. The optimisation should also take account of the yaw and turbulence structures within a realistic tidal channel flow.

9.2. Effects of Turbulence

The effects of turbulence have been dealt with to some extent in this thesis but the structure and effect of turbulence within the diffuser of a tidal stream device is considerably complex. In order to fully understand the interaction of the device with turbulence it is necessary to gain a full understanding of both the freestream turbulence of a tidal channel and also the turbulent structures shed by a diffuser augmented turbine. Quantification of these effects on the device's power output would be best achieved via experimental work utilising turbulence generation methods and detailed diffuser traverses.

9.3. Cavitation Inception

The likelihood of increased cavitation inception due to the sub-ambient pressures within the diffuser was mentioned within this thesis. The further study of the presence, distribution, extent of and mitigation mechanisms for cavitation would be necessary for the further development of diffuser augmented devices.

9.4. Effect of Shear Profiles and Wave Effects

The effects of shear and wave effects have been omitted within this thesis for separate reasons. It has been found that for bare rotors that volume averaging of the flow allows for sufficiently accurate replication of the performance characteristics of bare tidal stream rotors under sheared flows [35]. The effect of waves was assumed to be limited as the device depth was assumed to be sufficient that the effects were limited. In reality both of these effects are likely to impact upon diffuser augmented device performance to some extent, either through cyclical variations in the blade power output or induced turbulence. Interactions would be best examined experimentally in facilities which can combine velocity profile and free surface effects.

10. References

1. Solomon, S., et al., *Irreversible climate change due to carbon dioxide emissions.* Proceedings of the National Academy of Sciences, 2009. **106**(6): p. 1704-1709.
2. Alexander, L.V., et al., *Climate Change 2013: The Physical Science Basis: Summary for Policymakers*. 2013, Intergovernmental Panel on Climate Change.
3. IPCC, *Contribution of Working Group III to the Fourth Assessment Report of the Intergovernmental Panel on Climate Change*, in *Climate Change 2007: Mitigation of Climate Change*, B. Metz, et al., Editors. 2007.
4. Boden, T.A., G. Marland, and R.J. Andres, *Global, Regional, and National Fossil-Fuel CO2 Emissions*. 2010, Carbon Dioxide Information Analysis Center, Oak Ridge National Laboratory, U.S. Department of Energy: Oak Ridge, Tenn., U.S.A.
5. E.I.A, U.S., *International Energy Outlook 2013*. 2013, U.S. Energy Information Administration.
6. Pernick, R., C. Wilder, and J. Belcher, *Clean Energy Trends 2014*. 2014, Clean Edge.
7. Makower, J., R. Pernick, and C. Wilder, *Clean Energy Trends 2008*. 2008, Clean Edge.
8. MacKay, D.J.C., *Sustainable Energy - Without the Hot Air*. 2009: UIT Cambridge Ltd. 383.
9. IPCC, *Renewable Energy Sources and Climate Change Mitigation*, O. Edenhofer, R.P. Madruga, and Y. Sokona, Editors. 2012, Technical Support Unit Working Group III, Potsdam Institute for Climate Impact Research (PIK).
10. REN21, *Renewables 2010 Global Status Report*. 2010: Paris.
11. McCully, P., *Silenced Rivers: The Ecology and Politics of Large Dams*. 1996, London: Zed Books.
12. Graham-Rowe, D., *Hydroelectric power's dirty secret revealed*, in *New Scientist*. 2005, Reed Business Information Ltd.
13. Paish, O., *Small hydro power: technology and current status.* Renewable and Sustainable Energy Reviews, 2002. **6**(6): p. 537-556.
14. Wiemann, P., G. Muller, and J. Senior. *Review of current developments in low head, small hydropower*. in *32nd IAHR Conference*. 2007. Venice, Italy.
15. Bahaj, A.S., *Marine current energy conversion: the dawn of a new era in electricity production.* Philosophical Transactions of the Royal Society A: Mathematical, Physical and Engineering Sciences, 2013. **371**(1985).
16. Frau, J.P., *Tidal energy: promising projects: La Rance, a successful industrial-scale experiment.* Energy Conversion, IEEE Transactions on, 1993. **8**(3): p. 552-558.
17. Xia, J., R.A. Falconer, and B. Lin, *Impact of different operating modes for a Severn Barrage on the tidal power and flood inundation in the Severn Estuary, UK.* Applied Energy, 2010. **87**(7): p. 2374-2391.
18. Pethick, J.S., R.K.A. Morris, and D.H. Evans, *Nature conservation implications of a Severn tidal barrage- A preliminary assessment of geomorphological change.* Journal for Nature Conservation, 2009. **17**(4): p. 183-198.

19. DTI, *The World Offshore Renewable Energy Report 2004-2008*. 2004: Douglas Westwood Ltd.
20. MacLeay, I., *Digest of United Kingdom Energy Statistics 2013*. 2013: Department of Energy & Climate Change.
21. Khan, M.J., et al., *Hydrokinetic energy conversion systems and assessment of horizontal and vertical axis turbines for river and tidal applications: A technology status review.* Applied Energy, 2009. **86**(10): p. 1823-1835.
22. Spera, D.A., *Wind Turbine Technology: Fundamental Concepts of Wind Turbine Engineering*. 1994, New York: ASME Press. 638.
23. EMEC. *European Marine Energy Centre*. 2014 19th May 2014]; Available from: http://www.emec.org.uk/.
24. van Bussel, G.J.W., *The science of making more torque from wind: Diffuser experiments and theory revisited.* Journal of Physics: Conference Series, 2007. **75**(1): p. 012010.
25. Phillips, D.G., *An Investigation on Diffuser Augmented Wind Turbine Design*, in *Department of Mechanical Engineering*. 2003, University of Auckland. p. 370.
26. Kirke, B., *Developments in ducted water turbines.* 2003: p. 12.
27. Bowditch, N., *Chapter 9: Tides and Tidal Currents*, in *The American Practical Navigator*. 2013, Skyhorse Publishing.
28. Couch, S.J. and I. Bryden, *Tidal current energy extraction: Hydrodynamic resource characteristics.* Proceedings of the Institution of Mechanical Engineers, Part M: Journal of Engineering for the Maritime Environment, 2006. **220**(4): p. 185-194.
29. Easton, M.C., D.K. Woolf, and P.A. Bowyer, *The dynamics of an energetic tidal channel, the Pentland Firth, Scotland.* Continental Shelf Research, 2012. **48**(0): p. 50-60.
30. Bryden, I.G., et al., *Tidal current resource assessment.* Proceedings of the Institution of Mechanical Engineers, Part A: Journal of Power and Energy, 2007. **221**(2): p. 125-135.
31. EMEC, *Assessment of Tidal Energy Resource*. 2009, European Marine Energy Centre.
32. Cornett, A., *OES-IA Guidance on Assessing Tidal Current Energy Resources*, in *3rd International Conference on Ocean Energy*. 2010: Bilbao, Spain.
33. EMEC, *Tidal Resource Assessment*, EMEC, Editor. 2011.
34. Bryden, I.G., et al., *Matching tidal current plants to local flow conditions.* Energy, 1998. **23**(9): p. 699-709.
35. Mason-Jones, A., et al., *Non-dimensional scaling of tidal stream turbines.* Energy, 2012. **44**(1): p. 820-829.
36. Milne, I.A., et al., *Characteristics of the Onset Flow Turbulence at a Tidal-Stream Power Site*, in *EWTEC 2011*. 2011: Southampton.
37. Thomson, J., et al., *Measurements of Turbulence at Two Tidal Energy Sites in Puget Sound, WA.* Oceanic Engineering, IEEE Journal of, 2012. **37**(3): p. 363-374.
38. Maganga, F., et al., *Experimental characterisation of flow effects on marine current turbine behaviour and on its wake properties.* Renewable Power Generation, IET, 2010. **4**(6): p. 498-509.
39. Betz, A., *Das Maximum der theoretisch möglichen Ausnützung des Windes durch Windmotoren. Zeitschrift für das gesamte Turbinenwesen*, 1920. **26**: p. 307-309.

40. van Kuik, G.A.M., *The Lanchester–Betz–Joukowsky limit.* Wind Energy, 2007. **10**(3): p. 289-291.
41. Gorban, A.N., A.M. Gorlov, and V.M. Silantyev, *Limits of the Turbine Efficiency for Free Fluid Flow.* Journal of Energy Resources Technology, 2001. **123**(4): p. 311-317.
42. Thake, J., *Development, Installation and Testing of a Large Scale Tidal Current Turbine*. 2005, DTI.
43. Manwell, J.F., J.G. McGowan, and A.L. Rogers, *Wind Energy Explained: Theory, Design and Application*. 2002: John Wiley & Sons Ltd. 704.
44. de Vries, O., *Fluid Dynamic Aspects of Wind Energy Conversion*. 1979, Advisory Group for Aerospace Research and Development: Neuilly-sur-Seine, France.
45. Turnock, S.R., et al., *Modelling tidal current turbine wakes using a coupled RANS-BEMT approach as a tool for analysing power capture of arrays of turbines.* Ocean Engineering, 2011. **38**: p. 1300-1307.
46. MacLeod, A., et al. *Wake effects in tidal current turbine farms*. in *International Conference on Marine Renewable Energy*. 2002. Newcastle, UK.
47. Batten, W.M.J., M.E. Harrison, and A.S. Bahaj, *Accuracy of the actuator disc-RANS approach for predicting the performance and wake of tidal turbines.* Philosophical Transactions of the Royal Society A: Mathematical, Physical and Engineering Sciences, 2013. **371**(1985).
48. Bai, L. and R.R.G. Spence. *Investigation of the influence of array arrangement and spacing on tidal energy converter (TEC) performance using a 3-dimensional CFD model*. in *8th European Wave and Tidal Energy Conference*. 2009. Uppsala, Sweden.
49. Williams, A.J., et al., *Combined BEM-CFD Modelling of Tidal Stream Turbines Using Site Data* in *International Conference on Renewale Energies and Power Quality*. 2010: Granada, Spain.
50. Harrison, M.E., et al., *A comparison between CFD simulations and experiments for predicting the far wake of horizontal axis tidal turbines*, in *8th European Wave and Tidal Energy Conference*. 2009.
51. Bahaj, A.S., L.E. Myers, and G. Thompson, *Characterising the wake of horizontal axis marine current turbines*, in *Seventh European Wave and Tidal Energy Conference*. 2007.
52. Morris, C.E., et al. *Evaluation of the swirl characteristics of a tidal stream turbine wake*. in *10th European Wave and Tidal Energy Conference*. 2013. Aalborg, Denmark.
53. Gilbert, B.L., R.A. Oman, and K.M. Foreman, *Fluid dynamics of diffuser-augmented wind turbines.* Journal of Energy, 1978. **2**(6): p. 368-374.
54. ESDU, *Introduction to Design and Performance Data for Diffusers*. 1976, ESDU International Plc.
55. ESDU, *Performance Improvement of Axial Diffusers for Incompressible Flow*. 1988, ESDU International Plc.
56. Bedard, R., *Tidal in Stream Energy Conversion (TISEC) Devices - Project Definition Study*, in *Tidal in Stream Energy Conversion Feasibility Demonstration Project*. 2005, Electric Power Research Institute. p. 185.
57. McDonald, A.T. and R.W. Fox, *An experimental investigation of incompressible flow in conical diffusers.* International Journal of Mechanical Sciences, 1966. **8**(2): p. 125-139.
58. Gibson, A.H., *V. On the Resistance to Flow of Water through Pipes or Passages having Divergent Boundaries.* Earth and Environmental Science Transactions of the Royal Society of Edinburgh, 1912. **48**(01): p. 97-116.

59. Patterson, G.N., *Modern Diffuser Design.* Aircraft Engineering and Aerospace Technology, 1938. **10**: p. 267.
60. Cockrell, D.J. and E. Markland, *A Review of Incompressible Diffuser Flow: A Reappraisal of an Article by G. N. Patterson entitled 'Modern Diffuser Design' which was published in this journal twenty-five years ago.* Aircraft Engineering and Aerospace Technology, 1963. **35**(10): p. 286 - 292.
61. Fox, R.W., A.T. McDonald, and R.V. van Dewoestine, *Effects of swirling inlet flow on pressure recovery in conical diffusers.* AIAA Journal, 1971. **9**(10): p. 2014-2018.
62. Lohmann, R.P., E.T. Brookman, and S.J. Markowski, *Swirling Flow Through Annular Diffusers With Conical Walls.* Journal of Fluids Engineering, 1979. **101**(2): p. 224-229.
63. Elkersh, A.M., A.H. Elgammal, and N.R.L. Maccallum, *An Experimental Investigation of the Performance of Equiangular Annular Diffusers with Swirled Flow.* Proceedings of the Institution of Mechanical Engineers, Part C: Journal of Mechanical Engineering Science, 1985. **199**(4): p. 293-297.
64. Kumar, D.S. and K.L. Kumar, *Effect of swirl on pressure recovery in annular diffusers.* Journal of Mechanical Engineering Science, 1980. **22**(6): p. 305-313.
65. Clausen, P.D., S.G. Koh, and D.H. Wood, *Measurements of a swirling turbulent boundary layer developing in a conical diffuser.* Experimental Thermal and Fluid Science, 1993. **6**(1): p. 39-48.
66. Cerantola, D. and A. Birk. *Experimental analysis of swirl in short annular diffusers with negative wall angles*. in *ASME Turbo Expo 2014: Turbine Technical Conference and Exposition*. 2014: American Society of Mechanical Engineers.
67. Medici, D. and P.H. Alfredsson, *Measurements on a wind turbine wake: 3D effects and bluff body vortex shedding.* Wind Energy, 2006. **9**(3): p. 219-236.
68. Hoffmann, J.A., *Effects of Free-Stream Turbulence on Diffuser Performance.* Journal of Fluids Engineering, 1981. **103**(3): p. 385-390.
69. Hoffmann, J.A. and G. Gonzalez, *Effects of Small-Scale, High Intensity Inlet Turbulence on Flow in a Two-Dimensional Diffuser.* Journal of Fluids Engineering, 1984. **106**(2): p. 121-124.
70. Azad, R.S. and S.Z. Kassab, *Turbulent flow in a conical diffuser: Overview and implications.* Physics of Fluids A: Fluid Dynamics, 1989. **1**(3): p. 564-573.
71. Azad, R.S., *Turbulent flow in a conical diffuser: A review.* Experimental Thermal and Fluid Science, 1996. **13**(4): p. 318-337.
72. Klein, A., *Review: Effects of Inlet Conditions on Conical-Diffuser Performance.* Journal of Fluids Engineering, 1981. **103**(2): p. 250-257.
73. Fox, R.W. and S.J. Kline, *Flow Regimes in Curved Subsonic Diffusers.* Journal of Fluids Engineering, 1962. **84**(3): p. 303-312.
74. Dean, J.R.C. and Y. Senoo, *Rotating Wakes in Vaneless Diffusers.* Journal of Fluids Engineering, 1960. **82**(3): p. 563-570.
75. Adenubi, S.O., *Performance and Flow Regime of Annular Diffusers With Axial Turbomachine Discharge Inlet Conditions.* Journal of Fluids Engineering, 1976. **98**(2): p. 236-242.
76. Zierer, T., *Experimental Investigation of the Flow in Diffusers Behind an Axial Flow Compressor.* Journal of Turbomachinery, 1995. **117**(2): p. 231-239.

77. Senoo, Y. and M. Nishi, *Improvement of the Performance of Conical Diffusers by Vortex Generators.* Journal of Fluids Engineering, 1974. **96**(1): p. 4-10.
78. Lengani, D., et al., *Turbulent boundary layer separation control and loss evaluation of low profile vortex generators.* Experimental Thermal and Fluid Science, 2011. **35**(8): p. 1505-1513.
79. Santner, C., et al., *The Application of Low-Profile Vortex Generators in an Intermediate Turbine Diffuser.* Journal of Turbomachinery, 2012. **134**(1): p. 011023-011023.
80. Zhang, Y., H. Chen, and S. Fu, *A Karman-Vortex Generator for passive separation control in a conical diffuser.* Science China Physics, Mechanics and Astronomy, 2012. **55**(5): p. 828-836.
81. Nicoll, W.B. and B.R. Ramaprian, *Performance of Conical Diffusers With Annular Injection at Inlet.* Journal of Fluids Engineering, 1970. **92**(4): p. 827-835.
82. Kwong, A.H.M. and A.P. Dowling, *Active boundary-layer control in diffusers.* AIAA Journal, 1994. **32**(12): p. 2409-2414.
83. Lo, K.P., C.J. Elkins, and J.K. Eaton, *Separation control in a conical diffuser with an annular inlet: center body wake separation.* Experiments in Fluids, 2012. **53**(5): p. 1317-1326.
84. Abe, K., et al., *Experimental and numerical investigations of flow fields behind a small wind turbine with a flanged diffuser.* Journal of Wind Engineering and Industrial Aerodynamics, 2005. **93**(12): p. 951-970.
85. Bet, F. and H. Grassmann, *Upgrading conventional wind turbines.* Renewable Energy, 2003. **28**(1): p. 71-78.
86. Chen, T.Y., Y.T. Liao, and C.C. Cheng, *Development of small wind turbines for moving vehicles: Effects of flanged diffusers on rotor performance.* Experimental Thermal and Fluid Science, 2012. **42**(0): p. 136-142.
87. Flay, R., T. Nash, and D. Phillips, *Aerodynamic Analysis and Monitoring of the Vortec 7 Diffuser Augmented Wind Turbine*, in *Institution of Professional Engineers New Zealand (1998: Auckland, New Zealand)*. 1998, Institution of Professional Engineers New Zealand: Wellington, N.Z.
88. Fletcher, C.A.J., *Computational Analysis of Diffuser Augmented Wind Turbines.* Energy Conversion and Management, 1981. **21**(3): p. 10.
89. Foreman, K.M., *Preliminary Design and Economic Investigations of Diffuser Augmented Wind Turbines (DAWT).* 1981, Grumman Aerospace Corporation.
90. Foreman, K.M., *Size Effects in DAWT Innovative Wind Energy System Design.* Journal of Solar Energy Engineering, 1983. **105**(4): p. 401-407.
91. Gilbert, B.L. and K.M. Foreman, *Experiments With a Diffuser-Augmented Model Wind Turbine.* Journal of Energy Resources Technology, 1983. **105**(1): p. 46-53.
92. Hansen, M.O.L., N.N. Sørensen, and R.G.J. Flay, *Effect of Placing a Diffuser around a Wind Turbine.* Wind Energy, 2000. **3**(4): p. 207-213.
93. Igra, O., *Compact shrouds for wind turbines.* Energy Conversion, 1977. **16**(4): p. 149-157.
94. Igra, O., *Research and Development for Shrouded Wind Turbines.* Energy Conversion and Management, 1981. **21**(1): p. 35.
95. Matsushima, T., S. Takagi, and S. Muroyama, *Characteristics of a highly efficient propeller type small wind turbine with a diffuser.* Renewable Energy, 2006. **31**(9): p. 1343-1354.

96. Ohya, Y. and T. Karasudani, *A Shrouded Wind Turbine Generating High Output Power with Wind-lens Technology.* Energies, 2010. **3**(4): p. 634-649.
97. Ohya, Y., et al., *Development of a shrouded wind turbine with a flanged diffuser.* Journal of Wind Engineering and Industrial Aerodynamics, 2008. **96**(5): p. 524-539.
98. Phillips, D.G., P.J. Richards, and R.G.J. Flay, *Diffuser Development for a Diffuser Augmented Wind Turbine Using Computational Fluid Mechanics.* 2008, Department of Mechanical Engineering, The University of Auckland.
99. Belloni, C.S.K. and R.H.J. Willden. *Flow Field and Performance Analysis of Bidirectional and Open-centre Ducted Tidal Turbines*. in *European Wave and Tidal Energy Conference*. 2011. Southampton.
100. Gaden, D.L.F. and E.L. Bibeau, *A numerical investigation into the effect of diffusers on the performance of hydro kinetic turbines using a validated momentum source turbine model.* Renewable Energy, 2010. **35**: p. 1152-1158.
101. Huihui, S. and Y. Kyozuka. *Analysis of performances of a shrouded horizontal axis tidal turbine*. in *OCEANS, 2012 - Yeosu*. 2012.
102. Khunthongjan, P. and U. Teeboonma. *Duct Design for Water Current Turbine Application*. in *4th GMSARN International Conference on Energy Security and Climate Change: Problems & Issues in GMS*. 2009. Ha Long City, Vietnam.
103. Luquet, R., et al., *Design and model testing of an optimised ducted marine current turbine*, in *European Wave and Tidal Energy Conference*. 2011: Southampton.
104. Mehmood, N., Z. Liang, and J. Khan, *CFD Study of NACA 0018 for Diffuser Design of Tidal Current Turbines.* Research Journal of Applied Sciences, Engineering and Technology, 2012. **21**(4): p. 4552-4560.
105. Munch, C., et al., *Design and Performance Assessment of a Tidal Ducted Turbine*, in *3rd IAHR International Meeting of the Workgroup on Cavitation and Dynamic Problems in Hydraulic Machinery and Systems*. 2009, : Brno, Czech Republic.
106. Ponta, F.L. and P.M. Jacovkis, *Marine-current power generation by diffuser-augmented floating hydro-turbines.* Renewable Energy, 2008. **33**(4): p. 665-673.
107. Reinecke, J., T.W. von Backström, and G. Venter, *Effect of a Diffuser on the Performance of an Ocean Current Turbine*, in *European Wave and Tidal Energy Conference*. 2011: Southampton.
108. Setoguchi, T., N. Shiomi, and K. Kaneko, *Development of two-way diffuser for fluid energy conversion system.* Renewable Energy, 2004. **29**(10): p. 1757-1771.
109. Shives, M. and C. Crawford. *Overall Efficiency of Ducted tidal current turbines*. in *OCEANS 2010*. 2010.
110. Shives, M. and C. Crawford, *Developing an empirical model for ducted tidal turbine performance using numerical simulation results.* Proceedings of the Institution of Mechanical Engineers, Part A: Journal of Power and Energy, 2011. **226**(1): p. 112-125.
111. Loeffler, A.L., *Flow Field Analysis and Performance of Wind Turbines Employing Slotted Diffusers.* Journal of Solar Energy Engineering, 1981. **103**(1): p. 17-22.
112. Dick, E., *Power Limits for Wind Energy Concentrator Systems.* Wind Engineering, 1986. **10**(2): p. 98-115.
113. Lawn, C.J., *Optimization of the power output from ducted turbines.* Proceedings of the Institution of Mechanical Engineers, Part A: Journal of Power and Energy, 2003. **217**(1): p. 107-117.

114. Werle, M.J. and W.M. Presz, *Ducted Wind/Water Turbines and Propellers Revisited.* Journal of Propulsion and Power, 2008. **24**(5).
115. Shives, M., *Hydrodynamic Modeling, Optimization and Performance Assessment for Ducted and Non-ducted Tidal Turbines*, in *Department of Mechanical Engineering*. 2011, University of Victoria.
116. McIntosh, S.C., C.F. Fleming, and R.H. Willden, *Embedded RANS-BEM Tidal Turbine Design*, in *9th European Wave and Tidal Energy Conference*. 2011: Southampton, U.K.
117. Fleming, C.F., S.C. McIntosh, and R.H. Willden. *Design and analysis of a bi-directional ducted tidal turbine*. in *9th European Wave and Tidal Energy Conference*. 2011. Southampton, U.K.
118. Ohya, Y., et al., *Numerical Studies of Flow around a Wind Turbine Equipped with a Flanged-Diffuser Shroud using an Actuator-Disk Model.* Wind Engineering, 2012. **36**(4): p. 455-472.
119. Kogan, A. and A. Seginer, *Shrouded Aerogenerator Design Study II: Axisymmetrical Shroud Performance*. 1963, Department of Aeronautical Engineering, Technion - Israel Institute of Technology.
120. Bahaj, A.S., W.M.J. Batten, and G. McCann, *Experimental verifications of numerical predictions for the hydrodynamic performance of horizontal axis marine current turbines.* Renewable Energy, 2007. **32**(15): p. 2479-2490.
121. Bahaj, A.S., et al., *Power and thrust measurements of marine current turbines under various hydrodynamic flow conditions in a cavitation tunnel and a towing tank.* Renewable Energy, 2007. **32**(3): p. 407-426.
122. Sun, H. and Y. Kyozuka. *Analysis of performances of a shrouded horizontal axis tidal turbine*. in *OCEANS, 2012 - Yeosu*. 2012.
123. Fleming, C.F., S.C. McIntosh, and R.H.J. Willden, *Tidal Turbine Performance in Sheared Flow*, in *10th European Wave and Tidal Energy Conference*. 2013: Aalborg, Denmark.
124. Glauert, H., *Airplane Propellers*, in *Aerodynamic Theory*, W.F. Durand, Editor. 1935, Springer Verlag: Berlin.
125. Goldstein, S., *On the vortex theory of screw propellers.* Proceedings of the Royal Society of London, 1929. **123**(792).
126. Moriarty, P.J. and A.C. Hansen, *AeroDyn Theory Manual*. 2005: National Renewable Energy Laboratory.
127. Shen, W.Z., et al., *Tip loss corrections for wind turbine computations.* Wind Energy, 2005. **8**(4): p. 457-475.
128. Eggleston, D.M. and F.S. Stoddard, *Wind turbine engineering design*. 1987: Van Nostrand Reinhold.
129. Mikkelsen, R., *Actuator disc methods applied to wind turbines*, in *Department of Mechanical Engineering*. 2003, Technical University of Denmark: Lyngby.
130. McIntosh, S.C., C.F. Fleming, and R.H. Willden. *Embedded RANS-BEM Tidal Turbine Design*. in *9th European Wave and Tidal Energy Conference*. 2011. Southampton, U.K.
131. El-Behery, S.M. and M.H. Hamed, *A comparative study of turbulence models performance for separating flow in a planar asymmetric diffuser.* Computers & Fluids, 2011. **44**(1): p. 248-257.
132. DalBello, T., V. Dippold, and N.J. Georgiadis, *Computational Study of Separating Flow in a Planar Subsonic Diffuser*. 2005, NASA.
133. Shojaeefard, M.H., A. Mirzaei, and A. Babaei, *Shape optimization of draft tubes for Agnew microhydro turbines.* Energy Conversion and Management, 2014. **79**(0): p. 681-689.

134. Menter, F., R. Langtry, and S. Völker, *Transition Modelling for General Purpose CFD Codes.* Flow, Turbulence and Combustion, 2006. **77**(1): p. 277-303.
135. Langtry, R.B. and F.R. Menter, *Correlation-Based Transition Modeling for Unstructured Parallelized Computational Fluid Dynamics Codes.* AIAA Journal, 2009. **47**(12): p. 2894-2906.
136. Sharqawy, M.H., J.H. Lienhard, and S.M. Zubair, *Thermophysical properties of seawater: A review of existing correlations and data.* Desalination and Water Treatment, 2010. **16**(1-3): p. 354-380.
137. Crespo, A. and J. Hernandez, *Turbulence characteristics in wind-turbine wakes.* Journal of Wind Engineering and Industrial Aerodynamics, 1996. **61**(1): p. 71-85.
138. Apsley, D.D. and M.A. Leschziner, *Advanced Turbulence Modelling of Separated Flow in a Diffuser.* Flow, Turbulence and Combustion, 2000. **63**(1-4): p. 81-112.
139. Andrew, S., et al., *Improving the CFD Predictions of Airfoils in Stall*, in *43rd AIAA Aerospace Sciences Meeting and Exhibit*. 2005, American Institute of Aeronautics and Astronautics.
140. Simpson, T.W., et al., *Metamodels for Computer-based Engineering Design: Survey and recommendations.* Engineering with Computers, 2001. **17**(2): p. 129-150.
141. McKay, M.D., R.J. Beckman, and W.J. Conover, *A Comparison of Three Methods for Selecting Values of Input Variables in the Analysis of Output from a Computer Code.* Technometrics, 1979. **21**(2): p. 239-245.
142. Piegl, L.A. and W. Tiller, *The NURBS Book*. 1997: Springer. 646.
143. Wang, G.G. and S. Shan, *Review of Metamodeling Techniques in Support of Engineering Design Optimization.* Journal of Mechanical Design, 2006. **129**(4): p. 370-380.
144. Kleijnen, J.P.C., *Kriging metamodeling in simulation: A review.* European Journal of Operational Research, 2009. **192**(3): p. 707-716.
145. Huang, D., et al., *Global Optimization of Stochastic Black-Box Systems via Sequential Kriging Meta-Models.* Journal of Global Optimization, 2006. **34**(3): p. 441-466.
146. Wang, H., et al. *Aerodynamic Optimization System Development for Low Pressure Exhaust Hood of Steam Turbine*. in *ASME Turbo Expo 2010*. 2010. Glasgow.
147. Jeong, S., M. Murayama, and K. Yamamoto, *Efficient Optimization Design Method Using Kriging Model.* Journal of Aircraft, 2005. **42**(2): p. 413-420.
148. Sakata, S., F. Ashida, and M. Zako, *Structural optimization using Kriging approximation.* Computer Methods in Applied Mechanics and Engineering, 2003. **192**(7â€“8): p. 923-939.
149. Lophaven, S.N., H.B. Nielsen, and J. Sondergaard, *DACE: A Matlab Kriging Toolbox*. 2002, Technical University of Denmark.
150. Borries, O., *Surrogate Modelling using DACE*, in *Informatics and Mathematical Modelling*. 2009, Technical University of Denmark: Kongens Lyngby. p. 102.
151. Li, M., *An Improved Kriging Assisted Multi-Objective Genetic Algorithm.* Journal of Mechanical Design, 2008. **130**: p. 825-836.
152. Young, F.R., *Cavitation*. 1999: World Scientific.
153. Molland, A.F., et al., *Measurements and predictions of forces, pressures and cavitation on 2-D sections suitable for marine current turbines.* Proceedings

of the Institution of Mechanical Engineers, Part M: Journal of Engineering for the Maritime Environment, 2004. **218**(2): p. 127-138.
154. Batten, W.M.J., et al., *Experimentally validated numerical method for the hydrodynamic design of horizontal axis tidal turbines.* Ocean Engineering, 2007. **34**(7): p. 1013-1020.
155. Drela, M. and M.B. Giles, *Viscous-Inviscid Analysis of Transonic and Low Reynolds Number Airfoils.* AIAA Journal, 1987. **25**(10): p. 1347-1355.
156. Yarusevych, S., P.E. Sullivan, and J.G. Kawall, *On vortex shedding from an airfoil in low-Reynolds-number flows.* Journal of Fluid Mechanics, 2009. **632**: p. 245-271.
157. Saffman, P.G., *Vortex dynamics*. 1992: Cambridge university press.
158. Devenport, W.J., et al., *The structure and development of a wing-tip vortex.* Journal of Fluid Mechanics, 1996. **312**: p. 67-106.
159. MacEnri, J., M. Reed, and T. Thiringer, *Influence of tidal parameters on SeaGen flicker performance.* Philosophical Transactions of the Royal Society A: Mathematical, Physical and Engineering Sciences, 2013. **371**(1985): p. 20120247.
160. Li, Y., et al. *Inflow measurement in a tidal strait for deploying tidal current turbines: lessons, opportunities and challenges*. in *ASME 2010 29th international conference on ocean, offshore and arctic engineering*. 2010. Shanghai, China: American Society of Mechanical Engineers.
161. Thomson, J., et al. *Quantifying turbulence for tidal power applications*. in *OCEANS 2010*. 2010.
162. Milne, I.A., et al., *Characteristics of the turbulence in the flow at a tidal stream power site.* Philosophical Transactions of the Royal Society A: Mathematical, Physical and Engineering Sciences, 2013. **371**(1985).
163. Thomson, J., et al. *Tidal turbulence spectra from a compliant mooring*. in *Marine Energy Technology Symposium*. 2013. Washington, DC.
164. Elliott, D.L. and J. Cadogan, *Effects of wind shear and turbulence on wind turbine power curves.* Wind Energy, 1990. **1**: p. 10-14.
165. Blackmore, T., et al., *Influence of turbulence on the drag of solid discs and turbine simulators in a water current.* Experiments in Fluids C7 - 1637, 2013. **55**(1): p. 1-10.
166. Mycek, P., et al., *Experimental study of the turbulence intensity effects on marine current turbines behaviour. Part I: One single turbine.* Renewable Energy, 2014. **66**(0): p. 729-746.
167. Watkins, S., S. Ravi, and B. Loxton, *The effect of turbulence on the aerodynamics of low Reynolds number wings.* Engineering Letters, 2009. **18**(3): p. 279.
168. Devinant, P., T. Laverne, and J. Hureau, *Experimental study of wind-turbine airfoil aerodynamics in high turbulence.* Journal of Wind Engineering and Industrial Aerodynamics, 2002. **90**(6): p. 689-707.
169. Holzäpfel, F., et al., *Analysis of wake vortex decay mechanisms in the atmosphere.* Aerospace Science and Technology, 2003. **7**(4): p. 263-275.
170. Norris, G., *Flow Through S-Shaped Annular, Inter-Turbine Diffusers*, in *School of Engineering*. 1998, University of Durham. p. 228.
171. Sims-Williams, D.B. and R.G. Dominy, *The Design of a New Wind Tunnel for Vehicle Aerodynamics Research*, in *4th MIRA International Vehicle Aerodynamics Conference*. 2002: Warwick, U.K.
172. Sims-Williams, D.B. and R.G. Dominy, *The Design of an Open-Jet Wind Tunnel for Model Testing*, in *SAE Technical Paper*. 2002, SAE Int.

173. Mankowski, O.A., *The Wind Tunnel Simulation and Effect of Turbulent Airflow on Automotive Aerodynamics*, in *School of Engineering and Computing Sciences*. 2014, Durham University: Durham.
174. Garner, H.C., et al., *Subsonic wind tunnel wall corrections*. 1966, DTIC Document.
175. Ewald, B., *Wind Tunnel Wall Corrections (la Correction des effets de paroi en soufflerie)*. 1998, DTIC Document.
176. Chen, T.Y. and L.R. Liou, *Blockage corrections in wind tunnel tests of small horizontal-axis wind turbines.* Experimental Thermal and Fluid Science, 2011. **35**(3): p. 565-569.
177. Hughes, I.G. and T.P.A. Hase, *Measurements and Their Uncertainties: A Practical Guide to Modern Error Analysis*. 2010, Oxford: Oxford Univeristy Press.
178. ANSI, *Specification for Octave-Band and Fractional-Octave Band Analog and Digital Filters*. 2004.
179. Viterna, L.A. and R.D. Corrigan, *Fixed pitch rotor performance of large horizontal axis wind turbines.* Large Horizontal-Axis Wind Turbines, 1982. **1**: p. 69-85.
180. Stallard, T., et al. *Interactions between tidal turbine wakes: experimental study of a group of 3-bladed rotors*. in *Proceedings of the 9th European Wave and Tidal Energy Conference*. 2011. Southampton, U.K.
181. Rodman, L.C., N.J. Wood, and L. Roberts, *Experimental investigation of straight and curved annular wall jets.* AIAA Journal, 1989. **27**(8): p. 1059-1067.
182. Fingersh, L., M. Hand, and A. Laxson, *Wind Turbine Design Costs and Scaling Model*. 2006, NREL.
183. Li, Y., B.J. Lence, and S.M. Calisal, *An integrated model for estimating energy cost of a tidal current turbine farm.* Energy Conversion and Management, 2011. **52**(3): p. 1677-1687.
184. Bir, G.S., M.J. Lawson, and Y. Li, *Structural design of a horizontal-axis tidal current turbine composite blade*, in *ASME 30th International Conference on Ocean, Offshore and Arctic, Engineering*. 2011, National Renewable Energy Laboratory: Rotterdam, Netherlands.
185. Fraenkel, P.L., *Marine Current Turbines: An Update*, in *All Energy 2007*. 2007: Aberdeen.
186. ONS. *Consumer Price Indices - CPI indices*. 2014 30/07/2014]; Available from: http://www.ons.gov.uk/ons/datasets-and-tables/.
187. USBLS, *CPI Detailed Report - May 2014*. 2014, United States Bureau of Labor.
188. ECB. *Harmonised indices of consumer prices, breakdown by purpose of consumption*. 2014 30/07/2014]; Available from: www.ecb.europa.eu/stats/prices/hicp/.
189. Engels, W., T. Obdam, and F. Savenije, *Current developments in wind - 2009*. 2009, Energy Research Centre of the Netherlands.
190. Aly, H.H.H. and M.E. El-Hawary. *State of the art for tidal currents electric energy resources*. in *Electrical and Computer Engineering (CCECE), 2011 24th Canadian Conference on*. 2011.
191. Fraenkel, P. *Development and testing of Marine Current Turbine's SeaGen 1.2 MW tidal stream turbine*. in *3rd International Conference on Ocean Energy*. 2010. Bilbao, Spain.
192. Douglas, C.A., G.P. Harrison, and J.P. Chic, *Life cycle assessment of the Seagen marine current turbine.* Proceedings of the Institution of Mechanical

Engineers, Part M: Journal of Engineering for the Maritime Environment 2008, 2008. **222**(1).
193. Nystrom, H.E., et al., *Financial viability of fiber-reinforced polymer (FRP) bridges.* Journal of Management in Engineering, 2003. **19**(1): p. 2-8.
194. Matthews, S., *Marine Current Turbines Supply Chain Analysis: A review of the Kyle Rhea tidal energy project*. 2011, BVG Associates, Marine Current Turbines.
195. Trust, C., *Accelerating Marine Energy*. 2011, Carbon Trust.
196. SIOcean, *Ocean Energy: Cost of Energy and Cost Reduction Opportunities* 2013, Strategic Initiative for Ocean Energy.
197. Kirke, B., *Developments in ducted water current turbines.* Tidal paper, 2006(25-04).
198. Entec, *Cost Estimation Methodology: The Marine Energy Challenge approach to estimating the cost of energy produced by marine energy systems*. 2006, Entec UK Ltd., The Carbon Trust.
199. Bahaj, A.S. and L. Myers, *Analytical estimates of the energy yield potential from the Alderney Race (Channel Islands) using marine current energy converters.* Renewable Energy, 2004. **29**(12): p. 1931-1945.
200. Henfridsson, U., et al., *Wave energy potential in the Baltic Sea and the Danish part of the North Sea, with reflections on the Skagerrak.* Renewable Energy, 2007. **32**(12): p. 2069-2084.
201. Foreman, K.M. and B.L. Gilbert, *Further Investigations of Diffuser Augmented Wind Turbines Parts I and II*. 1979, Grumman Research Dept: New York.
202. Starling, M. and A. Scott, *Foundations and Moorings for Tidal Stream Systems*. 2009, BMT Cordah Limited, The Carbon Trust.
203. Clarke, J.A., et al., *Regulating the output characteristics of tidal current power stations to facilitate better base load matching over the lunar cycle.* Renewable Energy, 2006. **31**(2): p. 173-180.
204. Masters, G.M., *Renewable and efficient electric power systems*. 2013: John Wiley & Sons.
205. Arup, *Review of the generation costs and deployment potential of renewable electricity technologies in the UK*. 2011, Department of Energy and Climate Change.